THE UNIVERSITY OF TULSA

THE GRADUATE SCHOOL

A CONDITIONAL SIMULATION METHOD FOR RESERVOIR DESCRIPTION USING GEOLOGICAL AND WELL PERFORMANCE CONSTRAINTS

by
Kirk B. Hird

A dissertation submitted in partial fulfillment of

the requirements for the degree of Doctor of Philosophy

in the Discipline of Petroleum Engineering

The Graduate School

The University of Tulsa

1993

THE UNIVERSITY OF TULSA

THE GRADUATE SCHOOL

A CONDITIONAL SIMULATION METHOD FOR RESERVOIR DESCRIPTION USING GEOLOGICAL AND WELL PERFORMANCE CONSTRAINTS

by

Kirk B. Hird

A DISSERTATION

APPROVED FOR THE DISCIPLINE OF

PETROLEUM ENGINEERING

By Dissertation Committee

Balmoran G Kellear, Chairperson

Albert C. Reynolds

Clayton Cook

Jack R. Jones

ABSTRACT

Hird, Kirk B. (Doctor of Philosophy in Petroleum Engineering)

A Conditional Simulation Method for Reservoir Description Using Geological and Well Performance Constraints (261 pp. - Chapter VI)

Directed by Dr. Mohan G. Kelkar

(322 words)

Existing geological, petrophysical and geophysical conditioning data are always sparse in comparison to reservoir size and complexity. Although conditional simulation techniques have been developed to honor such information, the resulting so-called "equally probable" realizations of reservoir properties can result in widely varying simulated well performance. This is true even when the variogram adequately captures spatial correlation structures. Reservoir descriptions must be consistent with individual well performance before they can be considered as being realistic and thus valuable for optimizing reservoir management. However, the inverse problem of directly determining reservoir properties from well performance data is an extremely complex one, with no practical solution currently existing.

This dissertation investigates the applicability of simulated annealing to constraining reservoir descriptions to primary and waterflood performance. Quantifiable spatial distribution characteristics of petrophysical properties which impact well performance are identified. A conditional simulation method which incorporates conventional constraints (well conditioning data, univariate distribution and variogram) and these indirect performance constraints is developed. Various five-spot pattern synthetic case studies are used to validate the method. Although excellent matches of well performance are

obtained using the indirect performance constraints without including the variogram constraint, it is shown that the resulting alternative reservoir descriptions poorly reproduce actual spatial reservoir properties. Thus, it is concluded that spatial correlation structures cannot be extracted from performance data. The robustness and flexibility of the approach is demonstrated using a 59 well, two-dimensional, full-field system for which 327 constraints are imposed resulting in an excellent reproduction of actual well performance and reservoir porosity and permeability spatial distributions. Probability of exceedance maps are used to compare the relative contribution of various constraints in quantifying spatial uncertainties of petrophysical properties.

This technique can be used to significantly reduce the uncertainty of future well performance. Additionally, the uncertainty in the spatial distribution of reservoir properties can be significantly reduced. Thus, the impact of alternative operating conditions, such as infill drilling, can be more realistically evaluated.

ACKNOWLEDGEMENTS

There are many whom have provided assistance to the completion of this work. I greatly appreciate the technical guidance and direction given by Dr. Mohan Kelkar. The strong support Mohan provided while I attempted to maintain a balance of scholastic, work and family priorities was greatly appreciated. Also appreciated is the contribution by the other members of my committee, Dr. Albert Reynolds, Dr. Peyton Cook and Dr. Jack Jones.

I would like to thank Amoco Production Research for providing financial assistance and computing needs during my six years of scholastic endeavors.

A special thanks is extended to my father-in-law and mother-in-law, Tom and Janet Culpepper. Their continued support throughout this process is deeply appreciated. This work would have never reached a conclusion without the constant encouragement, love and prayers given by my wife Jenny and children Jessica, Jocelyn and Trevor. I dedicate this dissertation to Jenny, who has been my encourager throughout.

TABLE OF CONTENTS

TABLE OF CONTENTS (Continued)

TABLE OF CONTENTS (Continued)

TABLE OF CONTENTS (Continued)

LIST OF TABLES

LIST OF FIGURES

LIST OF FIGURES (Continued)

LIST OF FIGURES (Continued)

LIST OF FIGURES (Continued)

CHAPTER I

INTRODUCTION

The application of geostatistics to reservoir modeling has become popular in recent years. The primary reasons for this interest in geostatistics are threefold: 1) spatial reservoir heterogeneities can be quantified and modeled, 2) data at different scales, resolutions and degree of uncertainty ("softness") can be integrated into the reservoir description and 3) several alternative reservoir descriptions can be generated, all honoring the same input data (constraints), thereby providing a basis for quantifying uncertainty of future reservoir performance. The geostatistical technique possessing the above attributes is conditional simulation.

Conditional simulation methods have been developed which use several different data types/sources for conditioning. Considering how little of the reservoir is ever sampled or tested, it becomes extremely important to include all existing data when developing a reservoir description. Ironically, probably the most important and abundant data type is absent from the list of applied conditioning data--well performance data. Reproduction of historical well performance is considered one of the most important criteria for determining the validity of a reservoir description. However, the inverse problem of directly determining reservoir properties from well performance data is an extremely complex one, with no practical solution currently existing.

This dissertation addresses this deficiency in existing conditional simulation methods by investigating indirect means of constraining reservoir descriptions to well performance data. As is shown, incorporating these so-called "indirect performance constraints" into the conditional simulation framework not only results in reservoir descriptions which have simulated well performance comparable to historical well performance, but also are characterized by more realistic spatial reservoir properties. Hence, various operating strategies, such

as infill drilling, can be more realistically evaluated.

This introductory chapter summarizes the significant literary contributions pertinent to modeling reservoir heterogeneities. The motivation for quantifying heterogeneities and related methodologies will be presented. Conditional simulation will be discussed in greater detail. The characteristics of the modeling approach used in this work, simulated annealing, will be examined. Once the current state-of-the-art in reservoir modeling has been adequately presented, the objectives of this dissertation will be defined. Finally, an outline of subsequent chapters will be provided.

Background

The past decade has brought about a new awareness of the impact reservoir heterogeneities play on reservoir performance. More time and money is being invested in understanding and modeling the internal reservoir architecture than ever before. Such commitment is not without justification. Worldwide oil resources (discovered and undiscovered) are estimated to be 7.5 - 8.0 trillion bbls.[1] Remaining reserves at economic abandonment, based on existing technology, are estimated to be 5.3 - 5.6 trillion bbls. Based on current oil rates, this represents 250 years of production.[2] Although a large portion of this unrecoverable oil is considered irreducible, it is believed that a large fraction represents isolated, or compartmentalized reservoir structures. For example, infill drilling and extensions in Texas have resulted in considerably more additional reserves (73%) than new discoveries, tertiary recovery processes and delayed abandonment combined (16%).[3] The belief that only irreducible oil remains after secondary operations has been proven to be a fallacy. Realizing the potential of this huge resource base will require a good understanding of the impact heterogeneities have on reservoir performance.

Considering the paucity of measured data relative to reservoir size, the complexity of internal reservoir architecture and the complexity of rock/fluid interactions, it is not possible

to deterministically define the spatial distribution of reservoir properties. This limitation is being recognized with more regularity within the geoscience and engineering communities. Rather than a "best estimate" approach, probabilistic solutions are being pursued. Management is being presented with probability distributions of rates, reserves, net cash flow, etc., rather than downside, most likely and upside scenarios.

The increased awareness of the need for probabilistic solutions has led to the development of several probabilistic modeling techniques. Probabilistic models which are used to obtain spatial distributions of variables are referred to as stochastic models. Although several stochastic methods exist, the two basic methods are object-based and continuous. Descriptions of various stochastic techniques are included in Dubrule[4] and Haldorsen et al.[5] Several algorithms for generating reservoir architecture are presented in Haldorsen and MacDonald.[6] Other noteworthy discussions and comparisons of stochastic techniques are included in Haldorsen and Damsleth[7] and Alabert and Modot.[8]

Object-based techniques are also referred to as discrete, Marked-Point or Boolean methods. These methods are used to model the spatial distribution of geologic features, such as channel sands, deltas, offshore bars and faults. Several applications have been documented in the literature.[9-12] The geologic features are represented by simplistic geometric shapes distributed in space. Frequency distributions of dimensions, orientations and locations are used to determine the variability and placement of the geometric bodies. The distributions can be independent or correlated. Interaction of neighboring objects can be controlled by some of the techniques. The primary advantage of object-based models is their similarity to actual geologic depositional environments. A major disadvantage is the difficulties associated with conditioning such models with well data.

Modeling of continuous geologic variables falls in the area of geostatistics. Geostatistics refers to the modeling of regionalized variables, i.e., random variables which are distributed in space.[13] Geostatistical models used to generate equally plausible spatial distributions of a variable ("realizations") are typically referred to as conditional simula-

tions. Conditional simulations not only have an equal probability of occurrence, but each realization also honors the spatial distribution of the measured, or "hard" data. The theory and application of geostatistics is covered in Journel and Huijbregts,[13] Clark,[14] David[15] and Isaaks and Srivastava.[16]

The most common geostatistical function used to quantify spatial variability is the variogram. The variogram, $\gamma(h)$, is defined as the expectation of the squared difference between two random variables, Z(x) and Z(x+h), separated by a vector h:[13]

(1.1)

$$\gamma(h) = \frac{1}{2}E\{[Z(x) - Z(x+h)]^2\} = \gamma(x,h)$$

Application of this random function model requires multiple pairs of $Z(x)$ and $Z(x+h)$, i.e., measurements at the same location of multiple realizations of the same reservoir. To overcome this impractical limitation, the intrinsic hypothesis is applied, i.e., it is assumed that the variogram is not a function of x but of the separation vector h (lag) only. This assumption allows an estimator of the variogram, $\hat{\gamma}(h)$, to be calculated as follows:[16]

$$\hat{\gamma}(h) = \frac{1}{2N(h)} \sum_{i=1}^{N(h)} [z(x_i) - z(x_i+h)]^2 \qquad (1.2)$$

where $N(h)$ is the number of data pairs separated by lag h.

Geostatistics was first developed in the mining industry.[17] The principle geostatistical estimation technique used in mining is kriging. Unlike simulation, the purpose of kriging is to provide the minimum unbiased estimator of a variable; therefore, kriged estimates are characterized by minimum spatial variability whereas simulated estimates are characterized by representative variability. In petroleum applications, kriging is typically

used to estimate reservoir structure, thickness and any variable for which the best global or local estimate is desired, such as oil-in-place.

The conditional simulation technique extended in this work is simulated annealing. As the name implies, simulated annealing is a mathematical model which statistically mimics the molecular behavior of glass and metal while cooling from a liquid to a solid state during the annealing process. Early contributors to the development of this technique include Kirkpatrick et al.,[18] Cerny,[19] Metropolis et al.[20] and Geman and Geman.[21] In-depth discussion on the theory and application of simulated annealing are presented in Aarst and Korst[22] and Collins et al.[23] Farmer[24] was responsible for introducing simulated annealing to reservoir characterization. Others who have made significant contributions to the application of geologic modeling using simulated annealing include Perez,[25] Deutsch[26] and Ouenes.[27]

Central to all reservoir modeling techniques is the integration of data into the reservoir description. Since reservoir data are acquired by geologists, geophysicists and engineers, an interdisciplinary approach is required to integrate the data to obtain a consistent and realistic reservoir model. Sources of data include cores, logs, seismic surveys, outcrop surveys, pressure transient analyses, tracer surveys, production data and geologic interpretations. Integration of the above data types is not an easy task considering the wide variation in scales of measurement and degrees of resolution. For example, core plug-derived permeabilities represent a rock volume of about 0.0007 ft^3 whereas effective permeabilities obtained from pressure build-up surveys represent rock volumes on the order of 10^9 ft^3. Acoustic logs have a vertical resolution of about 2 ft; the vertical resolution of seismic acoustic velocities is at best 30 - 50 ft. Haldorsen[28] defines four scales of heterogeneity associated with reservoir modeling: microscopic, macroscopic, megascopic and gigascopic. Examples of these scales are pore throats, cores, grid blocks and reservoirs, respectively. Averaged volumes at one scale are used to obtain effective values at the next larger scale. Properly integrating all existing data at each respective

scale to obtain a consistent reservoir description which adequately captures heterogeneities impacting fluid flow is one of the central themes of reservoir characterization studies. The technique developed in this work is shown to be robust in integrating a variety of reservoir properties.

In general, a stochastic modeling approach is used in an attempt to translate geologic uncertainties to reservoir performance uncertainties. Integration of all available data into the reservoir description minimizes the range of uncertainty. It becomes very important to be able to identify the geologic characteristics which have the greatest impact on fluid flow and then focus on properly modeling their spatial geometries. Additional geologic constraints are identified in this dissertation which are shown to reduce reservoir performance uncertainties. Several recent case studies show the importance of identifying the heterogeneities which impact field performance.[29-36] Since the depositional environment can play a major role in dictating fluid flow characteristics, classification systems of internal reservoir architecture have been proposed.[30,37,38]

The concept of minimizing uncertainty by including additional conditional simulation constraints is illustrated in Figure 1.1. Stochastic modeling is used to generate several equally probable reservoir descriptions. These reservoir descriptions are then flow simulated to determine the range of possible outcomes. The frequency distribution of an example flow simulation output parameter, ultimate recovery, is depicted in Figure 1.1. If an insufficient number of constraints have been imposed on the system, it is very likely that the actual ultimate recovery represents an unlikely occurrence (i.e., it has a low probability of occurrence). This situation is represented by the frequency distribution labelled "conventional constraints." However, if additional constraints can be imposed, each having a significant influence on fluid flow characteristics, then the corresponding frequency distribution of outcome parameters should be greatly reduced. This is illustrated in Figure 1.1 by the distribution labelled "conventional & indirect performance constraints." Not only should the spread in possible outcomes be reduced but, as indi-

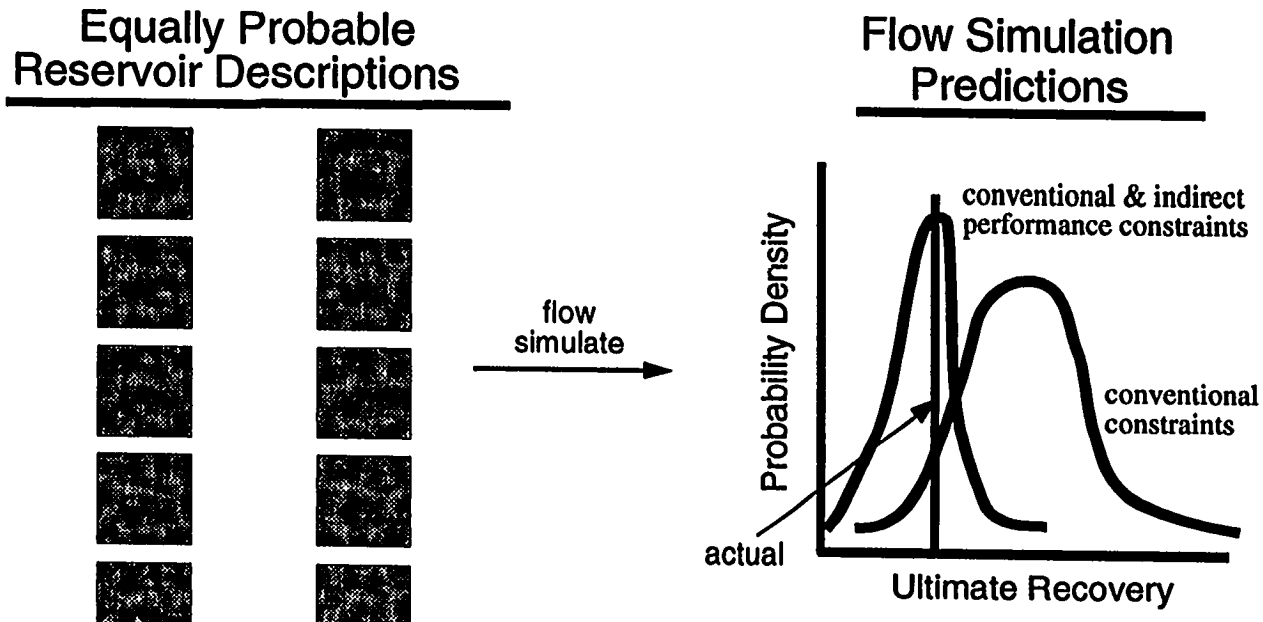

Figure 1.1 - Minimizing uncertainty using indirect performance constraints

cated by this second scenario, the actual value should fall well within the bounds of the revised frequency distribution. A more informed reservoir management decision can be made given the reduced range in possible outcomes.

Identifying and quantifying geologic characteristics which significantly impact fluid flow is not a simple task. In many cases, the most important reservoir characteristic which needs to be quantified is reservoir connectivity/continuity. The success of infill drilling, secondary and tertiary operations are very closely related to how well continuity has been defined, both vertically and laterally. In an analysis of the historical development of nine west Texas carbonate reservoirs, Barber et al.[39] show that infill drilling accounted for incremental oil recoveries ranging from 56% to 100%. The study also concluded that the perceived reservoir continuity consistently decreased as the result of each infill drilling program. The inability to quantify reservoir continuity from well data alone has lead to the development of statistical approaches. Weber[40] presents a probability distribution for shale intercalation lengths of several depositional environments. Higher energy depositional environments, such as distributary channels, are shown to have a much lower probability of having extensive shales than lower energy environments, such as marine. Lowry and Raheim[41] document sandstone body dimension statistics for several depositional systems. This type of information can be invaluable when attempting to model reservoir discontinuities. The reservoir connectivity measures developed in this dissertation are shown to be strongly correlated to waterflood efficiency and thus important conditional simulation constraints.

Haldorsen and Lake[42] document the state of the art in stochastic modeling of vertical flow barriers. Several stochastic modeling case studies have emphasized the importance of segregating realizations by their connectivity characteristics because of their influence on reservoir performance.[8,43-45] Empirical relationships of sand body geometry and deposition have been used to generate two- and three-dimensional reservoir descriptions of facies which are conditioned to a geological model and well data.[46-47]

Typically, facies are defined either as pay (sand) or non-pay (shale). Haldorsen and MacDonald[6] describe a similar technique in which appropriate conditioning rules are used to generate sands until a specified net fraction of sand is achieved. Well densities and locations are selected to determine the fraction of sand which is drainable ("accessibility factor") as a function of well spacing. The work documented in the following chapters demonstrates the usefulness of the new simulated annealing method in identifying potential infill drilling locations.

Others have used Boolean techniques to distribute sand bodies within a reservoir and determine the sand connectivity as a function of well spacing.[47] Stochastic indicator simulation[48] was developed to allow connectivity of extremes (high permeability streaks and shale barriers) to be honored. Indicator simulation and a random walker procedure was used by Srivastava[49] to determine the probability distribution of connected pore volume for a nine-spot pattern.

All of the above techniques use geological and statistical data to investigate connectivity. None of the methods use well performance data as conditioning constraints. Above all other reservoir data, well performance needs to be considered as the true litmus test when evaluating the validity of reservoir descriptions. After all, the underlying goal in a reservoir modeling study is to simulate reservoir performance, and this involves, by definition, the simulation of well rates and recoveries. Geologic models which do not result in realistic well performance are not realistic geologic models. So-called "equally probable" realizations are equally improbable if simulated well performance does not closely approximate historical well performance.

However, incorporating dynamic field data is a very complex problem due to the highly non-linear processes involved in typical reservoir systems. Several inverse modeling, or automatic history matching techniques have been published in the past.[50-54] These procedures have not become popular because of the overabundance of assumptions required, such as homogeneous layered systems. The first study which incorpo-

rated geostatistics within the history matching framework was Marsily et al.[55] Reservoir properties at a few number of strategically placed "pilot points" were used as estimation parameters. Values at the remaining grid blocks were estimated by kriging. Although the approach yields a kriging error variance for the property being estimated, it cannot be converted to an uncertainty without assuming the property is normally distributed. More importantly, no estimate of the uncertainty in future reservoir performance is obtained. Additionally, kriged estimates do not preserve spatial variability--an important fluid flow characteristic. Indirect well performance constraints are used in this present study as additional conditional simulation constraints, thereby allowing reservoir descriptions to be generated which not only possess realistic geologic characteristics, but also exhibit simulated well performance which is consistent with historical performance.

Outline

The primary objective of this investigation is to develop a reservoir characterization technique which not only honors geological spatial features, but also accounts for well performance characteristics. As a result, uncertainties in reservoir heterogeneities can be translated into a minimized uncertainty in future reservoir performance.

Field data present many difficulties when attempting to validate a new reservoir characterization technique. Unknown operating conditions, unmeasured water production and commingled production are a few of several troublesome problems which arise when trying to reconstruct historical field operations. To overcome these problems, a three-dimensional, synthetic field-scale reservoir description is developed in Chapter II. Primary and waterflood performance are simulated for 59 wells over a 20 year period. To maintain realism, the synthetic data set was developed using actual field data. Primary and waterflood performance constraints are defined and tested in Chapters III and IV, respectively. The simulated annealing technique is shown to be highly flexible in its ability to incorporate diverse spatial attributes. Synthetic field segment case studies are

used to demonstrate the degree of effectiveness of several parameters as conditional simulation constraints. The conditional simulation technique developed in Chapters III and IV is further demonstrated using a synthetic field case study in Chapter V. A two-dimensional version of the three-dimensional synthetic data set developed in Chapter II is used to show how the new technique would be used during the development and depletion of a reservoir. Lastly, conclusions are presented in Chapter VI.

CHAPTER II

THREE-DIMENSIONAL SYNTHETIC TRUTH CASE

This chapter documents the development of a three-dimensional reservoir description and corresponding flow simulation results. Well and field data collected from the Burbank Field located in Osage County, Oklahoma, were used in developing the reservoir description. Fluid flow simulation was performed to generate primary and waterflood performance. This exhaustive synthetic data set, or "3D Truth Case," can be used to evaluate the effectiveness of new reservoir characterization techniques. After presenting general characteristics of the Burbank Field, the well and core data are presented. Spatial analysis of the field data is then discussed. This is followed by a section which describes the conditional simulation approach and resulting realizations of reservoir properties. The chapter is concluded with a discussion on flow simulation results.

Burbank Field

The Burbank Field is located 90 miles northwest of Tulsa (Figure 2.1). The field produces from the Burbank Sandstone member of the Cherokee Shale (Pennsylvanian) at an average depth of 2900 ft. The Burbank Field is the largest oil field in the state of Oklahoma. The largest unitized area of the field is the North Burbank Unit,[56] discovered in 1920 and currently operated by Phillips Petroleum. This unit is approximately 18 miles long and 4.5 miles wide, encompassing about 18,000 acres. The average thickness, porosity and permeability of the Burbank Sandstone is 47 ft, 16.8% and 5 md, respectively. The original oil-in-place (OOIP) of the North Burbank Unit is estimated to be 671 MMBO. Primary production recovered 179 MMBO (27% OOIP) whereas waterflooding has recovered 131 MMBO (20% OOIP). Present day rates are about

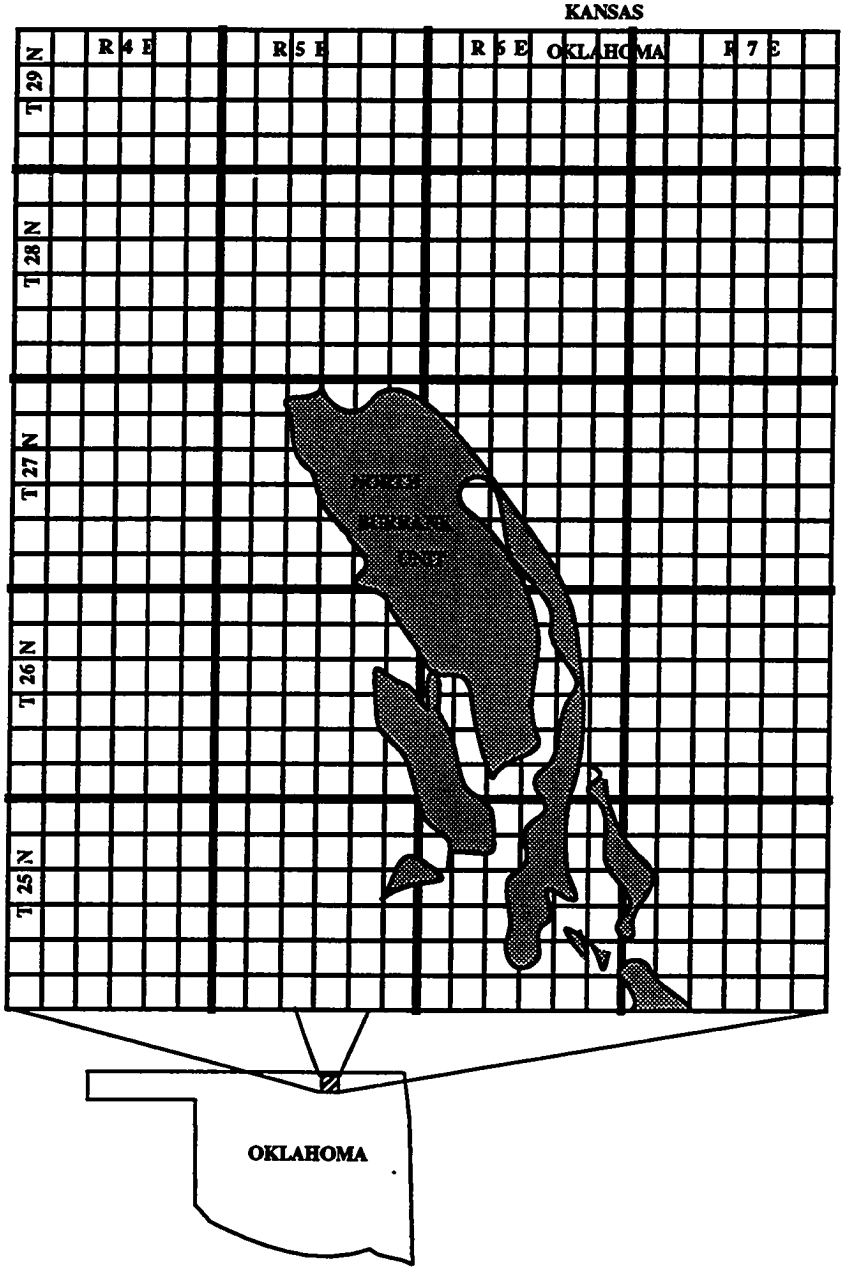

Figure 2.1 - Location of the North Burbank Unit

1100 STB/D of oil and 92,000 STB/D of water, resulting in a water-oil ratio (WOR) of 84. Although more than 2000 wells have been drilled in the Unit, only about 180 producers and 70 water injection wells are currently active. Pertinent data for the North Burbank Unit are listed in Table 2.1

The Burbank Field is one of the so-called "shoe-string" sands running north-south in eastern Kansas and Oklahoma. Although previously considered to be a series of overlapping offshore bars,[57] the Burbank Field is now believed to be fluvial in origin.[58] Core and log analyses indicate the sand is a series of fluvial channels superimposed on and laterally cut into each other, giving the appearance of a massive sand body. Other indications, such as burrowing, suggest there were periodic minor marine incursions. Sand discontinuities within the field structure suggest that the average channel width is approximately 1000 ft.

The top of the Burbank Sandstone gradually dips to the west at an average of 40 ft/mile. There are several localized high structures existing throughout the field, but they do not noticeably affect local production characteristics. The productive sand abruptly becomes impermeable on the east side of the field. A loss of permeability and a degradation to shale defines field limits to the west.[59,60]

Data Collection and Model Areas

The Model Area selected for study is shown in Figure 2.2. The Model Area is 7920 ft by 23,760 ft, or 4320 acres. This location was selected because of the existence of several cores and modern porosity and electric logs in the area. The cores and logs were obtained from infill wells drilled for a polymerflood and two polymerflood pilots initiated within the area. Log and core data from 92 wells located within the Model Area were used in the study. As shown in Figure 2.3, data were also collected from the surrounding two 160 acre tracts to the north, west and south. This information was included to improve estimated properties along the periphery of the Model Area. Within the exter-

Table 2.1

Pertinent data for the North Burbank Unit[56]

Location	Osage County, Oklahoma
Discovery	1920 by Marland Oil Company
Producing formation	Burbank Sandstone
Surface Area	12 mi x 4.5 mi (18,000 Ac)
Depth	2900 ft
Thickness	47 ft
Porosity	16.8%
Permeability	50 md
Pressure at discovery	1200 psi
Temperature	120°F
Solution GOR at discovery	415 SCF/bbl
Oil FVF at discovery	1.2 RB/STB
Oil gravity	39.5° API
Oil viscosity	3.0 cp
Natural drive mechanism	solution gas drive
Original oil-in-place	671 MMSTBO
Oil recovery, primary/secondary	179 MMSTBO/131MMSTBO

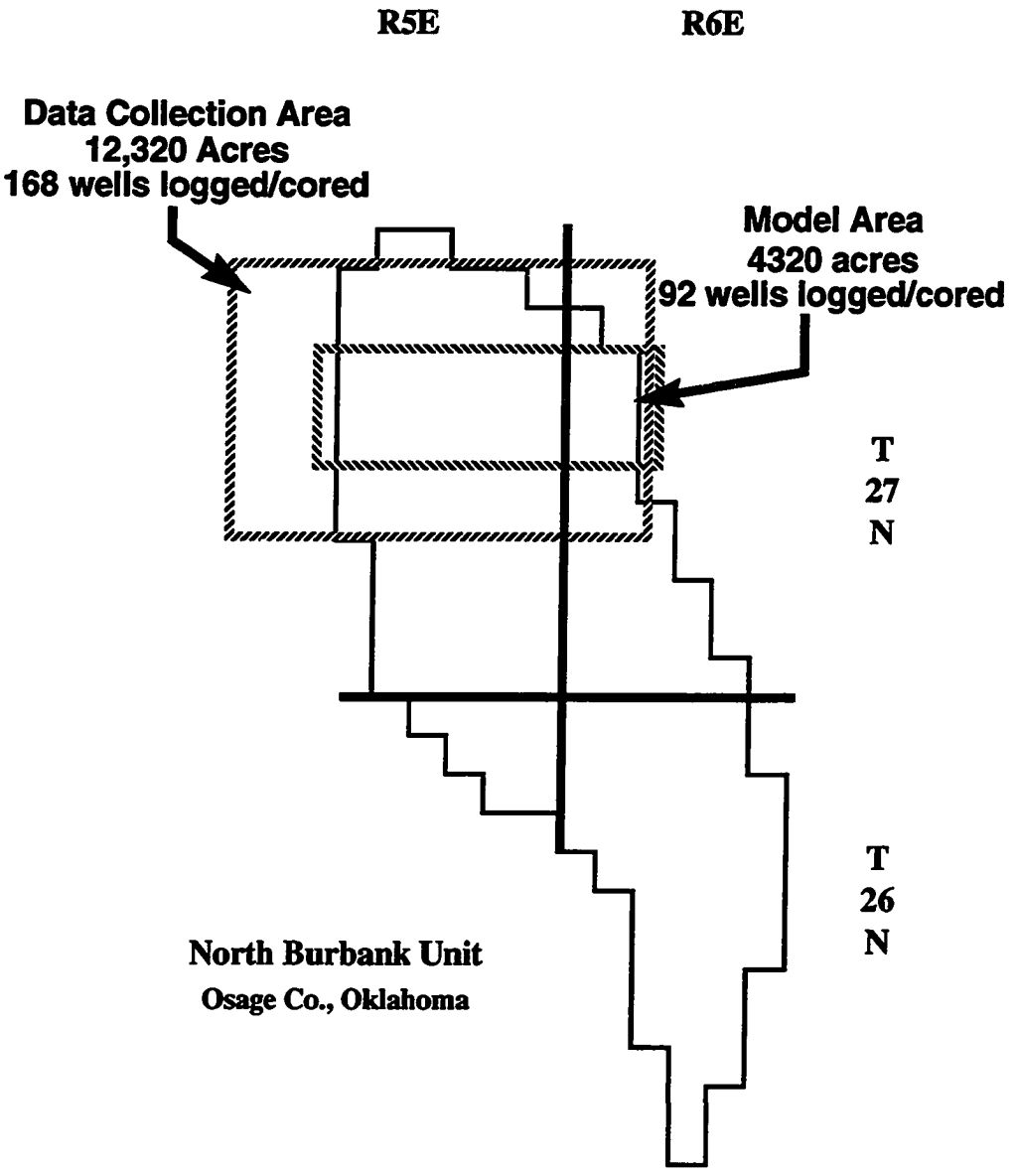

Figure 2.2 - Location of the Data Collection and Model Areas

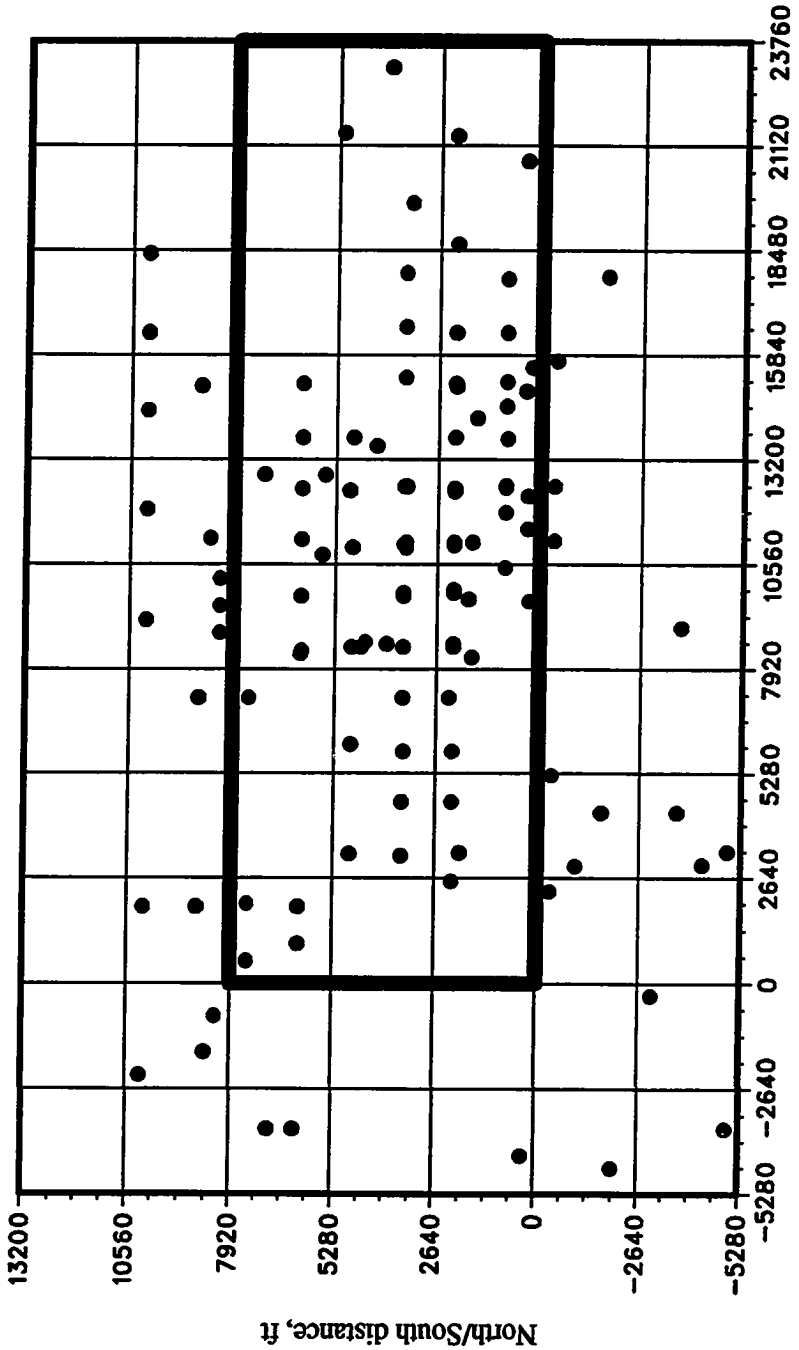

Figure 2.3 - Location of the North Burbank Unit wells used for conditioning

nal Data Collection Area, core and log data from an additional 76 wells were included in the study.

A typical core profile is shown in Figure 2.4. The vertical profile can be divided into three main zones. The top zone is a fine-grained sand interstratified with thin beds of green micaceous shale.[58] Permeabilities and porosities typically range from 0.1 - 100 md and 5 - 18%, respectively. A dense streak separates the upper zone from the middle zone. The middle zone is a clean, fine-grained sandstone and has well developed permeability (10 - 1200 md) and porosity (12 - 30%). It is by far the most productive of the three main zones. The lower interval is usually relatively thick, but due to poor sorting of the fine-grained sand, permeabilities rarely exceed 50 md and porosities are typically less than 20%.

The sand was subdivided into 10 flow units to capture as much of the vertical heterogeneities as possible (Figure 2.4). As described by Jackson et al.,[61] flow units should be defined such that all pertinent detailed geologic and petrophysical information are captured so that the resulting reservoir description retains the complexities of the reservoir architecture, including parameter variabilities. In this study, flow units correspond to distinct permeability and porosity intervals identified from core and log characteristics. Flow Unit 1 consists of the upper zone previously described. The dense zone separating the upper zone from the main sand body unit is Flow Unit 2. The middle zone is subdivided into 5 flow units (Flow Units 3 - 7). The transition between the middle and lower zones is defined as Flow Unit 8. This transition is frequently separated from the lower, thick interval by a tight streak. This tight interval is referred to as Flow Unit 9. The thick bottom zone is Flow Unit 10. A total of 30 log and core cross-sections were constructed for the purpose of identifying flow units from the log and core data. These cross-sections extend throughout the Data Collection Area.

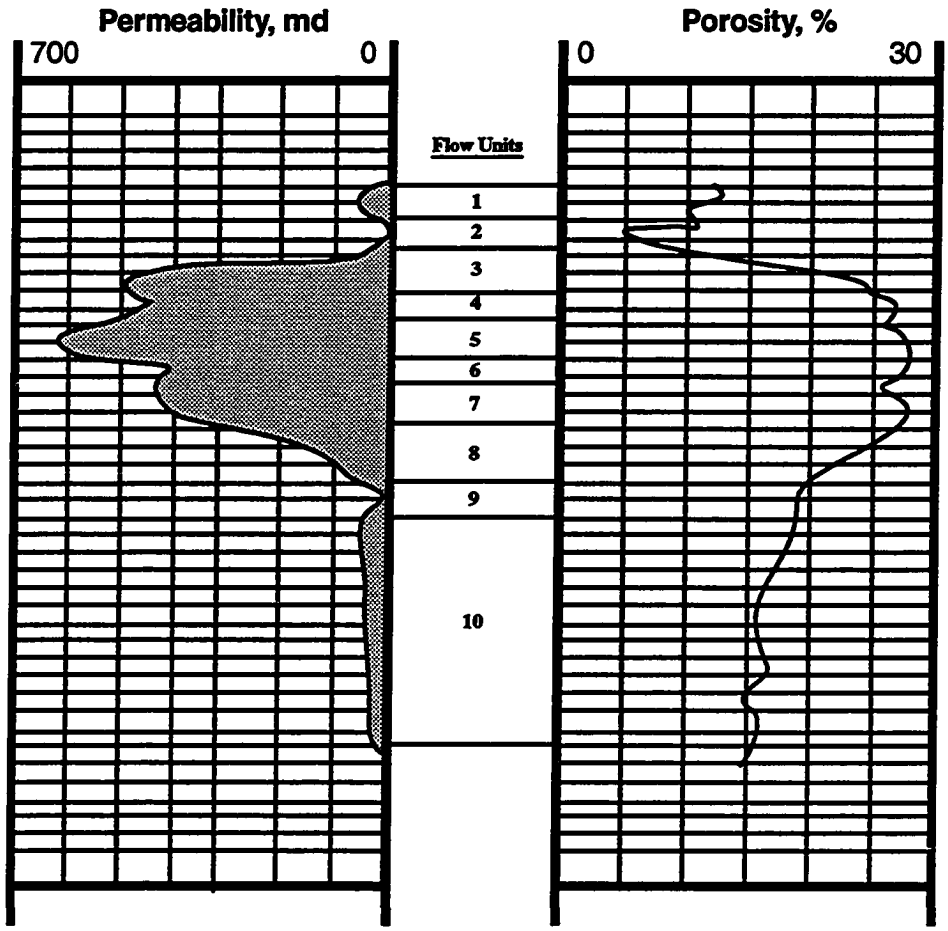

Figure 2.4 - Core porosity and permeability profiles for North Burbank Unit Well 34-29

Univariate and Bivariate Analyses

Burbank Sand thickness histograms are depicted in Figures 2.5 and 2.6. The overall gross thickness is shown to vary from 46 ft to 89 ft within the Data Collection Area. The average gross thickness is 65 ft. All of the flow units have average thicknesses of less than 8 ft except for Flow Unit 10 which averages 28 ft. The histograms for total gross thickness and Flow Unit 10 thickness are symmetrical while the other flow unit histograms are positively skewed.

Porosity histograms for Flow Units 1 - 10 are included in Figures 2.7 and 2.8. Flow Units 1 and 2 are shown to have the lowest average porosities (about 11%). Intervals with average porosities of more than 21% include Flow Units 3, 5 and 7. There are only a few porosity outliers, with coefficients of variation falling within the range of 0.20 - 0.41.

Cell declustering[62] was used to determine the global and prior local distributions of flow unit porosity and thickness due to the irregular spacing of the wells. This procedure is used to remove any bias in the frequency distribution of the data by computing weights for each data value. Values from clustered wells are given a smaller weight than those from wells in less developed regions. A comparison of the clustered and declustered cumulative distribution functions (cdf's) for Flow Unit 3 porosity is shown in Figure 2.9. If the clustered cdf had been used, the resulting realization of Flow Unit 3 porosity would have been biased towards high porosity values, indicating that the available samples are preferentially located in high porosity areas of the field. This is reasonable since most of the data were collected from wells recently drilled for two polymer injection pilots, and it is highly likely that the better portion of the field was selected for these pilots.

Core plug air permeability measurements were available for several wells throughout the Data Collection Area. Histograms of log(permeability) for all 10 flow units are shown in Figures 2.10 and 2.11. Most of the log(permeability) distributions are nega-

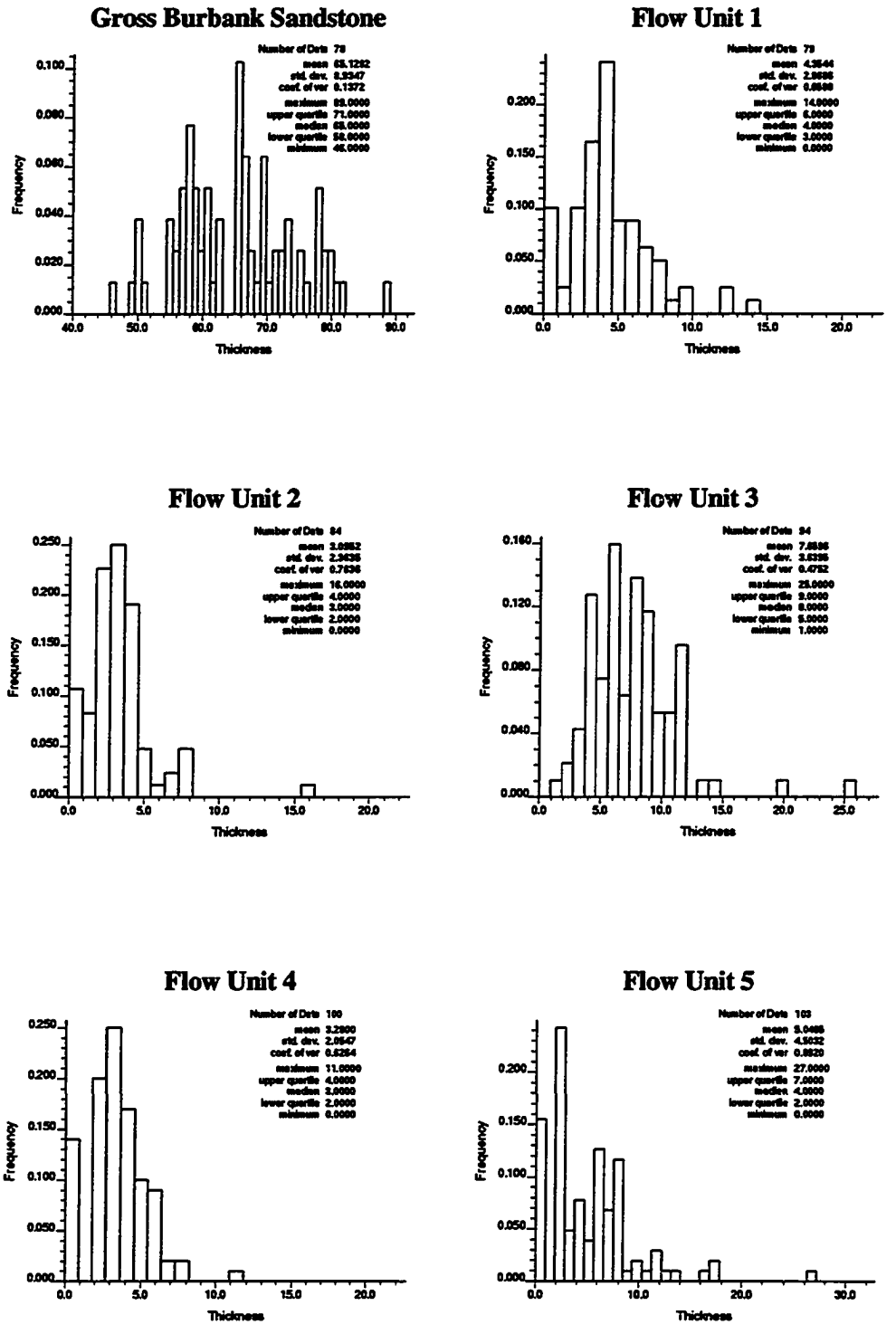

Figure 2.5 - Burbank Sandstone thickness for gross Burbank Sandstone and Flow Units 1 - 5

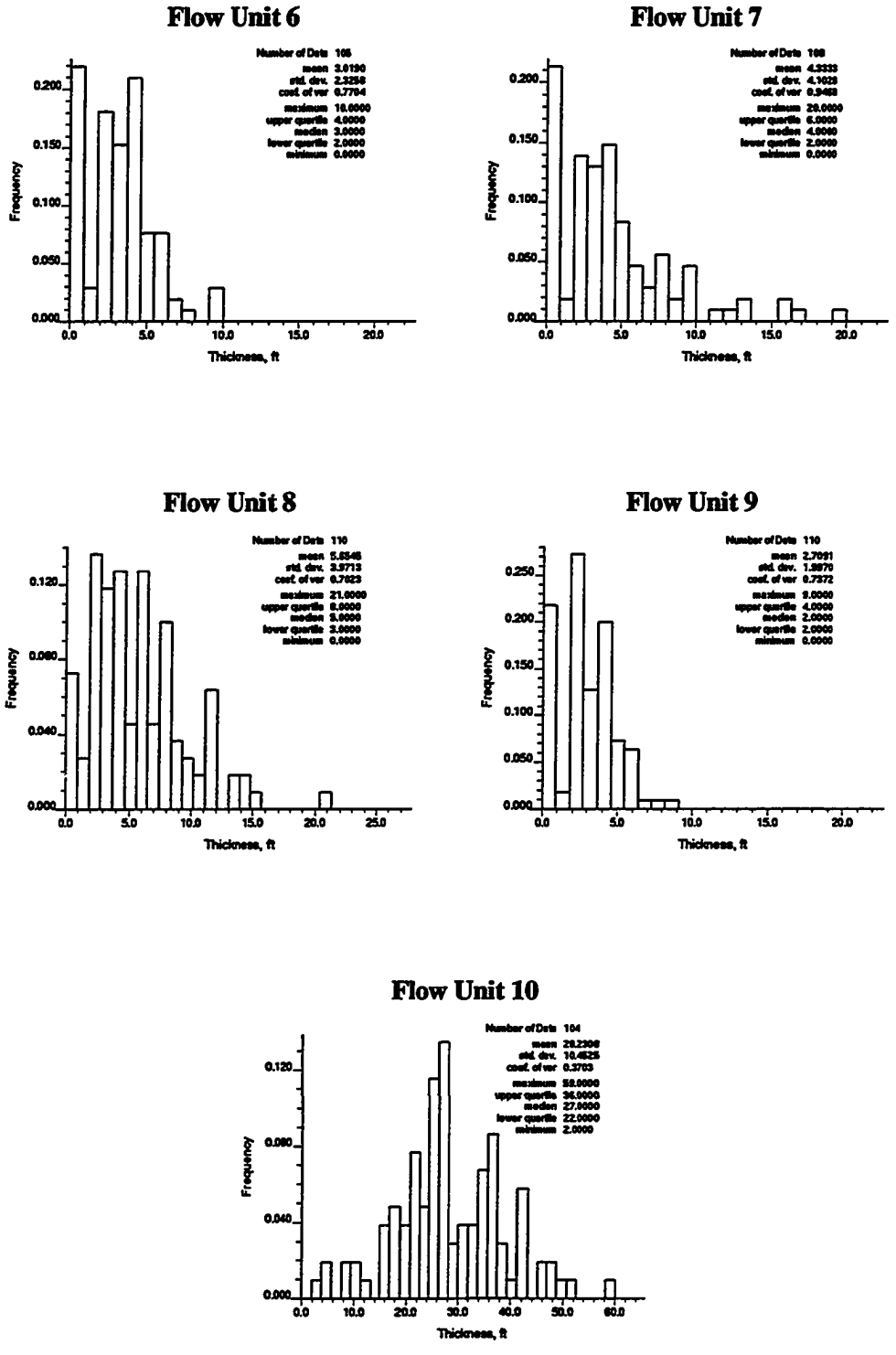

Figure 2.6 - Burbank Sandstone thickness for Flow Units 6 - 10

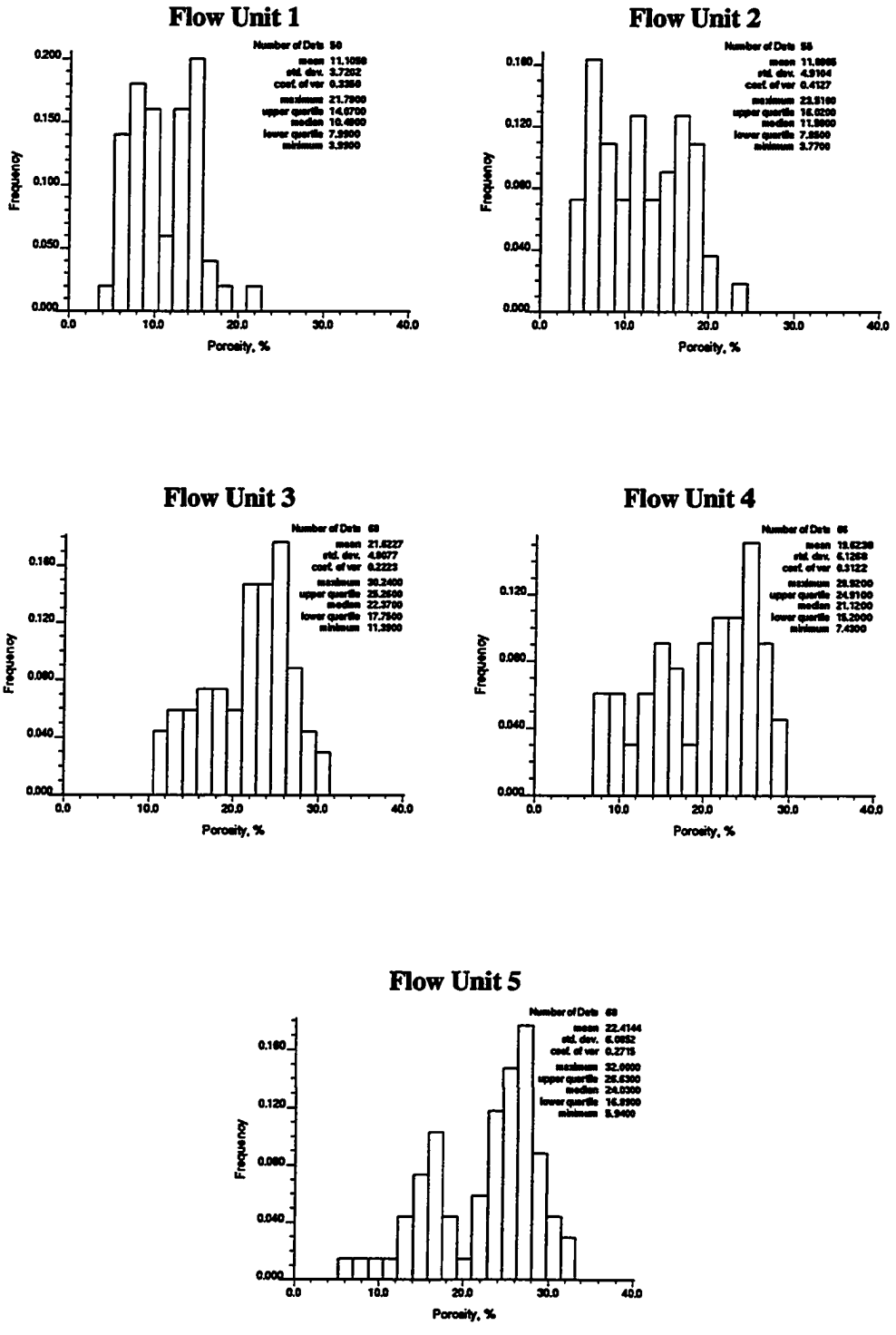

Figure 2.7 - Porosity histograms for Flow Units 1 - 5

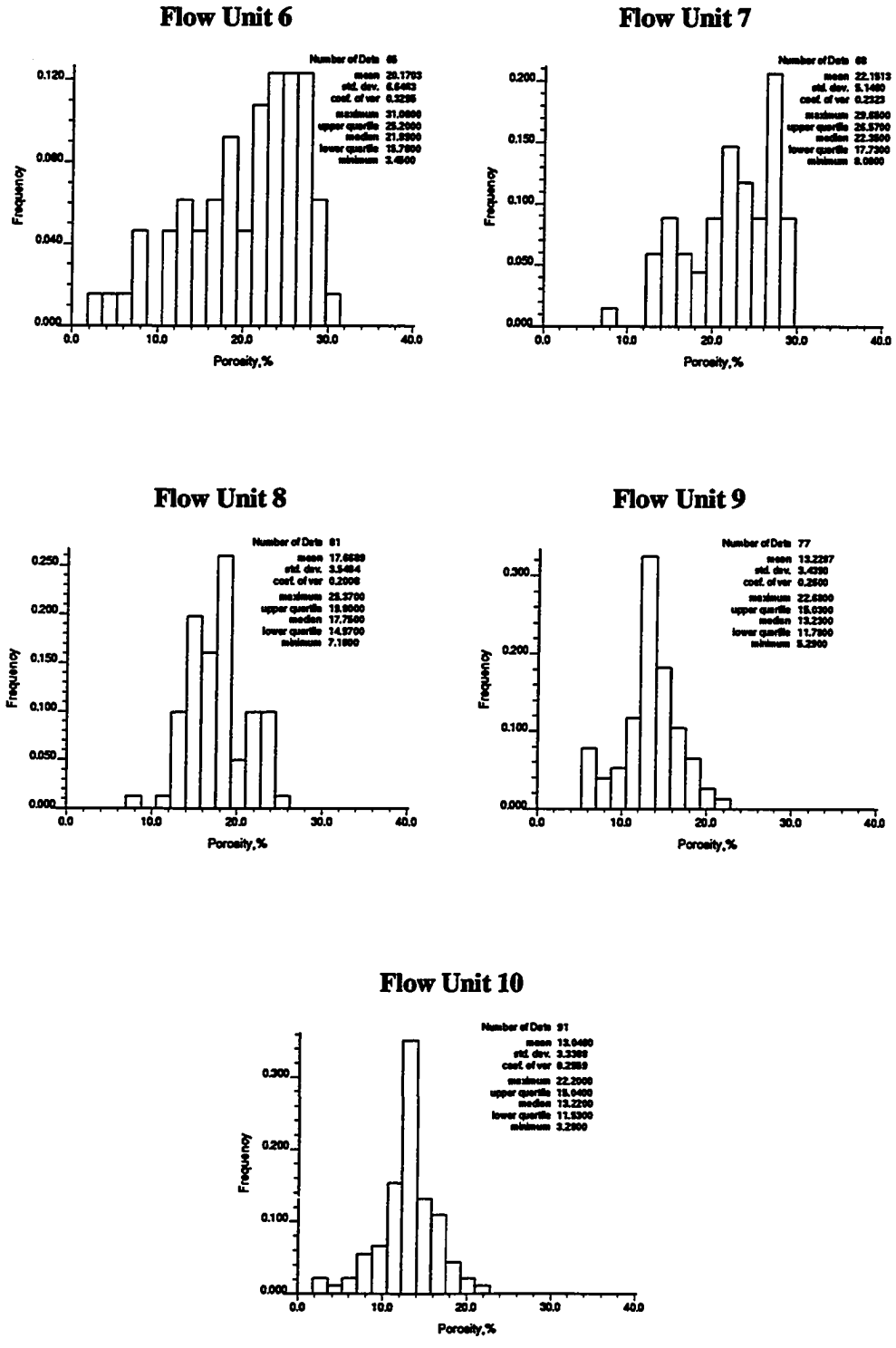

Figure 2.8 - Porosity histograms for Flow Units 6 - 10

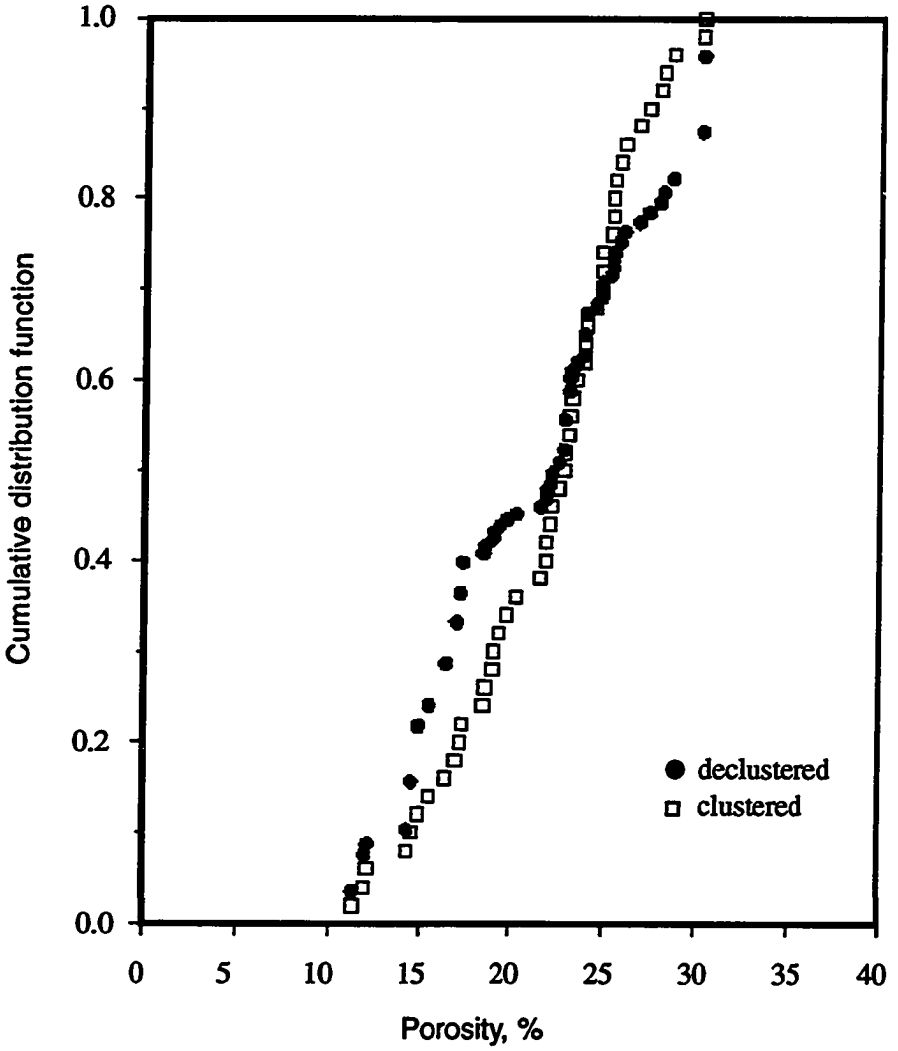

Figure 2.9 - Comparison of the clustered and declustered cumulative distribution functions for Flow Unit 3 porosity

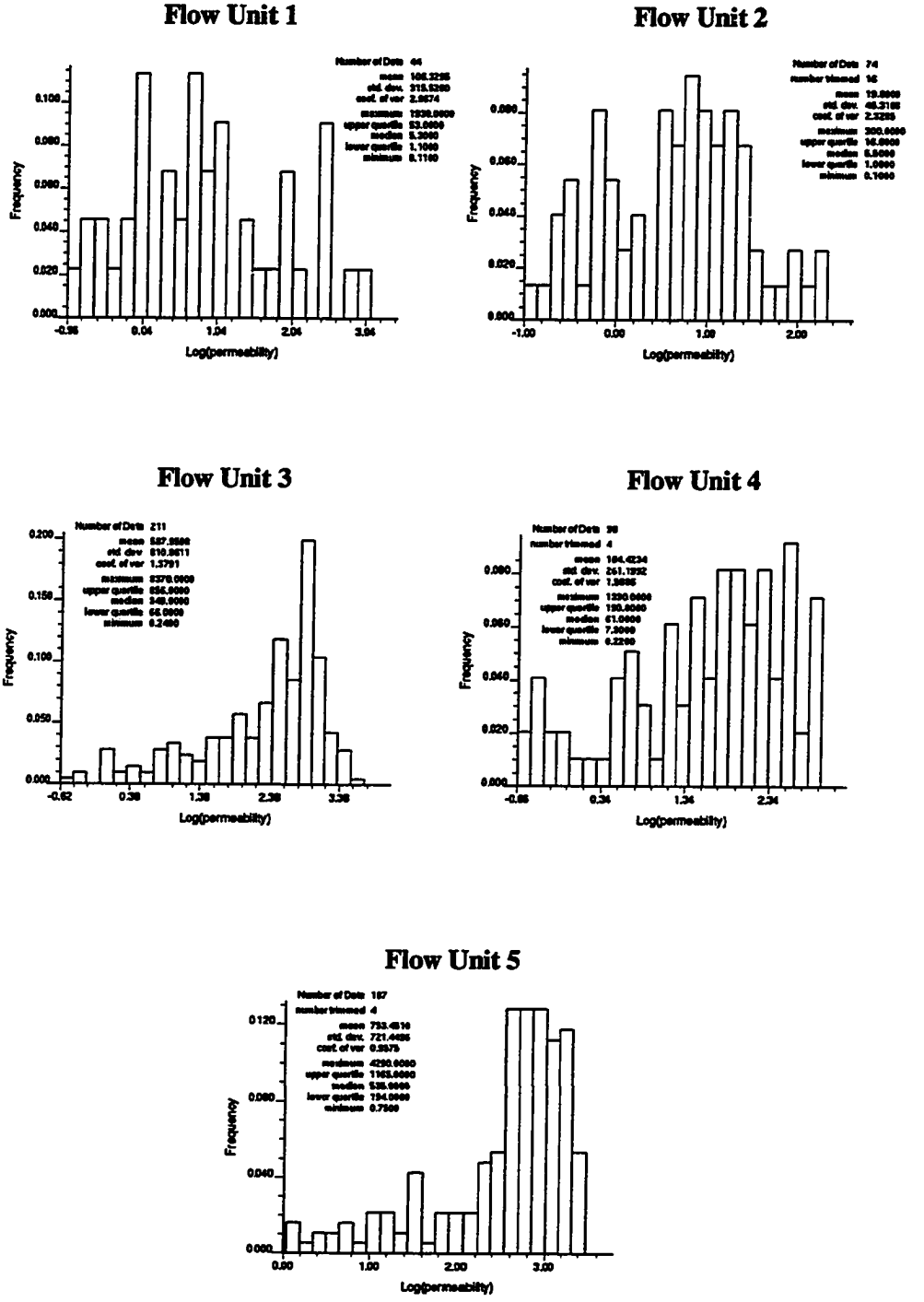

Figure 2.10 - Log(permeability) histograms for Flow Units 1 - 5

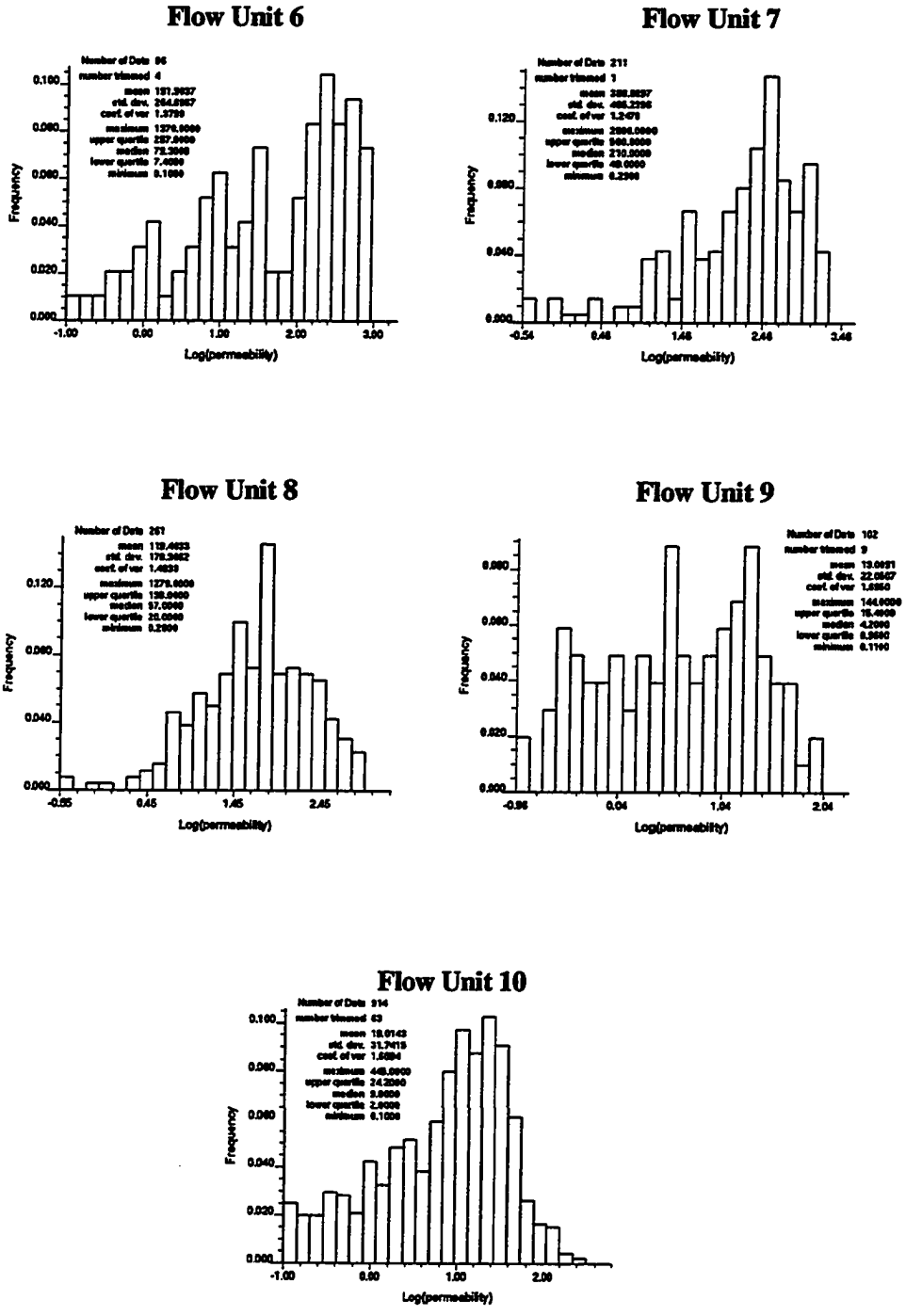

Figure 2.11 - Log(permeability) histograms for Flow Units 6 - 10

tively skewed. Flow Units 2, 9 and 10 have mean permeabilities of less than 20 md, whereas mean permeabilities for Flow Units 3, 5 and 7 are greater than 200 md. Permeabilities exceeding 1 Darcy were measured on core from all of the flow units within the main sand body unit (i.e., Flow Units 3 - 8).

Log(permeability) vs. porosity correlations for each of the flow units are presented in Figures 2.12 and 2.13. These plots indicate there is a strong correlation between permeability and porosity in the Burbank Sandstone. Correlation coefficients are all greater than 0.77, with Flow Unit 6 having a correlation coefficient of 0.95. It is interesting to note that for each of the flow units, the correlation bends downward between porosity values of 10 - 12%. The cause for this increased reduction in permeability at low porosity values is not known. Since there is such a strong correlation between porosity and permeability, it was decided to obtain permeability estimates from these porosity-permeability relationships and simulated porosities.

Spatial Structural Analysis

An experimental variogram for gross sand thickness is shown in Figure 2.14. Also shown is a nested spherical model having a total range of 10,000 ft. The nested model is comprised of short and long scale components to capture the corresponding spatial features. No directionality was evident in the gross sand thickness variogram. A contour map of kriged gross sand thickness of the Model Area is depicted in Figure 2.15. All of the greyscale maps included in this dissertation were generated using the software package GSLIB.[63] It can be seen that the sand is thickest in the central portion of the field and abruptly thins out toward the east side. A map of kriged standard deviation is included in Figure 2.16 and shows there is good well control in the central portion of the Model Area with the least control in the northeast corner.

Variograms and kriged contour maps of flow unit sand thickness were also generated. The thickness directional variogram for Flow Unit 3, one of the most productive

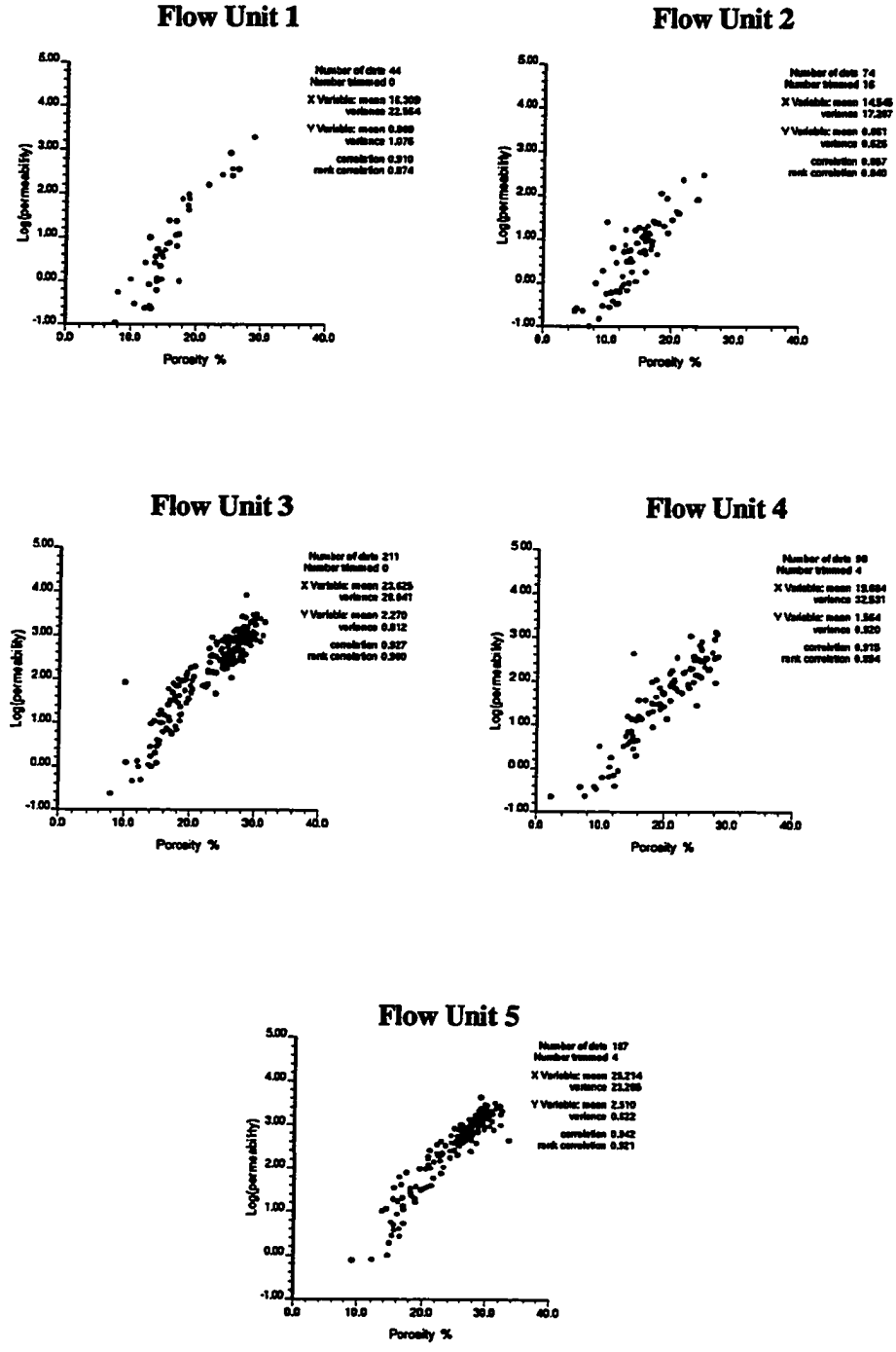

Figure 2.12 - Flow Units 1 - 5 core porosity vs. log(permeability) scatterplots

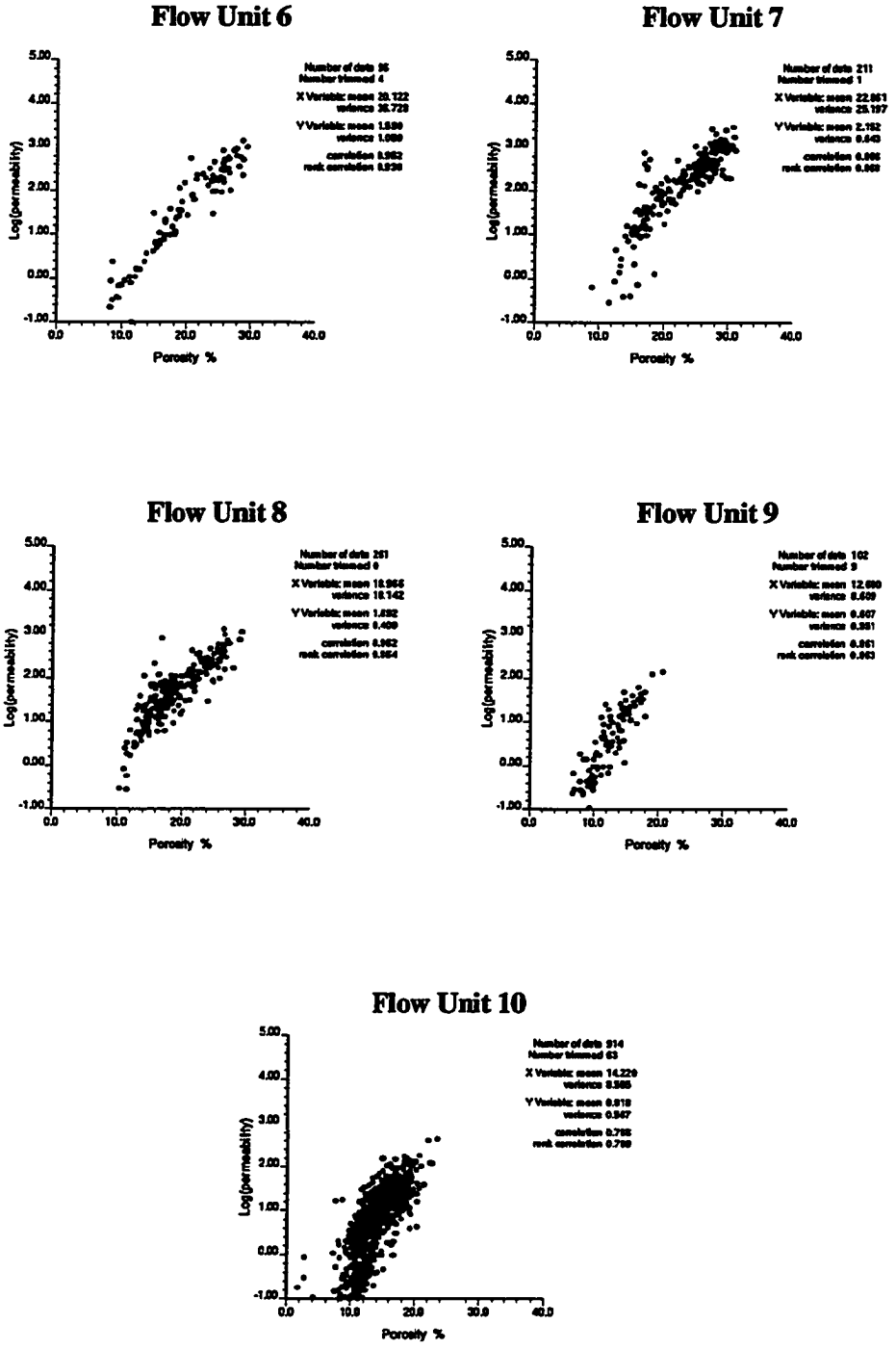

Figure 2.13 - Flow Units 6 - 10 core porosity vs. log(permeability) scatterplots

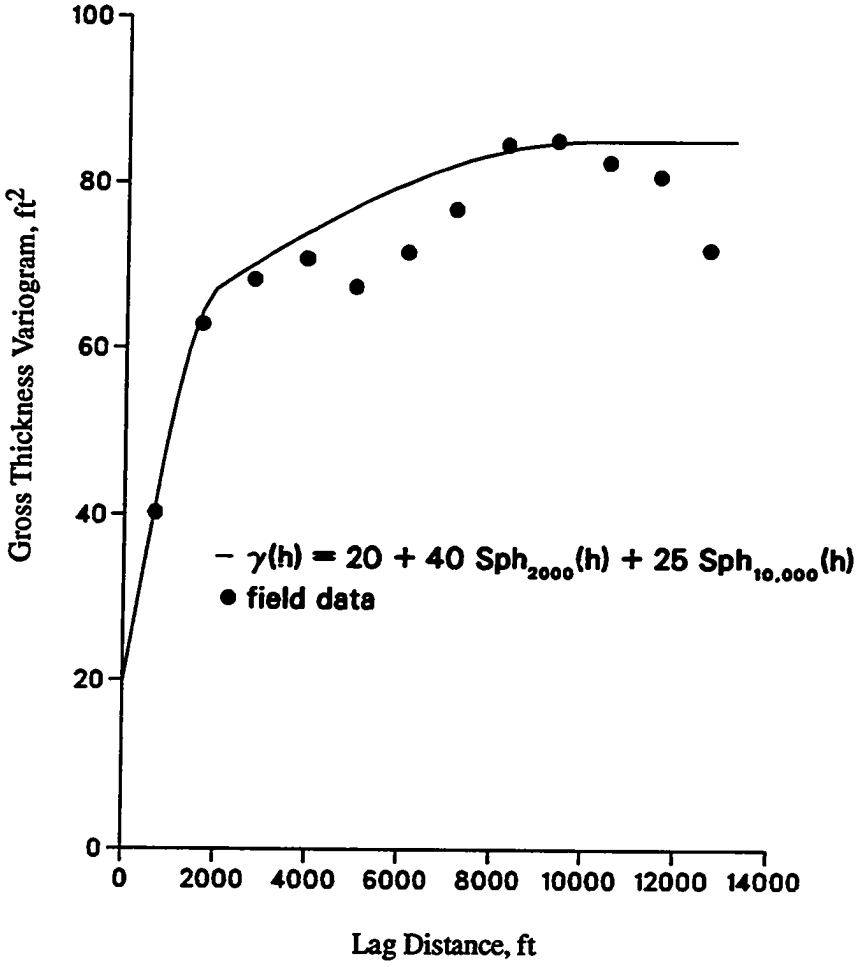

Figure 2.14 - Omnidirectional variogram for Burbank Sandstone gross thickness

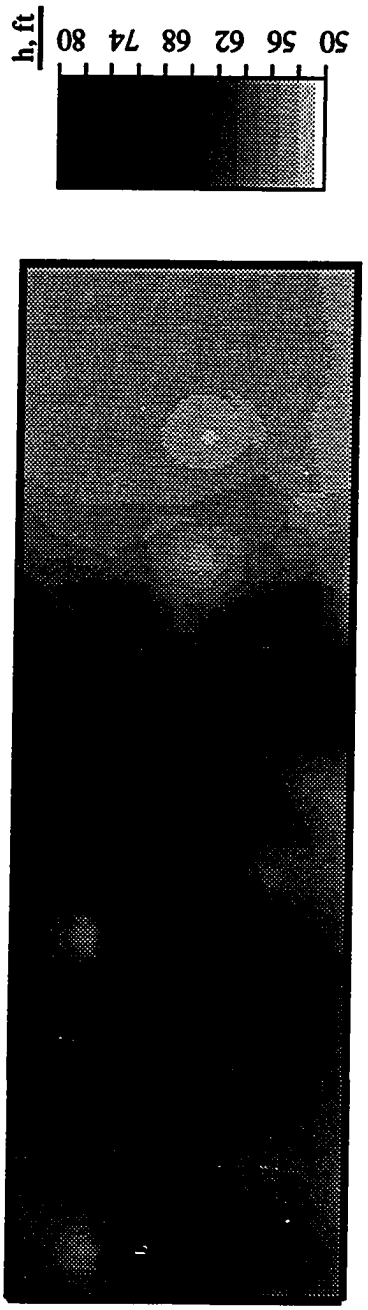

Figure 2.15 - Kriged gross thickness contour map for Burbank Sandstone

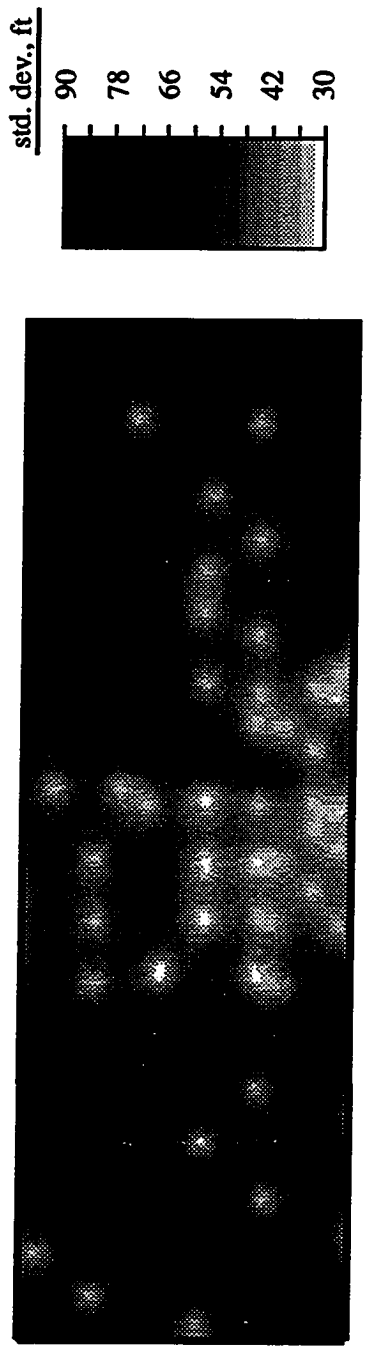

Figure 2.16 - Kriged standard deviation of Burbank Sandstone gross thickness

flow units, is shown in Figure 2.17. Flow Unit 3 thickness was found to have the longest correlation length (8000 ft) at N90°E with an anisotropy ratio of 3.0. Figure 2.18 is the kriged contour map of sand thickness for Flow Unit 3. The thickest portion of the Unit exists in the middle and east end of the Model Area, with sand thicknesses exceeding 10 ft. For the most part, sand thickness is less than 7 ft. Figure 2.19 is an omnidirectional variogram for Flow Unit 10 thickness, the thickest flow unit defined within the Model Area. The variogram for Flow Unit 10 thickness has a range of only 2000 ft. No directionality was found to exist. The corresponding thickness contour map is shown in Figure 2.20. Sand thickness increases to the south, exceeding 40 ft towards the south-central portion of the Model Area.

Sequential Indicator Conditional Simulation

Sequential indicator conditional simulation[64] was used to generate flow unit realizations of thickness and porosity. Plan view greyscale maps of sand thickness for Flow Units 1 - 10 are depicted in Figure 2.21. The size of the Model Area is 4.5 x 1.5 miles. All flow unit thickness realizations were generated using 108 x 36 cells (3880), with 220 ft side lengths. The same greyscale intervals are used for all 10 maps for direct comparison purposes. Note the large variations in the direction of maximum spatial continuity between flow units. Flow Units 6 and 7 have strong directional trends of thickness whereas the spatial continuity of Flow Unit 3 thickness appears to be isotropic. Flow Unit 10 thickness is in excess of 30 ft for the majority of the Model Area. Flow Unit 3 is the second thickest flow unit, averaging 11 ft.

Fine-scale conditional simulations of flow unit porosity were made. To be rigorous, these simulations should have been performed at the same scale as the well data, i.e., on the order of 1 ft. However, this would have required about 1.9 million cells and was considered to be too excessive. As a result, a rule-of-thumb commonly applied to block kriging was used.[16] For two-dimensional blocks, a 4 x 4 grid of cells is consid-

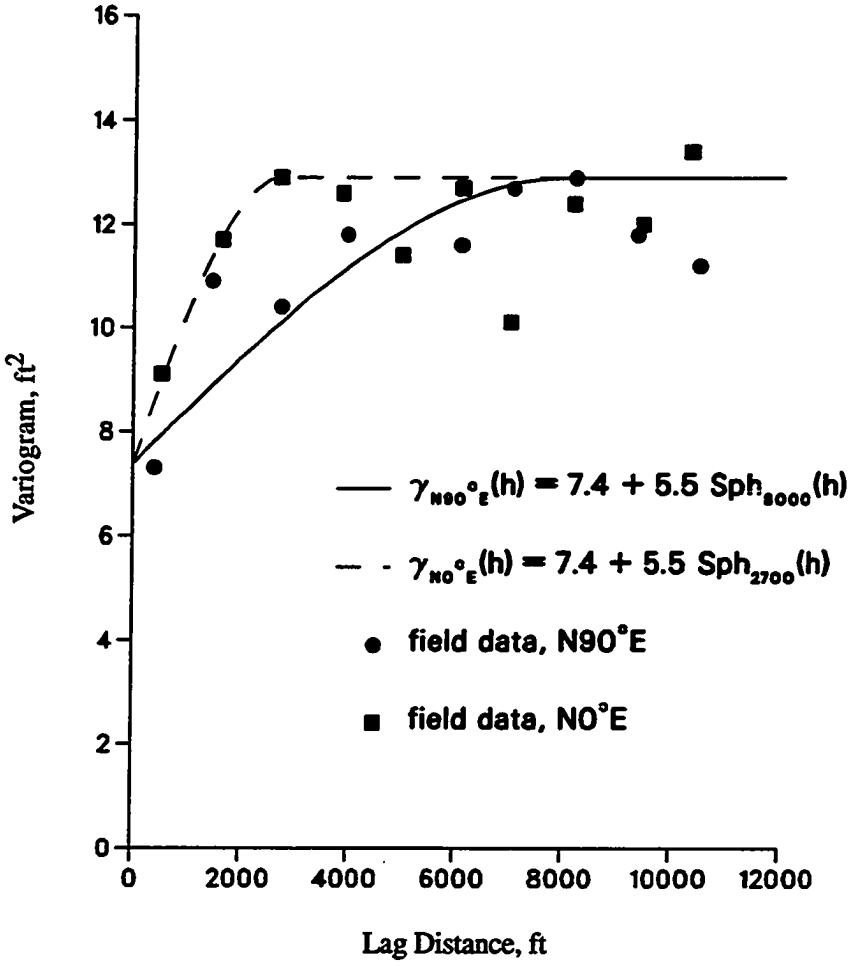

Figure 2.17 - Directional variograms for Flow Unit 3 thickness

Figure 2.18 - Kriged thickness of Flow Unit 3

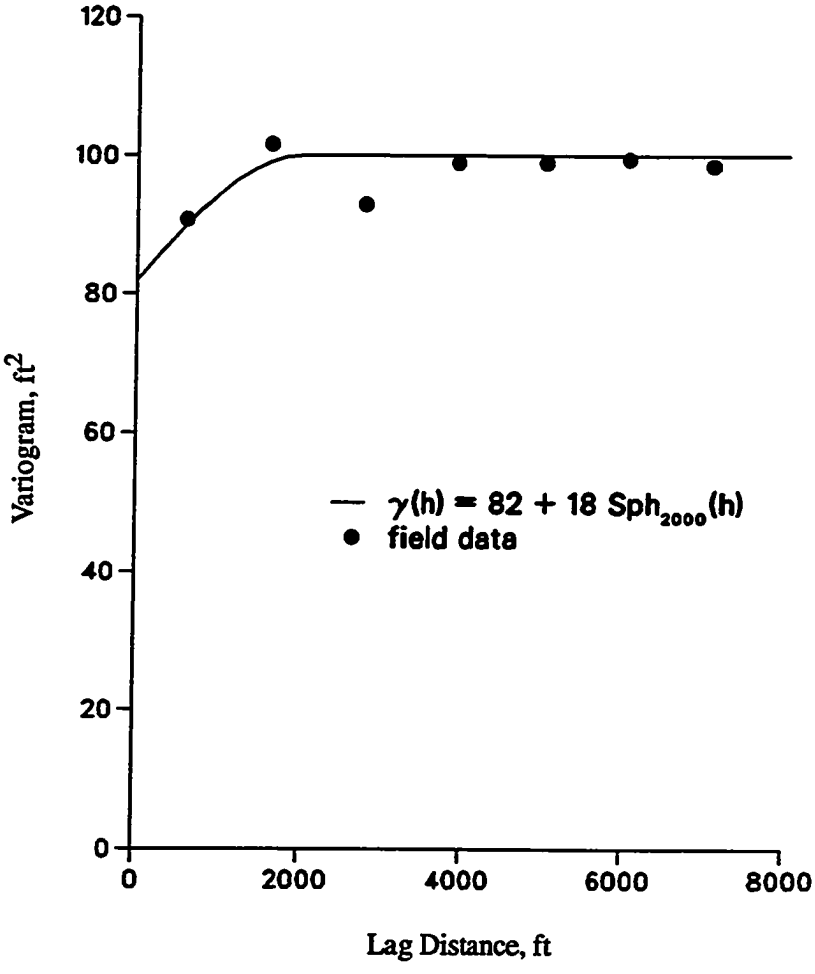

Figure 2.19 - Directional variograms for Flow Unit 10 thickness

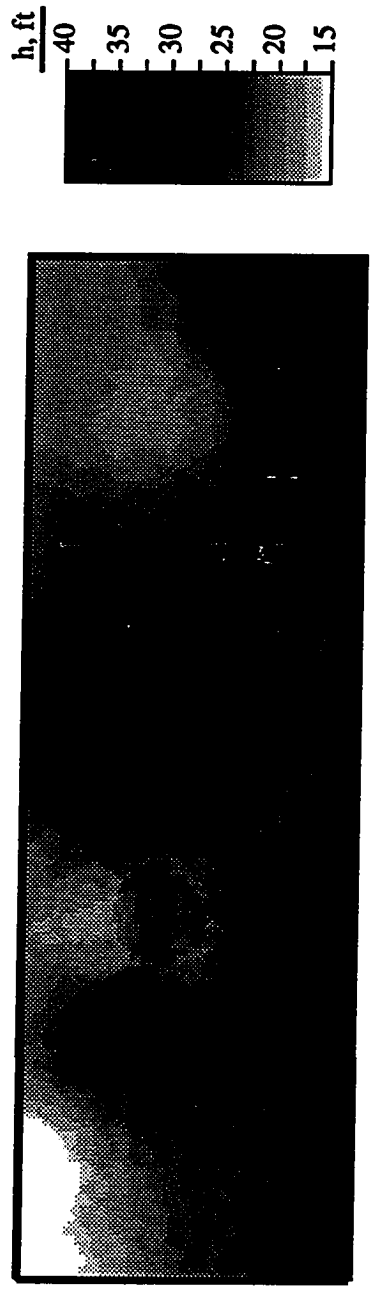

Figure 2.20 - Kriged thickness of Flow Unit 10

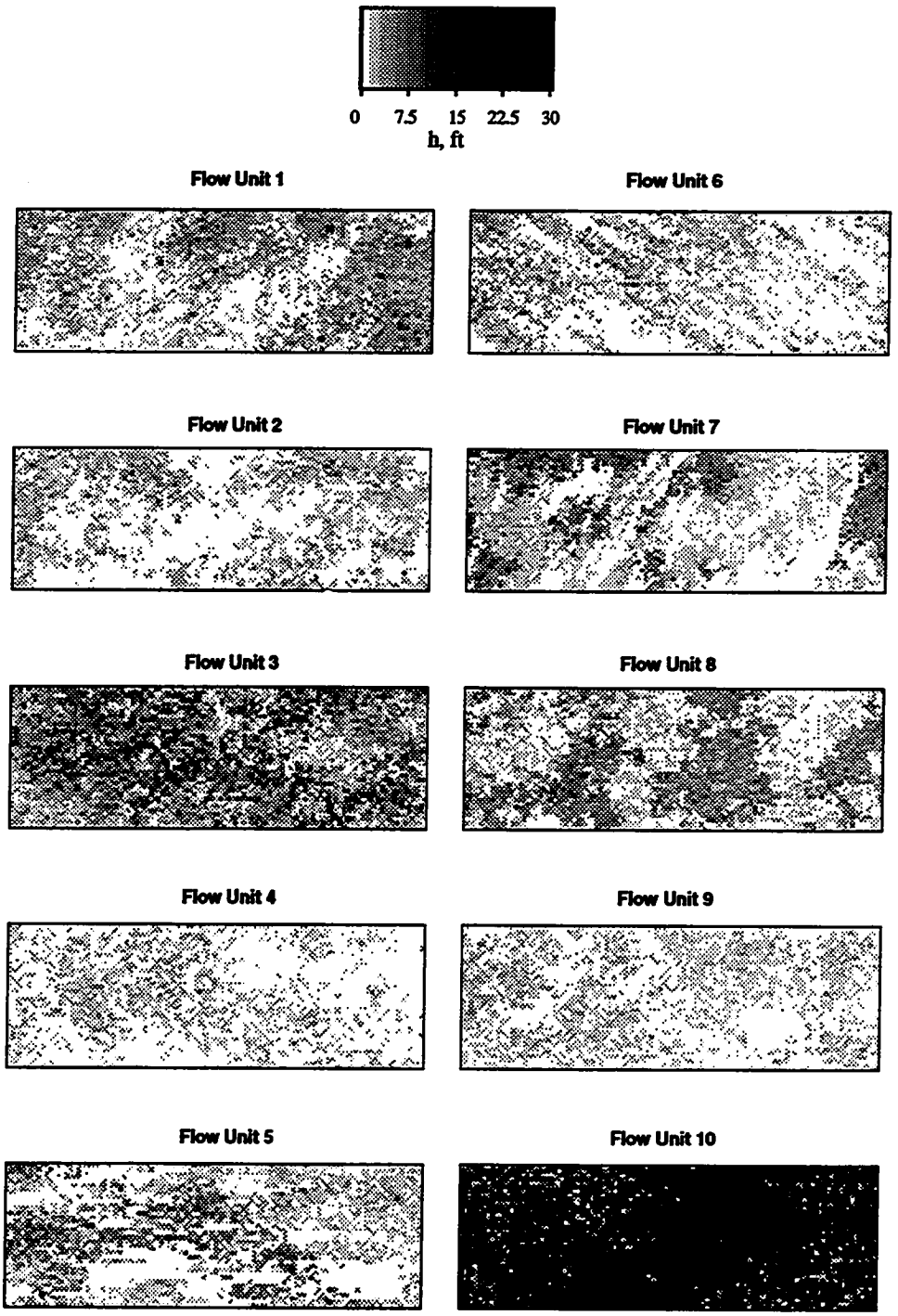

Figure 2.21 - Plan view images of simulated thickness for Flow Units 1 - 10

ered to result in sufficient accuracy for block kriging estimates. For three-dimensional blocks, a 4 x 4 x 4 grid, or 64 cells, is considered to be sufficient. Therefore, it was decided to discretize each 220 ft x 220 ft block into 64 cells with side lengths of 27.5 ft.

A realization of Flow Unit 3 porosity is presented in the top half of Figure 2.22. The fine-scale (flow unit scale) porosity realizations of the 10 flow units were upscaled to 220 ft x 220 ft blocks using arithmetic averages (grid block scale). The corresponding upscaled realization of Flow Unit 3 porosity is depicted in the lower half of Figure 2.22. Plan views of all flow unit grid block scale porosity fields are illustrated in Figure 2.23. Greyscale intervals are all the same for ease of comparison. The majority of the porosity is contained in Flow Units 3 - 8. Significant portions of Flow Units 4 and 7 have porosities in excess of 25%. Most of the high porosity intervals exist in the west-central portion of the Model Area. Although Flow Unit 10 is by far the thickest, its average porosity is only about 15%.

As previously noted, there is a very strong correlation between core porosity and permeability for each of the 10 flow units. Core data were used to determine the correlation between flow unit scale porosity and permeability. The core porosities were arithmetically averaged to obtain flow unit scale values. Core permeabilities also were arithmetically averaged to obtain flow unit scale permeabilities. Figure 2.24 is a scatter plot comparing core scale and flow unit scale permeabilities for Flow Unit 3. Linear least squares best fit correlations of log(permeability) vs. porosity were calculated for each of the 10 flow units. When necessary, two ranges of correlation were used resulting in two best fit lines for a flow unit. Flow unit scale permeability fields were obtained using the regression lines and the flow unit scale porosity realizations. The flow unit scale (27.5 ft x 27.5 ft) permeability fields were upscaled to the grid block scale (220 ft x 220 ft) using a geometric average. Although geometric averaging is best suited for uncorrelated permeability fields,[65] it was deemed to be sufficient for the purpose of this study.

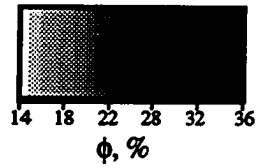

Flow Unit Scale

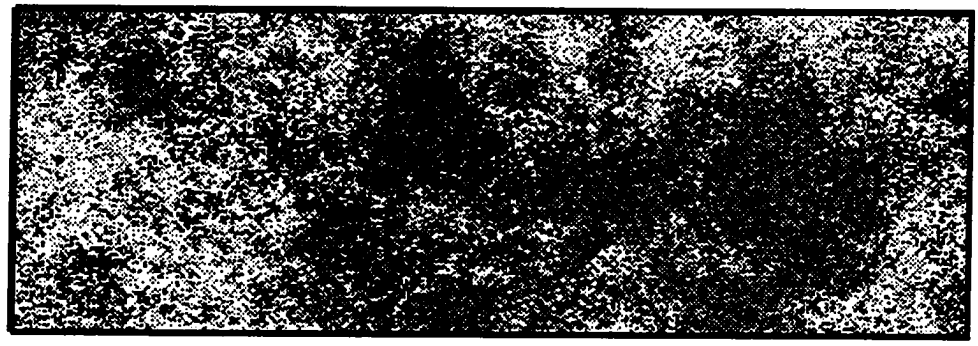

Grid Block Scale

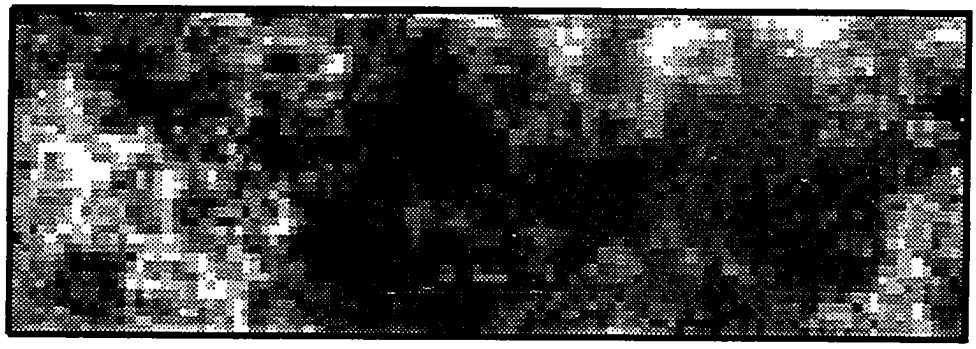

Figure 2.22 - Comparison between flow unit and grid block scale porosity for Flow Unit 3

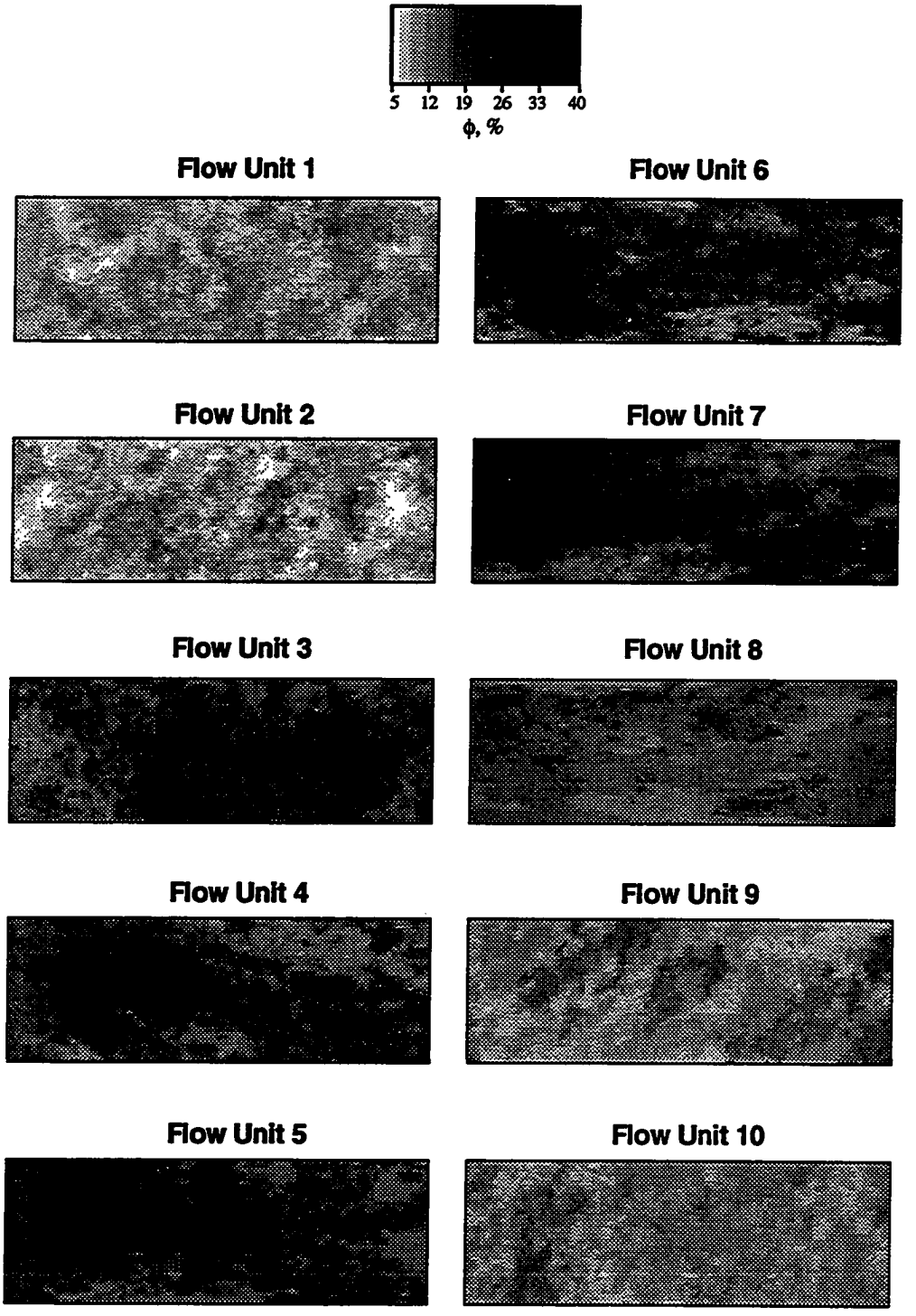

Figure 2.23 - Plan view images of simulated porosity for Flow Units 1 - 10

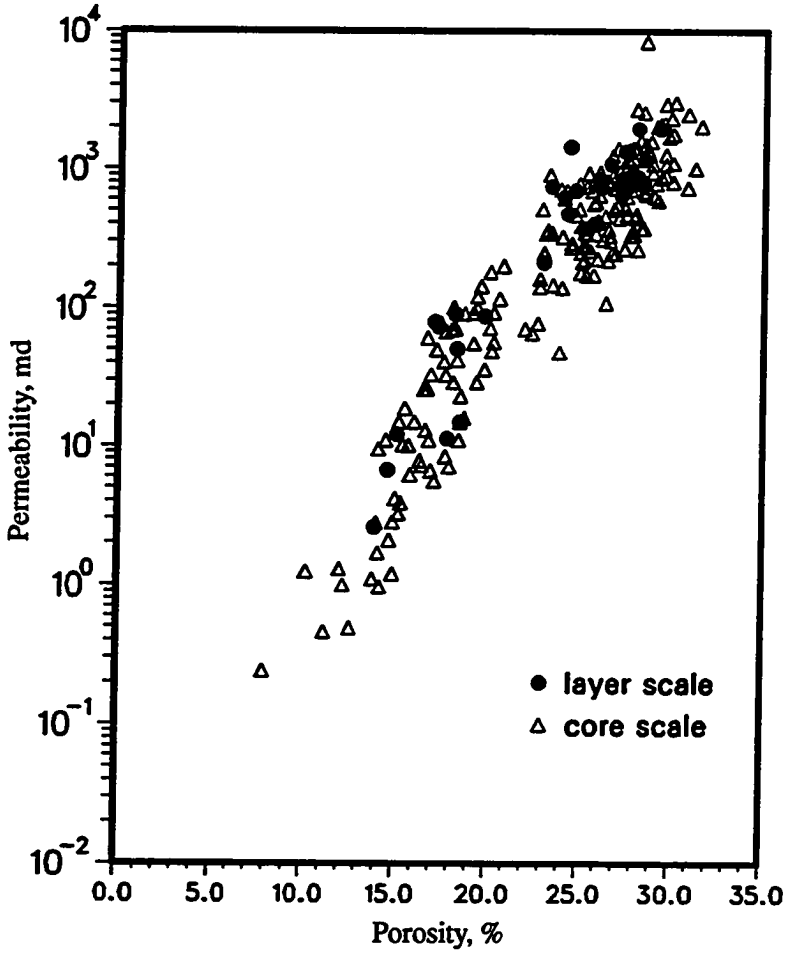

Figure 2.24 - Scatterplot of core scale and flow unit scale permeability vs. porosity for Flow Unit 3

Grid block scale permeability fields for Flow Units 1 - 10 are depicted in Figure 2.25. Again for comparison, equal greyscale intervals were used for all permeability fields. As expected, these contours are strongly correlated with the porosity realizations of Figure 2.23. Permeabilities in excess of 1 Darcy exist in significant portions of Flow Units 5 - 7. Most of Flow Unit 10 (the thickest unit) contains permeabilities in the range of 1 - 5 md.

Depths to the top of the Burbank Sandstone were available at each well location and were used to construct a kriged top of structure map (Figure 2.26). The structure dips to the west at an average rate of 3 ft/mile.

Flow Simulation

A three-dimensional black oil flow simulation was performed for the Model Area using the flow unit scale descriptions of thickness, porosity and permeability described above and depicted in Figures 2.21, 2.23 and 2.25, respectively. The kriged estimate of the structure top (Figure 2.26) was also included in the reservoir model. A constant vertical to horizontal permeability ratio of 0.1 was used. The Model Area was subdivided into 108 x 36 areal grids and 10 vertical grids for a total of 38,880 grid blocks. The areal blocks were all 220 ft x 220 ft in size. The thickness of each grid block was variable and was determined by the respective flow unit thickness at that particular node location. Flow units were absent at some of the nodes. In this special case, appropriate grid block modifications were made to allow communication between adjacent flow units, still conserving pore volume and transmissibility. The fluid properties, gas-oil relative permeability curves and water-oil relative permeability curves used in the flow simulation are shown in Table 2.2 and Figures 2.27 and 2.28, respectively. Although the fluid properties are based on published Burbank Field data, the relative permeability curves are typical black oil, water-wet curves. A uniform initial pressure of 1200 psi was used. The bubble point pressure of the black oil is 1024 psi. A uniform initial connate water saturation

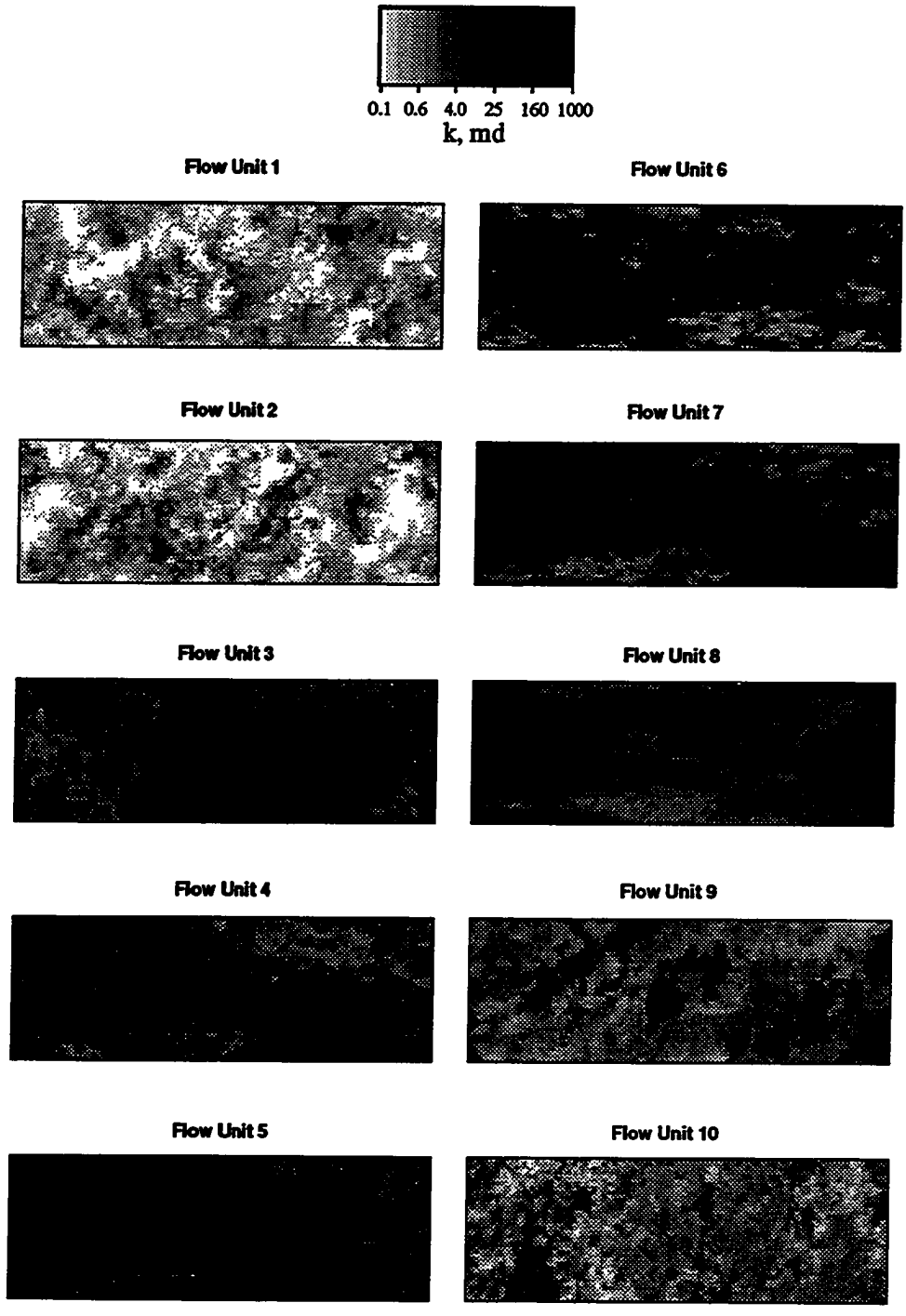

Figure 2.25 - Plan view images of grid block scale permeability for Flow Units 1 - 10

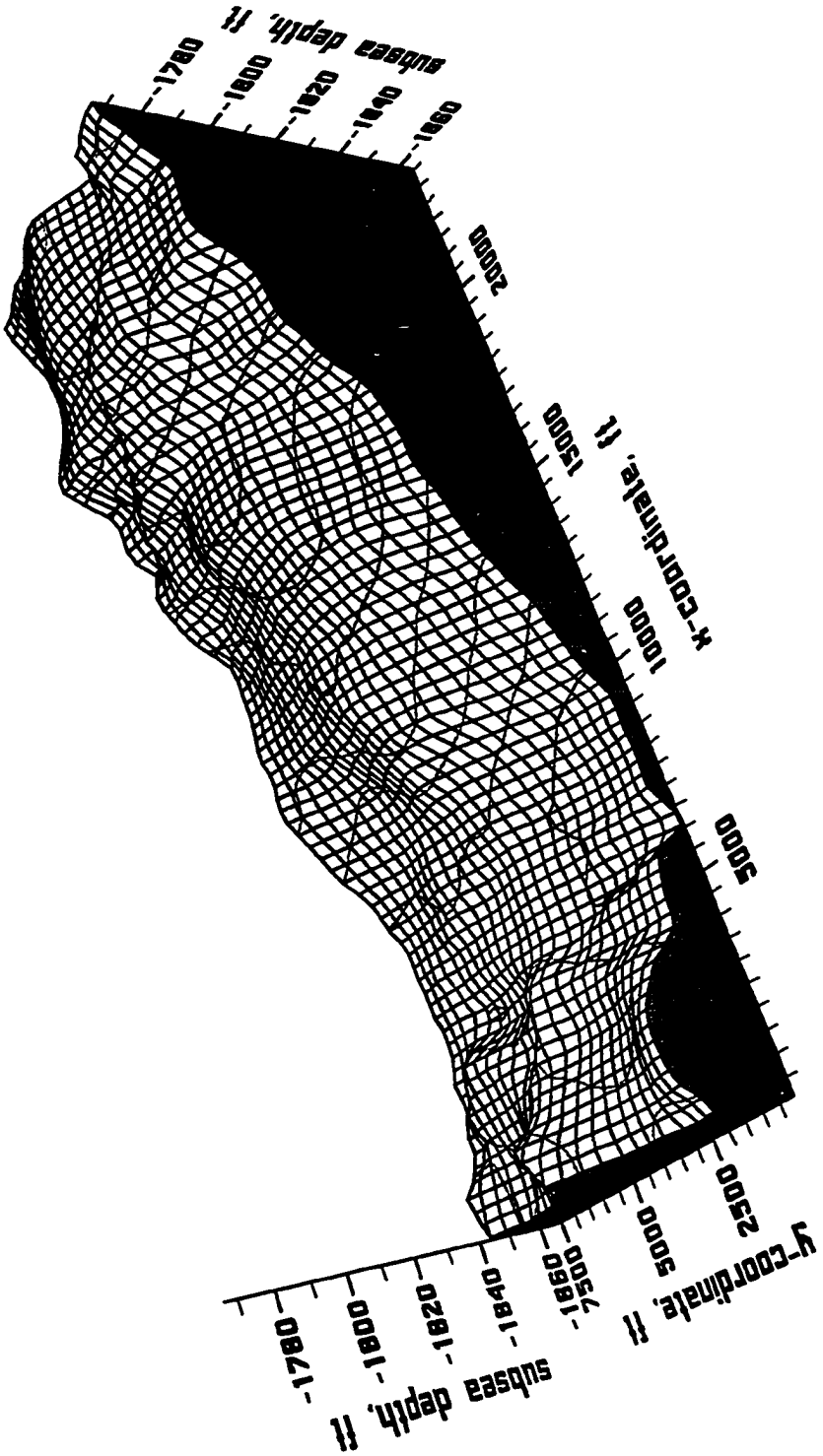

Figure 2.26 - Kriged top of structure map for Burbank Sandstone

Table 2.2

Black oil fluid properties used in flow simulations

Pressure, psi	B_o, RB/STB	μ_o, cp	B_g, RB/Mscf	μ_g, cp	R_s, Mscf/STB
14.7	1.0249	2.486	195.4	0.0086	0.000
50.0	1.0363	2.299	56.56	0.0099	0.022
100.0	1.0386	2.236	28.18	0.0108	0.031
150.0	1.0409	2.178	18.7435	0.0112	0.039
250.0	1.0471	2.059	11.1524	0.0116	0.057
350.0	1.0543	1.942	7.8864	0.0118	0.078
450.0	1.0617	1.837	6.0781	0.0119	0.099
700.0	1.0849	1.589	3.7942	0.0124	0.160
950.0	1.1128	1.380	2.7078	0.0129	0.229
1024.0	1.1215	1.326	2.4887	0.0131	0.250
1200.0	1.1197	1.341	2.0158	0.0136	0.250
1250.0	1.1192	1.345	1.9608	0.0143	0.250
1500.0	1.1168	1.366	1.6858	0.0150	0.250
1750.0	1.1146	1.386	1.4108	0.0157	0.250
2000.0	1.1124	1.407	1.1358	0.0164	0.250

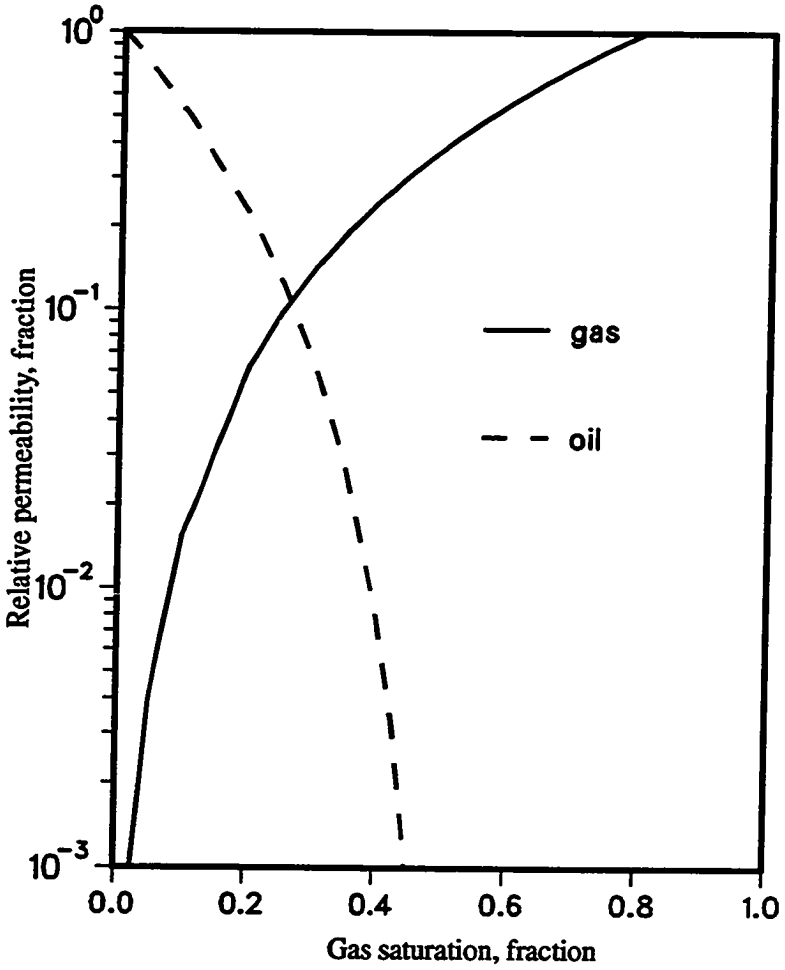

Figure 2.27 - Gas-oil relative permeability curves used in flow simulations

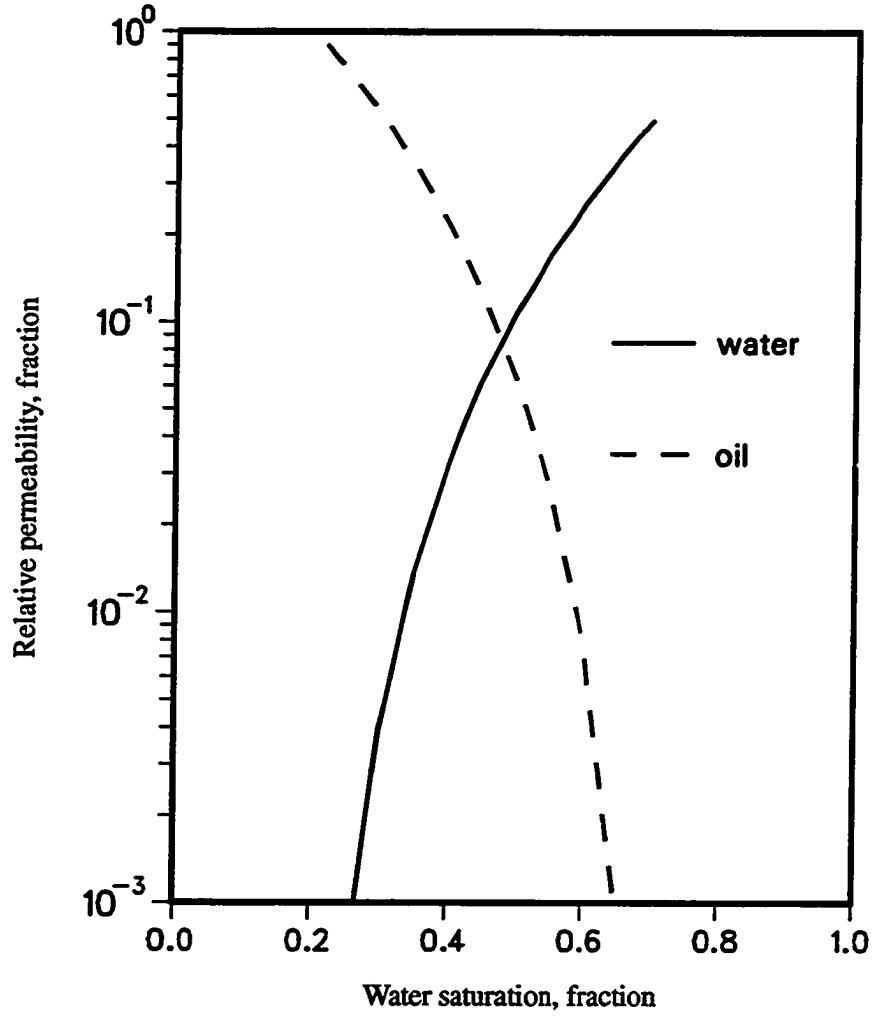

Figure 2.28 - Water -oil relative permeability curves used in flow simulations

of 20% was assumed.

Figure 2.29 shows the location of the 59 wells used in the flow simulation. The wells were "drilled" on 80 acre spacing. These well locations do not correspond with the actual location of wells in the Burbank Field. All of the wells were operated at a constant bottomhole pressure of 200 psi. A total of 10 years of primary production was simulated. Following primary production, 32 of the producers were converted to water injection wells to form 27 five-spot patterns (Figure 2.30). The injection pressure for all injection wells was set at 2000 psi. Water injection was continued for 10 years, resulting in a total simulation time of 20 years. Due to the heterogeneities, large number of grid blocks (38,880) and large number of wells (59), the flow simulation required 20 CPU hours on a CRAY computer. The flow simulator, GCOMP,[66] and computer time were furnished by Amoco Production Research.

Field performance is illustrated in Figure 2.31. Oil production decreased from an initial rate of 78,000 STB/D to 430 STB/D by the end of primary recovery. Although the increased reservoir pressure resulted in essentially an immediate increase in oil production, the effects of oil displacement by water first appeared after about 8 months of water injection. The peak secondary response of 9000 STB/D of oil occurred after 40 months of water injection. The field water injection rate peaked very early at about 50,000 B/D. The field WOR increased to 5 by the end of the simulation. Approximately 14.3% (33.2 MMSTBO) of the 232.5 MMSTBO originally in-place was produced during primary recovery. An additional 7.1% (16.6 MMSTBO) of the OOIP was recovered during waterflooding.

Figure 2.32 shows the variation in well performance within the Model Area. For the illustrated wells, initial oil production rates vary from a low of 200 STB/D (Well P48) to a high of 7500 STB/D (Well P44). Although direct comparison between simulated and actual well performance was not made, the simulated initial rates exhibited the same degree of variability and magnitude as the Burbank Field wells. Wells P44

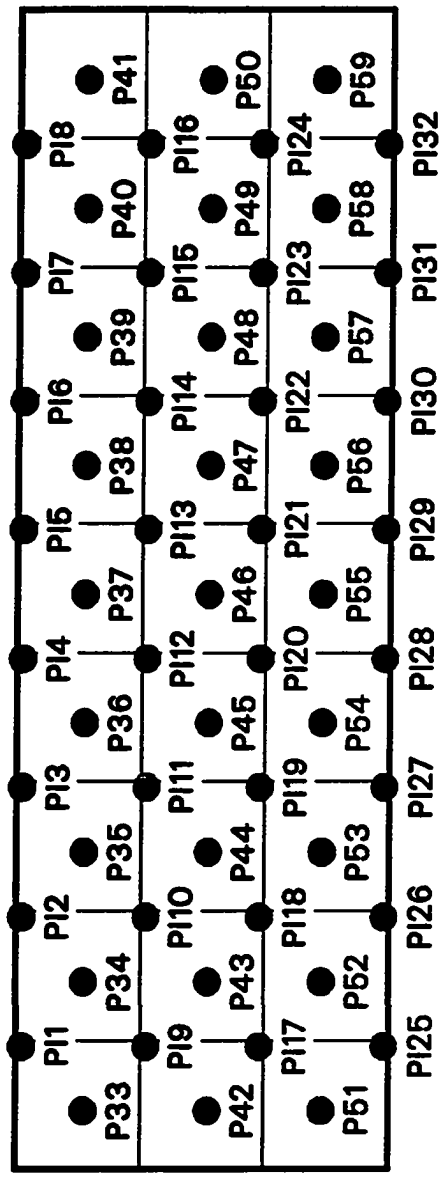

Figure 2.29 - Location of producers during simulated primary recovery

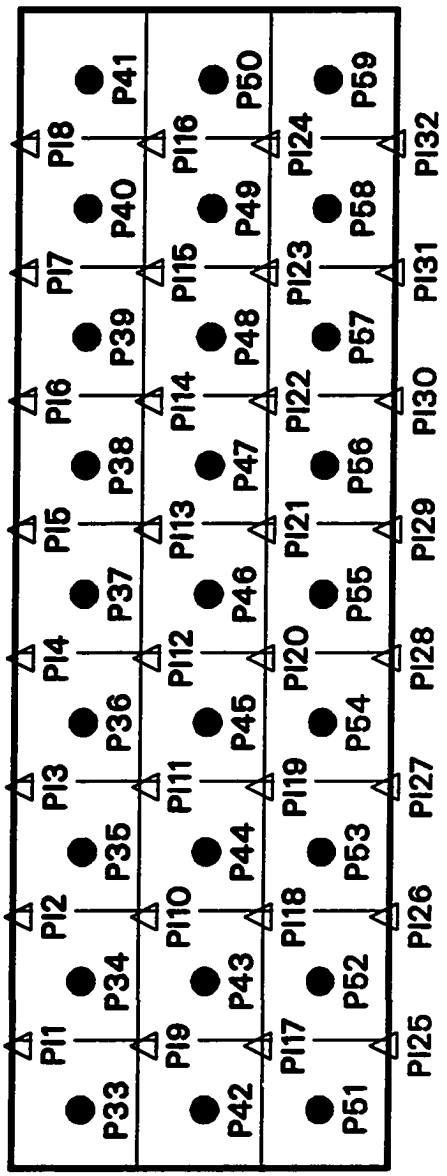

Figure 2.30 - Location of producers and injectors during simulated waterflood

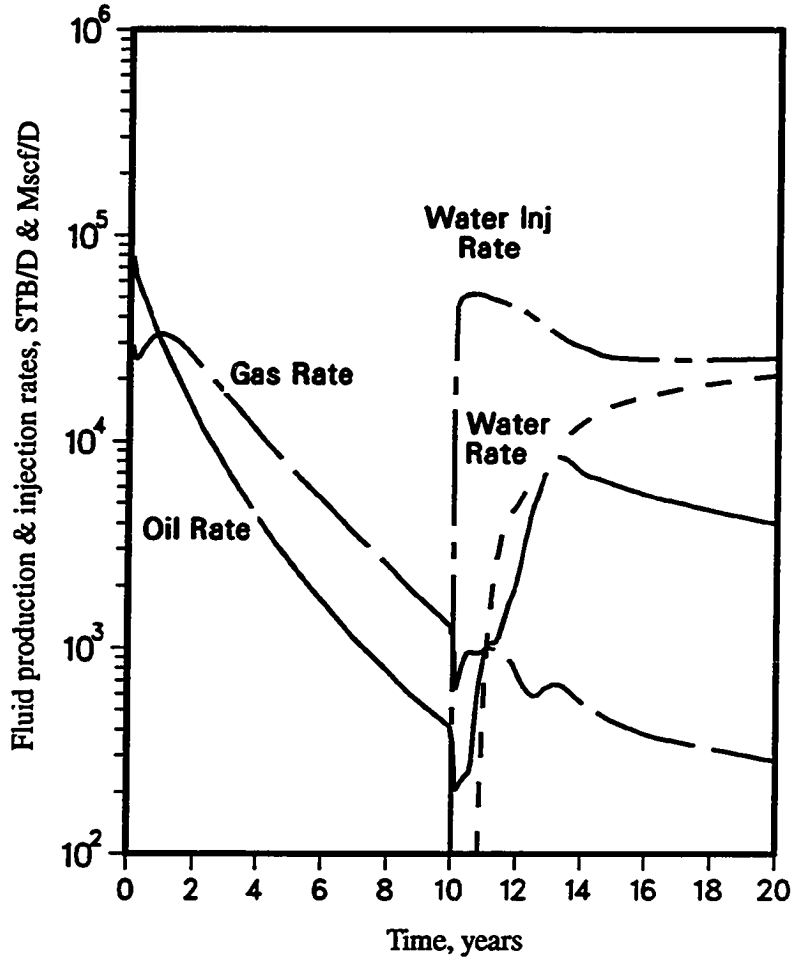

Figure 2.31 - Simulated field performance for Three-Dimensional Truth Case

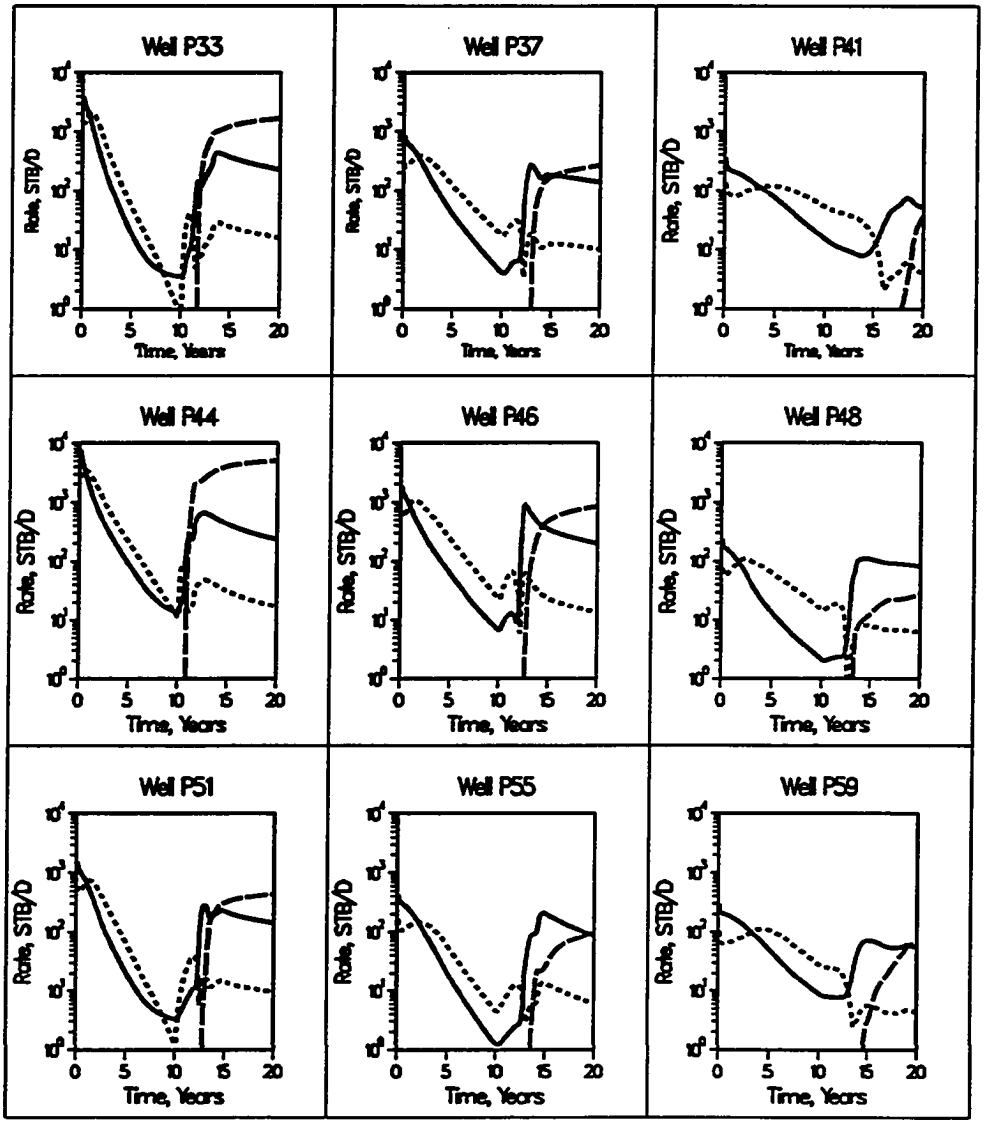

Figure 2.32 - Comparison of well performance for nine producers

and P48 are located in the west-central and east-central portions of the Model Area, respectively. Water breakthrough times range from 10 months (Well P44) to 8 years (Well P41). Well P41 is located in the north-east corner of the Model Area. The secondary response from several of the wells appears to be affected by multiple oil banks as evidenced by several peaks during early water injection.

Water injection histories of 9 water injection wells are compared in Figure 2.33. A large variation in local injectivity is evident with Wells PI8 (north-east) and PI29 (south-central) reaching a peak injection rate of only 600 B/D, whereas Well PI20 (central) achieves a maximum injection rate of 4000 B/D.

Plan view contour maps of Flow Unit 3 pressure at 2.5 year intervals are presented in Figure 2.34. During primary production, pressure depletion was greatest on the west side and gradually moved eastward. Essentially all of Flow Unit 3 had pressures between 200 - 300 psi at the end of primary production. The west-central portion of Flow Unit 3 repressurized the quickest during water injection. By the end of waterflooding, nearly all of Flow Unit 3 had pressures in excess of the initial reservoir pressure of 1200 psi.

Figure 2.35 illustrates reservoir pressure contours for Flow Unit 10 at 2.5 year intervals. A comparison of Figures 2.34 and 2.35 shows that reservoir pressure was relatively uniform vertically throughout the Model Area during primary and secondary recovery.

Plan view contour maps of Flow Units 3 and 10 gas saturation at 2.5 year intervals are included in Figures 2.36 and 2.37, respectively. Although pressure depletion was relatively uniform in all of the flow units, a comparison of Figures 2.36 and 2.37 shows that the amount of free gas greatly varied between flow units. Significant free gas migrated upward to the shallower flow units. The average gas saturation of Flow Unit 3 at the end of primary recovery was approximately 40% as compared to 10 - 15% for Flow Unit 10. Most of the gas was redissolved within 2.5 years of water injection.

Figures 2.38 and 2.39, respectively, are plan view contour maps of Flow Units 3

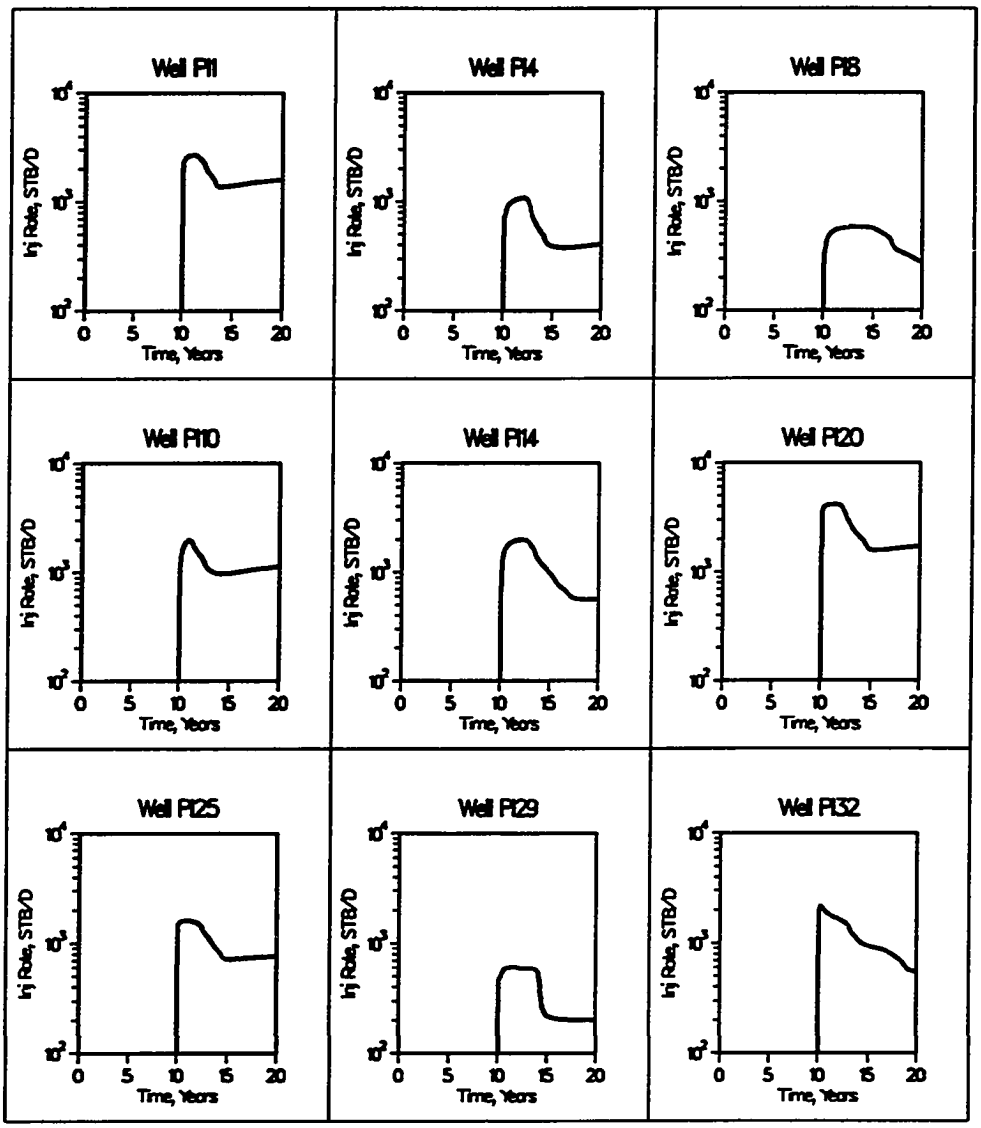

Figure 2.33 - Comparison of well performance for nine injectors

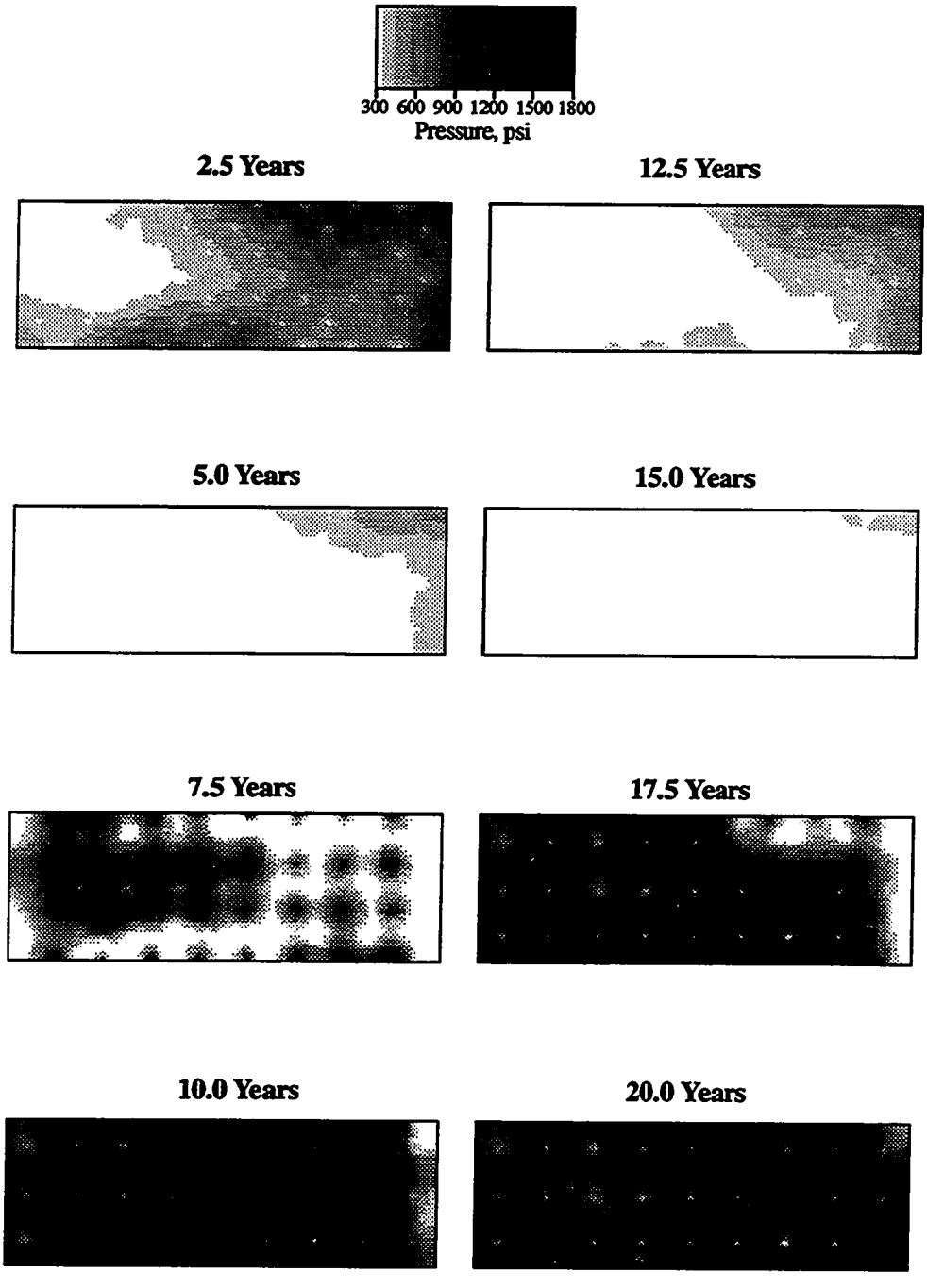

Figure 2.34 - Plan view of Flow Unit 3 pressure distribution at 2.5 year intervals

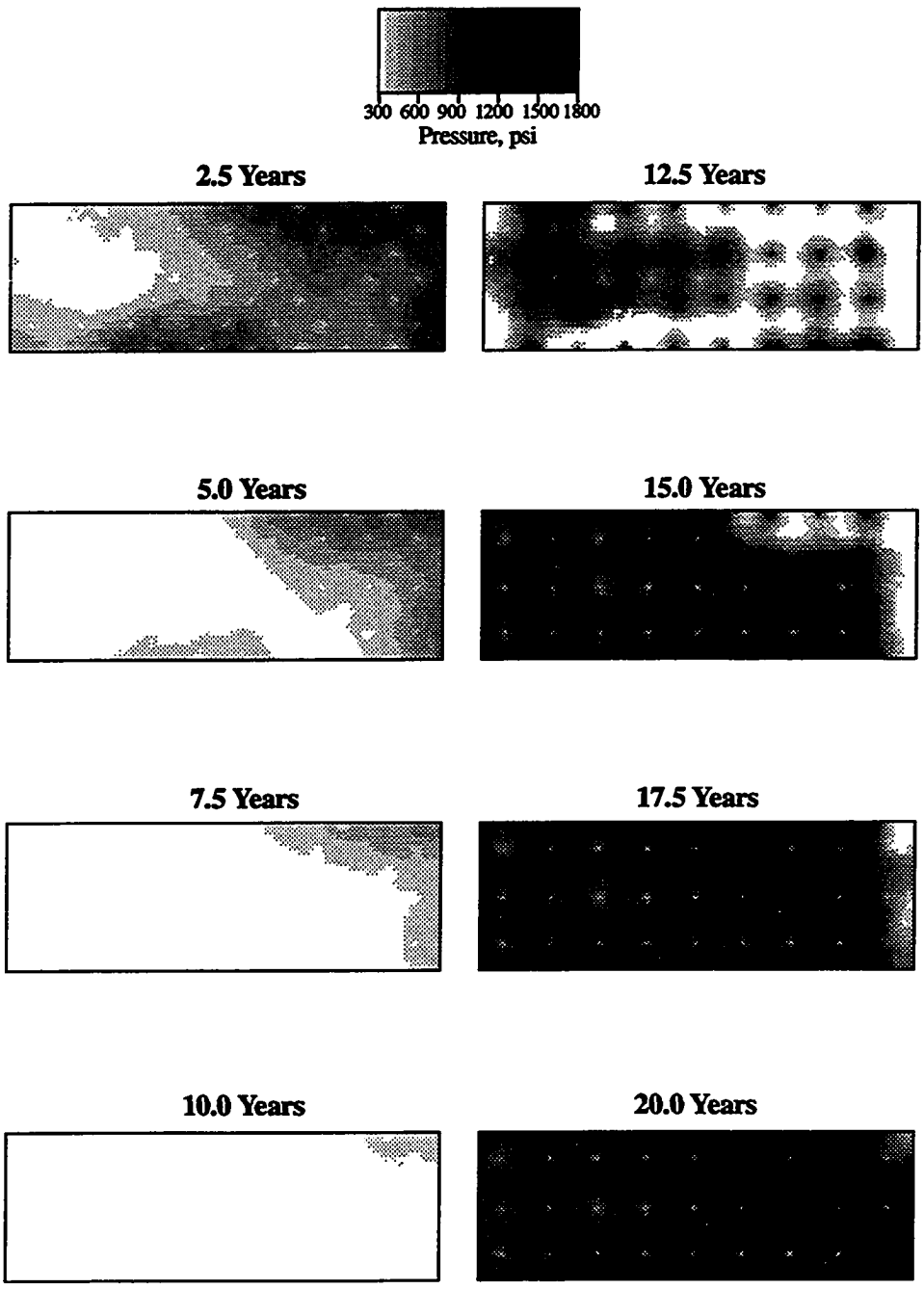

Figure 2.35 - Plan view of Flow Unit 10 pressure distribution at 2.5 year intervals

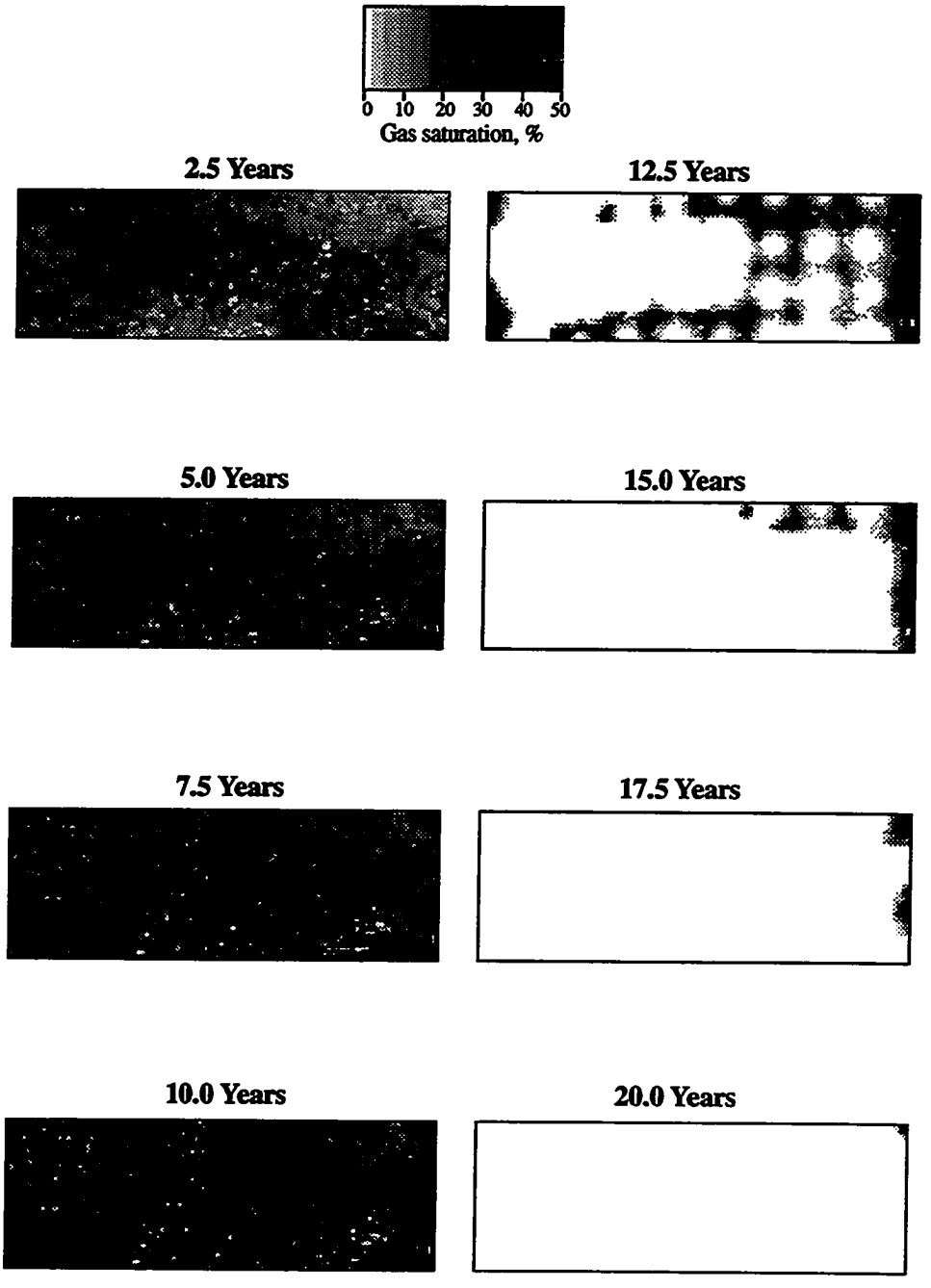

Figure 2.36 - Plan view of Flow Unit 3 gas saturation distribution at 2.5 year intervals

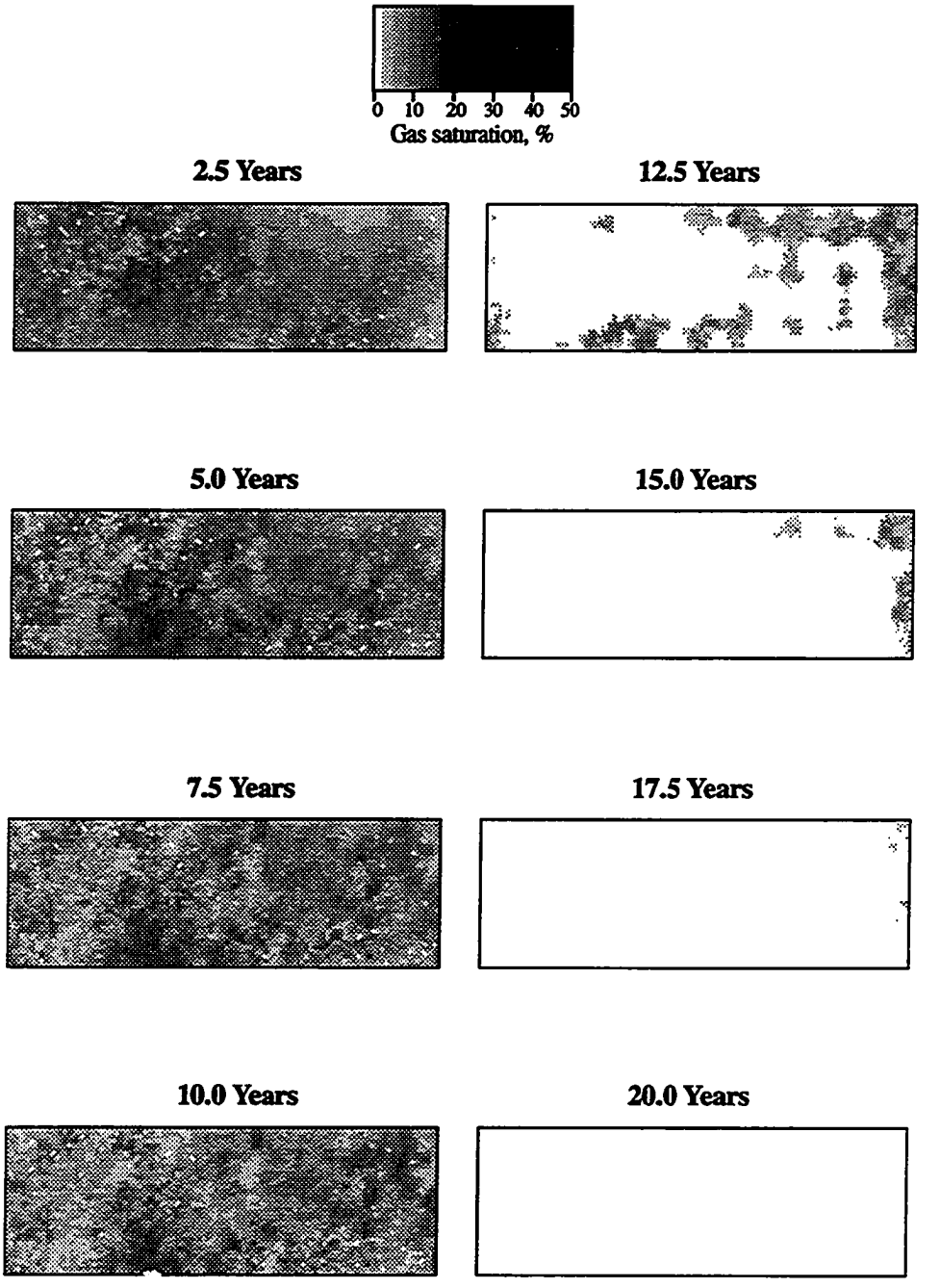

Figure 2.37 - Plan view of Flow Unit 10 gas saturation distribution at 2.5 year intervals

and 10 water saturation during waterflooding. Note that most of Flow Unit 3 was effectively swept by water whereas Flow Unit 10 had been poorly swept.

Exhaustive vs. Estimated Properties

It is interesting and insightful to compare grid block contours of thickness and porosity (Figures 2.21 and 2.23) to contours based on well data only. The software package SURFER[67] was used to generate contours of well thickness and porosity. A bilinear interpolation scheme was used for contouring. This contouring technique, or similar ones, has been used extensively in the past to estimate interwell grid block properties for flow simulation purposes.

Figure 2.40 shows a comparison between Flow Unit 3 grid block porosities and a contour of well porosities. For consistency, flow unit scale values of porosity (as opposed to grid block scale values) were used as well data since these data represent the scale at which porosity normally would be available. Note that although many of the gross features of the grid block data are reproduced, there is a significant loss in the spatial variability of porosity. Additionally, there are also anomalous trends produced by the well data. For instance, the well data contour map indicates a region of high porosity in the south-central area of the model. This high porosity region does not exist in the actual reservoir description.

A comparison between flow unit grid block scale values and well data based estimates for porosity and thickness are presented in Figures 2.41 - 2.44. A couple of points are worth mentioning. First, the spatial anisotropy of thickness prevalent in Flow Units 6 and 7 are not reproduced in their respective contours of well data (see Figure 2.44). It may be possible to capture this directional trend by variogram analysis. Second, as mentioned for Flow Unit 3, several other well data contours have anomalous trends, most notably Flow Unit 10 thickness (Figure 2.44). Well P35 (see Figure 2.29) is located within a grid block which contains less than 2 ft of Flow Unit 10, although most

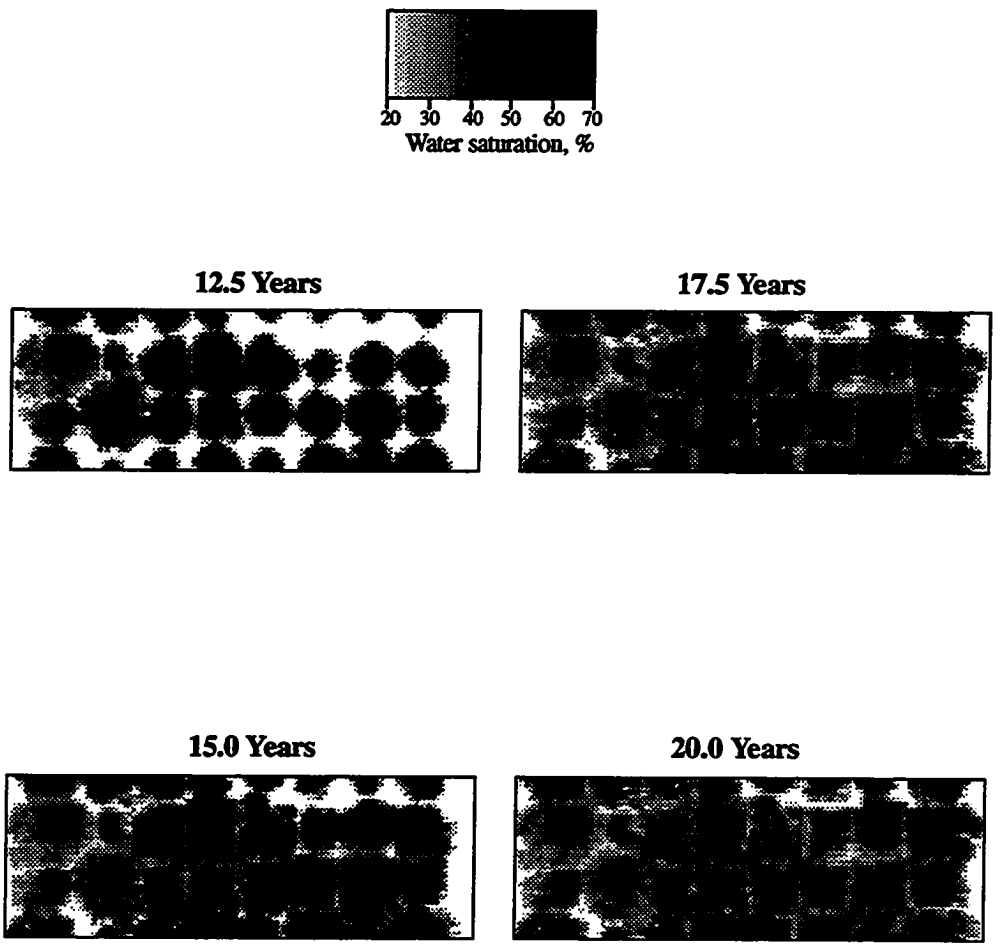

Figure 2.38 - Plan view of Flow Unit 3 water saturation distribution at 2.5 year intervals

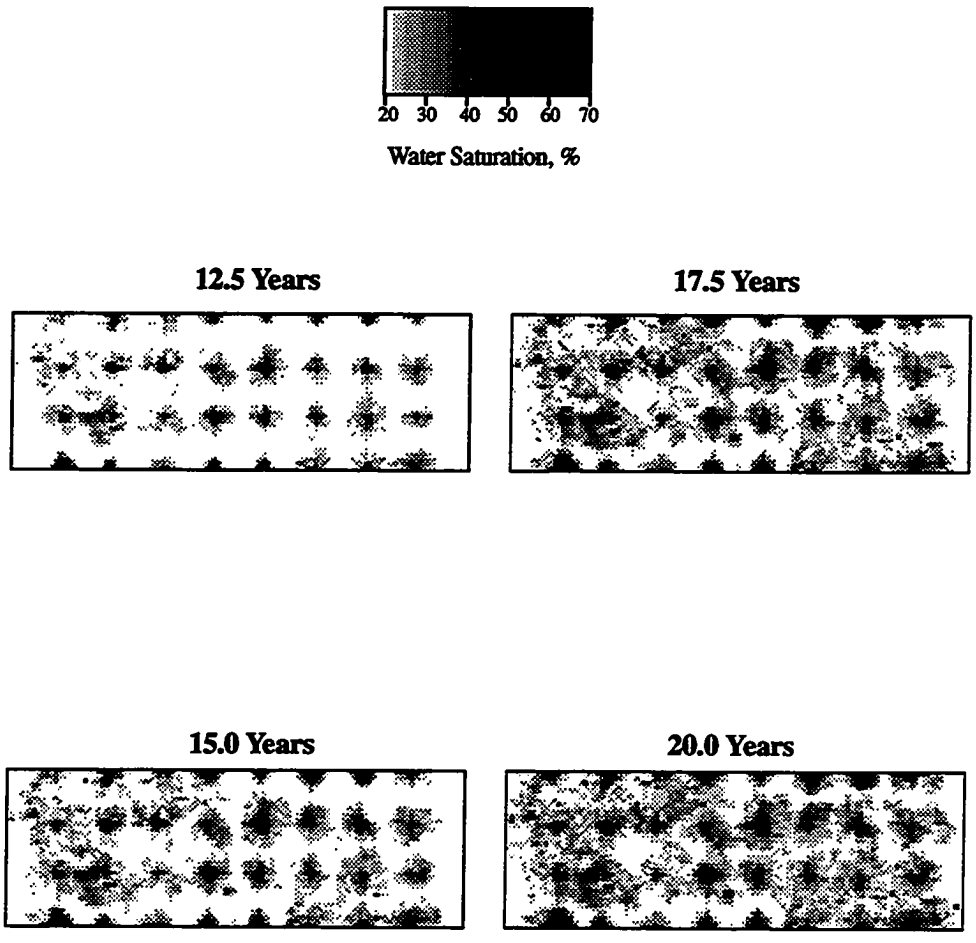

Figure 2.39 - Plan view of Flow Unit 10 water saturation distribution at 2.5 year intervals

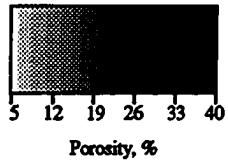

Exhaustive Grid Block Data

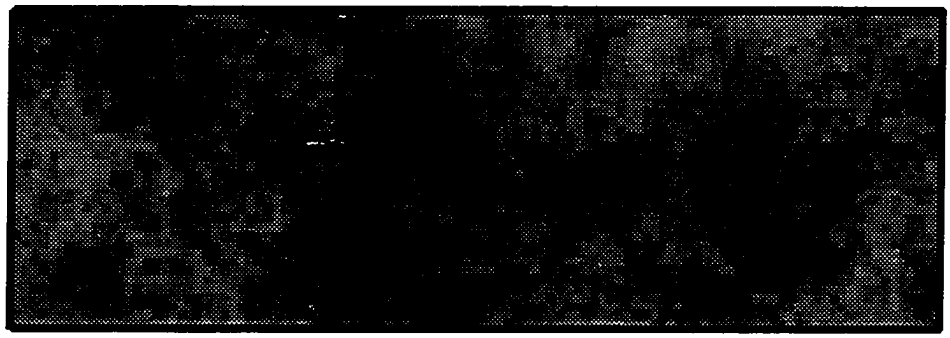

Contour Estimate From Well Data

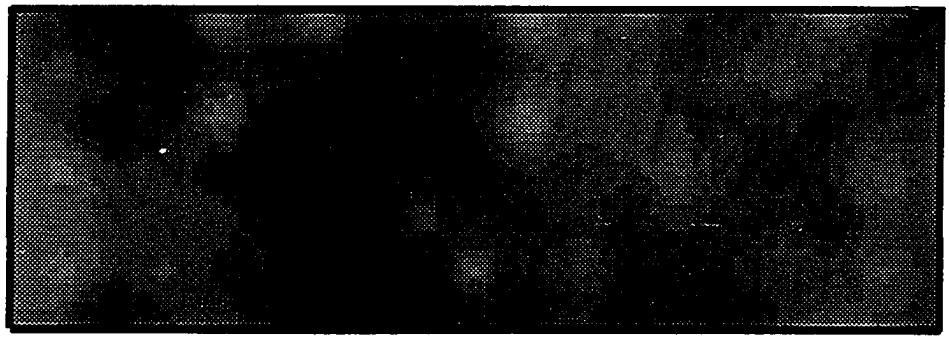

Figure 2.40 - Comparison of Flow Unit 3 porosity images: exhaustive grid block values vs. estimates obtained from contouring well porosity values

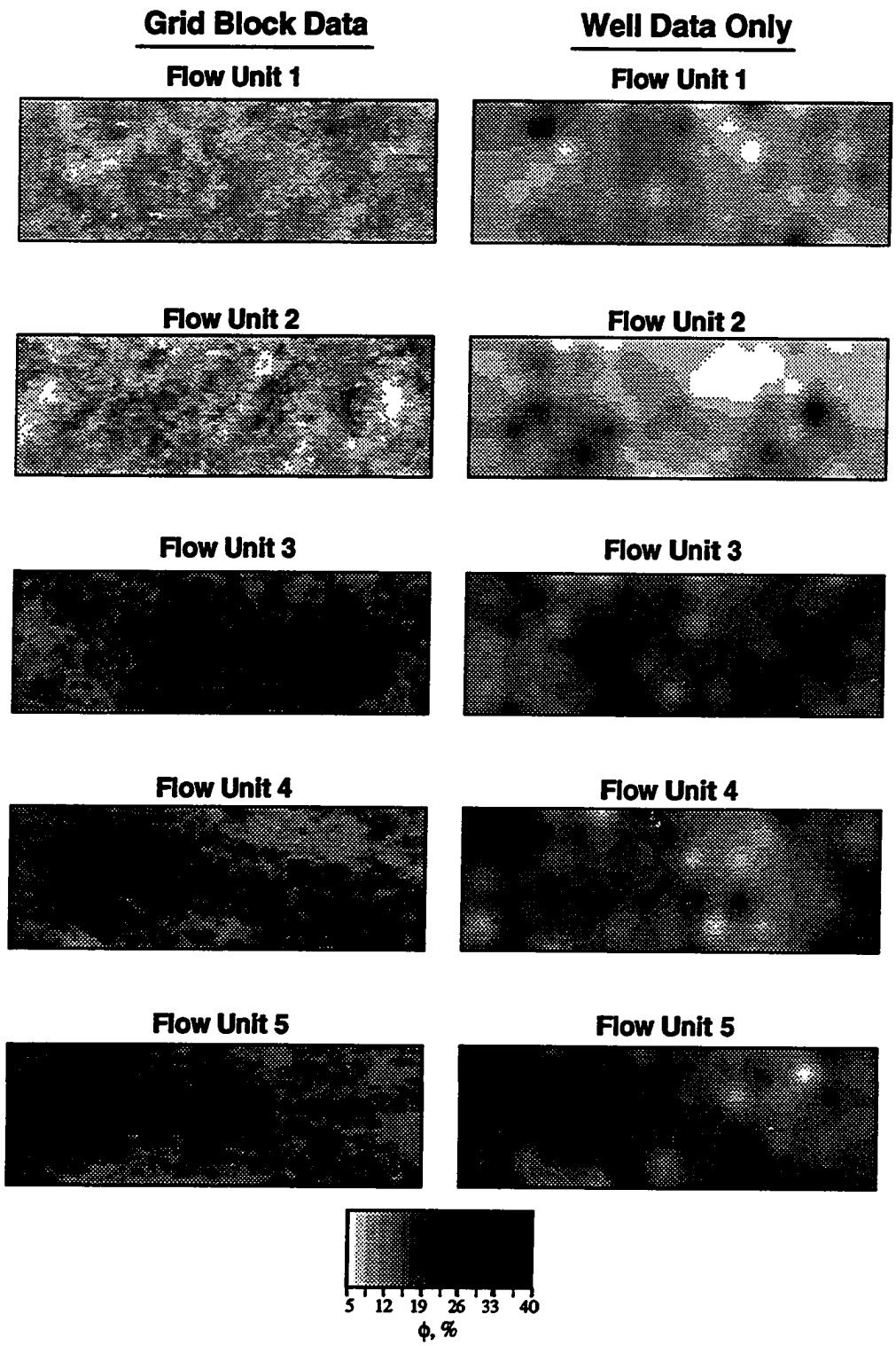

Figure 2.41 - Comparison of porosity images derived from exhaustive grid block values vs. estimates obtained from contouring well values; Flow Units 1 - 5

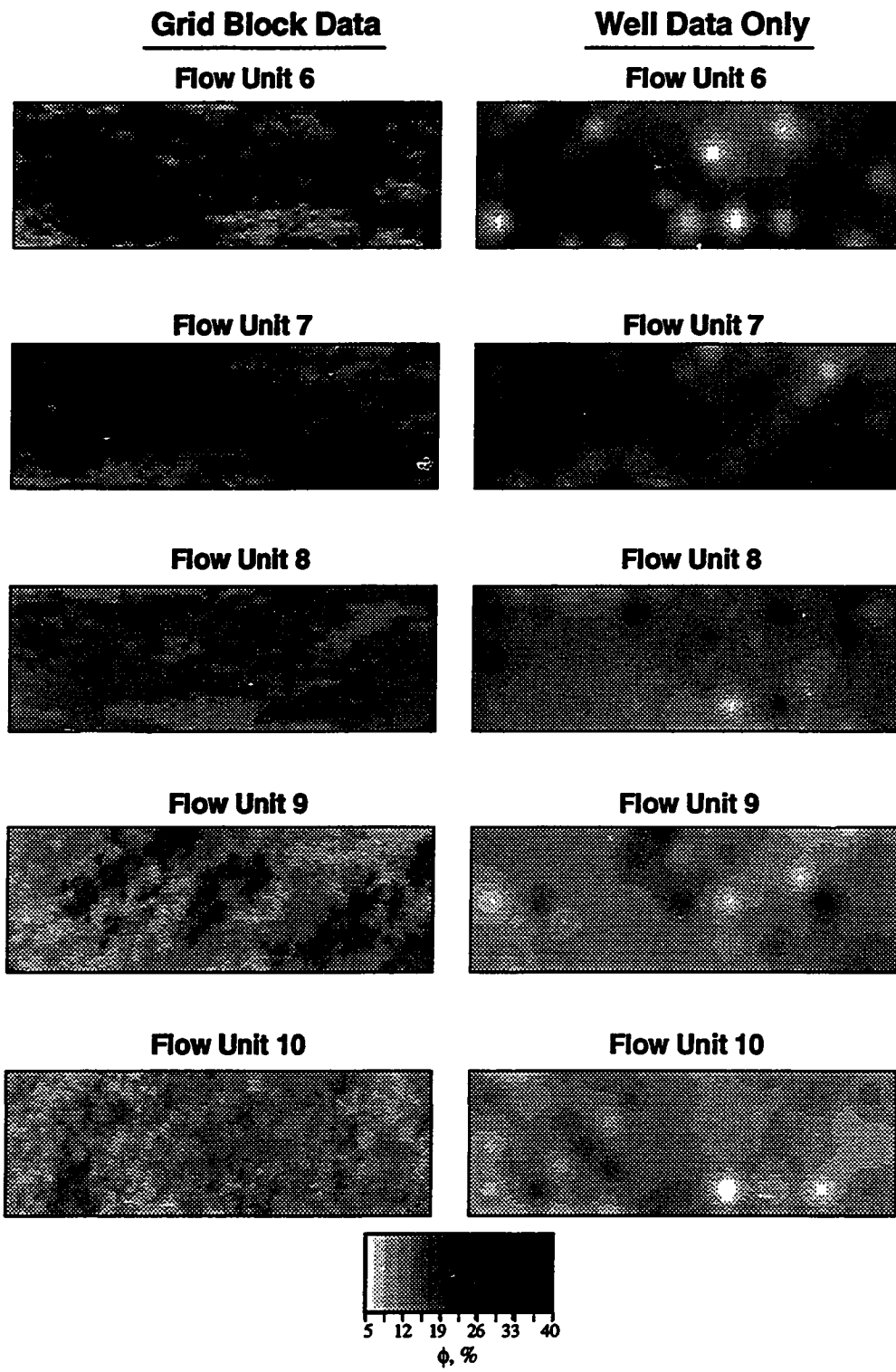

Figure 2.42 - Comparison of porosity images derived from exhaustive grid block values vs. estimates obtained from contouring well values; Flow Units 6 - 10

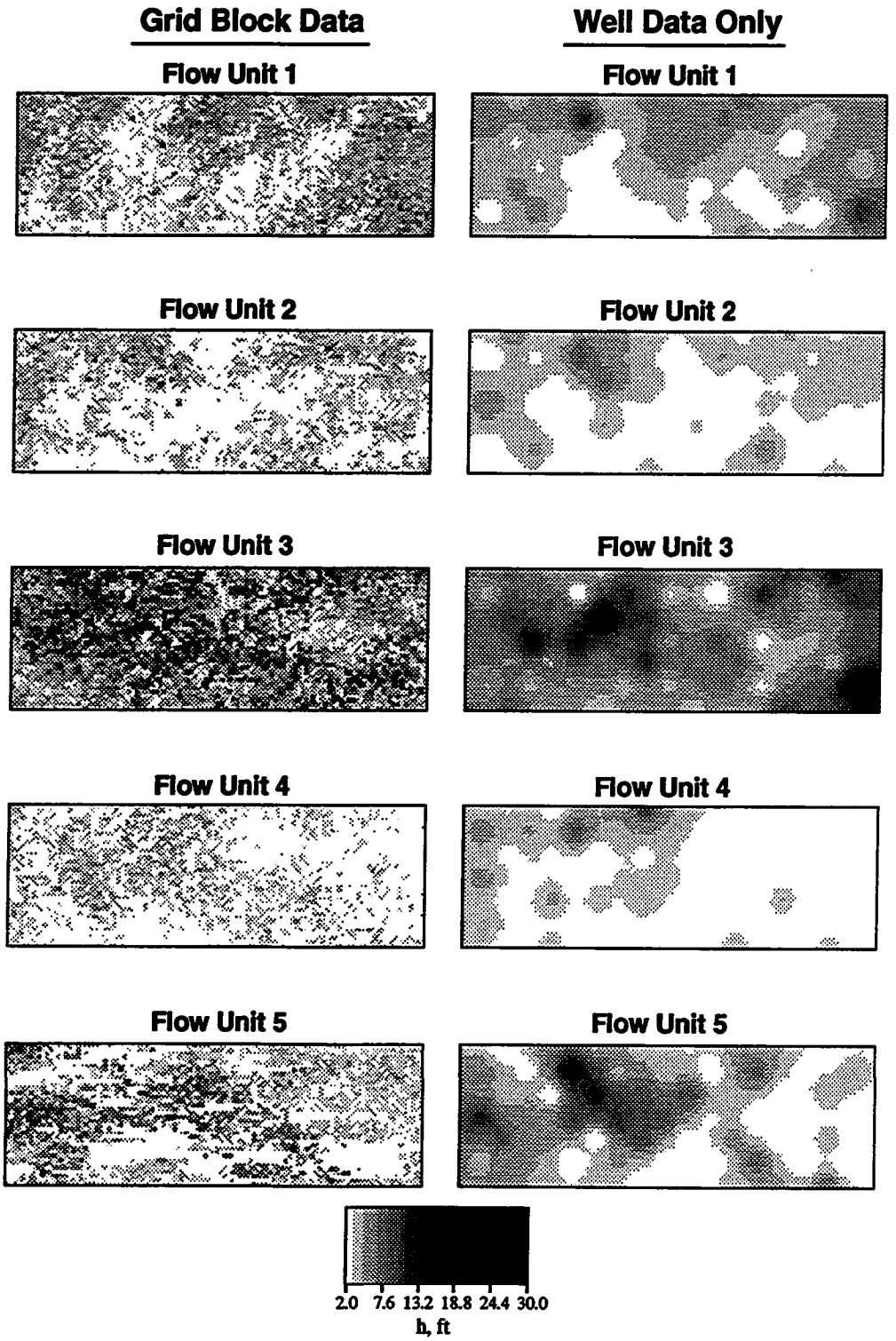

Figure 2.43 - Comparison of flow unit thickness images derived from exhaustive grid block values vs. estimates obtained from contouring well values; Flow Units 1 - 5

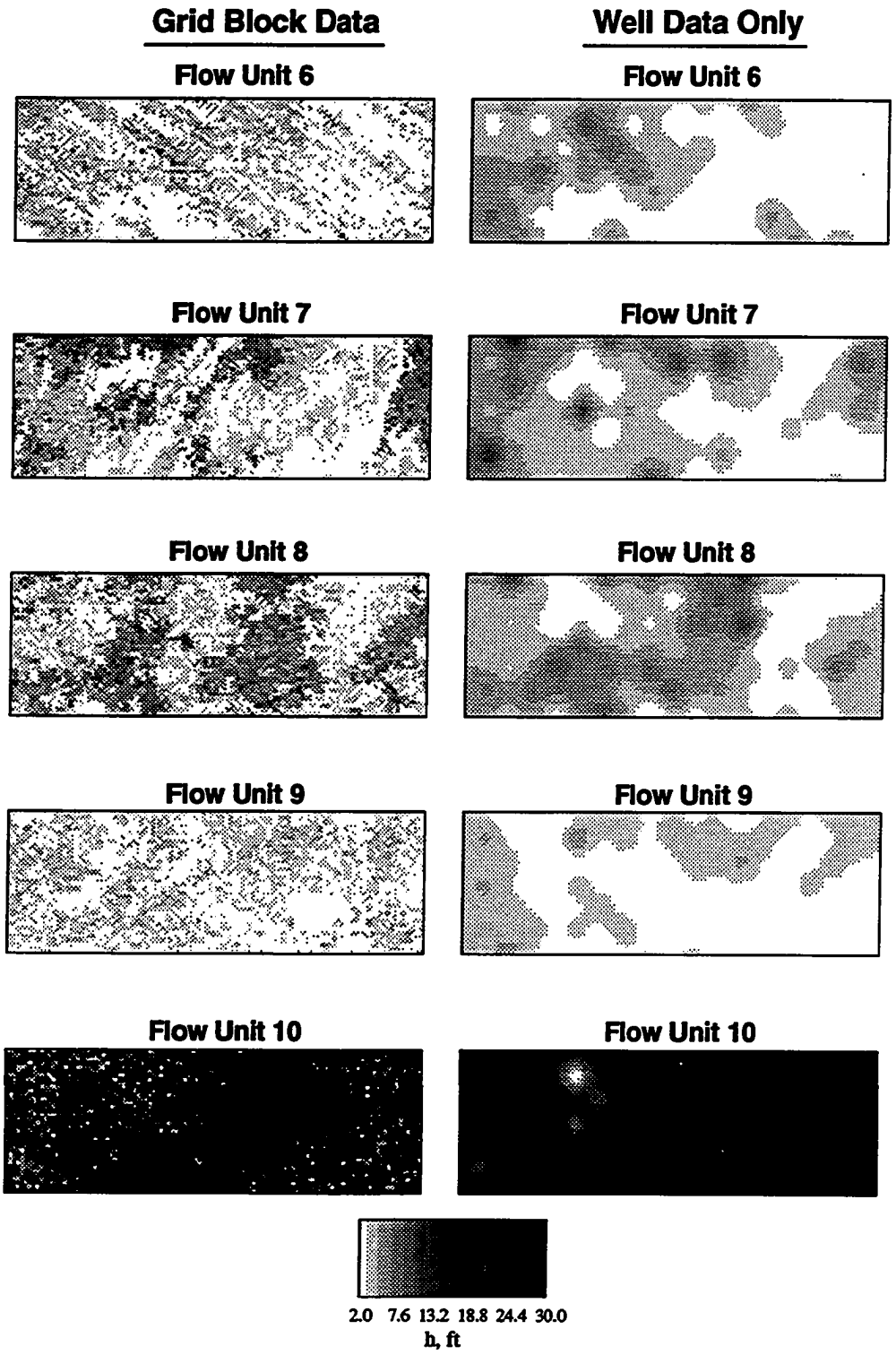

Figure 2.44 - Comparison of flow unit thickness images derived from exhaustive grid block values vs. estimates obtained from contouring well values; Flow Units 6 - 10

of the surrounding blocks have thicknesses in excess of 30 ft. As a result, the well data contour of Flow Unit 10 thickness incorrectly contains a significantly large area with sand thickness of 2 ft or less.

Contribution

The objectives of the work documented in this chapter were to develop a realistic three-dimensional reservoir description and generate corresponding synthetic primary and waterflood performance which have realistic characteristics. It is concluded that the above objectives have been achieved based on the flow simulation results documented above and the similarities between simulated well performance and actual Burbank Field well performance. Considering that all of the exhaustive reservoir properties, operating conditions, and flow rates are known, the 3D Truth Case becomes a valuable data set for evaluating reservoir characterization techniques.

The comparison of exhaustive reservoir properties to estimates obtained by contouring of well data illustrates the deficiencies of using estimation techniques for flow simulation purposes. Contoured estimates were shown to have significant errors in some cases. The variability and anisotropy characteristics evident in the exhaustive data were not preserved by contouring. Such spatial properties are important in most fluid flow modeling.

The 3D Truth Case reservoir description and corresponding simulated reservoir performance have been shown to be fairly complex. The large contrast in the rock properties between the main sand body (Flow Units 3 - 8) and Flow Unit 10 results in true three-dimensional fluid flow characteristics. This was illustrated by comparing the pressure and saturation histories of Flow Units 3 and 10. A more detailed analysis of cumulative production from these flow units shows that most of the production during the first five years of primary recovery is from the main sand body. The last five years of primary recovery is dominated by Flow Unit 10. Due to the complex nature of the 3D Truth

Case, it was decided to use a two-dimensional version of the data set for evaluating techniques developed during this study. The two-dimensional data set is discussed in Chapter V. The 3D Truth Case can be used for evaluating conditional simulation techniques once the technology has been adequately developed. For this reason, a 3-1/2" diskette containing ASCII files of the 3D Truth Case data set has been included as an attachment to this dissertation. Appendix A describes each file contained on the diskette.

CHAPTER III

PRIMARY PERFORMANCE CONSTRAINTS

This chapter investigates the correlation between primary well performance parameters and spatial distributions of porosity and permeability. In reservoir modeling, it is advantageous to identify as early as possible well performance characteristics which are influenced by heterogeneities. Such information can be used to better define internal reservoir architecture and optimize operating and development plans early in the life of a reservoir. The simulated annealing method will be described first since it is the conditional simulation technique used in this study for integrating spatial and well performance constraints. The correlation between initial production rates and permeability heterogeneities will then be discussed. Lastly, the influence of porosity heterogeneities on primary well performance will be investigated.

Simulated Annealing

Consistent with other conditional simulation techniques, spatial distributions of a variable generated using simulated annealing honor: 1) the conditioning data, 2) the univariate distribution and 3) the spatial correlation as represented by the variogram. The simulated annealing algorithm is described in detail elsewhere;[24-27] only a summary will be presented here. The primary intent of the method is to determine spatial distributions of a variable which honor the three constraints defined above.

The first constraint (honoring conditioning data) is easily met by assigning the conditioning data to their respective locations upon initiation of the algorithm. The second objective (honoring the univariate distribution) is attained by randomly sampling the cdf when assigning values to their initial locations. Essentially all of the computation time is

required for meeting the third constraint--honoring the variogram. This is achieved by iteratively swapping the location of pairs of values until the actual variogram is representative of the target variogram. Mathematically, this is obtained by minimizing a least squares objective function, O, of the variogram for a specified number of lag intervals, N_L:

$$O = \sum_{l=1}^{N_L} [\gamma_a(h_l) - \gamma_t(h_l)]^2 \tag{3.1}$$

where $\gamma_a(h_l)$ is the actual variogram and $\gamma_t(h_l)$ is the target variogram. Conventional practice is to normalize the variogram by the target variogram for each lag interval:

$$O = \sum_{l=1}^{N_L} \frac{[\gamma_a(h_l) - \gamma_t(h_l)]^2}{[\gamma_t(h_l)]^2} \tag{3.2}$$

This is done to give equal weight to variogram differences at all lag intervals, irrespective of variogram magnitude. As a result, variogram differences at large lag intervals do not dominate the objective function. It is often desirable to evaluate the variogram along more than one direction when computing the objective function:

$$O = \sum_{d=1}^{N_D} \sum_{l=1}^{N_{L,d}} \frac{[\gamma_a(h_{l,d}) - \gamma_t(h_{l,d})]^2}{[\gamma_t(h_{l,d})]^2} \tag{3.3}$$

where N_D is the number of directions and $N_{L,d}$ is the number of lag intervals for direction d.

The heart of the algorithm is the criteria used to evaluate whether a swap should be accepted or rejected. The swap is always accepted if the objective function is reduced. When a swap increases the objective function, the Boltzmann probability distribution is used to determine whether or not the swap is accepted.[22] The probability of accepting a swap, P_a, at the $k+1$ iteration is defined as:

$$P_a = \begin{cases} 1, & O_{k+1} \le O_k \\ exp\left[\dfrac{(O_k - O_{k+1})}{T}\right], & \text{otherwise} \end{cases} \tag{3.4}$$

where T represents the annealing "temperature." This is referred to as the Metropolis condition.[68] A random number is drawn from a uniform distribution between 0 and 1 and compared to P_a. The swap is accepted if P_a exceeds the random number; otherwise the swap is rejected. Similar to actual annealing, the probability of acceptance is a function of the temperature. Swaps which increase the objective function have a greater probability of being accepted at higher temperatures. As the temperature is decreased, the exponential function in Eq. 3.4 decreases, thereby reducing the probability of accepting swaps which increases the difference between the target and actual variograms. The possibility of accepting bad swaps (i.e., swaps which increase the objective function) allows the algorithm to escape from local minima.

An important feature of the algorithm is defining the temperature profile. Cooling the system too rapidly causes convergence to occur at a local minima. However, lowering the temperature too slowly results in excessive computational requirements. Although temperature profiles have been published which guarantee convergence,[21,22] these profiles are too slow for practical applications. The conventional approach is to reduce the temperature once a specified number of swaps have been accepted at that temperature, $N_{s,a}$, or after a specified number of swaps have been tried at the prevailing temperature, $N_{s,t}$. The parameters $N_{s,a}$ and $N_{s,t}$ are typically set to 5 - 20 and 75 - 150 times the number of cells, respectively. Typically, the temperature is lowered from an initial value, T_o, by applying a multiplicative factor, f_T, to the existing temperature, T_s, at each annealing step. The annealing parameters are referred to as the annealing schedule. Aarts and Korst[22] have proposed a method for estimating the initial temperature. Perez[25] has developed a procedure for optimizing the annealing schedule parameters $N_{s,a}$ and f_T.

The annealing algorithm can be summarized as follows (see Figure 3.1):

1. assign conditioning data to their respective cells. Randomly sample the cdf to obtain the initial, random spatial distribution.

2. compute the variogram model lag values; initialize the annealing parameters.
3. compute the actual variogram and the objective function.
4. randomly select a pair of locations for the potential swap.
5. compute the variogram and objective function. Compare the objective function to the value at the previous iteration. Accept/reject based on the Metropolis condition.
6. if the swap is accepted, exchange locations and update the variogram and the objective function. If the objective function is less than or equal to the specified convergence tolerance, output the results and stop; otherwise proceed to Step 8.
7. if the swap is rejected, determine if the maximum allowable swaps have been attempted; if so, then reduce the temperature and return to Step 4; otherwise, return directly to Step 4.
8. check to see if the maximum number of accepted or attempted swaps at the present temperature has been exceeded. If so, reduce the temperature and return to Step 4; otherwise, return directly to Step 4.

Although simulated annealing may appear to be an inefficient approach, it is actually best described by its versatility. Although the variogram is used as the minimization function in the conventional approach, any numerically quantifiable function or functions can be used. The functions can be of varying magnitude, "softness," types and units. One important restriction is that the parameter must not only be quantifiable, but from a practical viewpoint, it should also be capable of being locally updated. That is, the revised parameter value should be calculable given the previous value and the contributions from the pairs of interest:

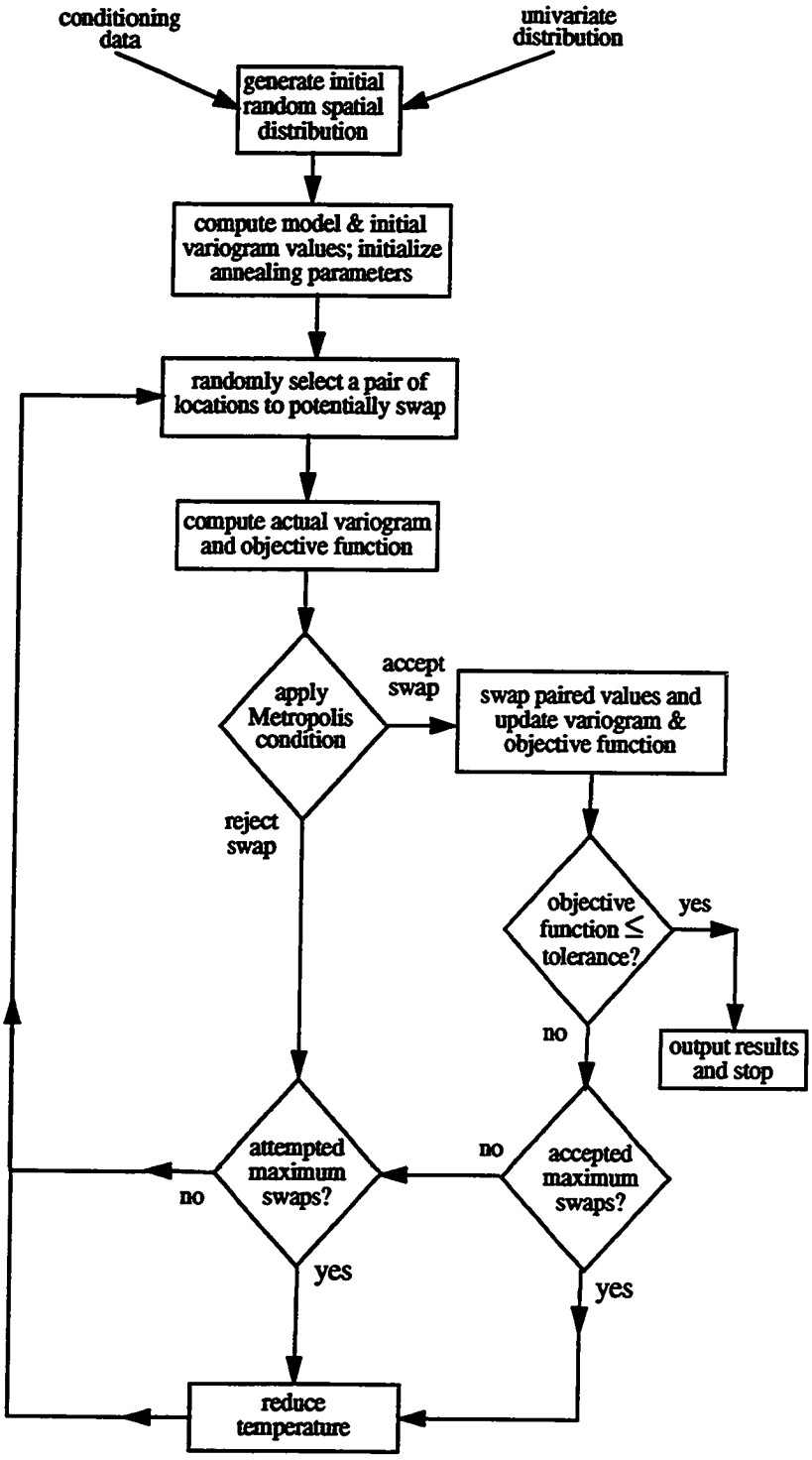

Figure 3.1 - Flow diagram of simulated annealing algorithm

$$V_{new} = V_{old} - V(i1,j1) - V(i2,j2) + V'(i1,j1) + V'(i2,j2) \tag{3.5}$$

where $V(i1,j1)$ and $V(i2,j2)$ represent any contribution by the values at $(i1,j1)$ and $(i2,j2)$ prior to the swap and $V'(i1,j1)$ and $V'(i2,j2)$ represent any contribution specific to the two locations after the swap. The advantage of variogram updating vs. recalculation is widely recognized.

The generalized form of the objective function can be written as:

$$O_T = \sum_{n=1}^{N_f} w_f(n) O(n) \tag{3.6}$$

where O_T is the total objective function, N_f is the number of functions comprising O_T and $w_f(n)$ represents the weighting function for objective function $O(n)$. The general form of $O(n)$ can be written as:

$$O(n) = \frac{[V_a(n) - V_t(n)]^2}{O_i(n)} \tag{3.7}$$

where $O_i(n)$ represents the initial objective function of component n. The weighting function serves two purposes. Normalizing the individual objective functions by $w_f(n)$ (and $O_i(n)$) removes any influence caused by varying magnitudes and units of each objective function component. Also, the weighting function allows the flexibility of assigning relative degrees of importance to each $O(n)$. This in effect is a means of considering some data softer than other data constraints.

Effective Near Well Permeability

It is well known that reservoir permeability has more of an effect on fluid flow than any other reservoir variable. Unfortunately, permeability is also one of the most difficult variables to quantify. Modern well logs are capable of measuring a wealth of information, but means for defining insitu vertical permeability profiles do not exist. Well tests are commonly used to estimate effective flow capacity, i.e., the product of net reservoir

thickness and effective reservoir permeability. However, such analytical techniques are frequently accompanied by a host of reservoir assumptions, including:

1. The reservoir is filled with a single phase fluid of constant viscosity and compressibility.
2. Uniform reservoir properties exist, including thickness, porosity and permeability.
3. Production is from a vertical, fully penetrating wellbore.
4. The surface production rate is constant.
5. Outer boundary conditions are either "infinite," no-flow or constant pressure and have a specific geometry, such as cylindrical.

Although several solutions have been developed in recent years which have eliminated some of the above restrictions, all assume some regularity in the permeability distribution. For example, solutions have been developed for defining radial permeability profiles, but with the assumption that permeability varies radially away from the wellbore. Such assumptions are hardly realistic but are necessary limitations due to the extremely limited amount of available information relative to the number of unknowns. In general, engineers are satisfied with a transient well test analysis if flow capacity and mechanical skin condition can be estimated with confidence.

Long term production is also strongly influenced by near well effective permeability. This will be illustrated by investigating steady-state flow characteristics. Although pseudo-steady state is more generally applicable to primary production, steady-state formulations will be used because of their simplicity and since the relevant conclusions are the same. The following formulation is based on a similar presentation by Muskat.[69] The partial differential equation governing steady-state fluid flow is:

$$\frac{1}{r}\frac{\partial}{\partial r}\left(r\frac{\partial p}{\partial r}\right) = 0 \tag{3.8}$$

where r is the radial distance from the wellbore and p is the reservoir pressure. This equation is commonly referred to as Laplace's equation. The inner and outer boundary conditions are defined as:

$$\begin{aligned} p &= p_{wf} \text{ at } r = r_w \\ p &= p_e \text{ at } r = r_e \end{aligned} \tag{3.9}$$

where p_{wf} is the flowing pressure at the wellbore radius, r_w and p_e is the pressure at the external radius r_e. The system pressure distribution is obtained by solving Eqs. 3.8 and 3.9:

$$p(r) = p_{wf} + \left[\frac{p_e - p_{wf}}{ln\left(\frac{r_e}{r_w}\right)}\right] ln\left(\frac{r}{r_w}\right) \tag{3.10}$$

Note that the pressure varies with the logarithm of the radial distance. Therefore, the largest pressure drop occurs near the wellbore. For example, for 80 acre well spacing and a wellbore radius of 0.25 ft, 44.2% of the entire pressure drop occurs within the inner 1% of the radial reservoir extent (10 ft). To investigate the impact of converging radial flow, Eq. 3.10 needs to be combined with Darcy's Law:

$$v_r = -\frac{k}{\mu}\frac{\partial p}{\partial r} = \frac{-q_r}{2\pi r_w h} \tag{3.11}$$

where v_r is the radial velocity, μ is the fluid viscosity, q_r is the bottomhole flow rate and h is the reservoir thickness. Solving Eqs. 3.10 and 3.11 results in the following flow rate relationship:

$$q_r = \frac{2\pi kh(p_e - p_{wf})}{\mu ln\left(\frac{r_e}{r_w}\right)} \tag{3.12}$$

or, in oil field units:

$$q_h = \frac{0.007082kh(p_e - p_{wf})}{\mu B ln\left(\frac{r_e}{r_w}\right)} \tag{3.13}$$

where q_h is the surface flow rate in STB/D, μ is the fluid viscosity in cp, B is the formation volume factor in STB/RB, k is the effective permeability in md, h is the formation thickness in ft, p_e is the external boundary pressure in psi, p_{wf} is the flowing wellbore pressure in psi, r_w is the wellbore radius in ft and r_e is the external reservoir radius in ft. Eq. 3.13 indicates that the flowrate varies logarithmically with radial distance.

The above steady-state formulation assumes a homogeneous reservoir. To investigate the impact of varying permeability, the flow equation for a two zone composite system will be investigated. The following will be assumed:

$$\begin{aligned} k &= k_i \text{ for } r_w < r < r_i \\ k &= k_o \text{ for } r_i < r \le r_e \\ r_w &< r_i < r_e \end{aligned} \tag{3.14}$$

The reservoir system of interest is illustrated in Figure 3.2. In addition to the two above boundary conditions (Eq. 3.14), pressure and flux continuity must be imposed at the radial interface:

$$\text{at } r = r_i,$$
$$p_i = p_o \text{ and } k_i \frac{\partial p_i}{\partial r} = k_o \frac{\partial p_o}{\partial r} \tag{3.15}$$

The pressure solution for Eqs. 3.8, 3.14 and 3.15 is:

$$\begin{aligned} r_w \le r \le r_i, \quad p(r) &= p_w + \frac{p_e - p_w}{ln\left(\frac{r_i}{r_w}\right) + \kappa ln\left(\frac{r_e}{r_i}\right)} ln\left(\frac{r}{r_w}\right) \\ r_i \le r \le r_e, \quad p(r) &= p_e + \frac{\kappa (p_e - p_w)}{ln\left(\frac{r_i}{r_w}\right) + \kappa ln\left(\frac{r_e}{r_i}\right)} ln\left(\frac{r}{r_e}\right) \end{aligned} \tag{3.16}$$

where $\kappa = k_i/k_o$. Applying Darcy's Law to Eq. 3.16 results in the following rate solution for the composite system:

$$q_c = \frac{2\pi k_i h (p_e - p_{wf})}{\mu\left[ln\left(\frac{r_i}{r_w}\right) + \kappa ln\left(\frac{r_e}{r_i}\right)\right]} \tag{3.17}$$

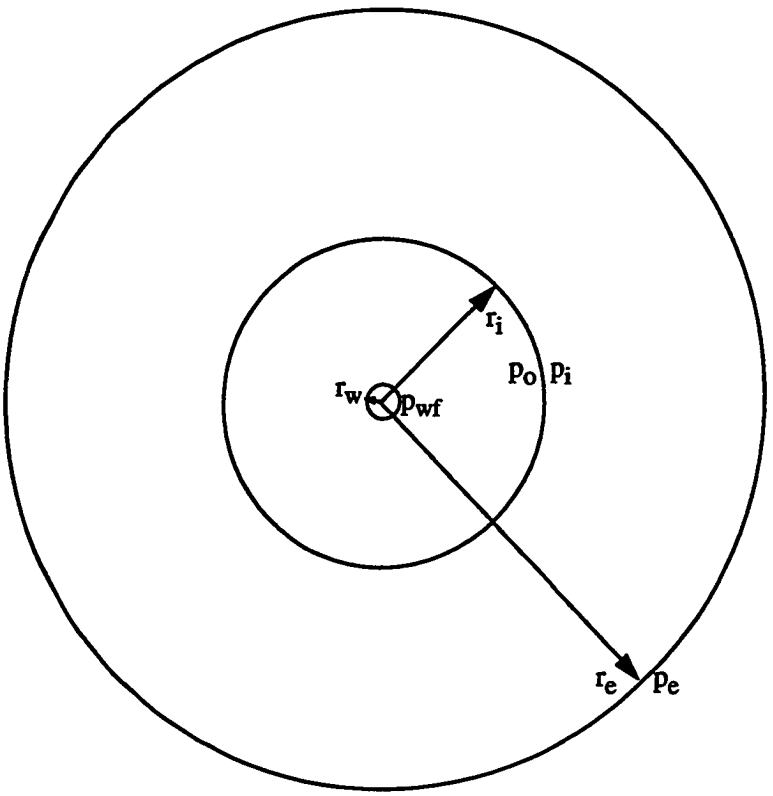

Figure 3.2 - Schematic of two-zone composite radial system

The impact of near well effective permeability can be illustrated by normalizing the homogeneous system flow rate solution (q_h, Eq. 3.13) by the composite system flow rate equation (q_c, Eq. 3.17):

$$\frac{q_c}{q_h} = \frac{\kappa ln\left(\frac{r_e}{r_w}\right)}{ln\left(\frac{r_i}{r_w}\right) + \kappa ln\left(\frac{r_e}{r_i}\right)} \tag{3.18}$$

Two examples will be used to illustrate the impact of Eq. 3.18. As before, it will be assumed that the well spacing is 80 acres and r_w is 0.5 ft. The first case will assume the inner 10 ft has one-tenth the permeability of the rest of the reservoir, i.e., κ is 0.1. Solving Eq. 3.18, it is seen that reducing the permeability of the inner 1% of the radial extent (10 ft) by a factor of 10 results in an 80% reduction in the flow rate. Conversely, if it is assumed that the inner 1% is 10 times more permeable than the outer region ($\kappa = 10$), a 67% increase in the flow rate is achieved compared to the homogeneous case. These examples aptly illustrate the dominating effect of the near well permeability on well performance.

Several recent papers have addressed the problem of calculating effective permeability from small scale permeability heterogeneities. The techniques can be categorized as numerical,[65,70-72] analytical[73-75] and streamtube[42,76,77] methods. Warren and Price[65] were the first to investigate this problem. Their results showed that a random distribution of permeability is best averaged using a geometric mean. Although more sophisticated approaches give better results for anisotropic, spatially correlated permeable mediums, such approaches cannot be updated--a highly desirable characteristic for simulated annealing applications.

The geometric averaged effective permeability, k_e, is defined as:

$$k_e = \left[\prod_{i=1}^{N_b} k_i\right]^{\frac{1}{N_b}} \tag{3.19}$$

where k_i is the fine-scale permeability of the N_b locations comprising the large-scale region. Frequently, stochastic modeling of permeability is performed based on the spatial correlation of the logarithmic permeability transform, $\log(k_e)$. In that case, the geometric average is simply the arithmetic average of the permeability logarithms:

$$\log(k_e) = \frac{1}{N_b}\sum_{i=1}^{N_b}\log(k_i) \tag{3.20}$$

In the context of simulated annealing, the effective permeability logarithm can be updated after a swap as follows:

$$\log(k_{e,new}) = \frac{N_b\log(k_{e,old}) - \log(k_i) + \log(k_{i'})}{N_b} \tag{3.21}$$

where $\log(k_{e,old})$ is the value prior to the swap and $\log(k_{e,new})$ represents the updated value after replacing $\log(k_i)$ with $\log(k_{i'})$. Obviously, this is a very simple, quick calculation and thereby should be used if the results are reasonable. The objective function previously defined in Eq. 3.3 can then be extended to include both permeability variogram and effective permeability constraints as follows:

$$O = w_v\sum_{d=1}^{N_D}\sum_{l=1}^{N_{L,d}}\frac{[\gamma_a(h_{l,d}) - \gamma_t(h_{l,d})]^2}{[\gamma_t(h_{l,d})]^2} + w_{k_e}\sum_{n=1}^{N_w}\frac{[k_{e,a}(n) - k_{e,t}(n)]^2}{O_{k_{e,i}}} \tag{3.22}$$

where $k_{e,a}$ and $k_{e,t}$ represent the actual and true effective permeabilities, respectively, and $O_{k_{e,i}}$ is the initial objective function of the effective permeability function. The permeability variogram and effective permeability weights w_v and w_{k_e} are included to allow different levels of importance for each objective function component.

Flow Simulation Comparisons

Conventional simulated annealing was used to generate 21 areal distributions of permeability. A log normal distribution was used having a mean log(k), $\mu_{\log(k)}$, of 2.0 (100 md) and a standard deviation, $\sigma_{\log(k)}$, of 0.40. For this $\mu_{\log(k)}$ and $\sigma_{\log(k)}$, 68% of

the values lie between 1.6 (40 md) and 2.4 (250 md). The Dykstra-Parsons coefficient[78] is 0.60. An omnidirectional spherical variogram model having a relative nugget of 20% and a range of 1200 ft was used for all conditional simulations. The 5280 ft x 5280 ft system was discretized into a 60 x 60 grid mesh, each grid block having 88 ft side lengths. Well grid blocks were distributed on regularly spaced 80 acre patterns, resulting in a 13 well system (Figure 3.3). A dimensionless correlation length, λ_D, of 0.643 is obtained when the variogram range (1200 ft) is divided by the drainage area side length (1867 ft). Well block permeabilities were considered as conditioning data and remained unchanged for all 21 conditional simulations.

Flow simulations were performed for each of the 21 permeability realizations. The only parameter varied between flow simulations was the permeability field. Reservoir porosity and thickness were assumed to be constant and equal to 25% and 30 ft, respectively. A uniform initial pressure of 1200 psi was used; bubble point pressure of the black oil was 1024 psi. The wells were operated at a 200 psi constant bottomhole pressure; well flow rates were dictated by the reservoir. A total of ten years of primary production was simulated. A finite-difference fluid flow simulator was used.[66] Flow simulation input parameters are summarized in Table 3.1. Black oil fluid properties are the same as previously listed in Table 2.2.

Flow simulation results for all 21 cases are summarized in Figure 3.4. Note the wide spread in rates and gas-oil ratios (GOR's). Initial rates vary from 1100 STB/D to 3100 STB/D. The large spread in producing rates at early times continues to grow throughout the ten year period. Although all 21 cases have equal pore volumes and permeability frequency distributions, cumulative recoveries at the end of 10 years vary significantly. The permeability fields, although having the same conditioning data and spatial correlation structure, have enough significant differences to result in a wide spread in well performance. It is obvious that additional conditional simulation constraints are required before realizations can be generated which are "equally probable"

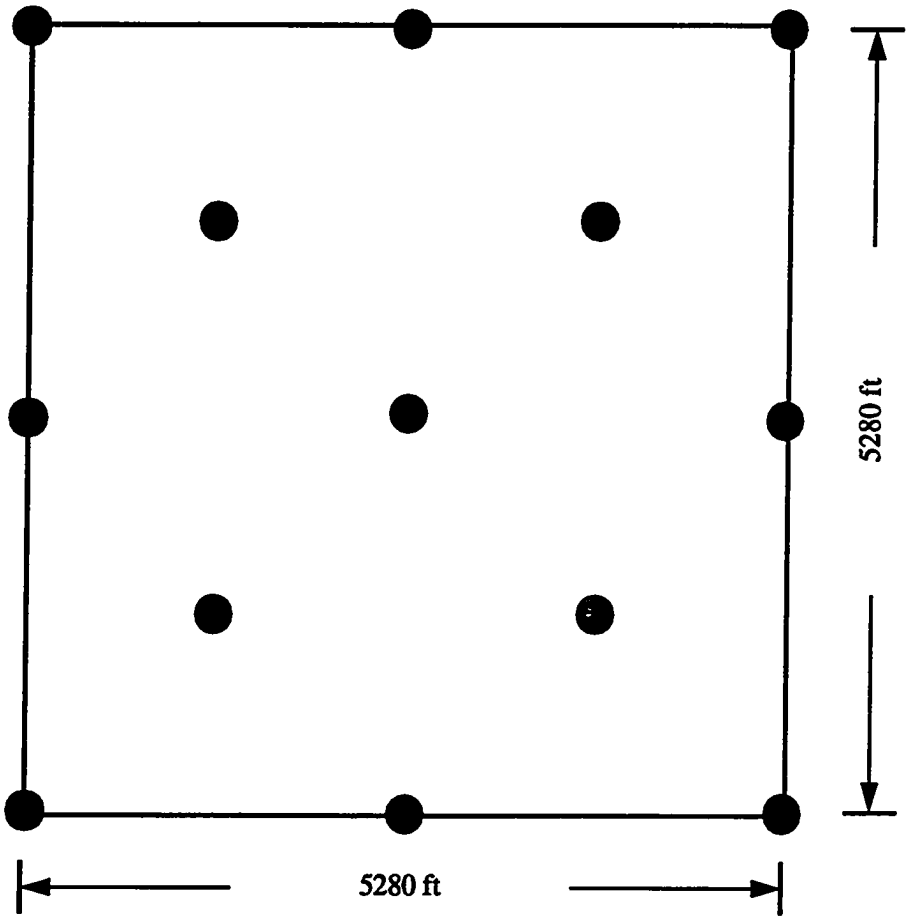

Figure 3.3 - Schematic of 13 well, 80 acre well spacing reservoir system

Table 3.1

Primary production flow simulation data

Type of Simulation	2D Primary
Well spacing	80 Ac
Initial pressure	1200 psi
Bottomhole producing pressure	200 psi
Bubble point pressure	1024 psi
Initial gas saturation	0%
Formation thickness	30 ft
Porosity	0.25, variable
Permeability	100 md, variable

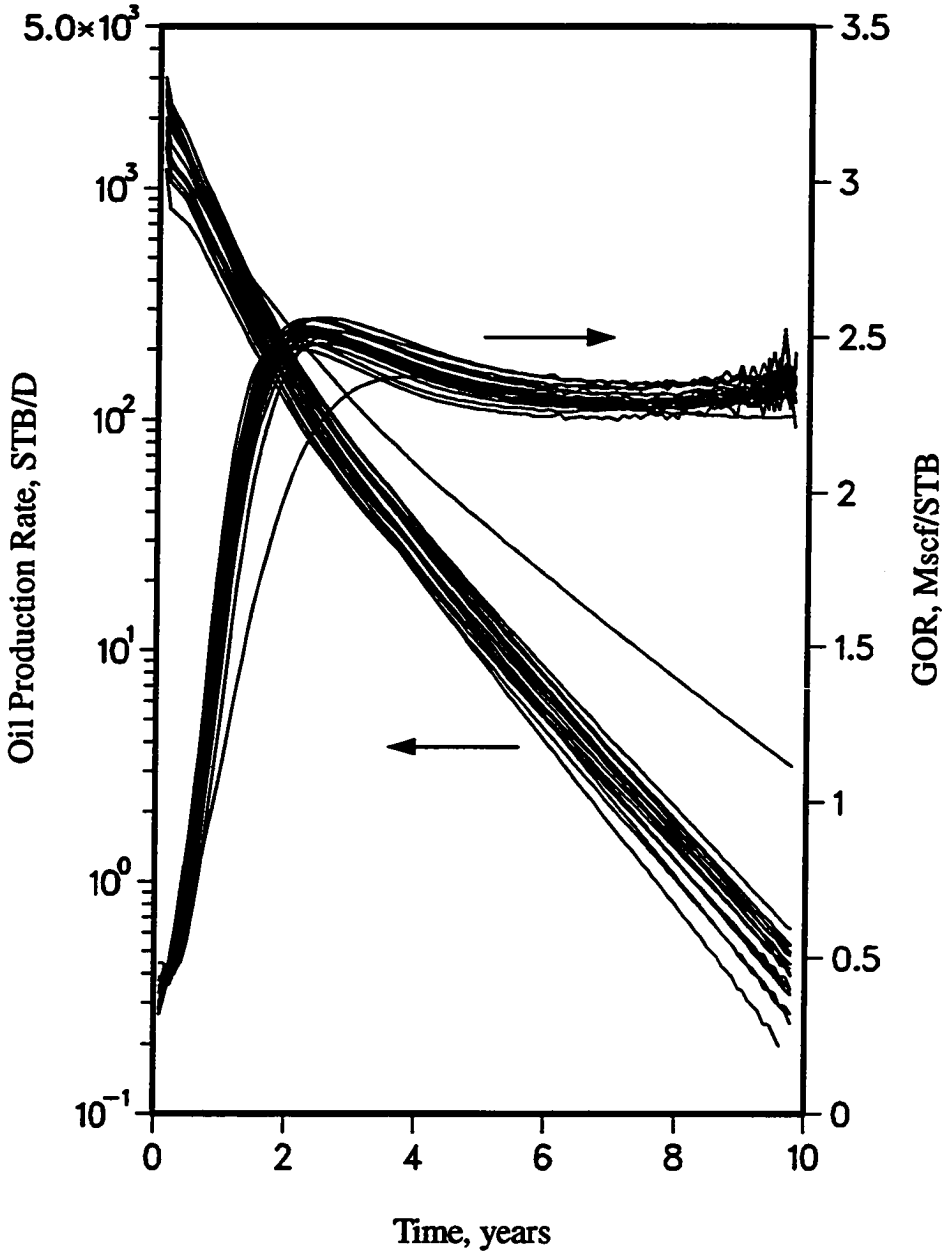

Figure 3.4 - Primary performance of central producer for base case realizations; more heterogeneous permeability distribution

from a well/reservoir performance viewpoint. Considering that the majority of the performance differences develop at the very start of the simulation, it is reasonable to infer that variations in near well permeability may be the primary reason for the wide variations.

The impact of near well permeability on well performance is further illustrated in Figure 3.5. Here, the initial producing rate (average rate for the first month) of the central producer for each of the 21 flow simulations is plotted as a function of the effective near well permeability, k_{NW}. The effective near well permeability was computed using a geometric average of the well block and the adjacent eight grid blocks (3 x 3 region). As shown in Figure 3.5, the correlation is excellent with the correlation coefficient being 0.98. Effective near well permeability was calculated for a variety of near well areas ranging from 3 x 3 grid blocks (264 ft x 264 ft, or 1.6 acres) to 27 x 27 grid blocks (2376 ft x 2376 ft, or 130 acres). The correlation coefficient of initial producing rate vs. k_{NW} is plotted as a function of fractional drainage area in Figure 3.6, where the fractional drainage area is the area included in the k_{NW} computation normalized by the well drainage area (80 acres). The correlation coefficient exceeds 0.95 for fractional drainage areas less than 0.30. These results cannot be generalized without investigating the impact of various types of spatial correlation structures on k_{NW}. Such an investigation is not within the scope of this study. The above results are sufficient to conclude that k_{NW} has a strong impact on well performance and thus should be implemented as a constraining parameter.

The simulated annealing objective function was modified to include both effective near well permeability and the permeability variogram as constraints. This was formulated as previously described by Eq. 3.22 with k_e replaced by k_{NW}:

$$O = w_\gamma \sum_{d=1}^{N_D} \sum_{l=1}^{N_{L,d}} \frac{[\gamma_a(h_{l,d}) - \gamma_t(h_{l,d})]^2}{[\gamma_t(h_{l,d})]^2} + w_{k_{NW}} \sum_{n=1}^{N_w} \frac{[k_{NW,a}(n) - k_{NW,t}(n)]^2}{O_{k_{N(W,i)}}} \quad (3.23)$$

Again, 21 permeability realizations were generated, all honoring conventional con-

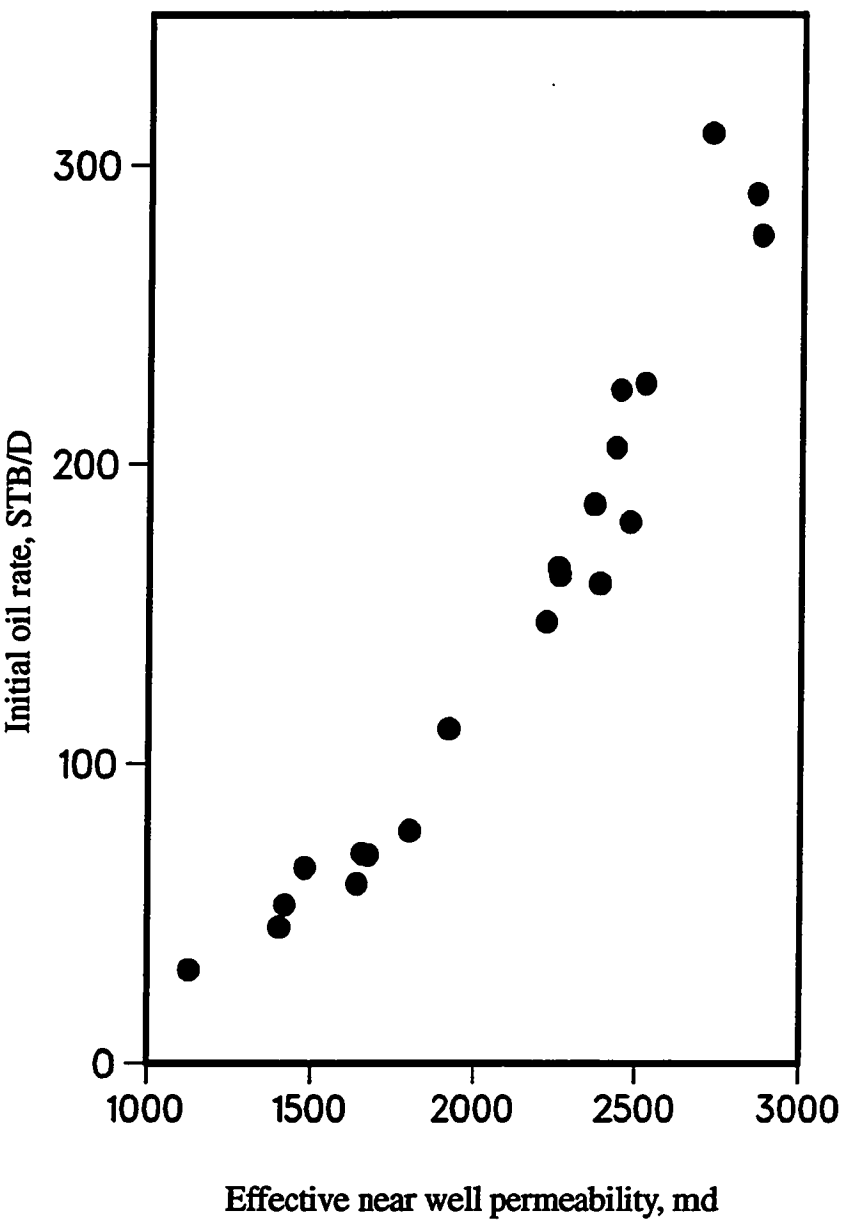

Figure 3.5 - Correlation of initial oil production rate to effective near well permeability

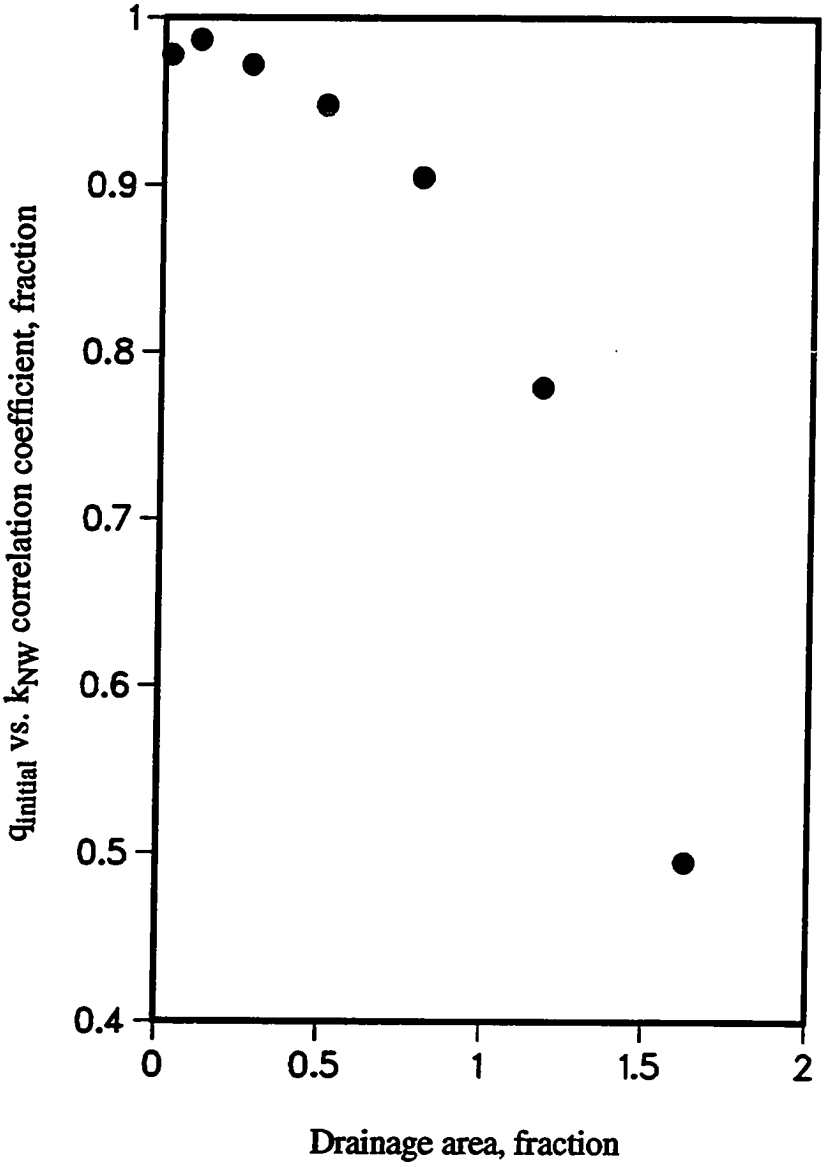

Figure 3.6 - Correlation coefficient of initial oil production rate vs. near well effective permeability as a function of fractional drainage area

straints (well block permeabilities, the permeability frequency distribution and variogram) and the additional k_{NW} constraint. The permeability fields were then used to simulate 10 years of primary performance for the 13 well system previously defined. The resulting performance of the central producer, for all 21 cases, is shown in Figure 3.7. A comparison of Figures 3.4 and 3.7 demonstrates the impact of k_{NW} on well performance. Inclusion of k_{NW} as a conditional simulation constraint is seen to result in permeability fields which have essentially the same primary performance characteristics. These permeability realizations truly can be referred to as "equally probable" since they honor all of the existing data. Uncertainty in future reservoir performance has been minimized, thus a more realistic reservoir modeling study can be performed for quantifying uncertainty. Fortunately, not only can good estimates of k_{NW} be obtained via well tests, but such information is typically available early in the life of a well.

Porosity Heterogeneities

The impact of porosity heterogeneities on well performance was also investigated. The most common type of porosity heterogeneity is a dual porosity system,[79] in which one reservoir medium is characterized by relatively good porosity but poor permeability, while the other medium has relatively poor porosity but good permeability. The low porosity, highly conductive medium serves as a conduit for transporting fluid from the high porosity, poorly conductive medium. A fractured chalk reservoir is a good example of a dual porosity system. A large contrast in permeability between the two mediums (at least two orders of magnitude) is necessary for dual porosity effects to be noticeable in well tests and performance. Dual porosity behavior not only requires both porosity and permeability heterogeneities, but also an inverse relationship between porosity and permeability. This study only investigates the independent effects of porosity and permeability heterogeneities on reservoir performance.

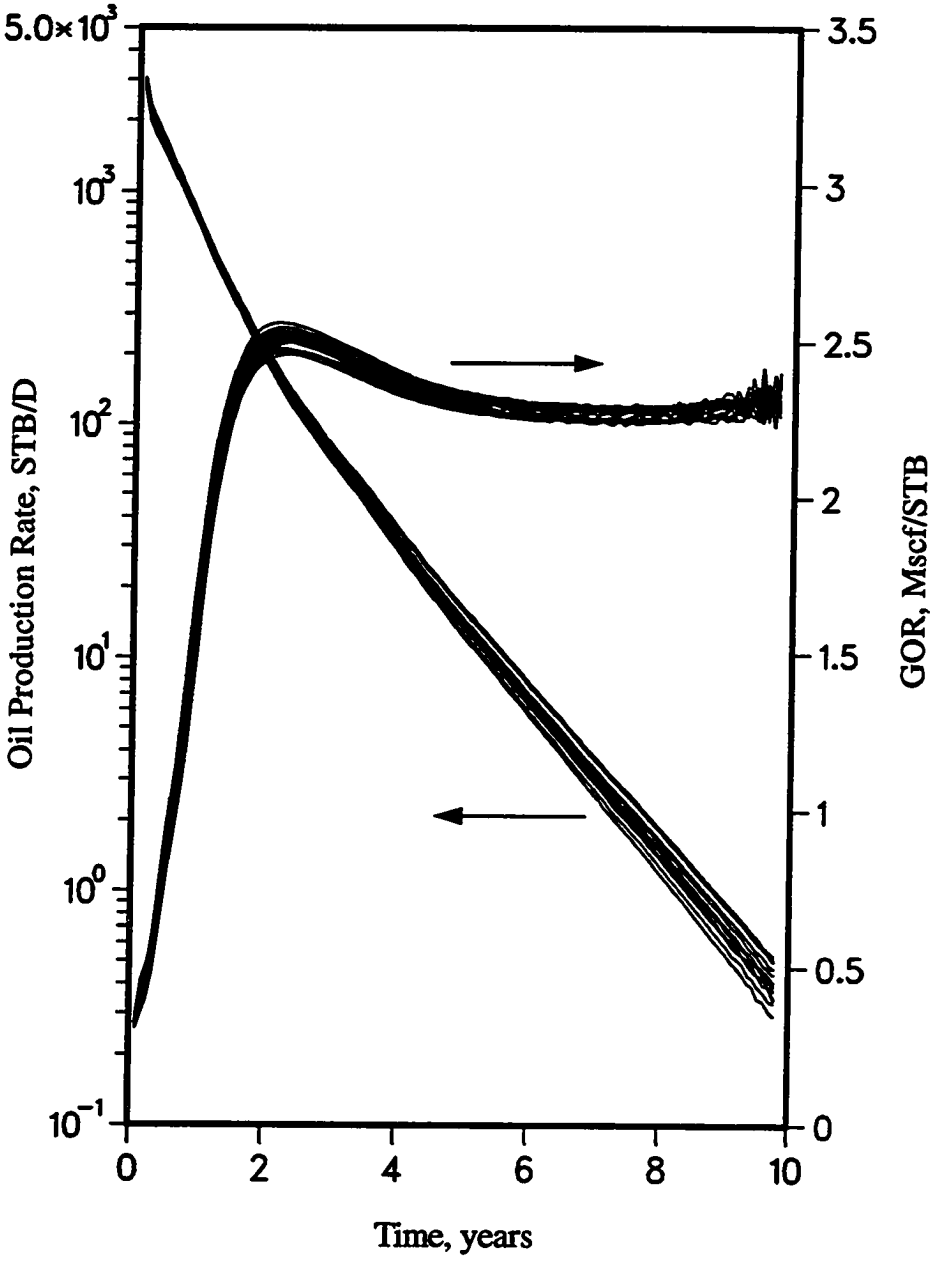

Figure 3.7 - Primary performance of central producer for k_{NW} constrained realizations; more heterogeneous permeability distribution

Generation of Porosity Fields

Heterogeneous porosity fields were generated by transforming the two sets of 21 permeability fields described above using the following transformation:

$$\varphi(i,j) = \frac{[\log([k(i,j)] - 0.667)]}{6.667} \tag{3.24}$$

where $\varphi(i,j)$ and $k(i,j)$ represent the porosity and permeability, respectively, for the ith column and jth row. This normal porosity distribution has a mean of 0.20 and a standard deviation of 0.060; 68% of the values lie between 0.14 and 0.26.

Flow Simulation Comparisons

Analogous to the k_{NW} study, flow simulations were performed for each of the 21 porosity fields. A uniform permeability of 100 md was used in each case. All other properties are the same as those described in Table 3.1. The central producer oil rate and GOR vs. time profiles for all 21 flow simulations are presented in Figure 3.8. The spread in primary performance between each case is very small--certainly not large enough to be able to quantify porosity heterogeneities from well performance characteristics. It can be concluded that a porosity heterogeneity constraint cannot be developed because of the insensitivity of primary well performance to porosity heterogeneities.

A global multiplier of 1.20 was applied to each $\varphi(i,j)$ for all 21 porosity fields to increase the average porosity from 0.20 to 0.24. Flow simulations were once again made using the revised porosity fields. Figure 3.9 compares the primary performance of the central producer for both sets of porosity fields (average porosities of 0.20 and 0.24). It can be seen that there is significant difference between the two sets of runs, but an insignificant difference within each set. Although porosity heterogeneities cannot be identified from primary performance, an estimate of drainage area average porosity/pore volume is often obtainable from a historical rate profile and thus should be used as a con-

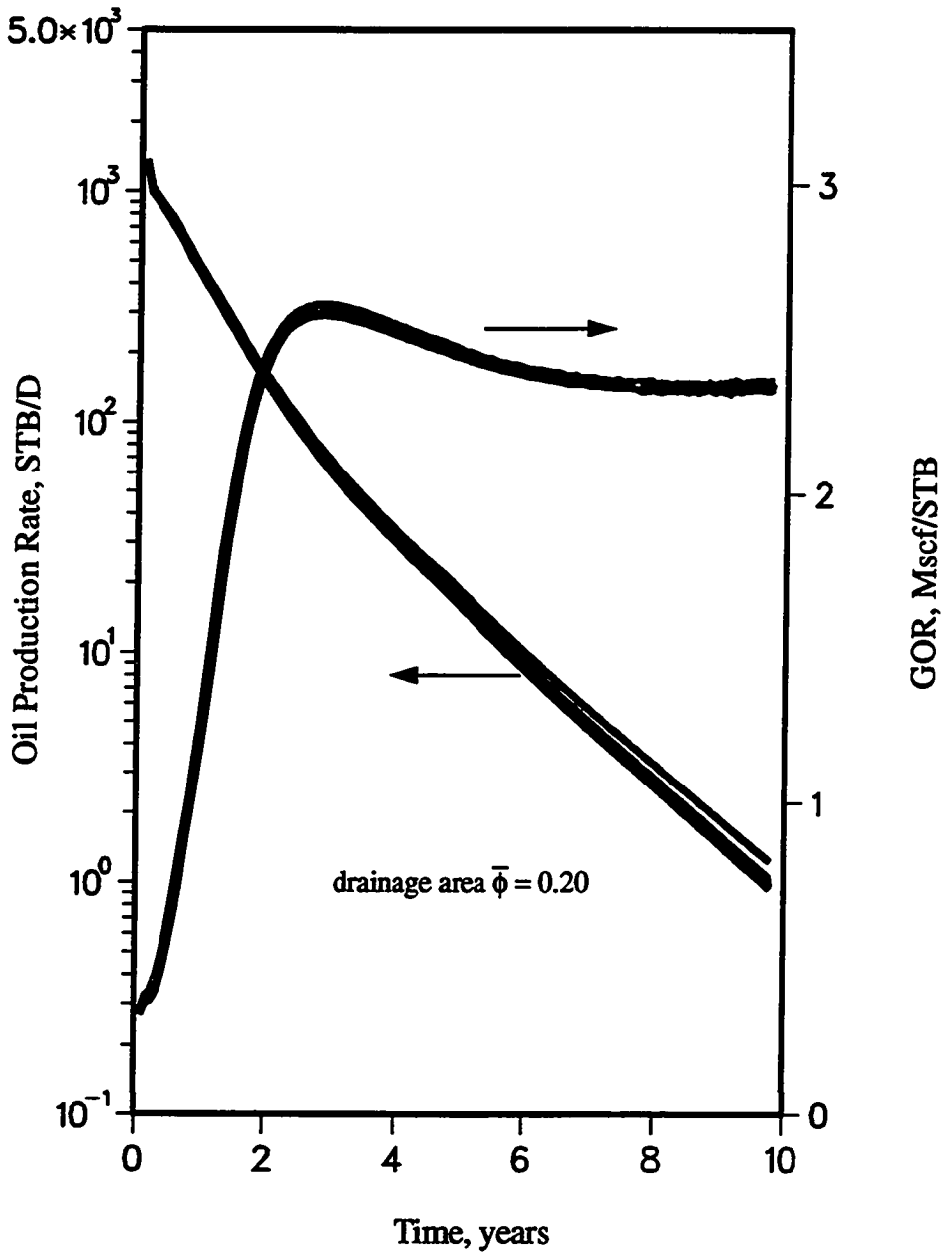

Figure 3.8 - Primary performance of central producer for porosity heterogeneous realizations; drainage area average porosity equals 0.20

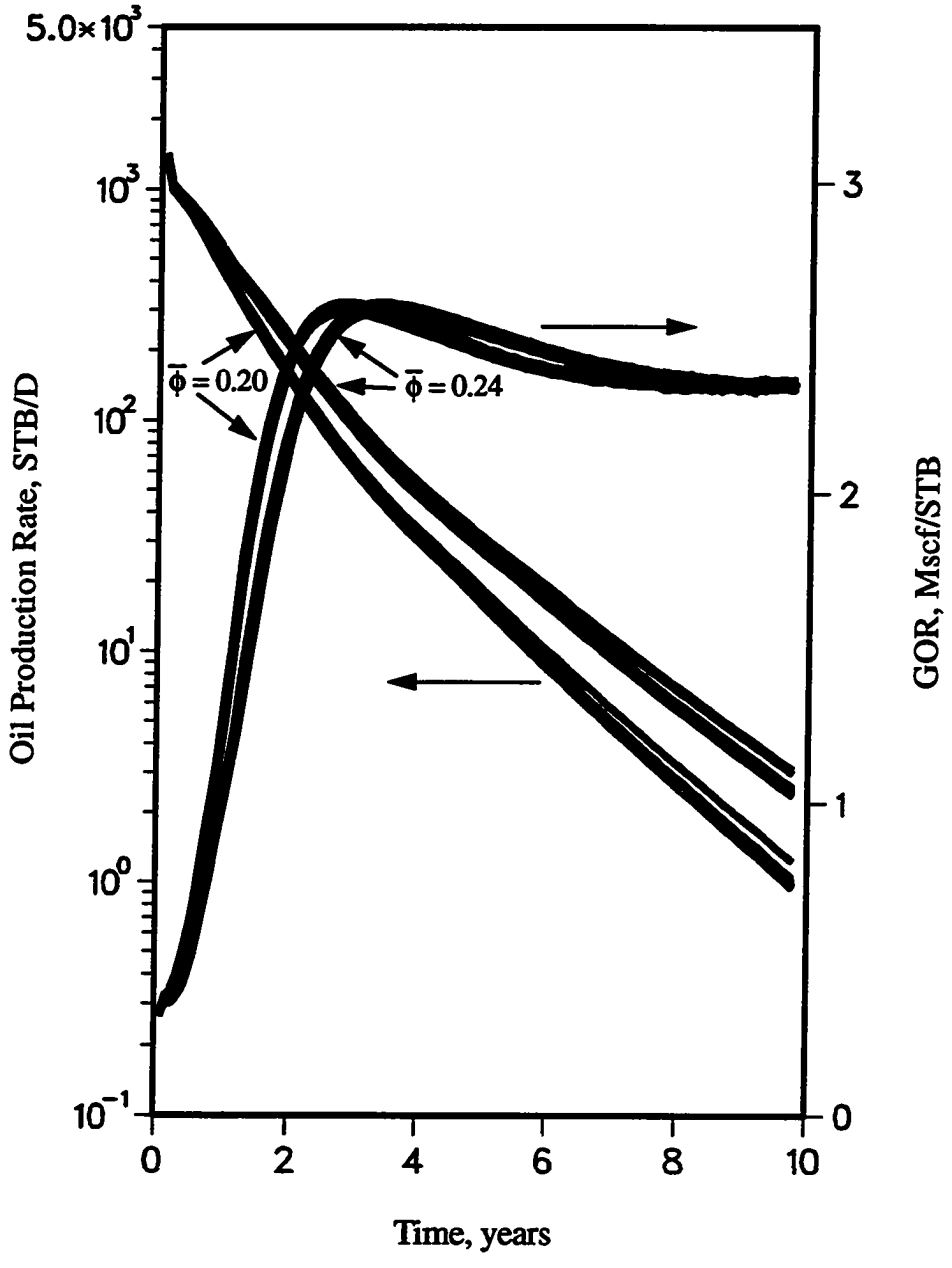

Figure 3.9 - Comparison of central producer primary performance for porosity heterogeneous realizations with average porosities of 0.20 and 0.24

ditioning parameter. Pore volume estimates via material balance or volumetric calculations are often obtainable early in the life of a well using rate and pressure data.

Summary of Results

The effective permeability of the near well region was found to be a dominating reservoir characteristic during primary production. This was illustrated analytically for radially homogeneous and composite reservoir systems and numerically for heterogeneous solution gas drive reservoirs. The correlation coefficient of initial producing rate vs. near well effective permeability for the central producer in a five well heterogeneous system was found to be 0.98. The spread in simulated primary performance between permeability realizations was greatly reduced when near well effective permeability was combined with conventional conditional simulation constraints. A geometric mean was found to be a sufficient estimator of effective permeability for the near well region. It was not possible to identify other permeability spatial distribution characteristics from primary performance data.

Porosity heterogeneities were found to have an insignificant impact on primary production characteristics. Hence, porosity heterogeneities cannot be quantified from primary performance. The benefit of including pore volume conditional simulation constraints was demonstrated.

Fortunately, both near well effective permeability and drainage area pore volume often can be estimated from well test and/or production data.

CHAPTER IV

WATERFLOOD CONSTRAINTS

As shown in Chapter III, primary performance is rather insensitive to areal reservoir heterogeneities, the exception being the near well region (and faults/fractures). There are several differences between primary and secondary recovery regarding well-to-well interactions. Primary individual well recoveries cannot be improved by placement of offset primary wells--only reduced as a result of interference (this does not imply that primary field recovery is not improved by infill drilling). Fluid recovery is strictly dependent on the rock properties existing between the location of the fluid and each offset well (i.e., well "fluid pulling" characteristics). These characteristics of primary recovery do not apply to secondary recovery operations. Interwell reservoir characteristics become much more important. Secondary recovery efficiency is strongly influenced by local reservoir connectivity between each injector/producer pair (i.e., well "fluid pulling and pushing" characteristics).

The importance of interwell reservoir connectivity on secondary performance is the primary subject of this chapter. Reservoir connectivity measures will be defined based on the spatial arrangement of permeability. This approach is used since permeability typically has a stronger influence on flow characteristics than any other variable. The techniques developed in this study quantify reservoir connectivity relative to specific well locations. Although existing definitions of connectivity may be used to improve predictions of overall field rates and recoveries, local measures of connectivity are required to better predict interactions between specific wells. Subsequent to defining connectivity measures, synthetic case studies will be used to illustrate the effectiveness of the waterflood indirect performance constraints.

Fractional Connectivity Function

For the first method, connectivity is defined by a functional relationship between fractional area connected and permeability percentile cutoffs. Both connectivity of high permeabilities and low permeabilities are considered. A description of the procedure used to define the connectivity function for a given permeability field follows. Grid block permeability values are transformed to binary indicators (i.e., 0's and 1's) depending on whether they are equal to or greater than the cutoff values (1's) or less than the cutoff values (0's). For the connectivity of high values, two adjacent grid blocks are considered as being "connected" if their permeability indicators are both 1's. Conversely, adjacent blocks having 0's as permeability indicators are defined as being "connected" for the connectivity of low values. For both cases, a "connected path" is defined as a series of connected blocks which extend from an injector to an offset producer (or vice versa). The "fractional area connected" is obtained by dividing the number of connected grid blocks by the total number of grid blocks. Only horizontal and vertical directions (not diagonal) are considered for connectivity computations in this study. The relationship between permeability percentile cutoff and fractional area connected for both high permeabilities, C_H, and low permeabilities, C_L, is considered to completely define the connectivity characteristics of the injector/producer pair.

An example is presented to illustrate this concept. Figure 4.1 is a greyscale image of permeability for one-quarter of a five-spot pattern generated using conventional simulated annealing. The 1^{st} through 6^{th} permeability deciles of this image are 61 md, 142 md, 165 md, 215 md, 374 md and 445 md, respectively. Figure 4.2 displays the indicator greyscale maps corresponding to the six percentile cutoffs. The grid blocks with permeabilities exceeding each respective cutoff are shaded black. Assuming the injection well is located in the lower left corner and the producer is in the upper right corner, the connectivity of high values is determined by computing the fraction of blocks which have an indicator value of 1 and are part of a connected path (defined above) extending

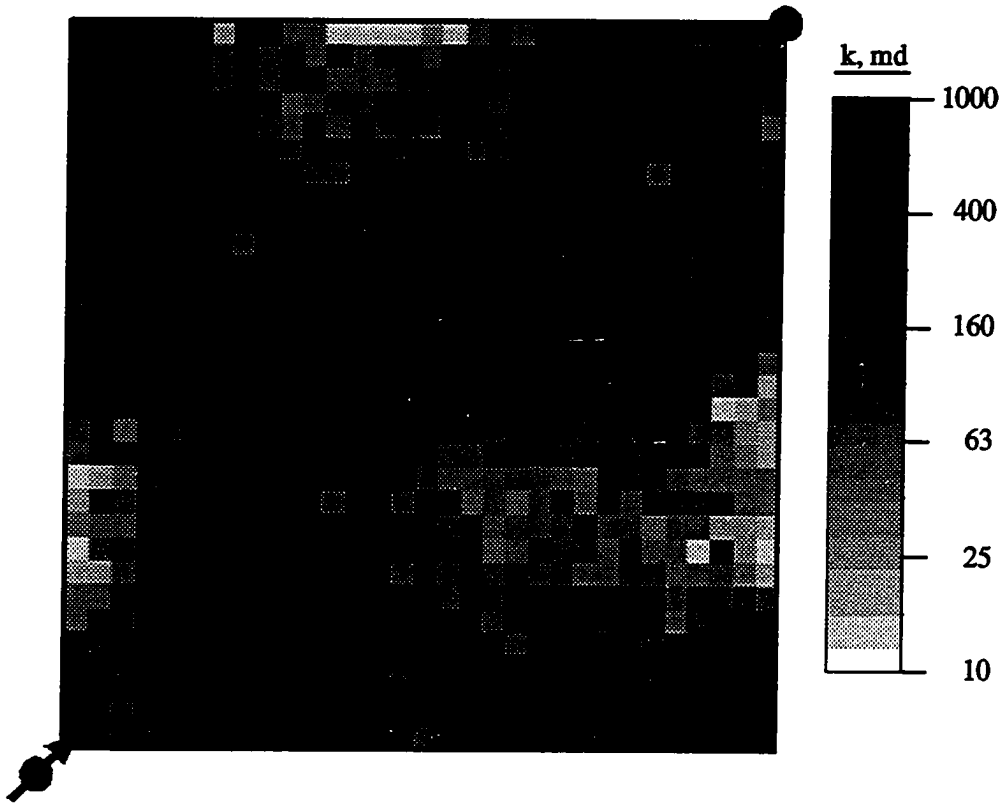

Figure 4.1 - Example permeability field for one-quarter of a five-spot pattern

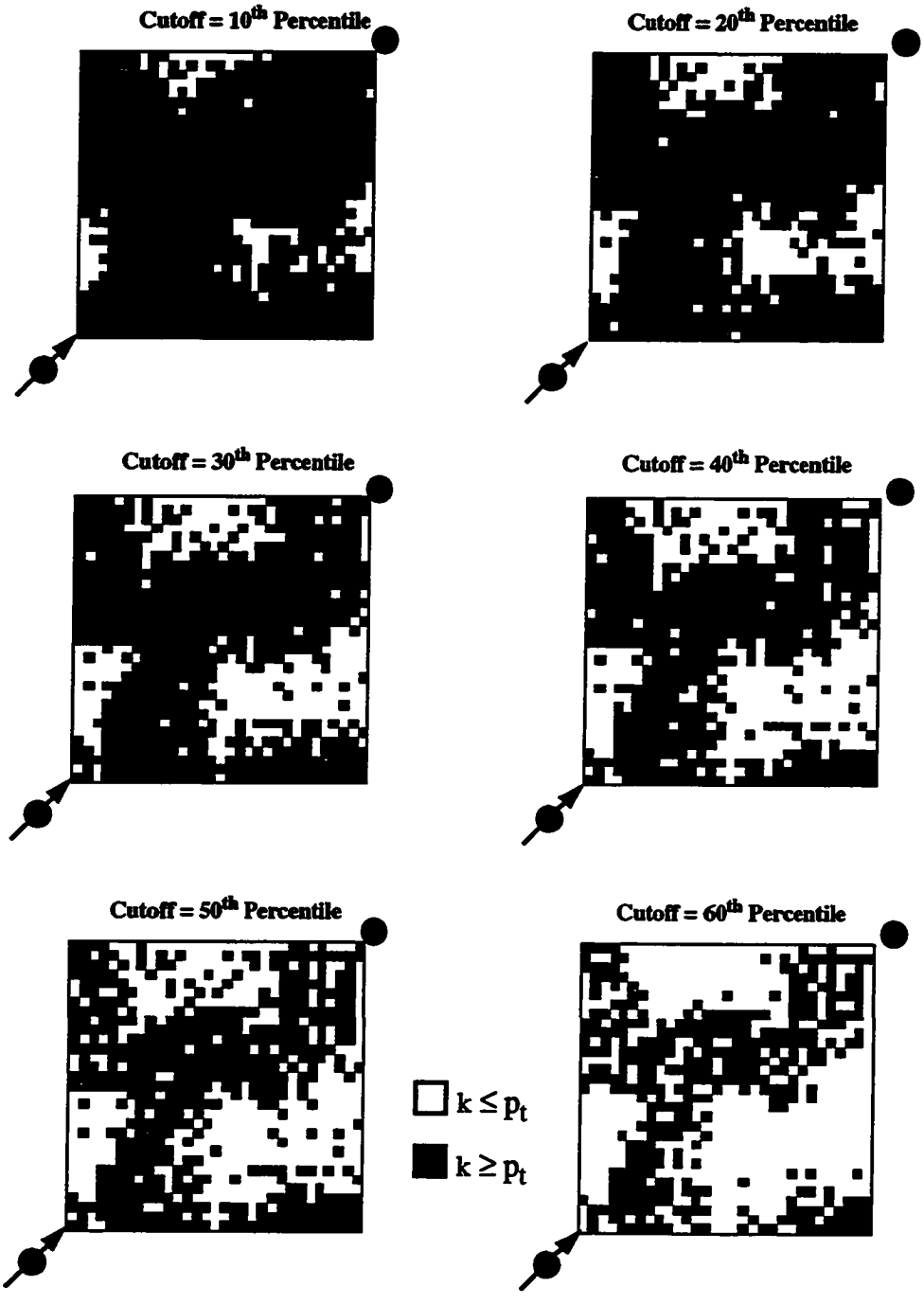

Figure 4.2 - Connectivity indicators at various permeability percentile cutoffs

between the injector and the producer. The upper limit of connectivity is equal to the fraction of blocks having an indicator of 1 while the lower limit is 0. The existence of isolated or unconnected grid blocks of value 1 will result in the percentage of connected blocks being less than the cutoff percentile. Figure 4.3 shows the connected (shaded black), isolated (shaded gray) and dead end (unshaded) grid blocks for these six percentiles. The fractional connectivity function shown in Figure 4.4 is obtained by evaluating the connectivity of highs and lows at each percentile. The permeability percentile at which connectivity is first reduced to zero is defined as the permeability percentile threshold, p_t. In Figure 4.4, the thresholds for the connectivity of high values, p_{tH}, and low values, p_{tL}, are the 54^{th} percentile (400 md) and the 76^{th} percentile (621 md), respectively. Note that whereas most of the previously published definitions of connectivity refer to global reservoir connectivity characteristics, the fractional connectivity function defined above is dependent on the locations of the injector and producer. A different connectivity function would be obtained if the wells were located elsewhere.

The determination of the connectivity function can be computationally intensive and cannot be easily updated. Fortunately, it was found that the characteristic of the connectivity function which most strongly influences waterflood performance for the cases considered is p_{tH}. This value represents the largest minimum permeability value of all paths which connect the injector to the producer. Other paths may contain more higher permeability values, but in each case contain at least one permeability which falls below the permeability represented by p_{tH}. The determination of p_{tH} is much easier than computing the entire connectivity function; only one path rather than all possible paths needs to be identified. Systematically searching for a connected path was found to be more efficient than using a random walk approach. Beginning at one of the wells, the perimeter of the connected area between a injector/producer pair is traced. Connectivity exists if the second well is visited prior to revisiting the first well. If connectivity doesn't exist, p_{tH} has been exceeded, thus the actual threshold is a smaller value.

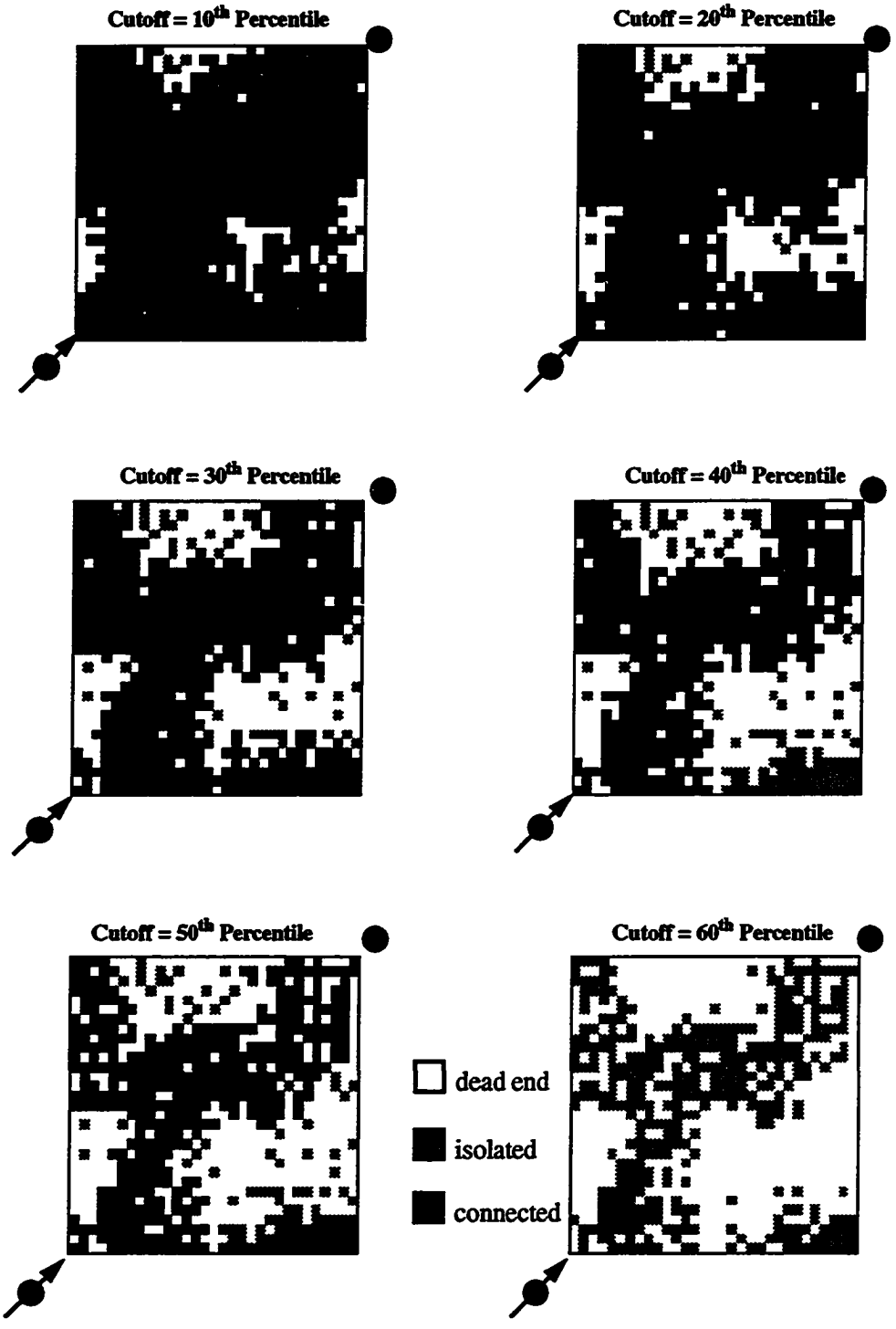

Figure 4.3 - Identification of connected, isolated and dead end grid blocks

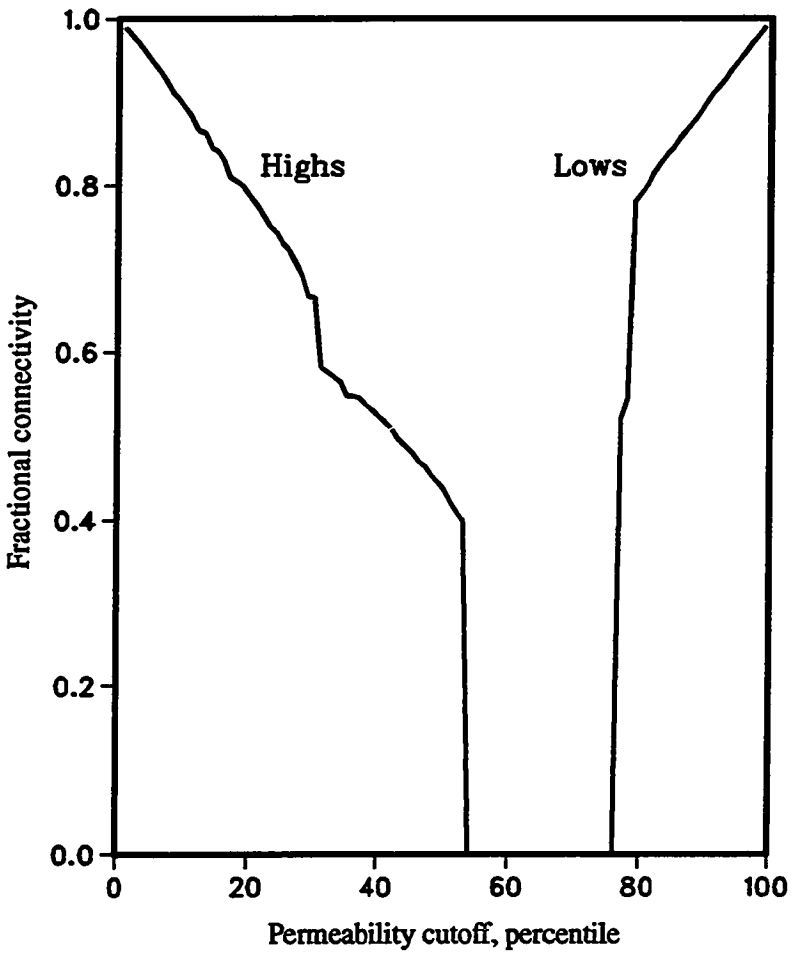

Figure 4.4 - Fractional connectivity function for simulated annealing example

Flow Pattern Permeability Coefficient

The second connectivity parameter investigated incorporates curvilinear fluid flow geometry. Idealized unit mobility streamlines for a homogeneous five-spot pattern were used to determine the effective permeability of the flow pattern segments (i.e., streamtubes). This second parameter, referred to as CV_{k^*}, represents the coefficient of variation (standard deviation divided by the mean) of a distance-normalized flow pattern segment permeability, k*:

$$CV_{k^*} = \frac{\sigma_{k^*}}{\mu_{k^*}} \tag{4.1}$$

where k* is defined for the n^{th} flow pattern segment as

$$k^* = \frac{k(n)}{l_D^2(n)} \tag{4.2}$$

and

$$\sigma_{k^*} = \sqrt{\frac{1}{N_s}\sum_{n=1}^{N_s}(k^*_n - \mu_{k^*})^2} \tag{4.3}$$

$$\mu_{k^*} = \frac{1}{N_s}\sum_{n=1}^{N_s}\frac{k(n)}{l_D^2(n)} \tag{4.4}$$

$$l_D(n) = \frac{l(n)}{l_o} \tag{4.5}$$

The variables $k(n)$ and $l(n)$ represent the effective permeability and average length, respectively, of the n^{th} flow pattern segment. Note that a value for the permeability parameter k^* is obtained for each flow pattern segment. The mean and standard deviation of k^* are then used to compute CV_{k^*}. The effective permeability $k(n)$ is calculated from the grid block permeabilities located within the n^{th} flow pattern segment. The line bisecting the n^{th} flow pattern segment is used to estimate $l(n)$. The total number of segments used for each one-quarter of a five-spot pattern was 8 ($N_s = 8$). As indicated

by Eq. 4.5, flow pattern segment lengths are normalized by the interwell diagonal length, l_o. High permeability streaks existing directly between the injector and the producer influence waterflood response more so than indirect high permeability paths. This effect was accounted for by normalizing the flow pattern segment permeabilities by the square of the dimensionless flow pattern length, $l_D(n)$. This measure of connectivity has an advantage over the fractional connectivity function in that the intensity of high and/or low permeability streaks can be accounted for. Flow pattern segment permeabilities were estimated using a geometric average of the grid block permeabilities. More accurate permeability averaging techniques could be used such as renormalization,[75] but as previously discussed, the geometric average was selected because it can be updated easily and it gives acceptable results. Similarly, a more rigorous method of computing flow pattern segment geometry could have been used instead of assuming idealized ones. This would have required costly recomputations during the annealing process. Considering the high quality of the results obtained using idealized flow pattern segments, it was decided not to pursue the rigorous approach.

Thus, the process for determining CV_{k^*} for each injector/producer one-quarter five-spot pattern is as follows. Idealized unit mobility streamlines are determined given the injector/producer locations. Grid block permeability values are assigned to all flow pattern segments for which the grid blocks are members. The effective permeability parameter k^* is then computed (using Eq. 4.2) for each of the n flow pattern segments comprising the injector/producer one-quarter five-spot pattern. The value of CV_{k^*} can then be determined from the standard deviation (using Eq. 4.3) and mean (using Eq. 4.4) of k^*. This process is repeated until a value of CV_{k^*} is obtained for each injector/producer one-quarter five-spot pattern.

Procedure

Based on previous results, it was decided to investigate only the effect of areal per-

meability heterogeneities on secondary well performance; reservoir porosity and thickness are assumed to be constant. Permeability is assumed to be a stationary random function with a known log-normal frequency distribution and spatial correlation structure. Two permeability frequency distributions were investigated. The first is the same as was used in the primary performance work, i.e., $\mu_{\log(k)}$ and $\sigma_{\log(k)}$ are 2.0 (100 md) and 0.40, respectively. The second permeability frequency distribution is characterized by $\mu_{\log(k)}$ and $\sigma_{\log(k)}$ values of 2.5 (250 md) and 0.2, respectively. As previously mentioned, 68% of the permeabilities lie between 40 md and 250 md for the first distribution. For the second, less heterogeneous distribution, 68% of the values lie between 200 md and 500 md. These two distributions will be referred to as the less heterogeneous permeability distribution ($\sigma_{\log(k)} = 0.2$) and the more heterogeneous permeability distribution ($\sigma_{\log(k)} = 0.4$) throughout the remainder of this dissertation. The variogram model used was an omnidirectional spherical model having a relative nugget of 20% and a correlation length of 1000 ft. This represents a λ_D of 0.536 for 80 acre well spacing. All permeability fields were generated using simulated annealing, with modifications made to the objective function to account for the various constraints.

Waterflood response for one-quarter, full and extended five-spot patterns were simulated using the black-oil option of a finite-difference fluid flow simulator.[66] In each case, 80 acre well spacing and 160 acre five-spot patterns were used. Grid block dimensions were 40 ft for the one-quarter and full five-spot patterns cases and 88 ft for the extended five-spot simulations. Initial conditions of all flow simulations assumed depleted primary conditions with a uniform initial reservoir pressure of 300 psi and a uniform initial gas saturation of 20%. Injection wells and producers were pressure-constrained at 2000 psi and 200 psi, respectively. A slightly favorable mobility ratio of 0.96 was used. Pertinent flow simulation data are summarized in Table 4.1.

The effectiveness of the various constraints was determined by comparing the simulated waterflood performance of 20 flow simulations to "truth" case results. The truth

Table 4.1

Pertinent data used in waterflood flow simulations

Type of Simulation	2D Black Oil Waterflood
Waterflood pattern type	1/4 five-spot
Pattern size	160 Ac
Well spacing	80 Ac
Areal grid dimensions	40 ft by 40 ft
Areal grid density	33 by 33
Sand thickness (uniform)	30 ft
Porosity (uniform)	30%
Initial pressure (uniform)	300 psi
Bubble point pressure	1024 psi
Initial gas saturation (uniform)	20%
Mobility ratio	0.96
Injection pressure	2000 psi
Producing pressure	200 psi

case permeability field and corresponding simulated reservoir performance were considered to be the actual permeability distribution and performance of the reservoir. The permeability field was the only input variable changed for each flow simulation. The same well block permeabilities were assumed to be conditioning data for all cases. The waterflood performance of 20 flow simulations obtained using conventional simulated annealing constraints was assumed to represent the base case, i.e., they represent typical results using a conventional approach. Five-spot segment synthetic case studies were performed using both of the permeability frequency distributions described previously.

One-Quarter Five-Spot Pattern

Producer and injector grid block permeabilities were assumed to be 250 md and 125 md, respectively, for the more heterogeneous permeability distribution. For the second, less heterogeneous permeability frequency distribution, respective producer and injector grid block values were 250 md and 355 md. Base case and truth case results for both permeability frequency distributions will be presented first. This will be followed by results obtained when including the additional constraints of connectivity and near well effective permeability.

Base Case Results

A total of 21 permeability realizations were generated using the conventional simulated annealing algorithm and the variogram model described previously (see Table 4.1). A greyscale map of the realization selected as the first "truth" case is depicted in Figure 4.5. The permeability fields were used to simulate waterflood performance over a 20 year period. Waterflood performance for the 21 flow simulations, based on water injection rates, oil producing rates, water producing rates and WOR's is presented in Figure 4.6. Performance is seen to vary significantly between flow simulations. For

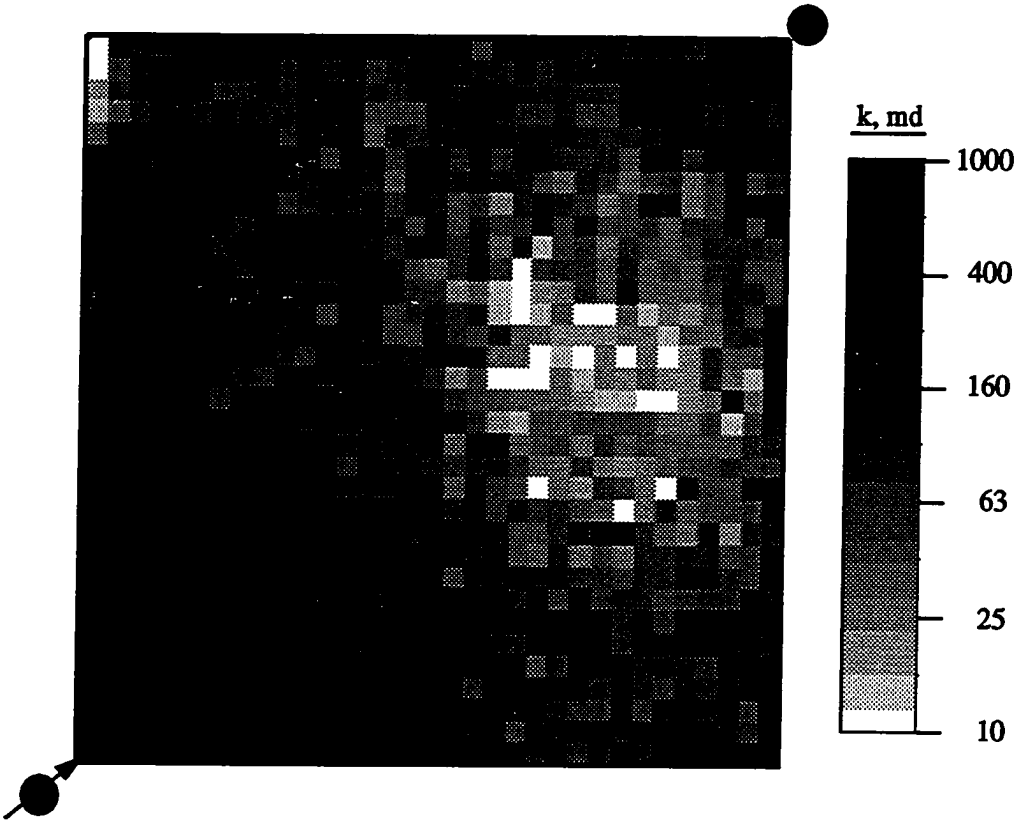

Figure 4.5 - Permeability field for the first one-quarter five-spot pattern truth case

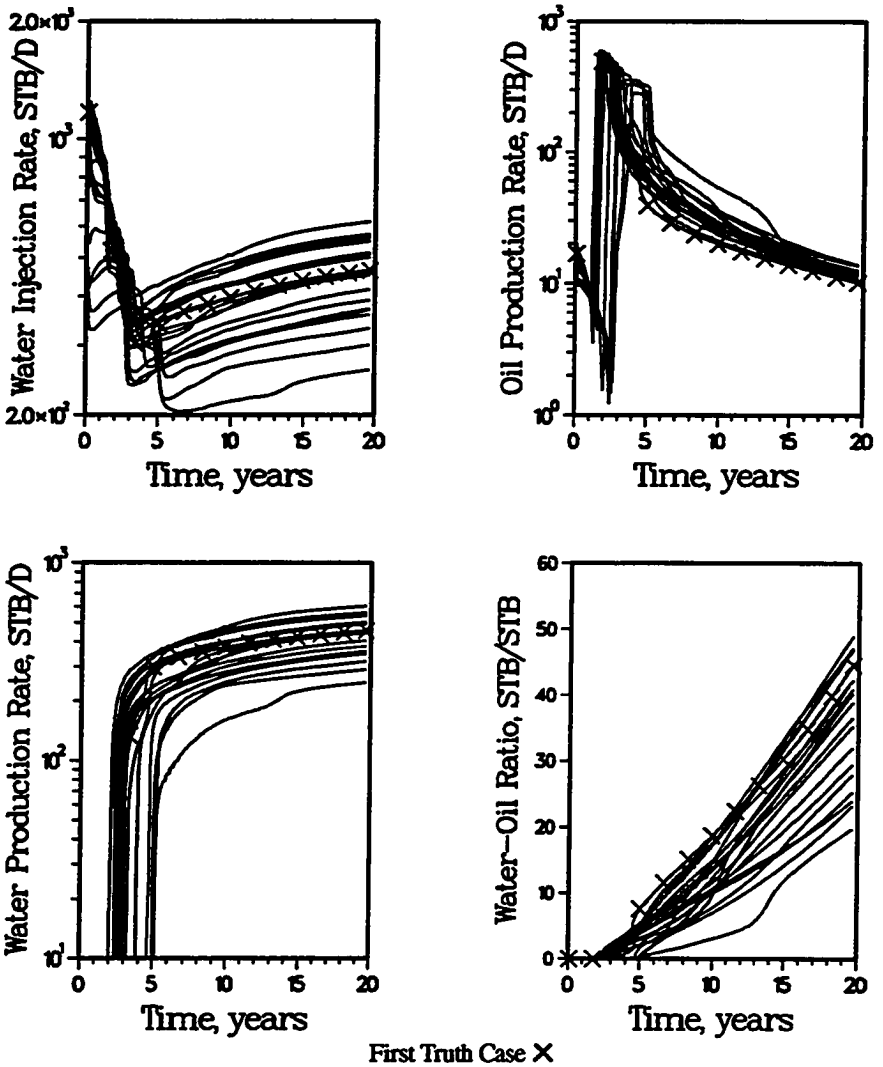

Figure 4.6 - Simulated waterflood performance of the first truth case and the 20 first base flow simulations; one-quarter five-spot pattern system

example, initial water injection rates vary from 410 to 1200 STB/D, water breakthrough times range from 2.0 years to 5.1 years and peak oil responses vary from 170 to 600 STB/D. At the end of the 20 year simulation period, WOR's range from 19 to 50 STB/STB. It is obvious that additional constraints are required before these reservoir descriptions can be considered as being "equally probable." Note that the performance of the first truth case has been highlighted (using x's). Its permeability spatial characteristics and waterflood performance will be used to test the effectiveness of connectivity and near well effective permeability constraints.

This particular permeability realization was selected to represent the first truth case because it has an anomalous WOR trend. A large increase in WOR occurs approximately two years after water breakthrough. Also, the near well effective permeability surrounding the injector (approximately 400 md) is significantly greater than that surrounding the producer (approximately 200 md). However, as previously stated, the injection well grid block permeability (125 md) is less than the producer grid block value (250 md). This anomaly is apparent in the performance data, with the initial injection rate for the first truth case being greater than any other run. Perhaps even more of an anomaly is the existence of a low permeability region just offset to the high permeability near well region surrounding the injector.

Base case permeability realizations and corresponding waterflood performance were also generated using the second, less heterogeneous permeability distribution. The permeability realization selected to be the second truth case is shown in Figure 4.7. Note that the permeability surrounding the injection well (approximately 600 md) is greater than the permeability surrounding the producer (approximately 350 md). This is consistent with the well block permeability relationships. Figure 4.8 depicts the flow rates and WOR trends based on flow simulations using the second truth case and the other 20 permeability realizations. The variations in waterflood performance are less than that observed for the first base case because of the smaller degree of heterogeneity, but are

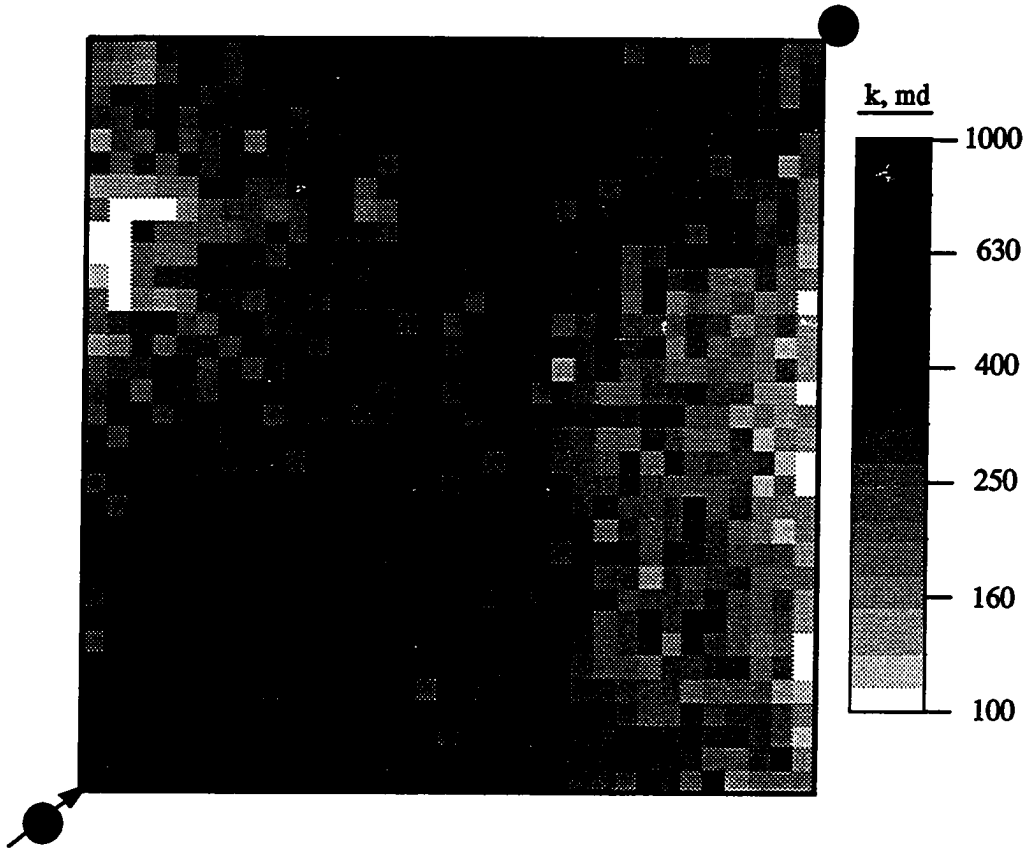

Figure 4.7 - Permeability field for the second one-quarter five-spot pattern truth case

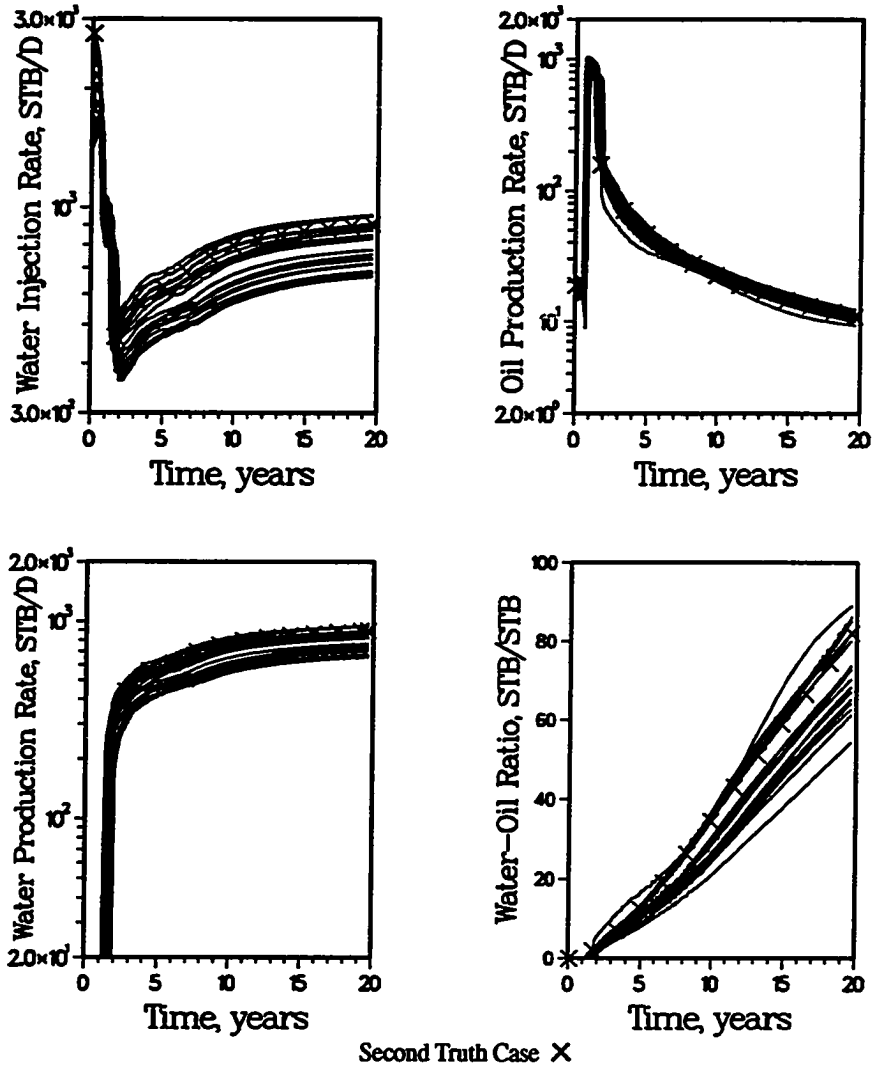

Figure 4.8 - Simulated waterflood performance of the second truth case and the 20 second base case flow simulations; one-quarter five-spot pattern system

still much greater than the desirable range. Note that the initial injectivity of the second truth case is greater than any other base case run.

Connectivity Threshold Constraint Results

The value of p_{tH} for the first truth case was determined to be 0.319; i.e., the largest minimum permeability value of all connected paths between the injector and producer is greater than or equal to 31.9% of all permeability values. The simulated annealing with connectivity algorithm was used to generate 20 permeability realizations, all having a p_{tH} of 0.319. Although all permeability realizations have the same interwell connectivity, inspection of their spatial structures shows that the locations of high and low permeability regions vary from realization to realization. Waterflood performance for the first truth case and the 20 flow simulations are included in Figure 4.9. A comparison of Figures 4.6 and 4.9 indicates that although the inclusion of the connectivity constraint reduced the spread in waterflood performance, the results appear to be biased. None of the 20 flow simulations reproduced the WOR trend exhibited by the first truth case. This biased behavior is evident also in the producing oil rate history.

The value of p_{tH} for the second truth case is 0.298. This value was used to generate 20 additional permeability realizations using the simulated annealing with connectivity algorithm. Once again, although connectivity is preserved, the location of high and low permeability regions change from realization to realization. Many of the realizations exhibit a region of high permeability surrounding the injector because of its high well block permeability. Inspection of the corresponding performance plots (Figure 4.10) shows that the resulting trends are unbiased with respect to the second truth case. Also, the spread in performance has been reduced somewhat in comparison to the base case results (Figure 4.8). These variations in performance could be reduced if the initial injectivity and productivity were better constrained.

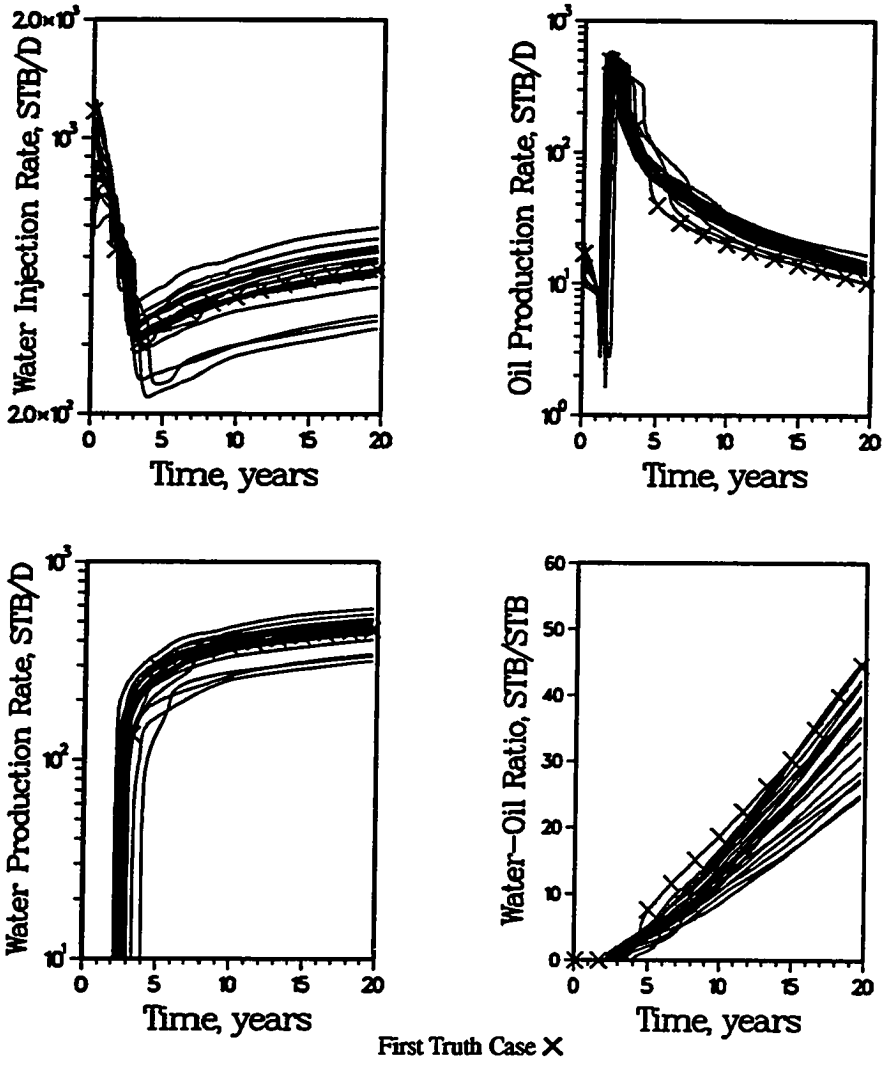

Figure 4.9 - Simulated waterflood performance comparing the first truth case and 20 flow simulations based on $p_{tH} = 0.319$; one-quarter five-spot pattern system

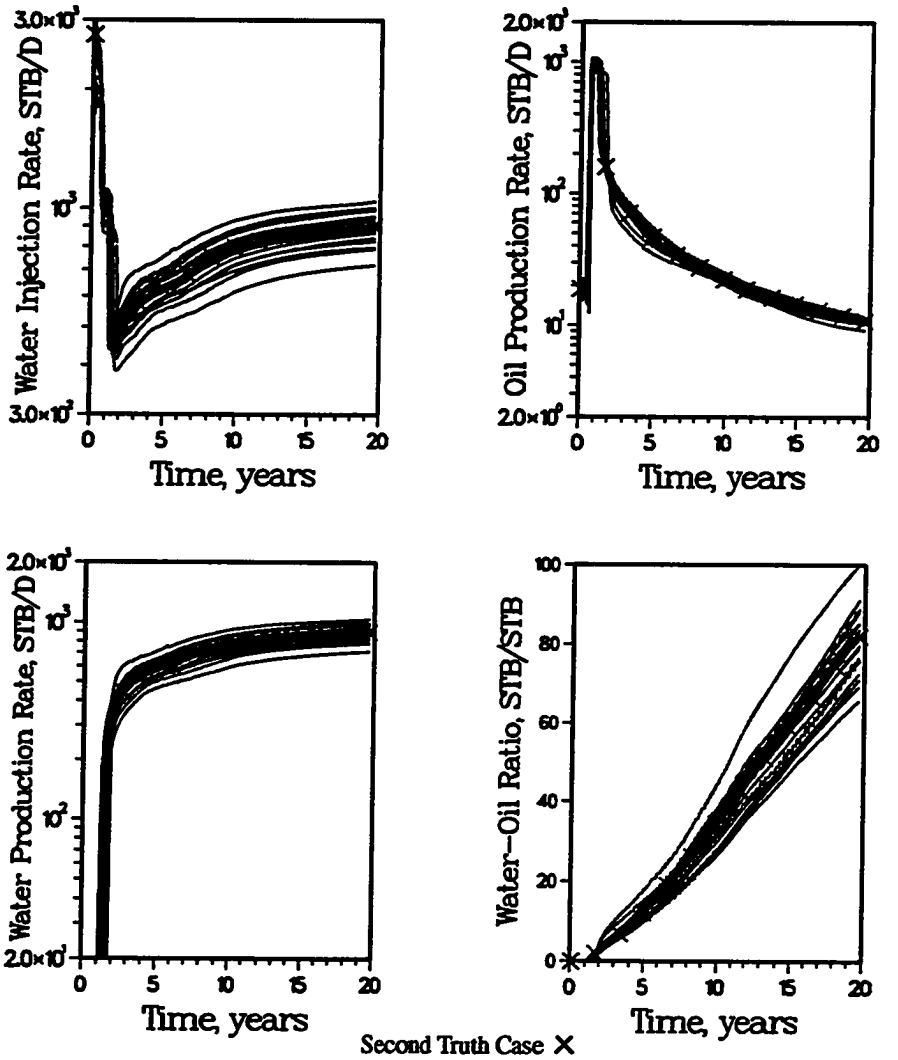

Figure 4.10 - Simulated waterflood performance comparing the second truth case and 20 flow simulations based on $p_{dH} = 0.298$; one-quarter five-spot pattern system

k_{NW} and p_{tH} Constraints Results

The simulated annealing with connectivity algorithm was extended to include the additional constraint of k_{NW}. Two more synthetic case studies were performed, using properties from the two previously discussed truth cases as the specified constraints.

For the first truth case, the producer k_{NW} (k_{NWp}) and the injector k_{NW} (k_{NWi}) are 190 md and 370 md, respectively. Once again, 20 permeability realizations were generated, this time using k_{NW} constraints in addition to the p_{tH} and conventional constraints. Waterflood performance plots of the corresponding flow simulations (and the first truth case) are illustrated in Figure 4.11. The improvement resulting from including k_{NW} as a constraint can be observed by comparing the performance curves shown in Figure 4.11 with the base case curves (Figure 4.6) and the results obtained when excluding the k_{NW} constraint (Figure 4.9). It can be seen that the spread in waterflood performance is significantly reduced, especially during early waterflood performance. However, the results are still biased compared to the truth case performance. Examination of the permeability realizations shows that the low permeability regions are located mostly in the diagonal corners of the pattern, as far as possible from the high permeability region surrounding each well. This is not true of the first truth case which has a region of high permeability surrounding the producer, quickly degrading into a low permeability region. This is the primary reason for the discrepancy between the truth case and all attempts to reproduce it.

The near well permeabilities of the second, less heterogeneous truth case were used as additional constraints to generate 20 permeability realizations. The values of k_{NW} for the producer and injector for the second truth case are 340 and 575 md, respectively. Corresponding waterflood performance plots are illustrated in Figure 4.12. An extremely good comparison is obtained between the second truth case and the other 20 flow simulations. Not only is performance from the second truth case reproduced very well, but the scatter between the 20 simulated waterflood performances is very small.

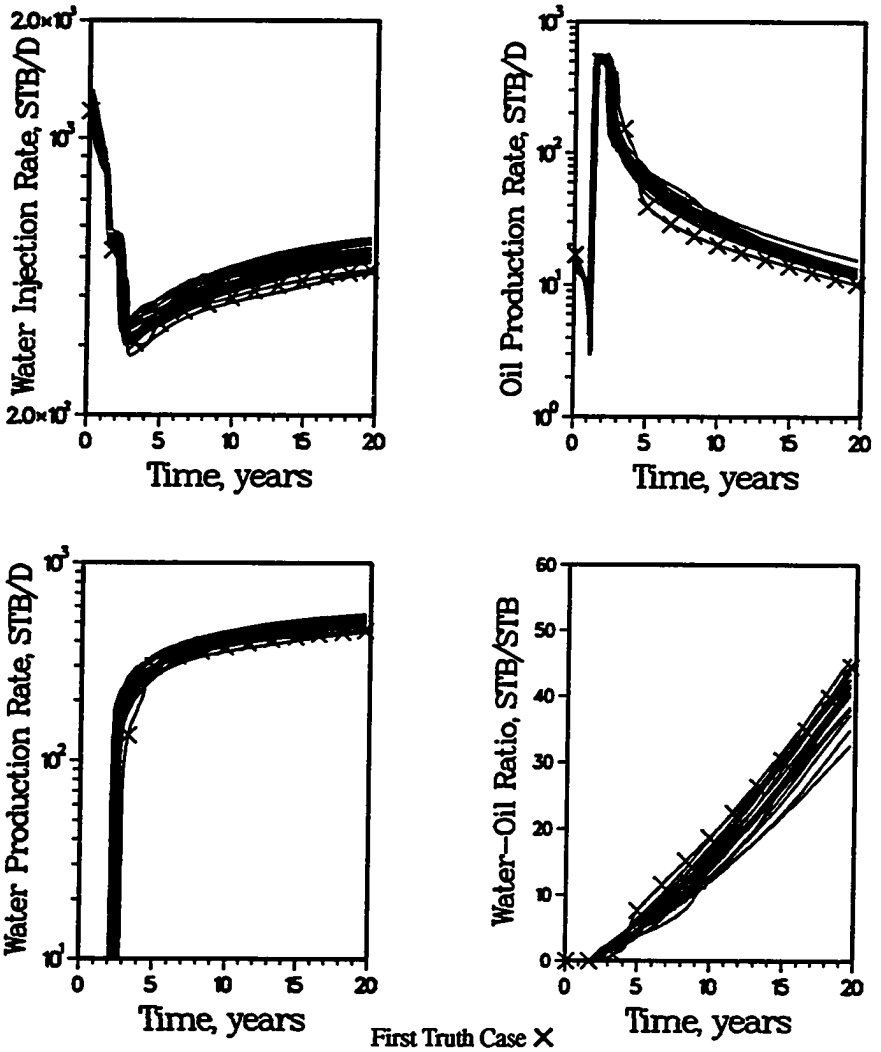

Figure 4.11 - Simulated waterflood performance comparing the first truth case and 20 flow simulations based on k_{NWp} = 190 md, k_{NWi} = 370 md and p_{tH} = 0.319; one-quarter five-spot pattern system

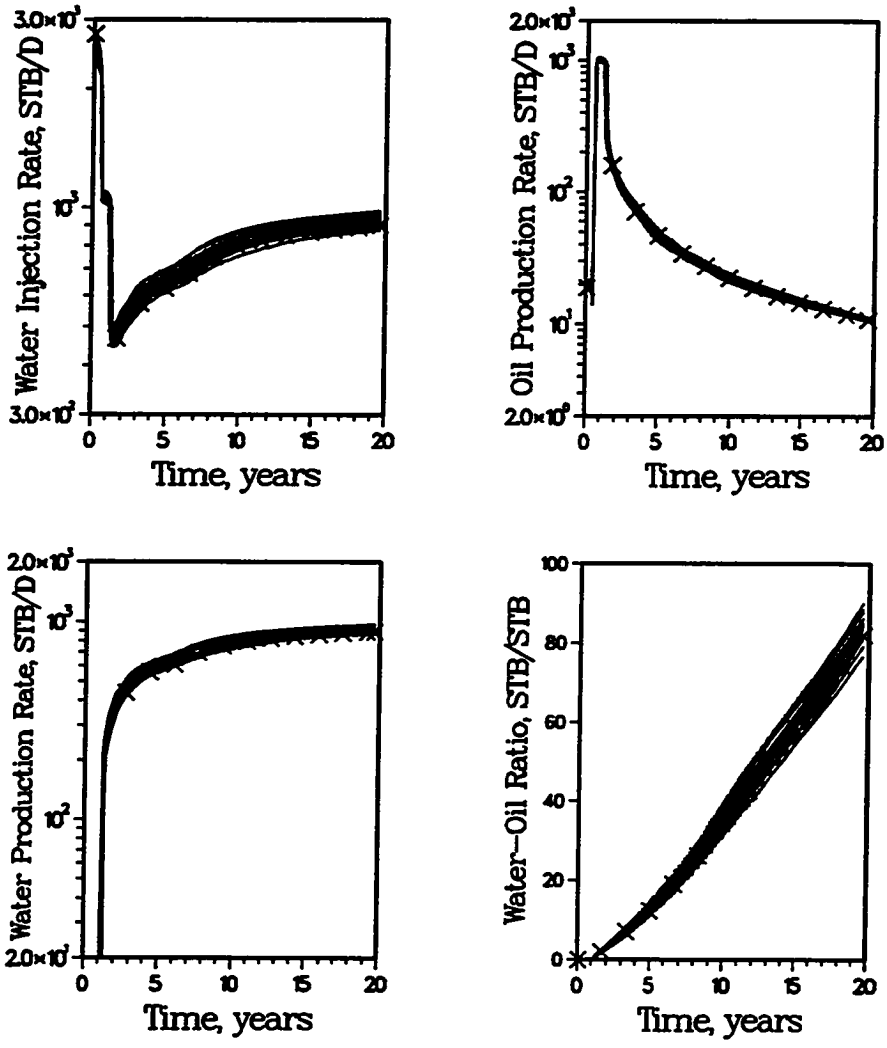

Figure 4.12 - Simulated waterflood performance comparing the second truth case and 20 flow simulations based on k_{NWp} = 340 md, k_{NWi} = 575 md and p_{tH} = 0.298; one-quarter five-spot pattern system

This represents a significant improvement over the results obtained using just the connectivity threshold constraint. Unlike the first truth case, the regions of low permeability for the second, less heterogeneous truth case are located in the diagonal corners (see Figure 4.7). This spatial distribution of permeability is a much more likely outcome and therefore is easier to reproduce.

k_{NW} and CV_{k^*} Constraints Results

A total of 20 permeability fields were generated using simulated annealing, the more heterogeneous permeability frequency distribution and additional constraints of k_{NW} (k_{NWp} = 190 md and k_{NWi} = 370 md) and CV_{k^*} (0.186). These values are characteristic of the first truth case. Inspection of the permeability images shows that the CV_{k^*} constraint has reduced the connectivity between the injector and the producer by forcing the low permeability region to be spread out between the two wells, much like the first truth case permeability field (see Figure 4.5). The corresponding waterflood performance is illustrated in Figure 4.13. Variations in waterflood performance have been greatly reduced. Unlike previous attempts, the anomalous characteristics of the truth case waterflood performance are reproduced. The additional constraint of CV_{k^*} has reduced the domain of possible solutions to a set with flow characteristics similar to the first truth case.

Analogous results, but based on characteristics of the second truth case, are shown in Figure 4.14. Values of k_{NWp}, k_{NWi} and CV_{k^*} for the second truth case and the other 20 permeability fields are 340 md, 575 md and 0.300, respectively. The locations of the low permeability regions for all 20 permeability fields compare very favorably with the second truth case. As a result, the waterflood performance of all 21 flow simulations also compare very well--especially oil rates. The reduction in the variation of waterflood performance in comparison to the base case results (Figure 4.8) is significant.

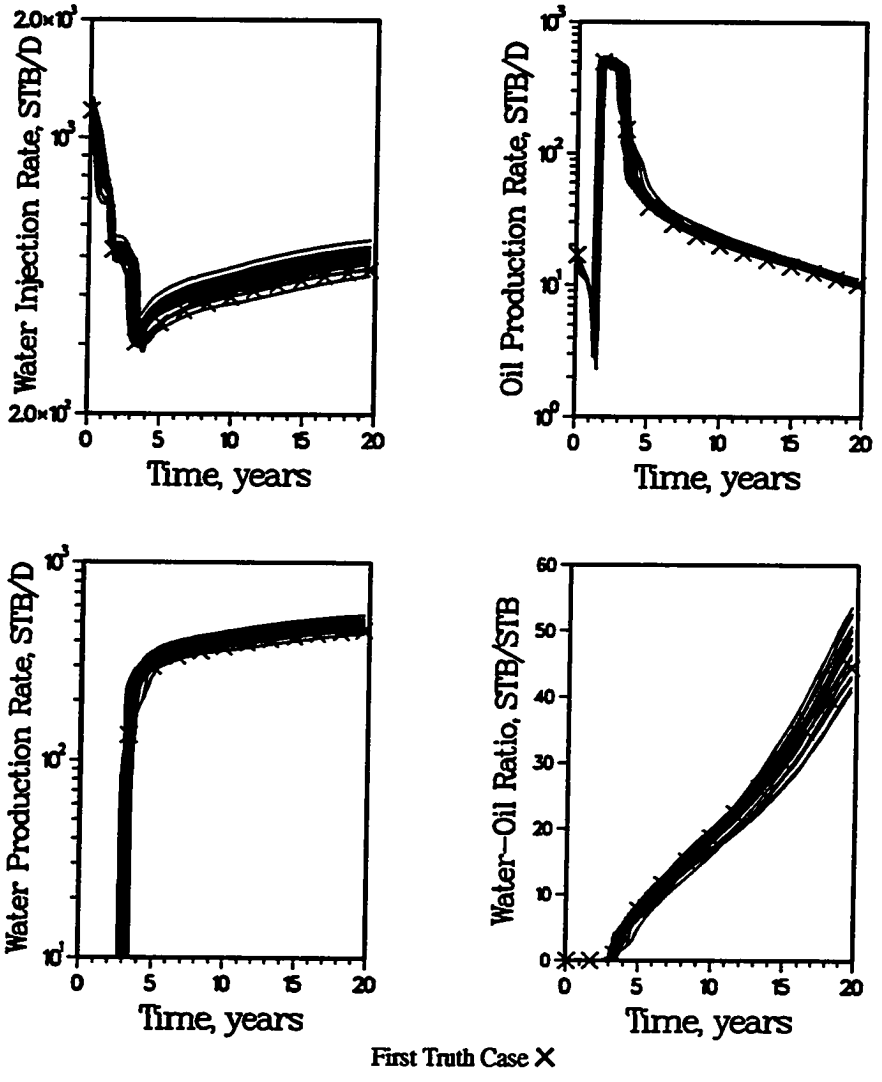

Figure 4.13 - Simulated waterflood performance comparing the first truth case and 20 flow simulations based on k_{NWp} = 190 md, k_{NWi} = 370 md and CV_{k^*} = 0.186; one-quarter five-spot pattern system

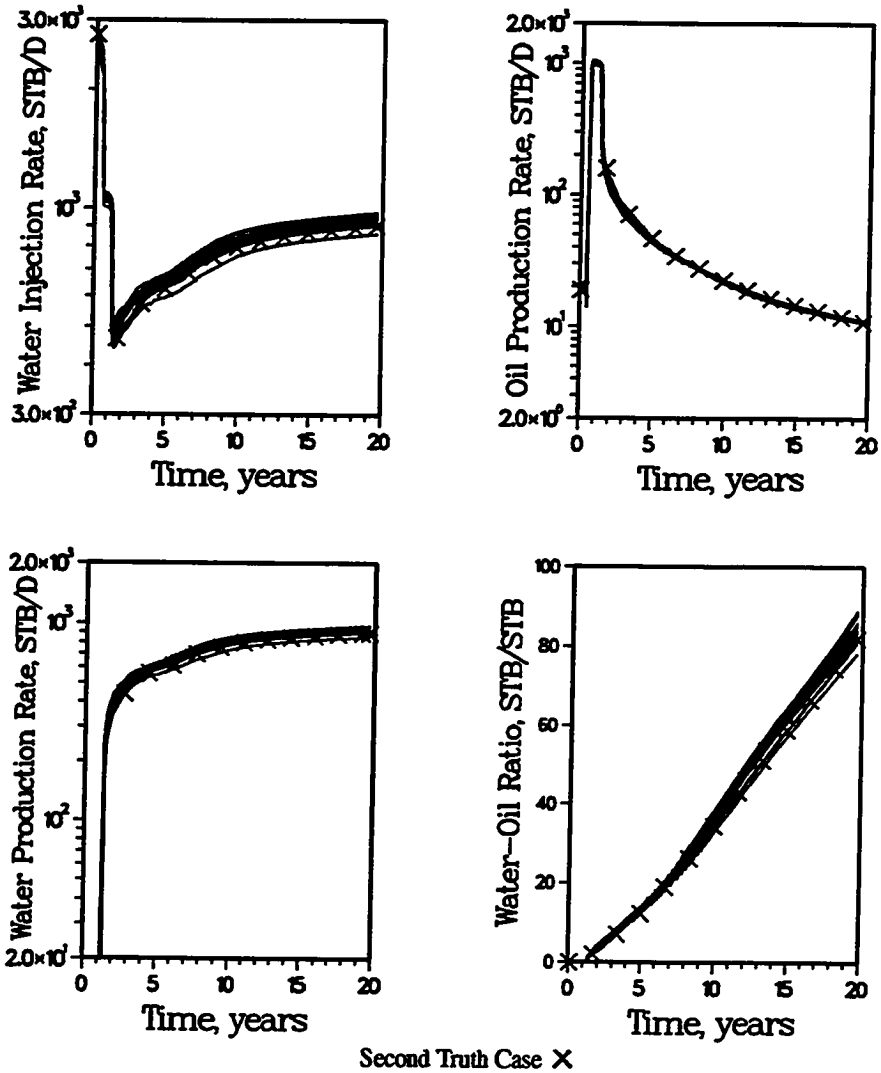

Figure 4.14 - Simulated waterflood performance comparing the second truth case and 20 flow simulations based on k_{NWp} = 340 md, k_{NWi} = 575 md and CV_{k^*} = 0.300; one-quarter five-spot pattern system

Connectivity Estimation from Waterflood Performance

The above two synthetic case studies were performed with the assumption that the values of p_{tH} and CV_{k^*} were known a priori. Since they cannot be measured directly, a correlation between waterflood performance parameters and the connectivity measures must be developed for estimation purposes. Sensitivities of CV_{k^*} were performed over a wide range of values to illustrate the strong relationship between CV_{k^*} and waterflood performance. Values of CV_{k^*} were varied from 0.05 to 0.40 with five permeability realizations generated at each value of CV_{k^*}. All other constraints were characteristic of the first truth case and were held constant. One-quarter of a five-spot pattern flow simulations were then performed using each permeability field. Figure 4.15 contains waterflood performance plots for the CV_{k^*} sensitivity flow simulations and the first truth case. For clarity, only one result per CV_{k^*} value has been included in Figure 4.15. The effect of varying CV_{k^*} results in a decrease in water breakthrough time. Although not shown, flow simulations with equal values of CV_{k^*} have similar waterflood performance behavior. The performance of the first truth case (highlighted) is about average compared to the other cases. This is expected since its value of CV_{k^*} is approximately mid-range.

Figure 4.16 better demonstrates the correlation between water breakthrough time and CV_{k^*}. Data from all 21 flow simulation sensitivities have been plotted in Figure 4.16. Note that as CV_{k^*} is increased, the spread in breakthrough times for the same CV_{k^*} is reduced. Larger values of CV_{k^*} reflect stronger trends between the two wells. The effect of CV_{k^*} on waterflood efficiency is illustrated in Figure 4.17. Here, waterflood efficiency is represented by the cumulative WOR after one hydrocarbon pore volume of water injected (HCPVI). These results demonstrate that CV_{k^*} does have a strong effect on waterflood performance. Hopefully, its value can be estimated by performing a sensitivity study.

Of course, the waterflood response of a producer is impacted by all neighboring injection wells. Therefore, the CV_{k^*} estimated from water breakthrough time and cumu-

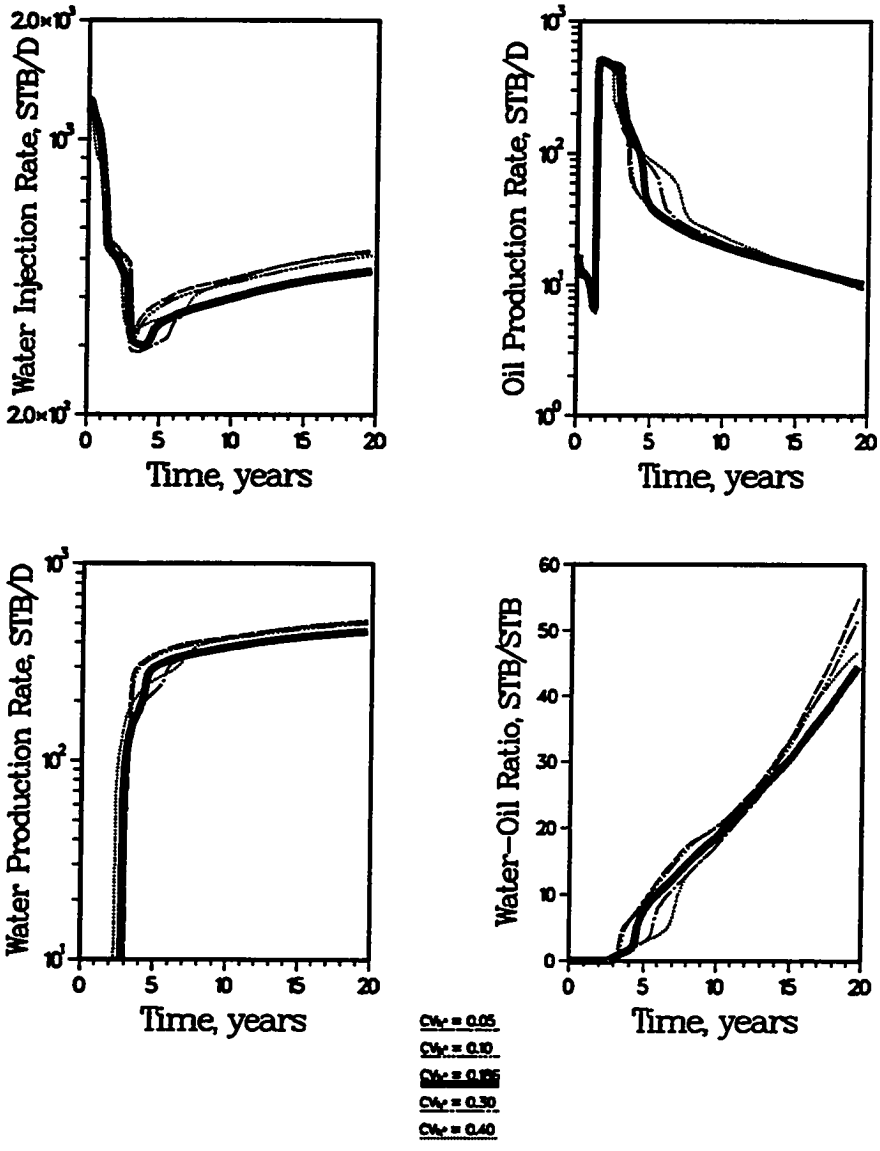

Figure 4.15 - Simulated waterflood performance showing the sensitivity of waterflood response to CV_{k^*}; one-quarter five-spot pattern system (first truth case highlighted)

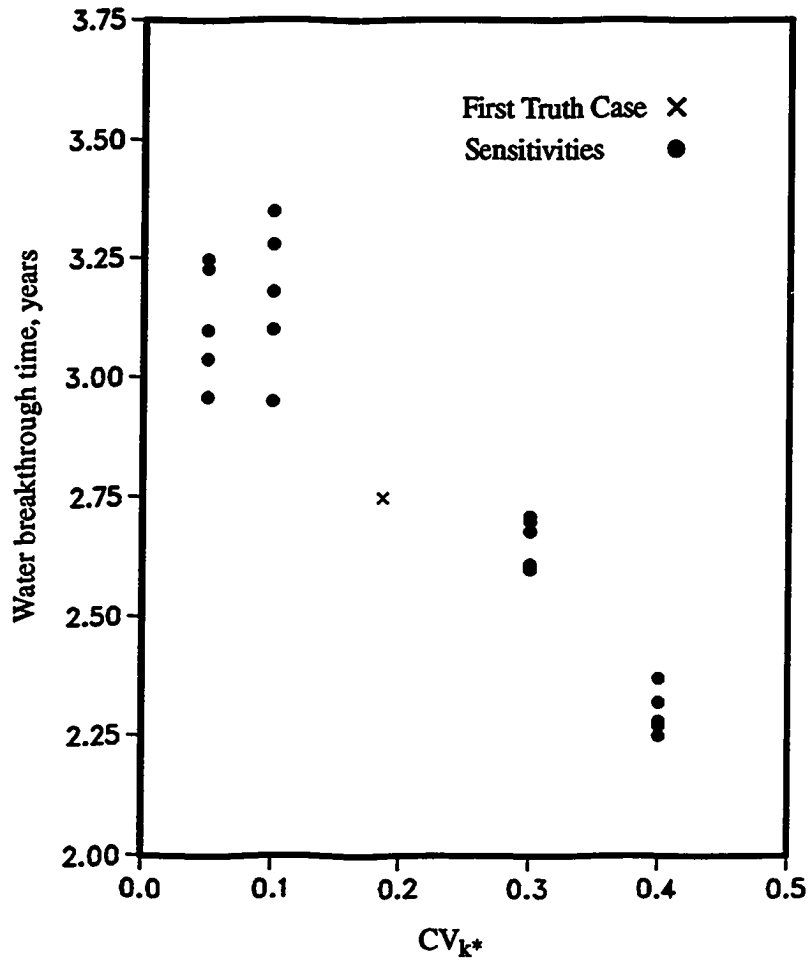

Figure 4.16 - Sensitivity of water breakthrough time to CV_{k^*}

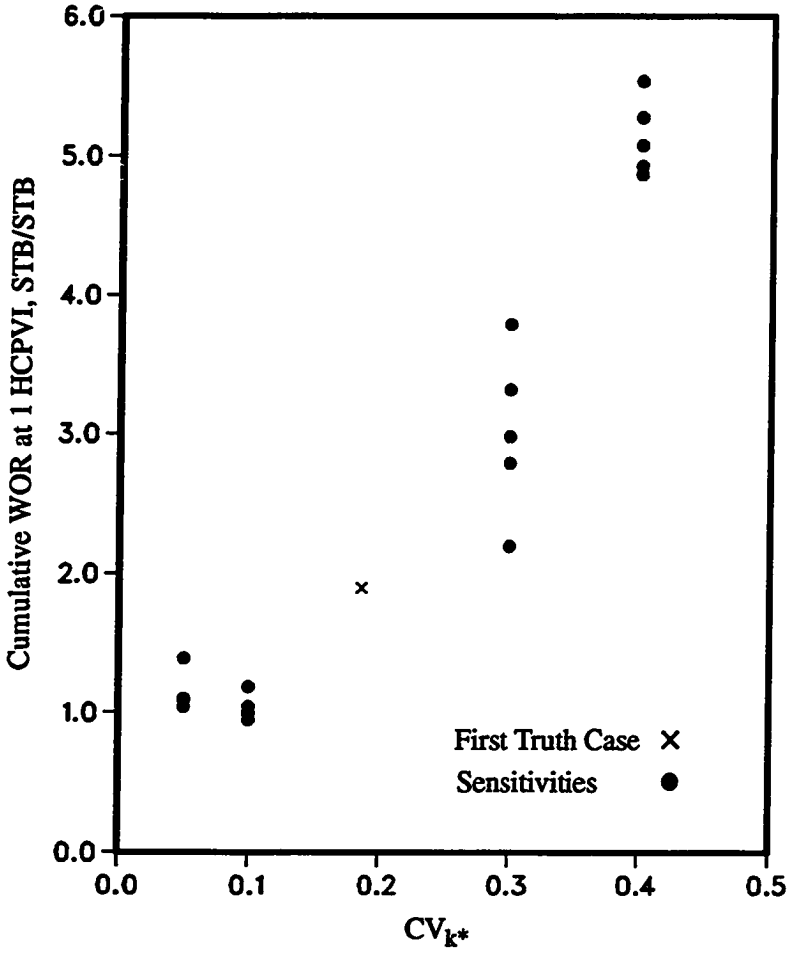

Figure 4.17 - Sensitivity of cumulative water-oil ratio to CV_{k*}

lative WOR's is an average of the four associated one-quarter five-spot patterns. Sensitivity studies would have to account for the possibility of varying CV_{k*}'s within a five-spot pattern. More work is required to determine the best approach for estimating each injector/producer CV_{k*}.

The correlation between CV_{k*} and reservoir connectivity is also apparent when examining the 21 permeability fields generated for the sensitivity study. A permeability image representing each value of CV_{k*} investigated is depicted in Figure 4.18. It can be seen that as CV_{k*} is increased, the high and low permeability trends become more aligned with the direction of fluid flow. Thus, higher values of CV_{k*} result in more continuous/conductive paths, decrease water breakthrough time and increase WOR trends, thereby decreasing waterflood efficiency.

Probability of Exceedance Maps

As more local reservoir constraints are defined, the variation in the spatial distribution of permeability between realizations is reduced. As a result, the uncertainty in defining regions of high and low permeability is also reduced. This becomes important when evaluating a reservoir for alternative operating strategies, e.g., infill drilling. Probability of exceedance maps can be used as a tool to quantify uncertainty. These maps are used to display the probability of exceeding a cutoff value at each grid block location. The probability of exceeding a cutoff at a grid block is calculated by determining the percentage of simulated values that exceed the cutoff at the particular grid block. This calculation is repeated for each grid block. A comparison of probability of exceedance maps representing the first truth case, the first base case and the corresponding results using k_{NW} and CV_{k*} constraints is presented in Figure 4.19. For this particular case, a low permeability percentile of 30% was used so that the regions which are most likely to have low permeability (but still floodable) would be highlighted. Such regions would most likely be good candidates for infill drilling in a mature waterflood. Since the permeabil-

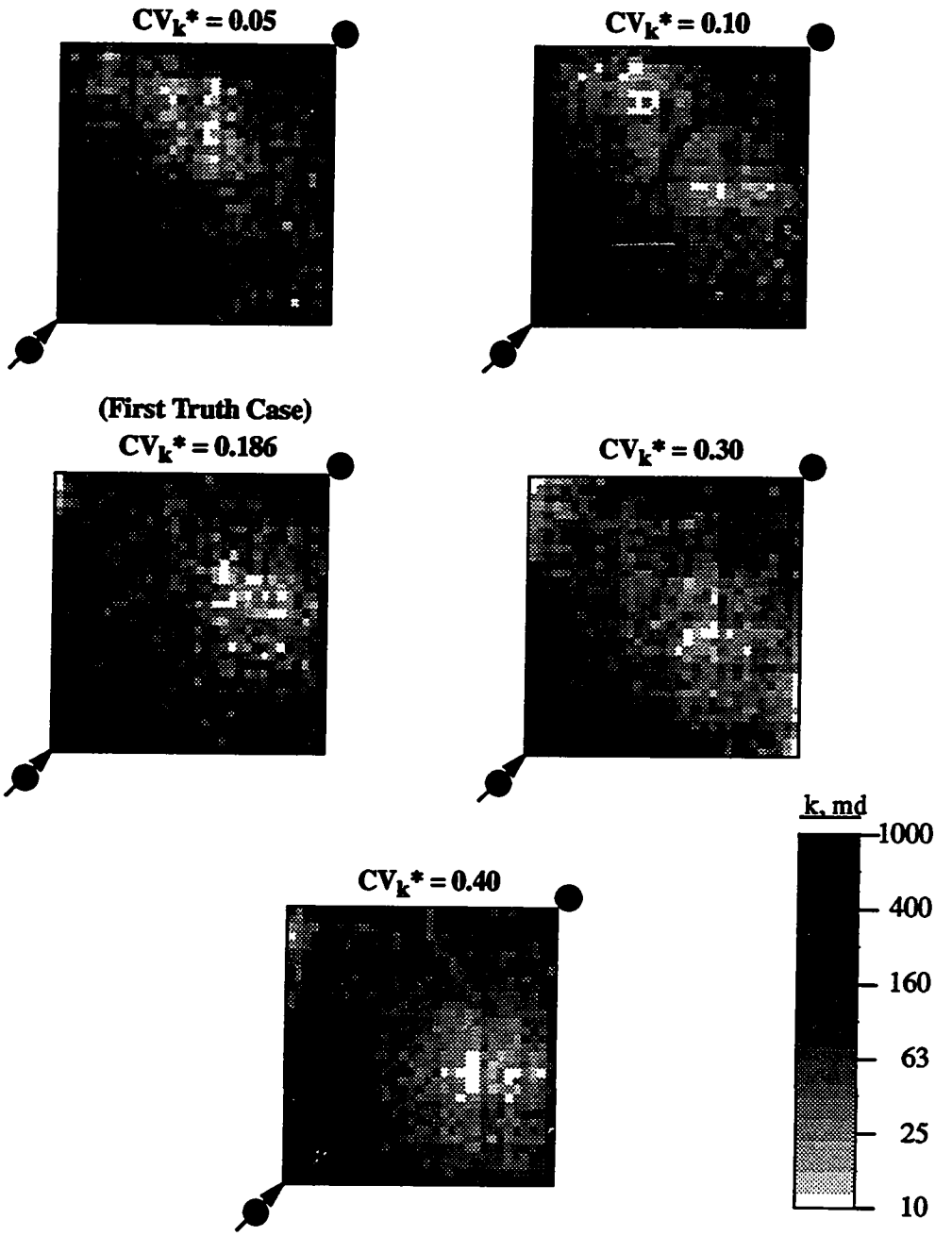

Figure 4.18 - One-quarter five-spot pattern permeability realizations for various values of CV_k^*

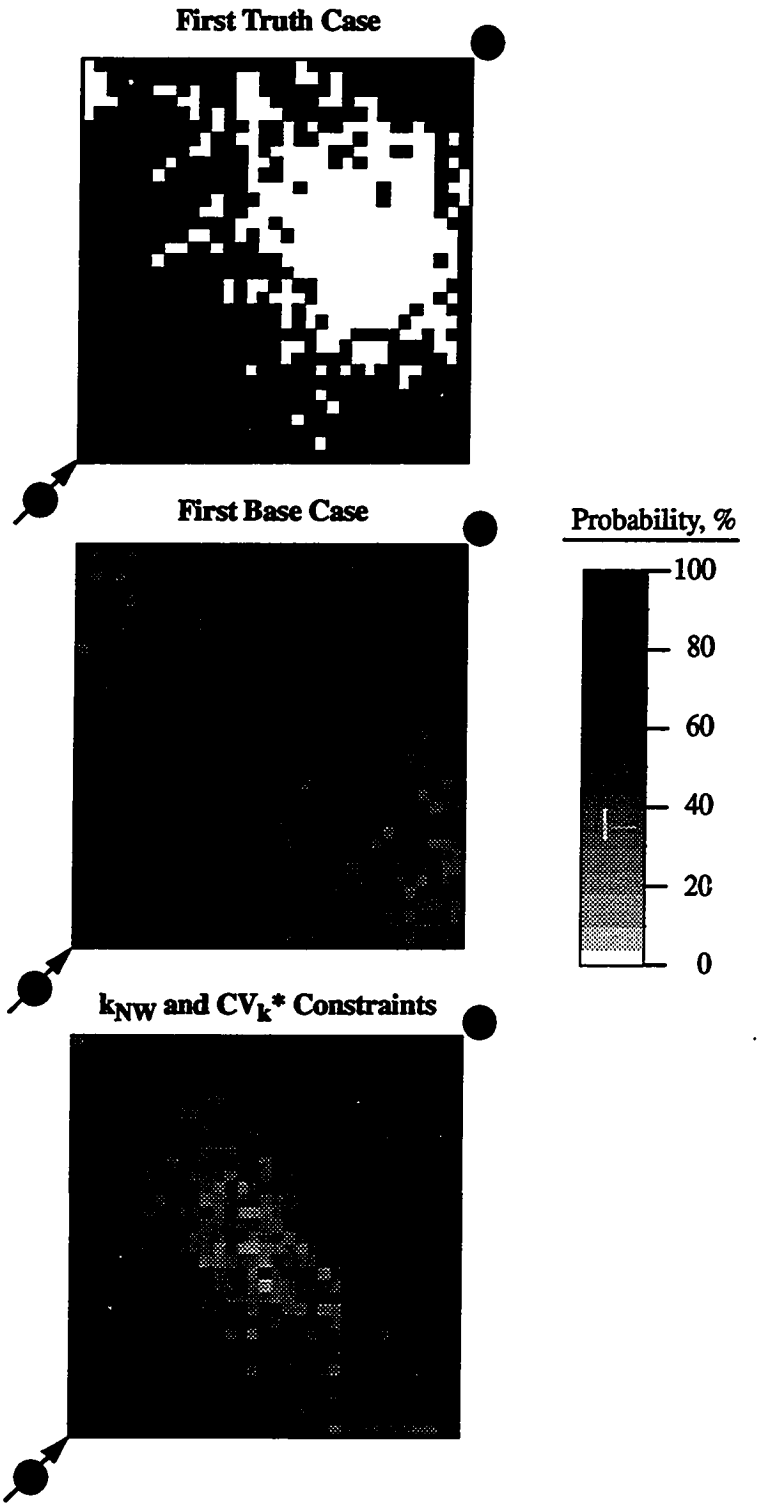

Figure 4.19 - Comparison of one-quarter five-spot pattern permeability probability of exceedance maps, 30th percentile

ity field for the truth case is known (i.e., deterministic), its grid blocks are either unshaded or darkly shaded, indicating a 100% certainty of their permeability values. On the other hand, the grid blocks for the other two cases are shades of gray, indicating some degree of uncertainty. Note that the regions exhibiting a low probability of exceedance for the connectivity constrained cases are consistent with the truth case. This is not true of the base case probability of exceedance map. The k_{NW} and CV_{k^*} constraints are shown to reduce the uncertainty in identifying high and low permeability regions, and thus, potential infill drilling locations.

Full Five-Spot Pattern

Base Case Results

Conventional simulated annealing was used to generate 21 permeability realizations for a full five-spot pattern. An omnidirectional spherical variogram having a relative nugget of 20% and a correlation length of 1000 ft (λ_D = 1.15) was used for characterizing the spatial structure. The more heterogeneous permeability distribution ($\mu_{\log(k)}$ = 2.0, $\sigma_{\log(k)}$ = 0.4) was assumed to be representative of the five-spot pattern. The only other conditioning data were the well block permeabilities. Figure 4.20 shows the permeability field arbitrarily selected to be the full five-spot pattern truth case. Waterflood performance of the central producer for all 21 flow simulations, based on oil producing rates, water producing rates and WOR's is presented in Figure 4.21. The waterflood performance of the truth case has been highlighted. Similar to previous results, waterflood performance is seen to vary significantly between flow simulations. Obviously, additional constraints are required to better reproduce the truth case performance.

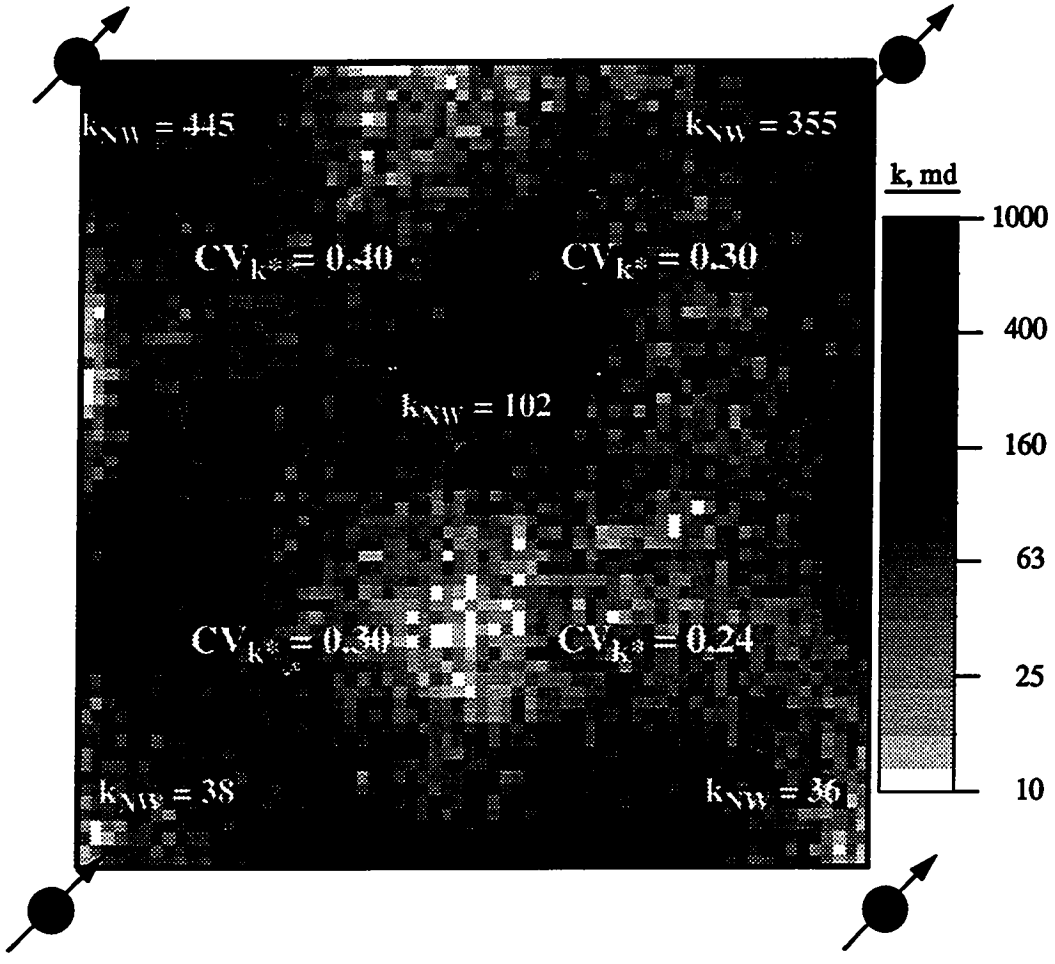

Figure 4.20 - Truth case permeability field for full pattern study

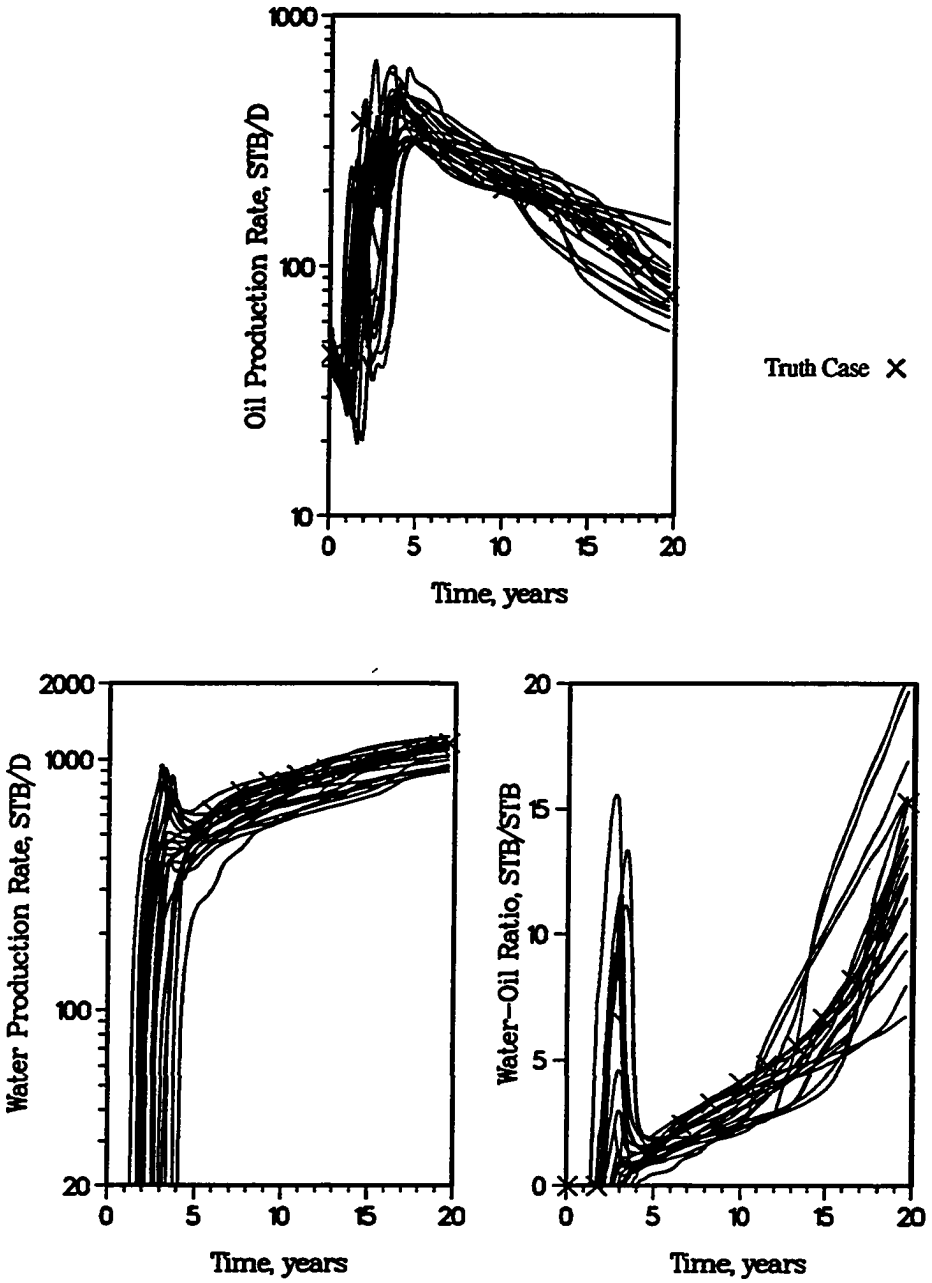

Figure 4.21 - Simulated waterflood performance of the full pattern truth case and the 20 base case flow simulations

k_{NW} and CV_{k^*} Results

The truth case k_{NW}'s and CV_{k^*}'s are also depicted in Figure 4.20. A total of 20 permeability fields were generated with these two indirect performance constraints included within the objective function as additional conditioning parameters. The water-flood performance for the 20 corresponding flow simulations and the truth case are shown in Figure 4.22. A comparison of Figures 4.21 and 4.22 indicates that although most of the performance curves cluster about the truth case, there are several anomalous cases.

Inspection of five-spot pattern permeability fields and water saturation contours of the most anomalous cases indicates that edge grid block permeabilities overly influence simulated results. Unlike more conventional reservoir descriptions obtained using contoured spatial properties, the orthogonal no-flow outer boundaries imposed on the five-spot pattern are not realistic for heterogeneous systems of the type addressed in this study. This statement is not meant to be construed that the author does not believe in the existence of no-flow boundaries. Such boundaries do exist; however, the assumption that these boundaries are accurately represented by those depicted in Figure 4.20 does not appear to be true for areally heterogeneous systems. Due to these apparent model artifacts, it was decided to reduce the impact of the no-flow boundaries by extending the model coverage area to include the offset rows and columns of producers. The corresponding results of the "extended" five-spot pattern modeling study follow.

Extended Five-Spot Pattern - Less Heterogeneous Permeability Distribution

Base Case Results

The permeability field used for the first extended five-spot pattern truth case is shown in Figure 4.23. The less heterogeneous permeability distribution ($\mu_{\log(k)} = 2.5$,

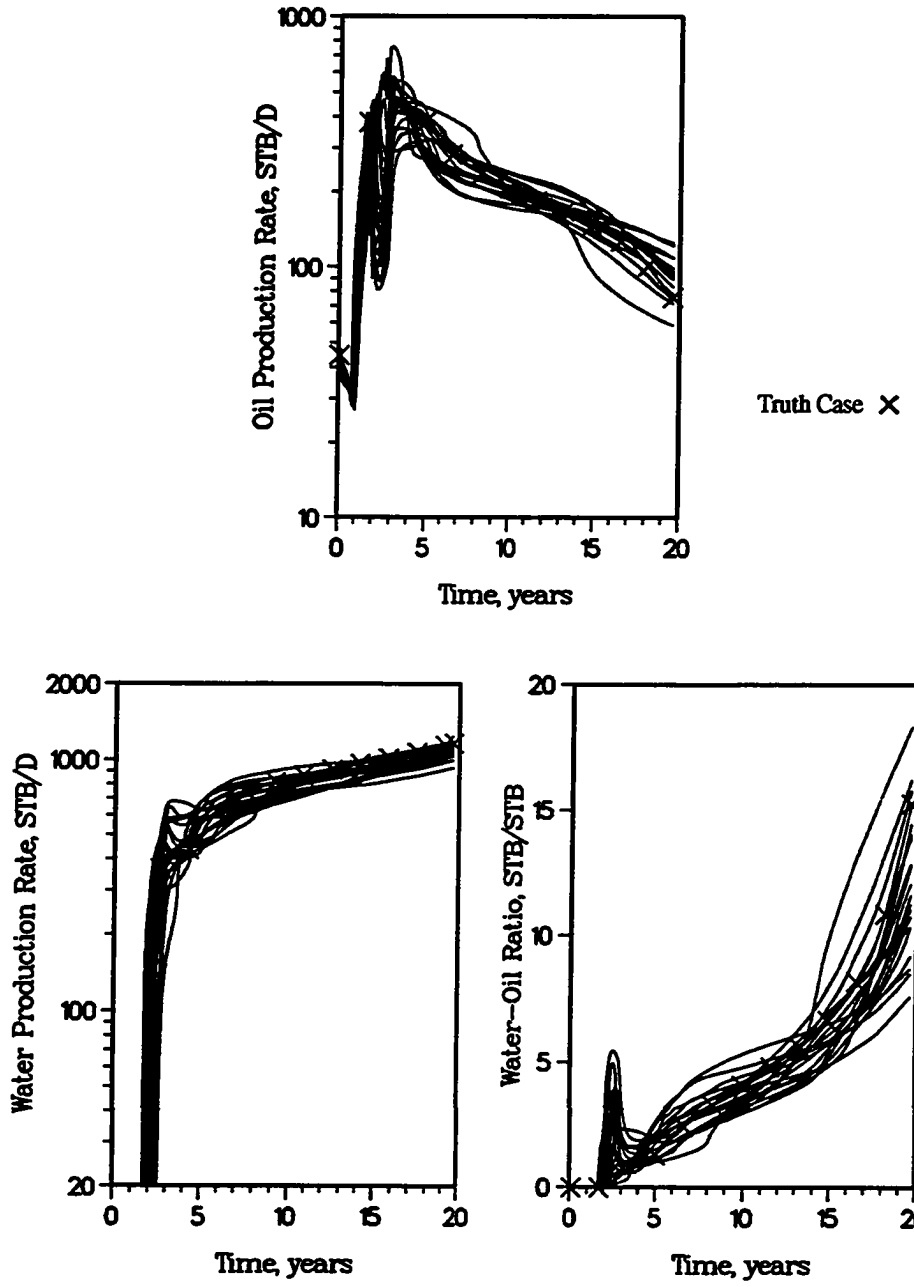

Figure 4.22 - Simulated waterflood performance comparing the full pattern truth case and 20 flow simulations based on k_{NW} and CV_{k^*} constraints

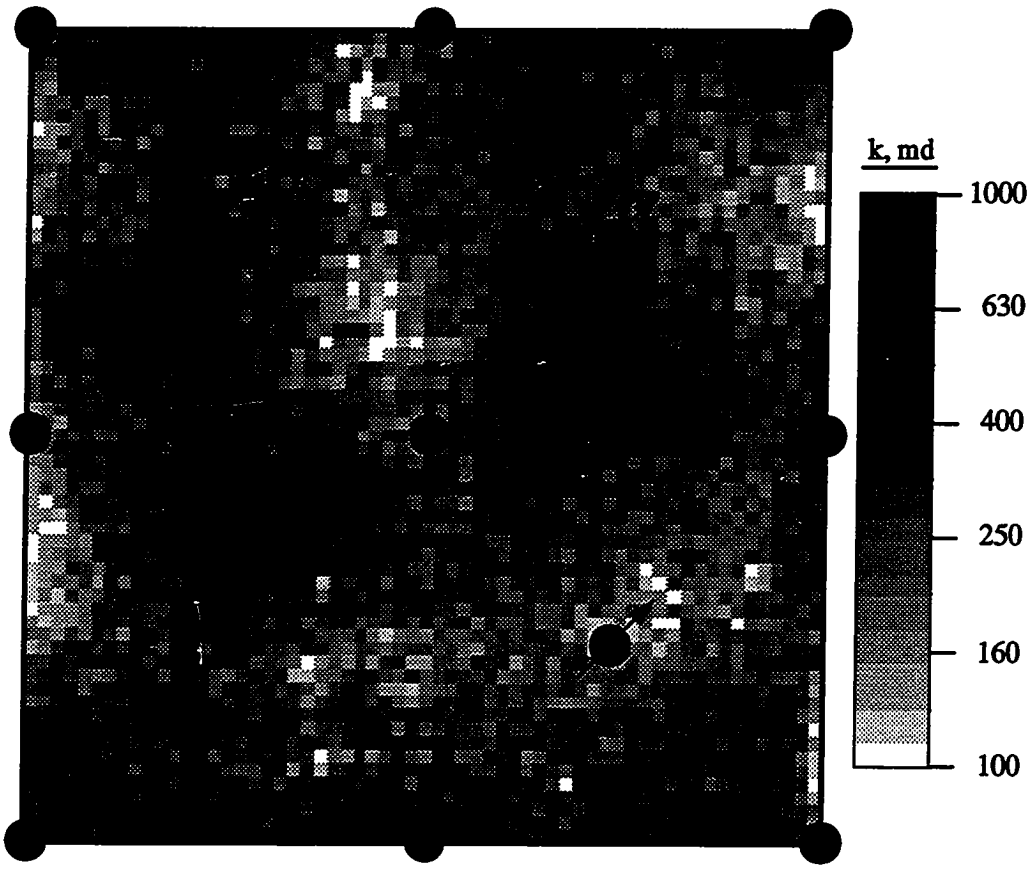

Figure 4.23 - Truth case permeability field for extended five-spot pattern study; less heterogeneous permeability distribution

$\sigma_{log(k)} = 0.2$) was used to generate this truth case. The permeability correlation length was increased from 1000 ft to 1500 ft ($\lambda_D = 0.803$). All other pertinent data remain unchanged from the full five-spot pattern study (see Table 4.1). As before, 20 additional permeability fields were generated using conventional simulated annealing. The waterflood performance of the inner five-spot producer and four injectors are illustrated in Figures 4.24 and 4.25. These base case results represent the typical range in simulated waterflood performance using conventional conditional simulation constraints for the given system. As expected, the variability exhibited by the flow simulation results is less than that obtained for the full five-spot pattern cases due to the reduced permeability variance. The injection rates vary more than production rates between simulations because the injectors have a much greater differential pressure (relative to the average reservoir pressure) than the producers.

k_{NW} and CV_{k^*} Results

The k_{NW} of each well and CV_{k^*} of each injector/producer pair representing the truth case were used as constraints in generating 20 additional permeability fields. Waterflood performance of the inner five-spot wells are included in Figures 4.26 and 4.27. A comparison of these two figures to their counterparts, Figures 4.24 and 4.25, indicates that the inclusion of the constraints k_{NW} and CV_{k^*} significantly increases the probability of generating a reservoir description with waterflood performance similar to the truth case. Several of the permeability fields have spatial characteristics very similar to the truth case (see Figure 4.28). This is not the case for the 20 base case permeability fields. However, there are a few performance curves which do differ noticeably from the truth case performance. Probably of most concern is the tendency of the WOR curves of the inner five-spot producer (Figure 4.26) to fall below the truth case WOR curve--two significantly more so than the others.

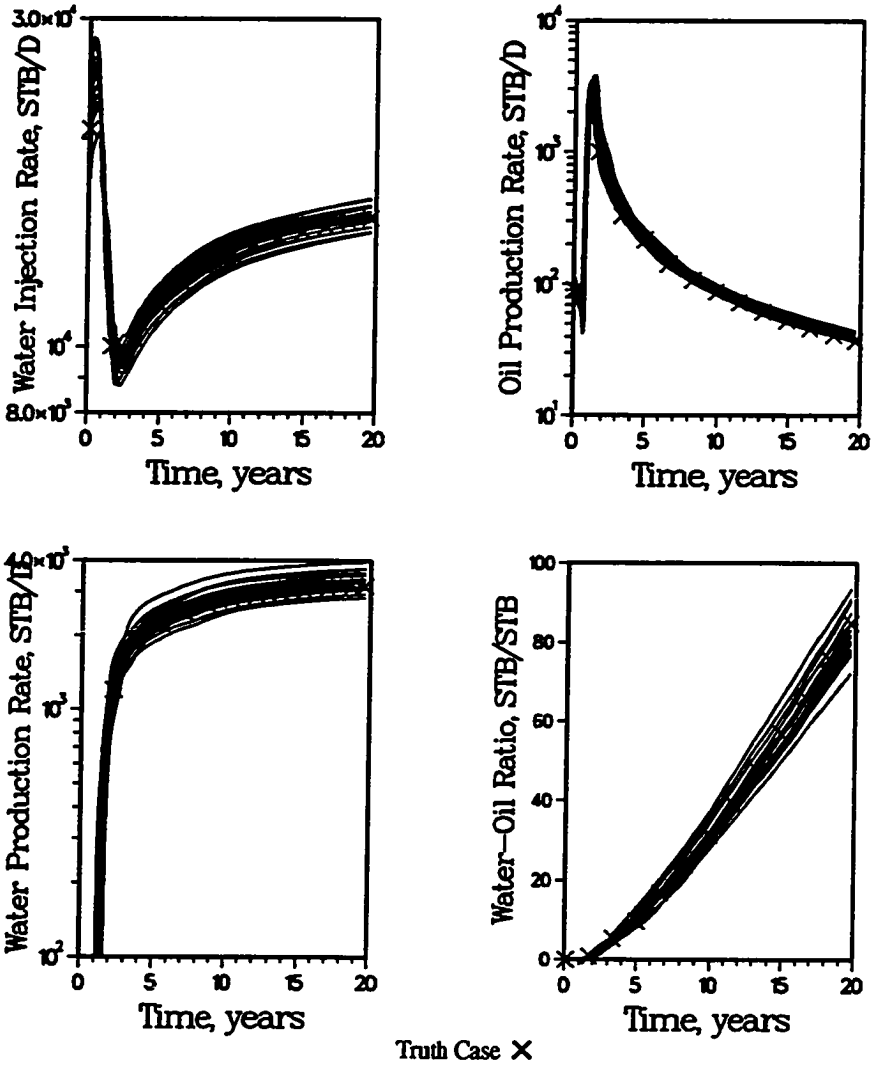

Figure 4.24 - Base case waterflood performance for the inner five-spot pattern wells; extended five-spot pattern study using the less heterogeneous permeability distribution

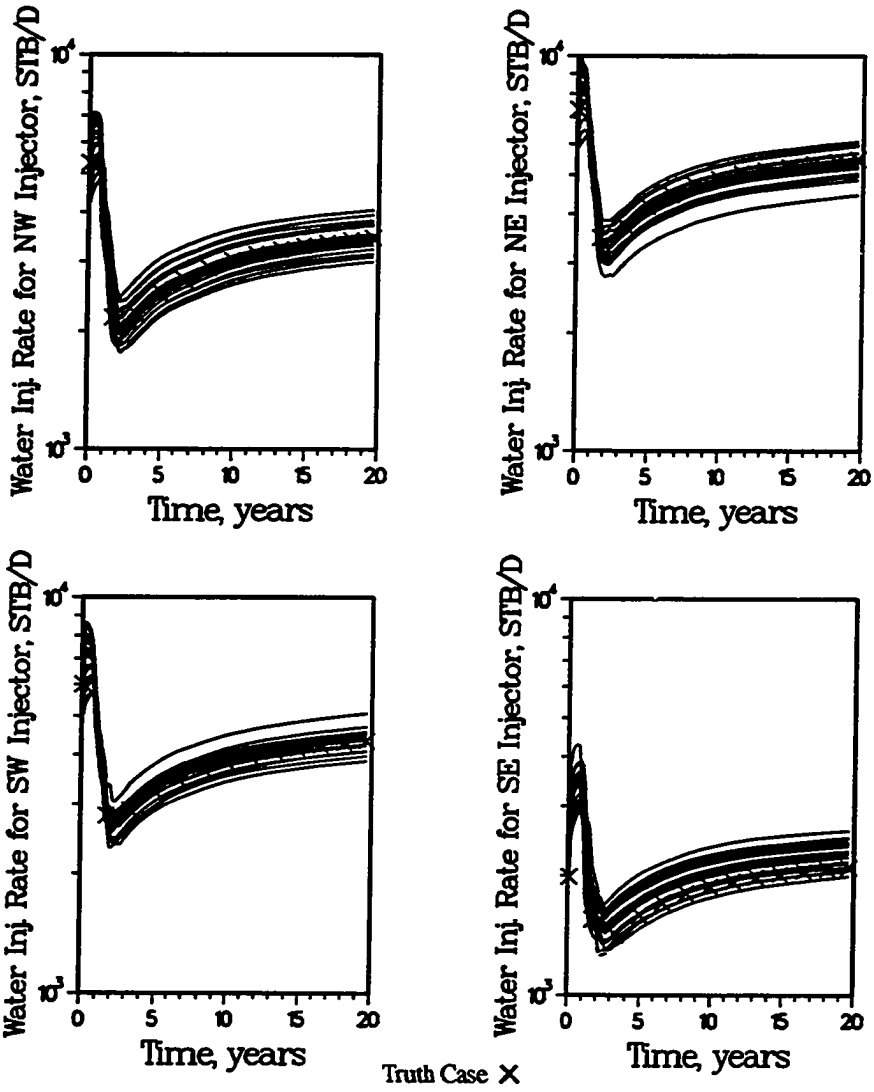

Figure 4.25 - Base case waterflood performance for the inner five-spot pattern injection wells; extended five-spot pattern study using the less heterogeneous permeability distribution

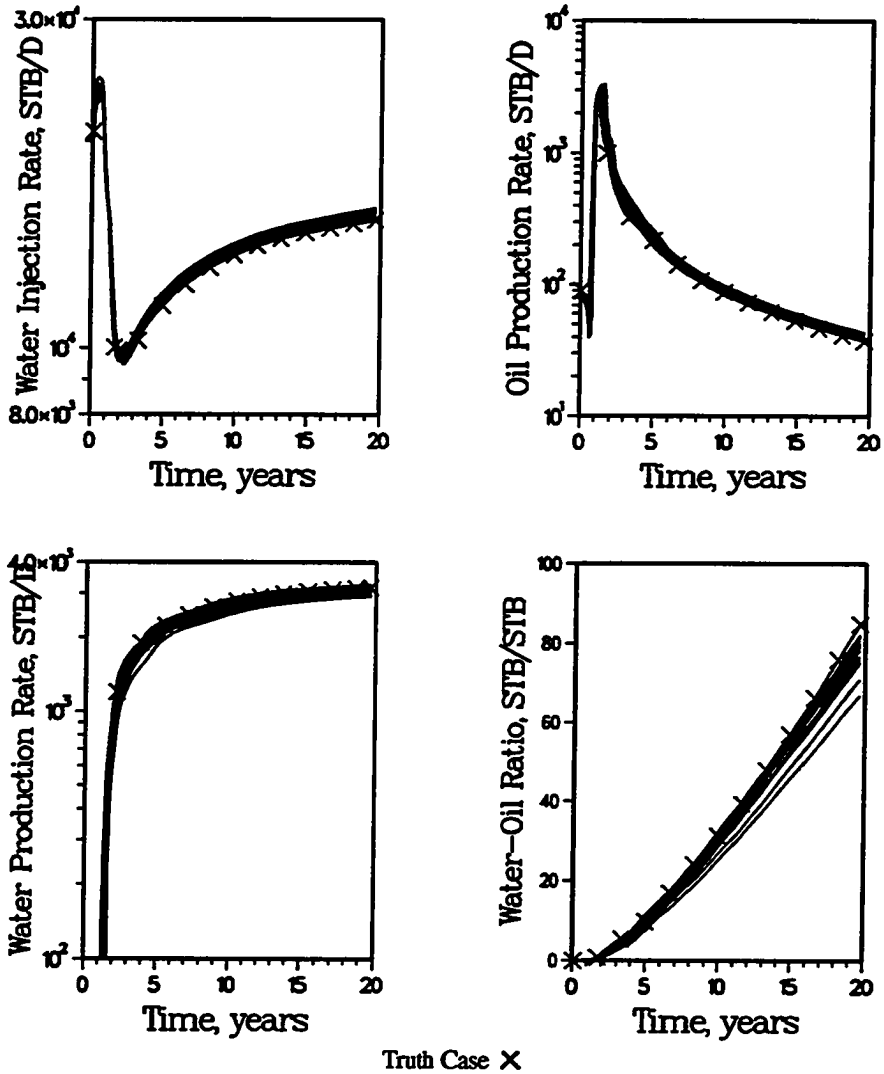

Figure 4.26 - CV_{k*} and k_{NW} constraints case waterflood performance for the inner five-spot pattern wells; extended five-spot pattern study using the less heterogeneous permeability distribution

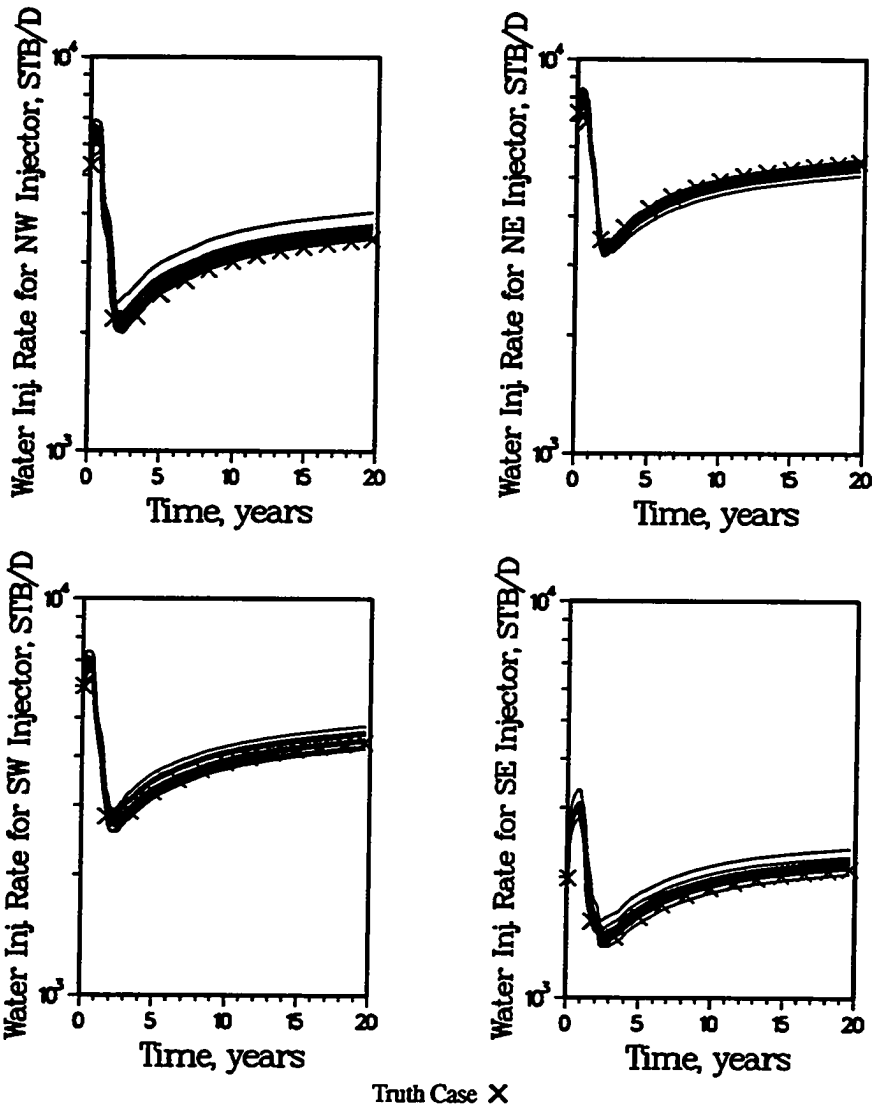

Figure 4.27 - CV_{k^*} and k_{NW} constraints case waterflood performance for the inner five-spot pattern injection wells; extended five-spot pattern study using the less heterogeneous permeability distribution

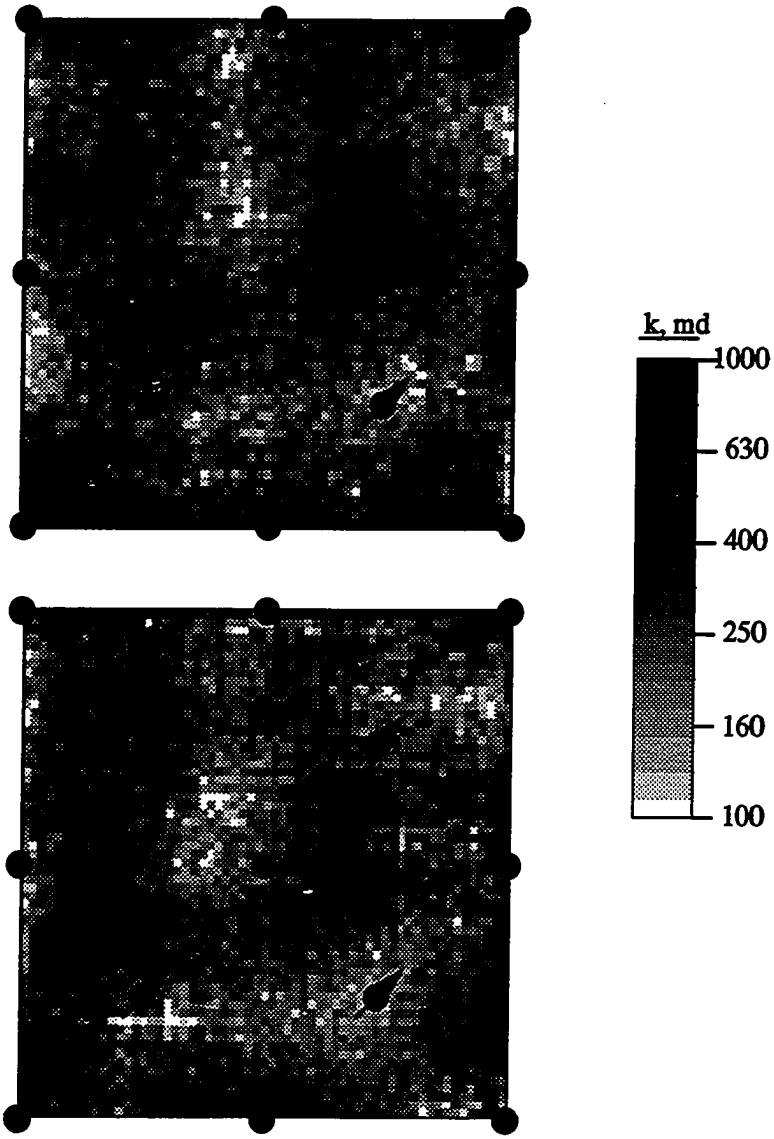

Figure 4.28 - Comparison of truth case permeability field and an indirect performance constraints case permeability field; extended five-spot pattern waterflood study using the less heterogeneous permeability distribution

The permeability fields responsible for the anomalously low WOR trends are shown in Figure 4.29. Note that these two permeability fields are very similar. Also note that the most significant difference between these two permeability fields and the truth case (Figure 4.28) is the spatial distribution of permeability between the central producer and the northeast injector. Although all three permeability fields have identical values of CV_{k^*} for this injector/producer pair, the average permeability of the corresponding area of influence for the truth case is considerably higher. As a result, the truth case area of influence of these two wells is processed much faster. It should be noted that CV_{k^*} represents the standard deviation of a permeability normalized by its mean. Therefore, two injector/producer pairs may have the same CV_{k^*} but vastly different k* means.

It is concluded that whereas k_{NW} constrains early time injectivity/productivity and CV_{k^*} constrains reservoir connectivity, (relative) estimates of the average permeability between an injector/producer pair may be required to reproduce time dependent variations in historical waterflood performance. This additional waterflood constraint, referred to as k_{PAT}, becomes significant only when large variations in average permeability of neighboring injector/producer areas of influence exist. Otherwise, the parameter k_{PAT} has no more than a secondary effect. Although this study has studied the significance of k_{PAT}, it is not known how the parameter can be obtained from field data.

Extended Five-Spot Pattern - More Heterogeneous Permeability Distribution

The more heterogeneous permeability distribution was used to further investigate the impact of large variations in the average permeability for adjacent injector/producer pairs. It was felt that the large range in permeabilities would increase the potential of having large variations in the average permeability of injector/producer pairs. This would increase the likelihood of requiring k_{PAT} as a constraint. As before, base case results using conventional constraints are presented first. Subsequently, the results

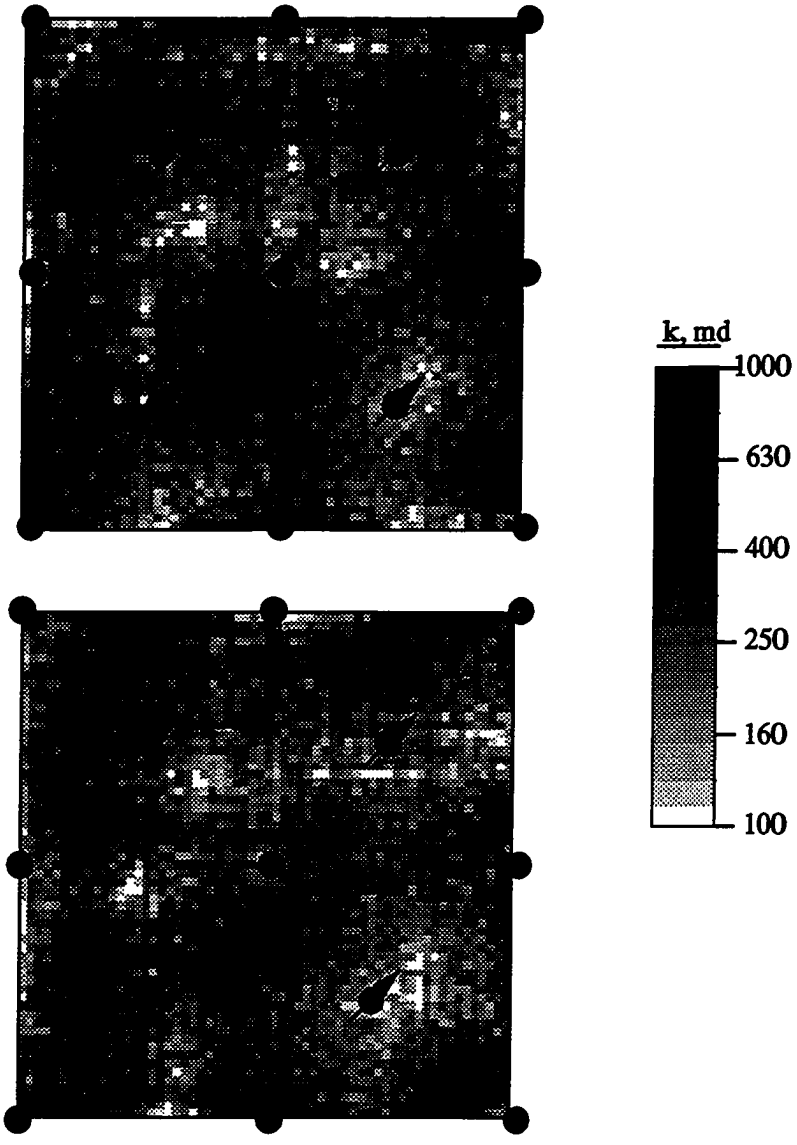

Figure 4.29 - Permeability fields generated using indirect performance constraints and characterized by anomalous water-oil ratio trends; extended five-spot pattern waterflood study using the less heterogeneous permeability distribution

obtained when additional constraints are imposed are compared to the base case results to determine the degree of improvement.

Recall that the more heterogeneous permeability distribution is log-normally distributed having a mean log(k) of 2.0, or 100 md, and a standard deviation of 0.6. Consequently, 68% of the permeabilities lie between 40 and 250 md. The same 13 well, 80 acre well spacing, 160 acre five-spot waterflood pattern system will be used. All permeability realizations were generated using an omnidirectional spherical variogram having a 20% relative nugget and a correlation length of 1200 ft, or λ_D of 0.643. Refer to Table 4.1 for additional details.

Base Case Results

Conventional simulated annealing was used to generate 21 permeability realizations, all having the same permeability frequency distribution, variogram and well block permeability values. One of the permeability realizations was arbitrarily selected to represent the actual reservoir permeability field, i.e., to be the truth case permeability field. The truth case permeability field is shown in Figure 4.30. Some of the more prominent features of the truth case permeability field are: 1) a high permeability zone surrounding the central producer, 2) a rim of low permeability surrounding the central producer high permeability zone, 3) a high permeability streak connecting the central producer and the injection well offset to the southeast and 4) a high permeability connectivity streak running north/south along the west side.

Waterflood performance plots for the inner five-spot pattern wells are presented in Figures 4.31 and 4.32. As expected for a highly heterogeneous system, performance varies considerably from realization to realization. For the central producer, water breakthrough time varies from less than 2 years to more than 4 years. The initial oil production rate for the central producer varies from 25 STB/D to 70 STB/D. The well's WOR after 20 years ranges from 13 to 33 STB/STB. Similar variations are evident in

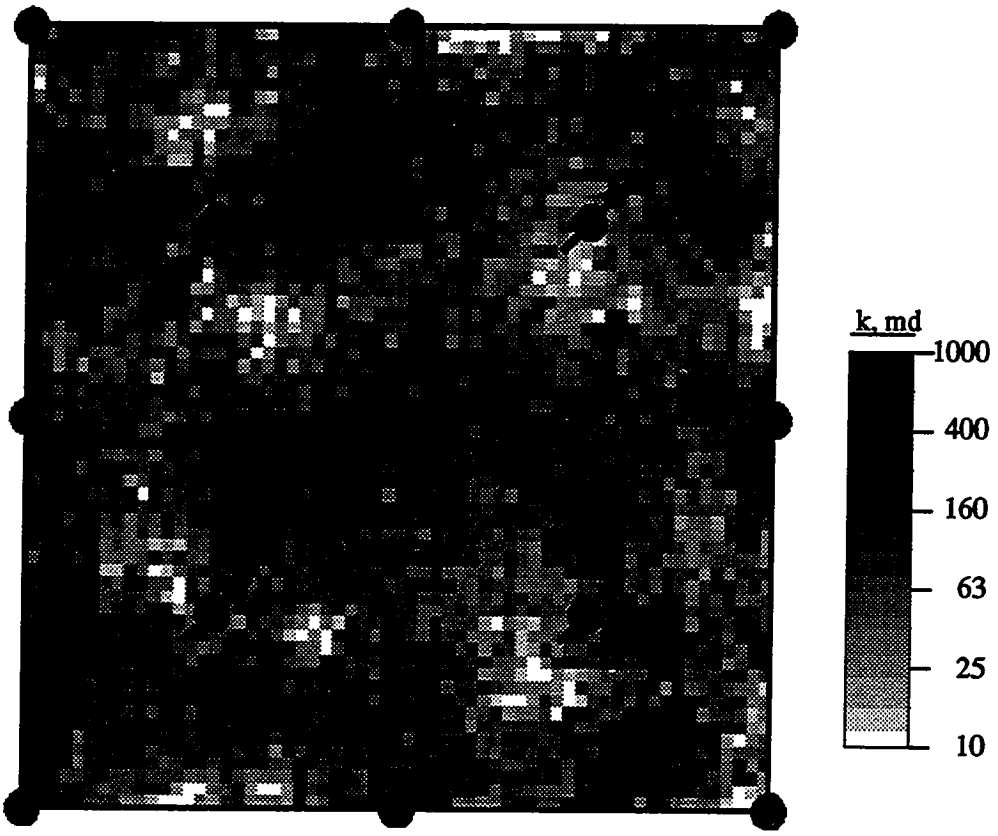

Figure 4.30 - Truth case permeability field for the more heterogeneous permeability distribution; extended five-spot pattern

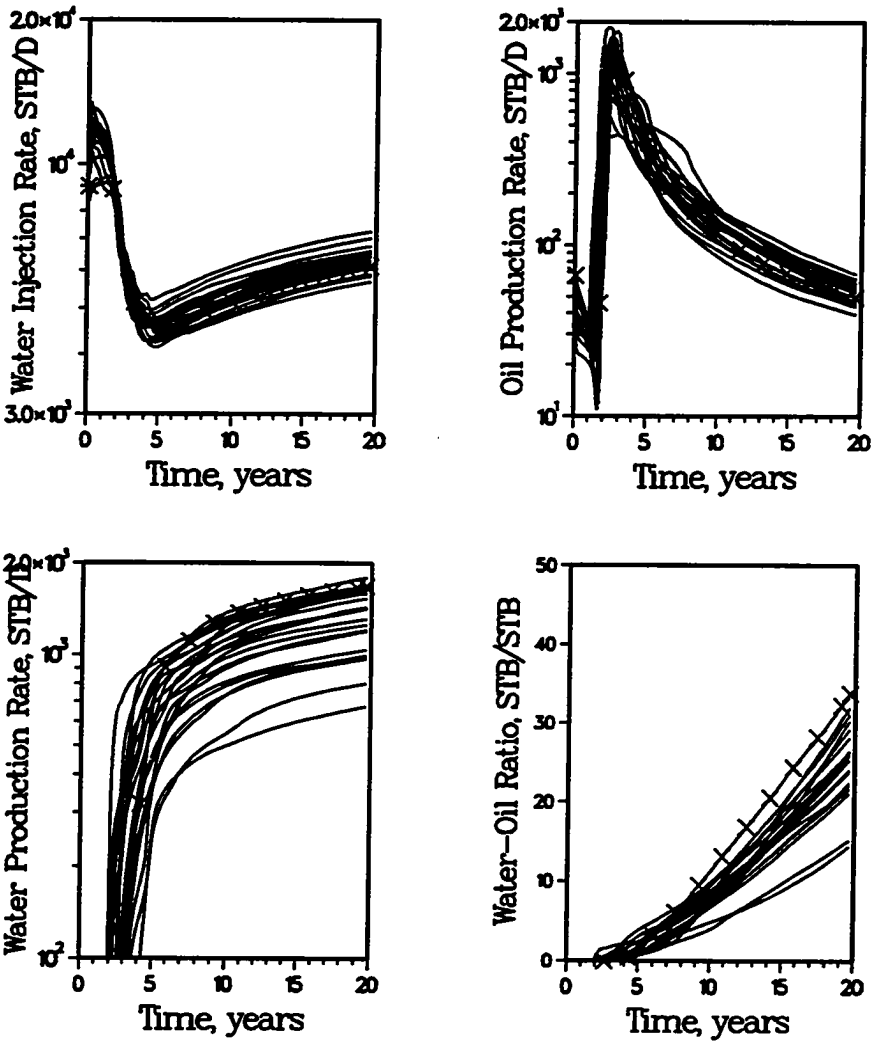

Figure 4.31 - Base case waterflood performance for the inner five-spot pattern wells; extended five-spot pattern study using the more heterogeneous permeability distribution

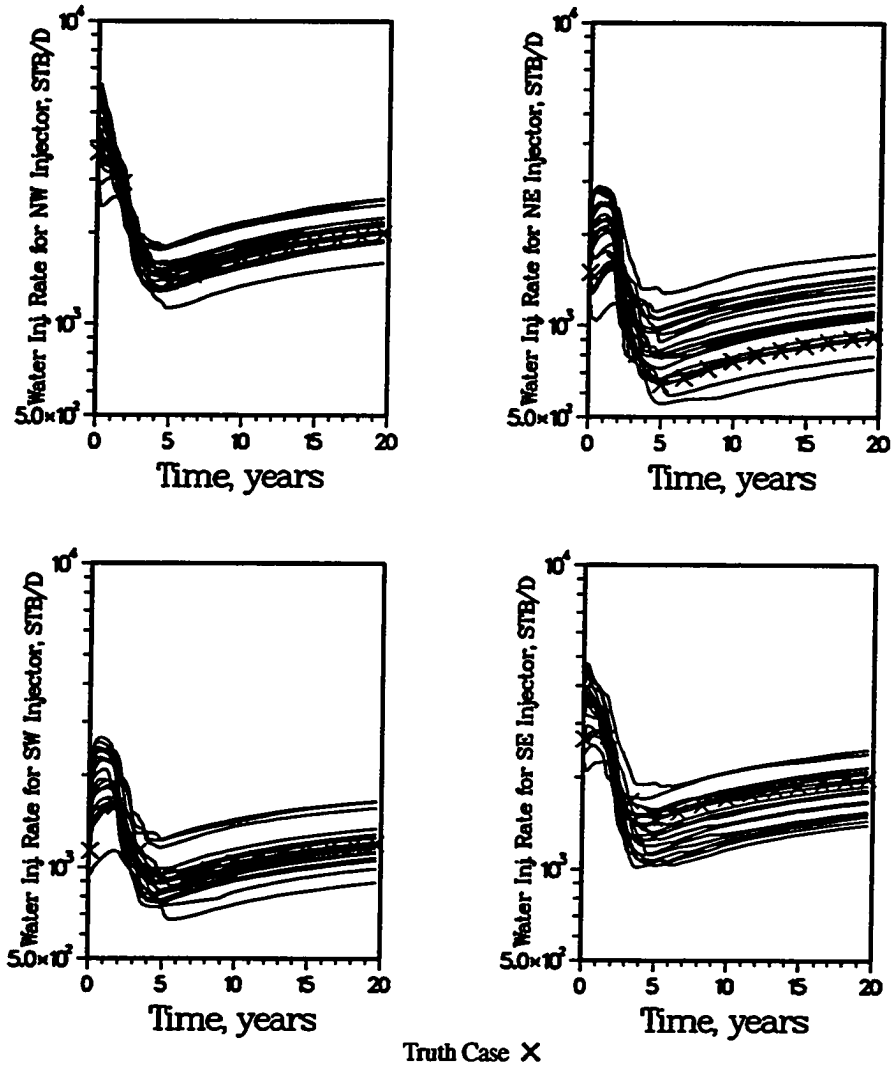

Figure 4.32 - Base case waterflood performance for the inner five-spot injection wells; extended five-spot pattern study using the more heterogeneous permeability distribution

the rate profiles of the four inner five-spot pattern injection wells (Figure 4.32). Such large variations would result in extremely broad waterflood performance probability distributions. Additional information must be integrated into the reservoir description before realistic probability distributions can be obtained.

Variations in the spatial distribution of permeability between realizations are illustrated in Figure 4.33. Three of the 20 permeability realizations generated using conventional simulated annealing are compared to the truth case image. Although the same degree of heterogeneity (permeability frequency distribution and spatial correlation) exists in all four realizations, local well-to-well heterogeneities differ greatly. This, of course, is the reason for the large variation in waterflood performance depicted in Figures 4.31 and 4.32. For example, the central producer is surrounded by a high permeability region for both the truth case and Realization 3. However, the high permeability streak connecting the central producer to the northeast injection well does not exist for the truth case. As a result, the pore volume connecting these two wells will be processed much faster and less efficiently for Realization 3 than the truth case. Such adverse discrepancies exist throughout the 13 well area for all 20 realizations when compared to the truth case.

As previously mentioned, the ability of a technique to reduce uncertainty can be illustrated using probability of exceedance maps. A comparison of probability of exceedance maps at the 30^{th} permeability percentile for the truth case and the base case realizations is given in Figure 4.34. As before, the 30^{th} permeability percentile was used to accentuate the low permeability regions. The base case probability map summarizes the degree of certainty obtained when using conventional constraints. Note that most of the 13 well area has about a 70 percent probability of exceeding the 30^{th} percentile. This is no better than an a priori guess, i.e., performing the conditional simulations helped very little in reducing the uncertainty in the interwell spatial distribution of permeability.

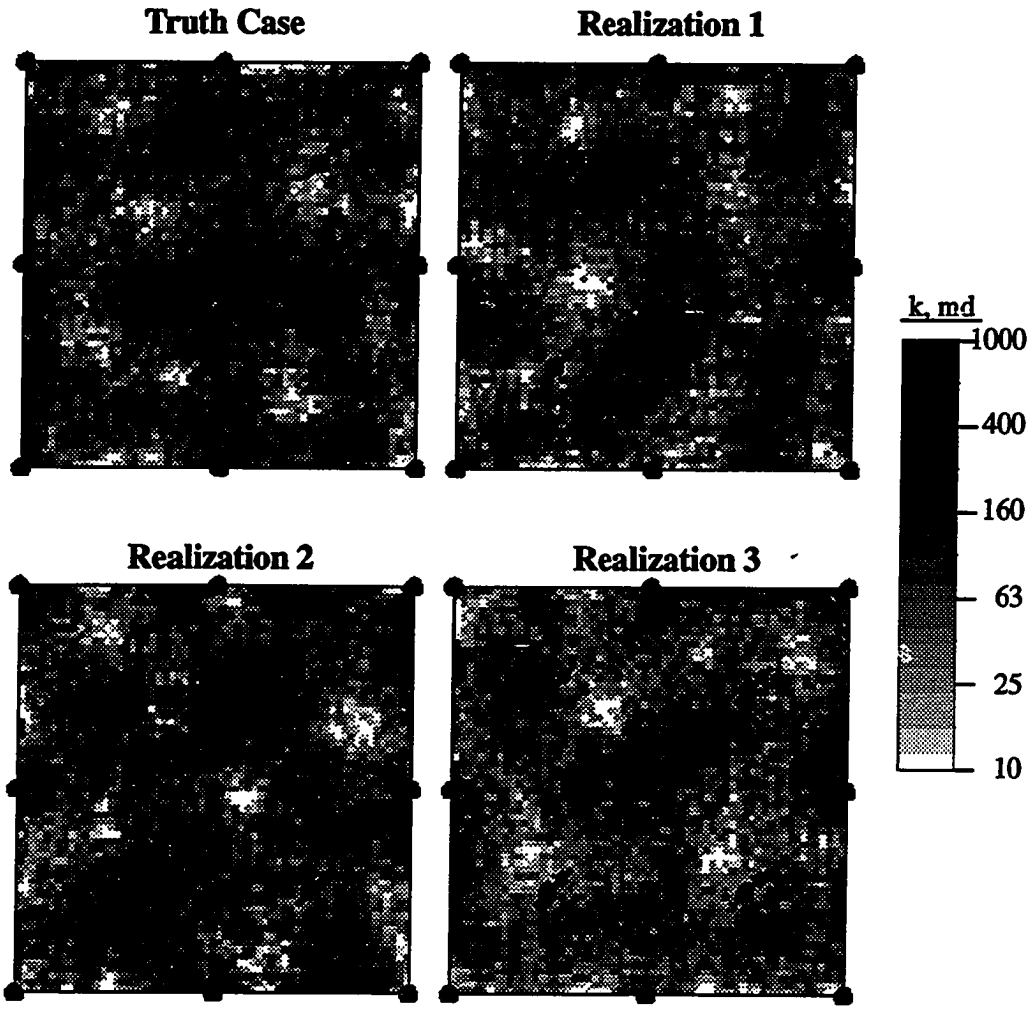

Figure 4.33 - Comparison of extended five-spot pattern truth case permeability field to three permeability fields generated using conventional conditional simulation constraints

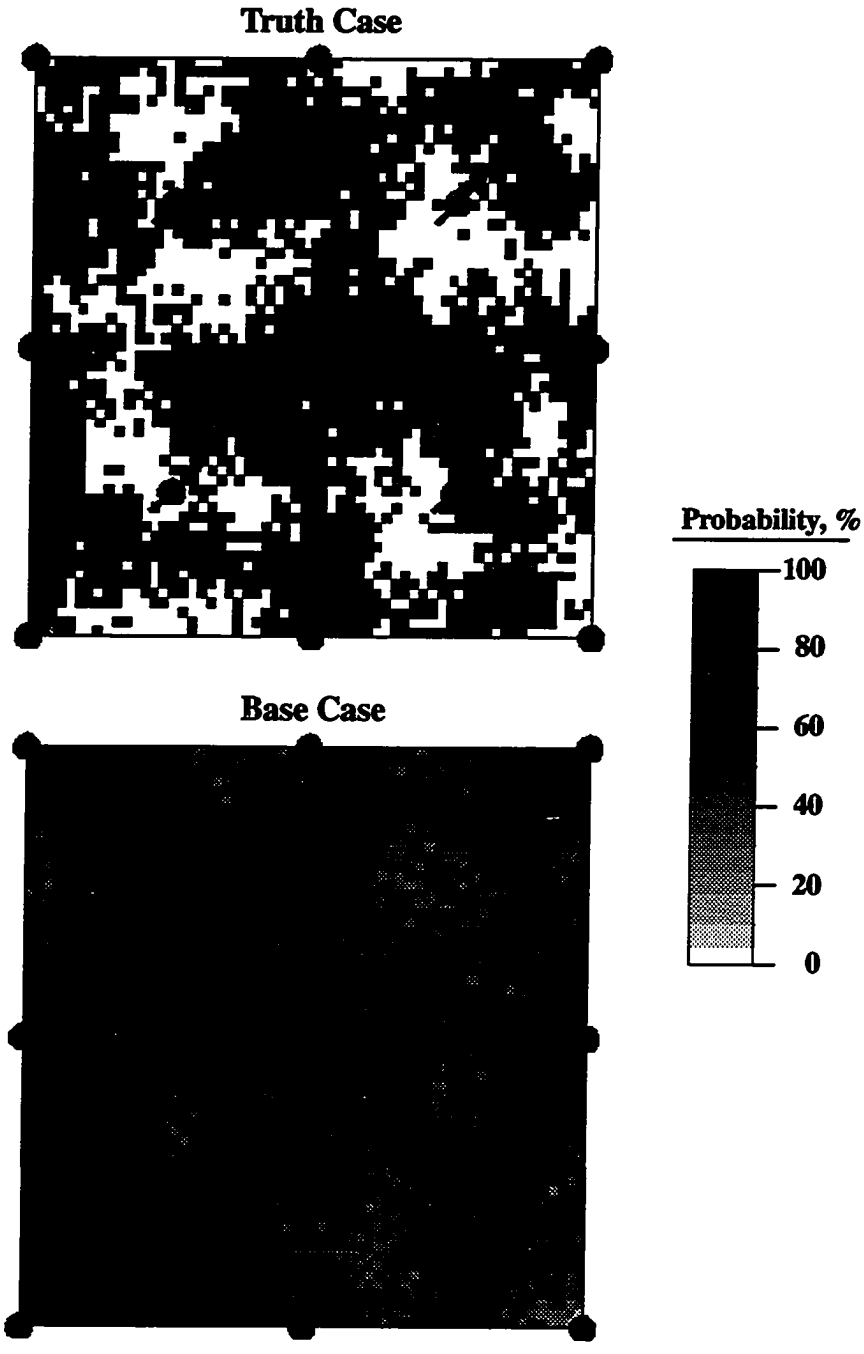

Figure 4.34 - Comparison of extended five-spot pattern probability of exceedance maps at the 30th permeability percentile cutoff for the truth case and base case (conventional constraints)

k_{NW}, CV_{k^*} and k_{PAT} Results

For comparison, 20 additional permeability realizations were generated using the conventional constraints and the three indirect performance constraints--k_{NW}, CV_{k^*} and k_{PAT}. The waterflood performance of these 20 permeability realizations are depicted in Figures 4.35 and 4.36. Also included in these figures are the results for the truth case. A comparison of these results to those obtained using conventional constraints (Figures 4.31 and 4.32) shows the added benefit of including the indirect performance constraints. The permeability realizations generated with the indirect performance constraints have waterflood performance characteristics very similar to the truth case. This is true for the central producer and the four offset injection wells. All available data--geological, petrophysical and production--are now being integrated into the reservoir description.

Three permeability realizations obtained using the three indirect performance constraints are compared to the truth case permeability field in Figure 4.37. Close inspection of these permeability images shows that most of the truth case high and low permeability regions are correctly reproduced by the three realizations. However, as would be expected considering the large number of unknowns, all three realizations do not perfectly reproduce the truth case permeability field. A probabilistic approach is still required to quantify uncertainty.

Probability of exceedance maps at the 30^{th} permeability percentile cutoff are compared in Figure 4.38 for the truth case and for the 20 permeability fields which were generated using all three indirect performance constraints. Unlike the probability map obtained using conventional constraints only (Figure 4.34), very high and very low probabilities are evident when the three indirect performance constraints are used. This can be considered as increased resolution compared to the base case results. The high and low probability regions are also spatially consistent with the truth case probability map.

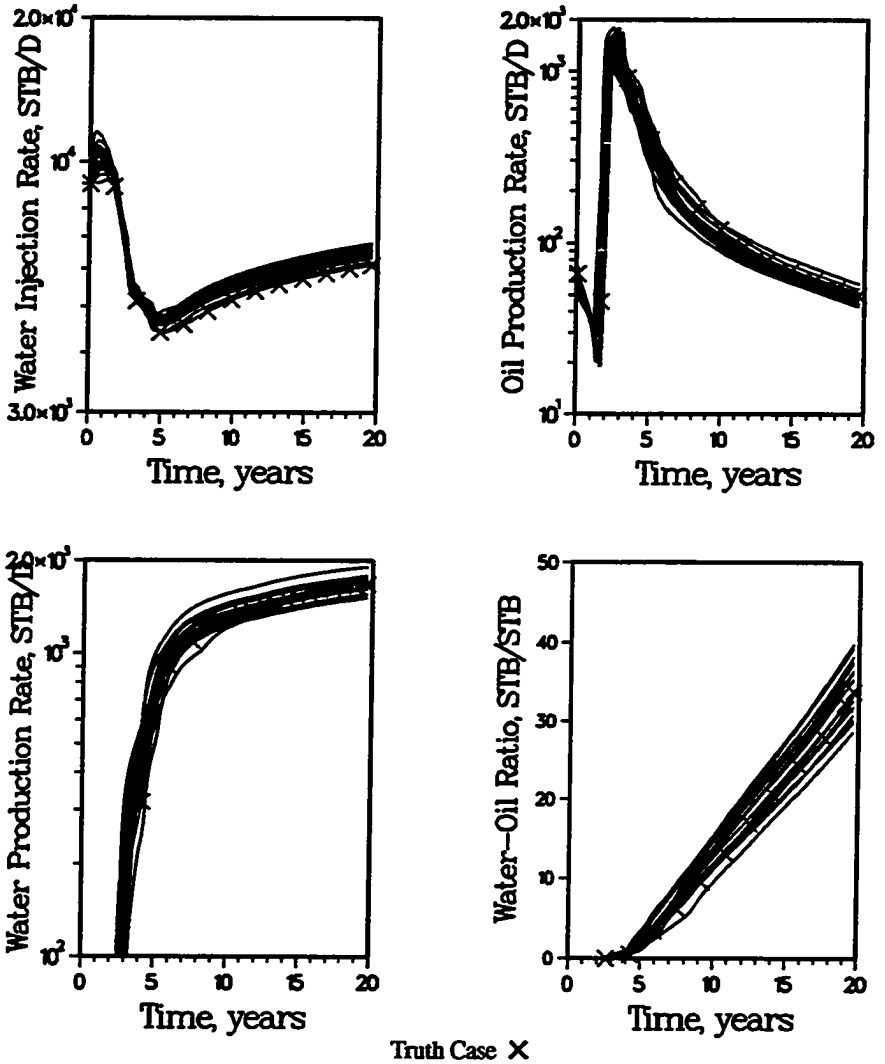

Figure 4.35 - Conventional and k_{NW}, CV_{k^*} and k_{PAT} indirect performance constraints case waterflood performance for the inner five-spot pattern wells; extended five-spot pattern study using the more heterogeneous permeability distribution

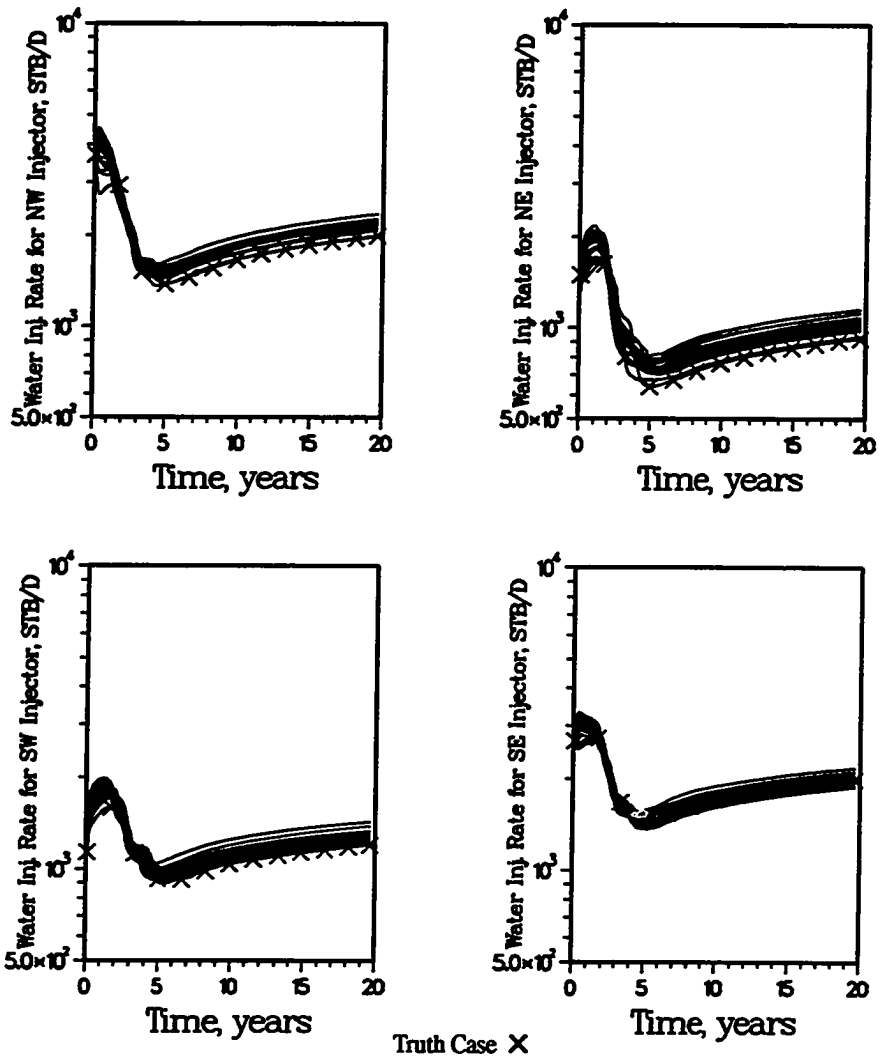

Figure 4.36 - Conventional and k_{NW}, CV_{k^*} and k_{PAT} indirect performance constraints case waterflood performance for the inner five-spot pattern injection wells; extended five-spot pattern study using the more heterogeneous permeability distribution

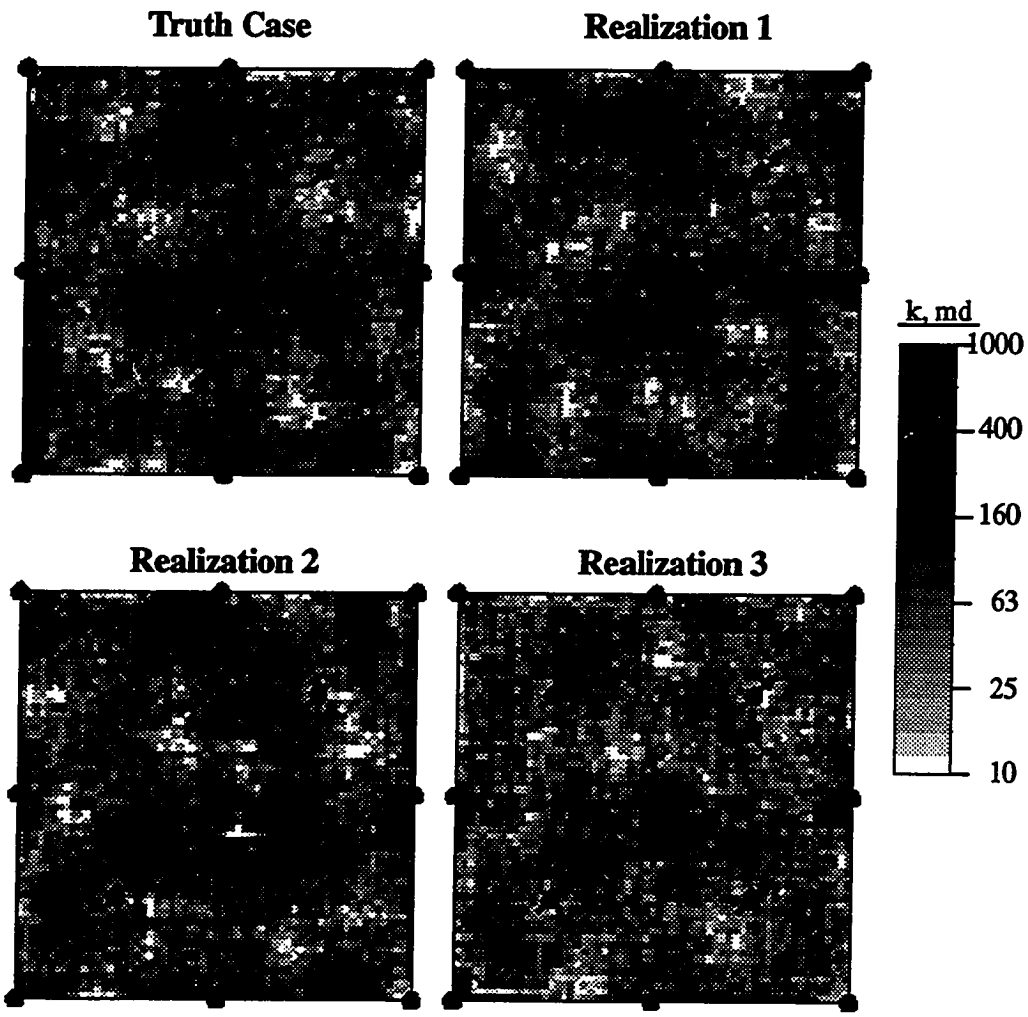

Figure 4.37 - Comparison of extended five-spot pattern truth case permeability field to three permeability fields generated using conventional and indirect performance constraints k_{NW}, CV_{k^*} and k_{PAT}

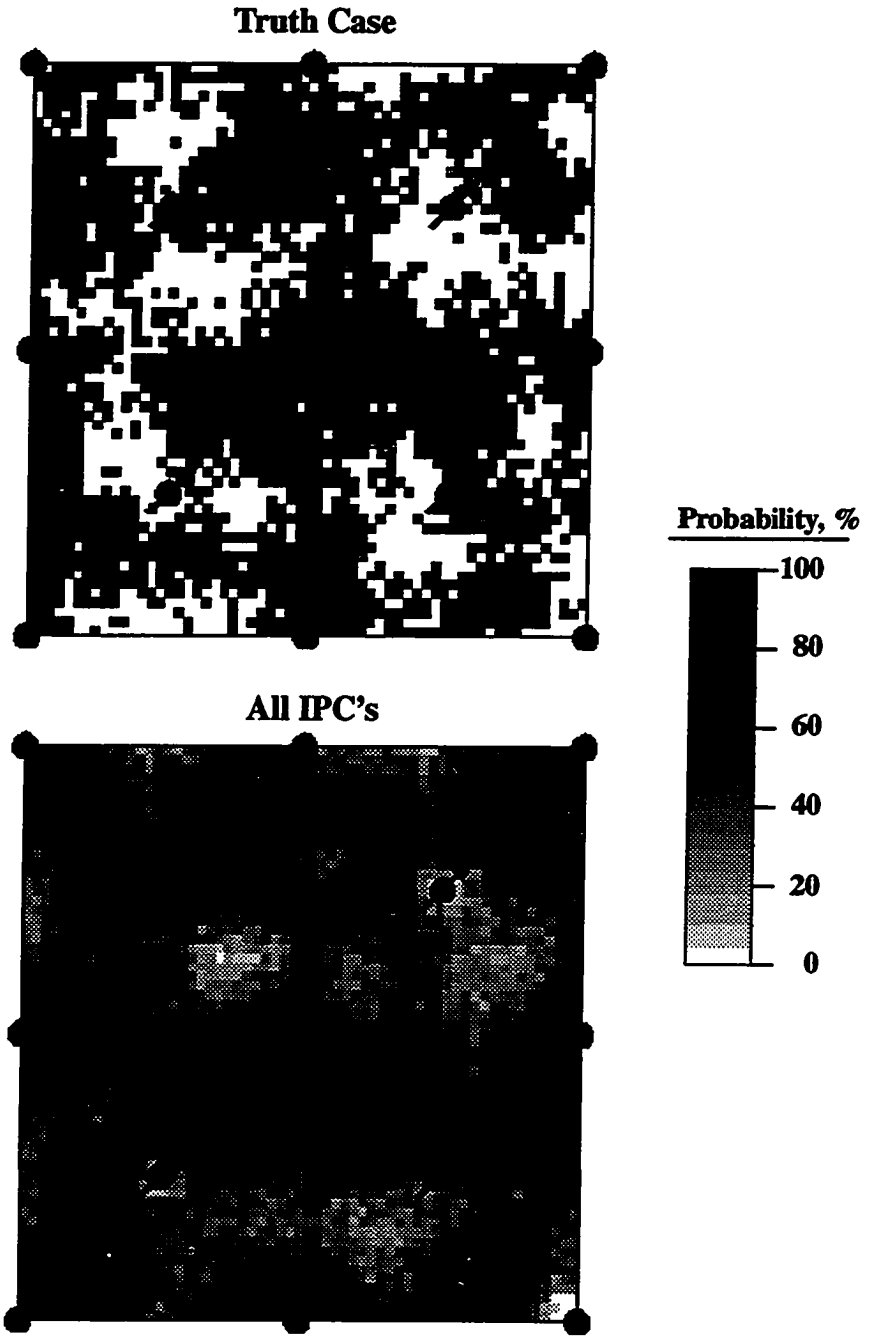

Figure 4.38 - Comparison of extended five-spot pattern probability of exceedance maps at the 30th permeability percentile cutoff for the truth case and k_{NW}, CV_{k^*} and k_{PAT} indirect performance constraints case

This represents an increase in accuracy compared to the conventional approach. Several regions are shown to have a 20 percent or less probability of exceeding the 30th permeability percentile. Since this is a low probability for exceeding a relatively low permeability value (61 md), these areas would be interpreted to have a high probability of being low permeability regions. Fortunately, these regions which were consistently simulated to have low permeabilities actually are low permeability regions in the truth case.

k_{NW} and CV_{k^*} Results

It was previously concluded that inclusion of the k_{PAT} constraint would reduce the spread in simulated waterflood performance when large variations in the effective permeability of injector/producer regions of influence existed. To further examine this, permeability realizations were generated using the conventional constraints and the indirect performance constraints k_{NW} and CV_{k^*} (not k_{PAT}). The corresponding waterflood performance of the inner five-spot pattern wells are depicted in Figures 4.39 and 4.40. When comparing these results to those obtained using all three indirect performance constraints, there are many similarities. The only significant difference is the increased spread in water breakthrough times as a result of not including k_{PAT}. Water breakthrough times for the central producer range from 2.5 to 4.5 years when k_{PAT} is not included as a constraint (Figure 4.39) and from 2.5 to 3.2 years when k_{PAT} is included.

Figure 4.41 compares the truth case permeability field to three realizations obtained using the indirect performance constraints k_{NW} and CV_{k^*}. Inspection of these permeability fields shows that the truth case regions of high and low permeability are not as well reproduced as the permeability realizations shown in Figure 4.37. This is further demonstrated when comparing the probability of exceedance maps shown in Figures 4.38 and 4.42. Inclusion of the additional constraint k_{PAT} increases the size of the regions with low and high probability of exceeding the 30th permeability percentile cut-

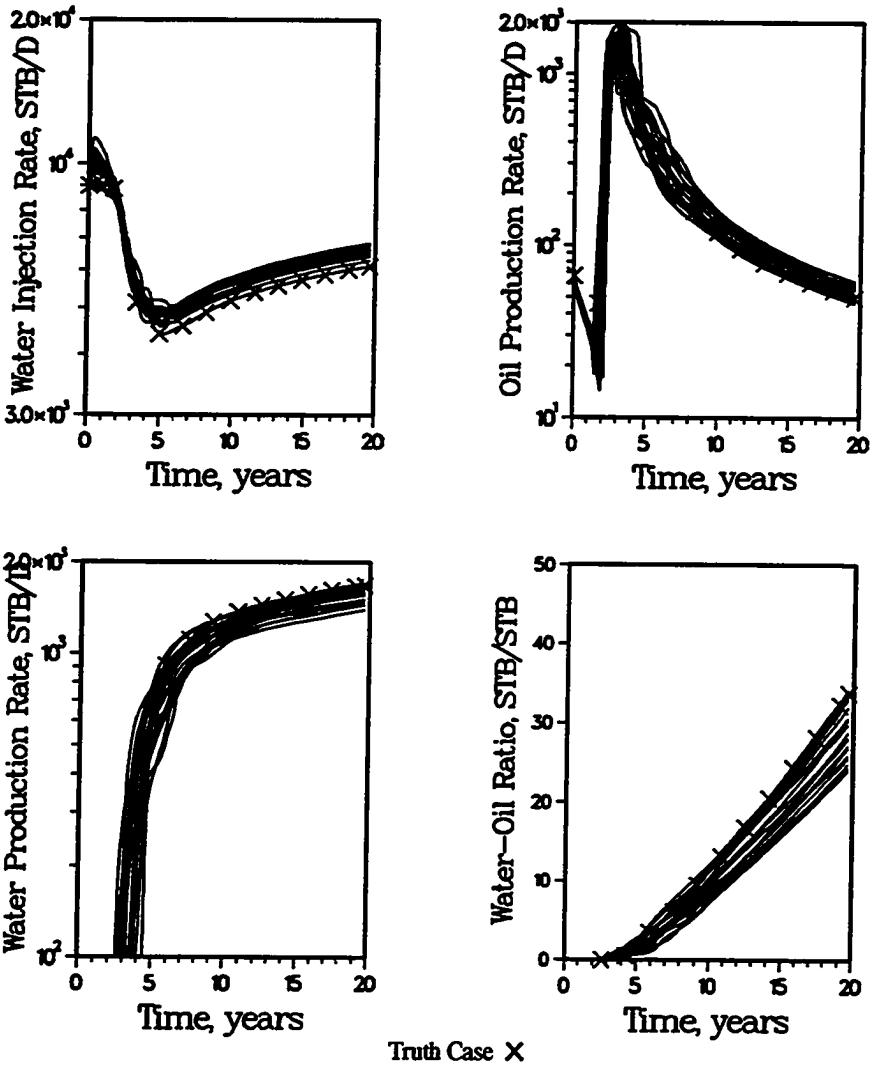

Figure 4.39 - Conventional and k_{NW} and CV_{k^*} indirect performance constraints case waterflood performance for the inner five-spot pattern wells; extended five-spot pattern study using the more heterogeneous permeability distribution

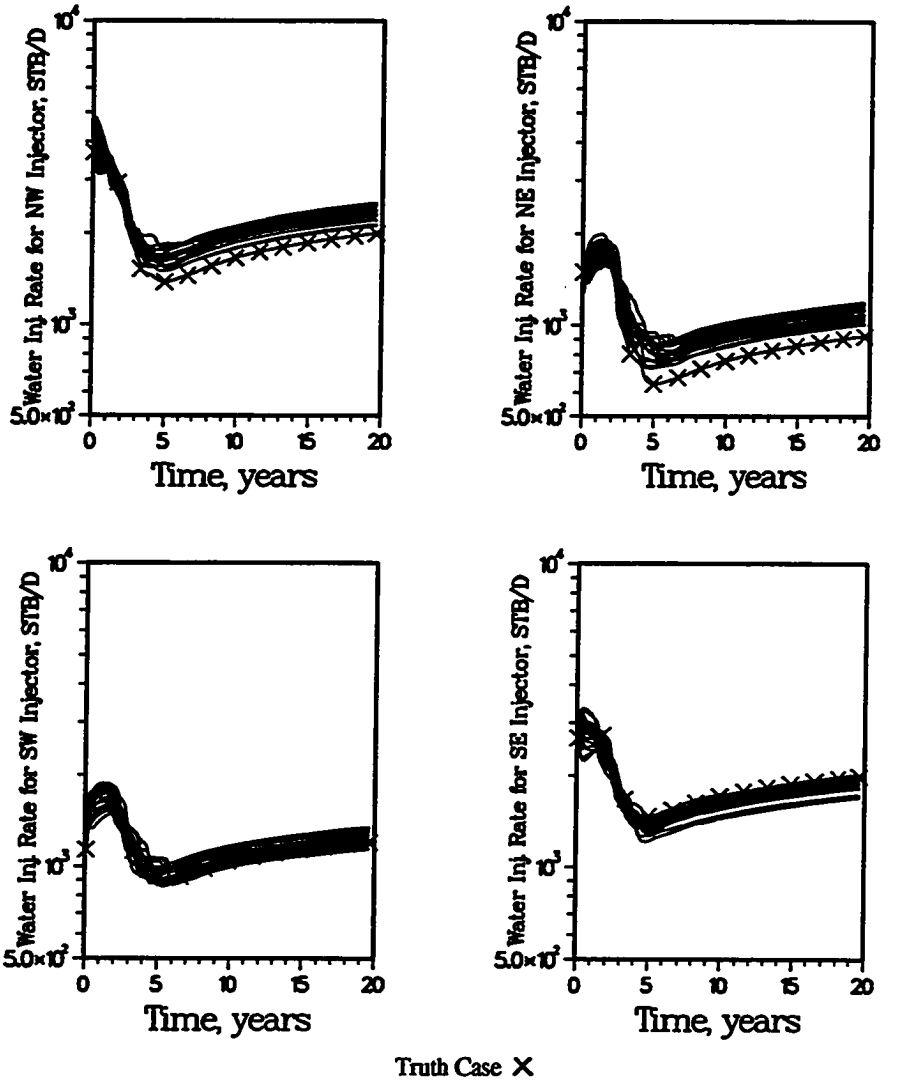

Figure 4.40 - Conventional and k_{NW} and CV_{k^*} indirect performance constraints case waterflood performance for the inner five-spot pattern injection wells; extended five-spot pattern study using the more heterogeneous permeability distribution

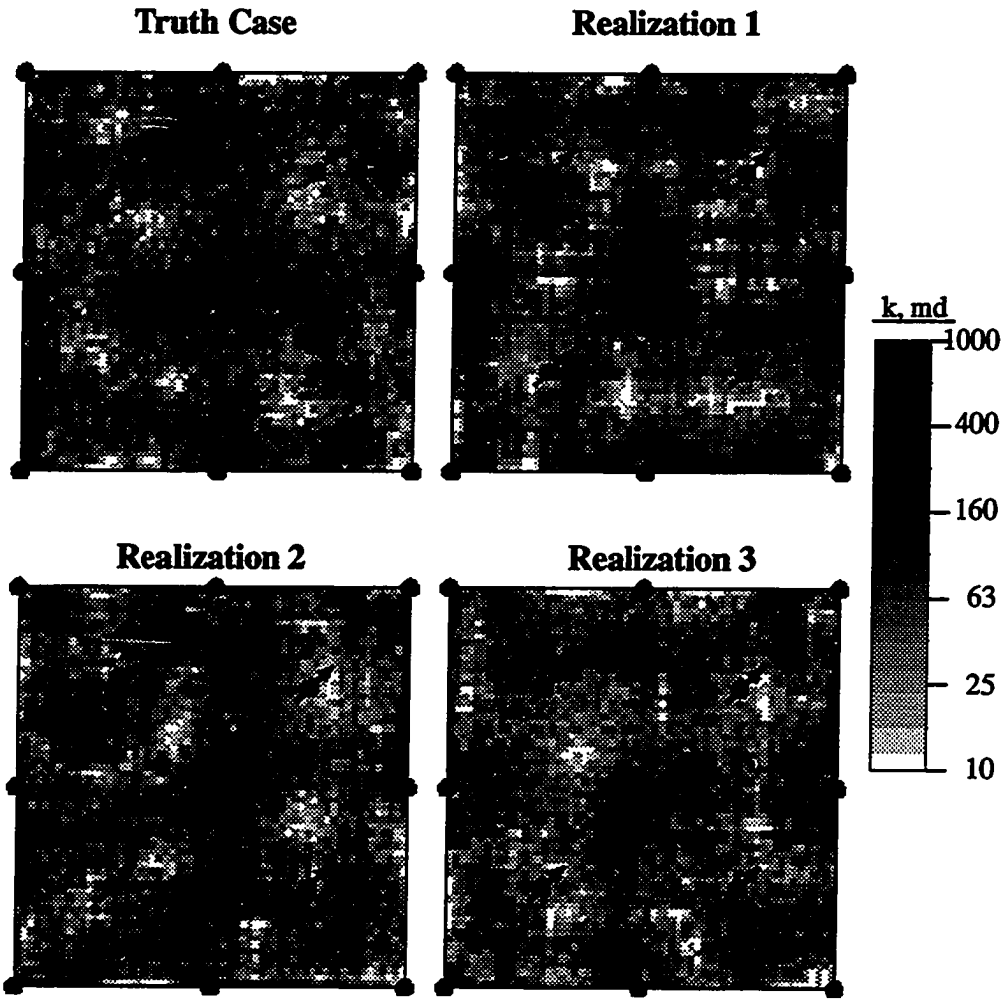

Figure 4.41 - Comparison of extended five-spot pattern truth case permeability field to three permeability fields generated using conventional and indirect performance constraints k_{NW} and CV_{k^*}

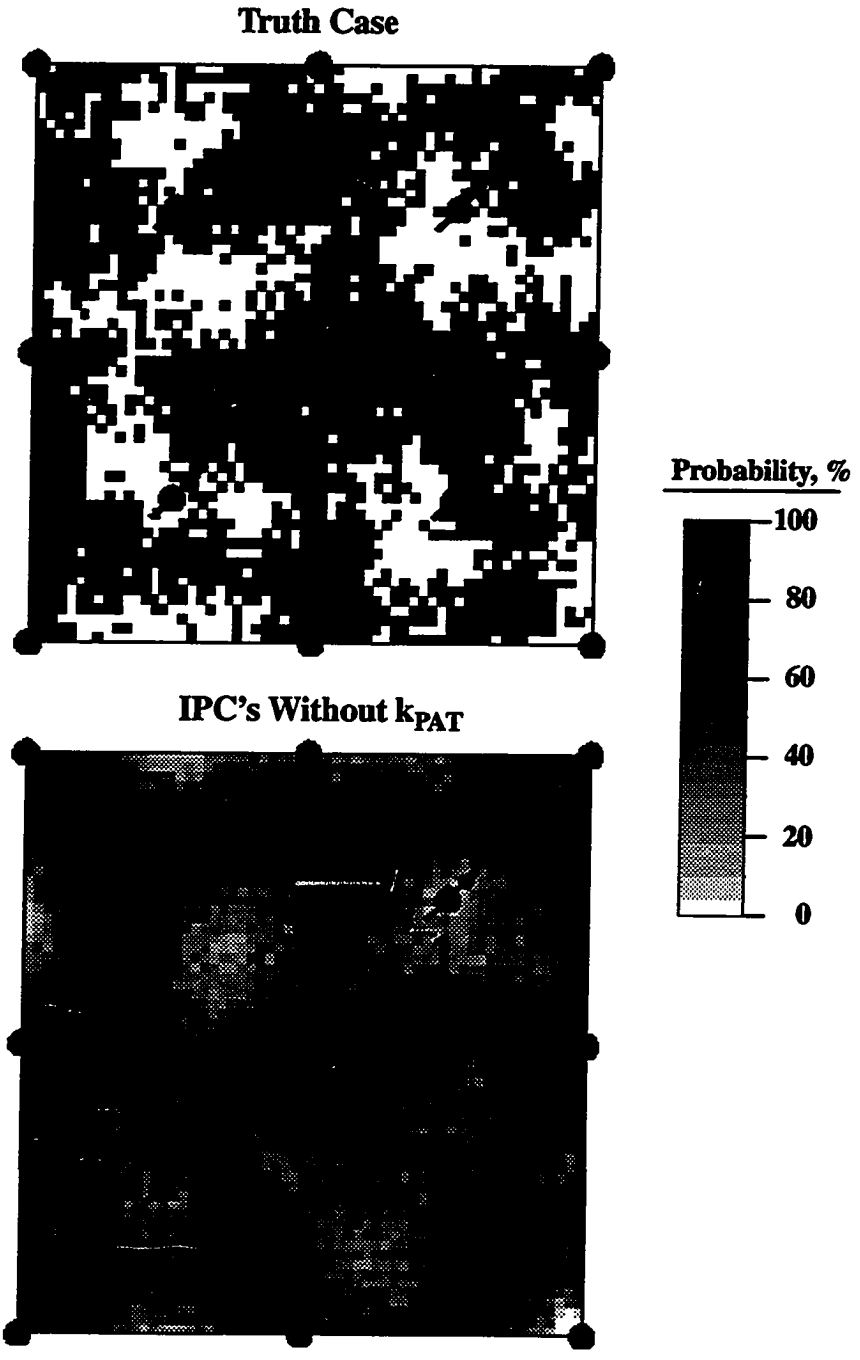

Figure 4.42 - Comparison of extended five-spot pattern probability of exceedance maps at the 30th permeability percentile cutoff for the truth case and k_{NW} and CV_{k^*} indirect performance constraints case

off. Again, this becomes important only when extreme variations in permeability occur within a waterflood pattern.

Indirect Performance Constraints Results Without Variogram Constraint

Considering the significant improvement obtained when including indirect performance constraints when generating permeability realizations, the necessity of the variogram constraint could be questioned. Realizing the difficulties involved in quantifying spatial correlation, especially for distances less than interwell distances, it would be of great benefit to eliminate its need. The time and money invested in acquiring and processing seismic data, studying outcrops and variogram analysis are very significant. The ability to extract spatial correlation characteristics from production data would greatly simplify reservoir characterization methodologies.

With this in mind, another synthetic case study was performed with all conventional and indirect performance constraints applied except for the permeability variogram constraint. As in previous case studies, the truth case properties were used to generate an additional 20 permeability realizations. Waterflood performance for the inner five-spot pattern wells for each realization and the truth case are shown in Figures 4.43 and 4.44. Note the extremely small spread in each performance curve and the good reproduction of the truth case performance. These results are actually better than any of the previous results (see Figures 4.31, 4.32, 4.35, 4.36, 4.39 and 4.40). The best reproduction is the oil production rate profile, of obvious importance. It can be concluded from these results that waterflood performance can be simulated and predicted into the future using the indirect performance constraints without the aid of the permeability variogram constraint. This assumes that operating conditions are not altered during the course of the waterflood.

Three of the 20 corresponding permeability realizations are depicted in Figure 4.45 and compared to the truth case permeability field. The absence of spatial correlation is

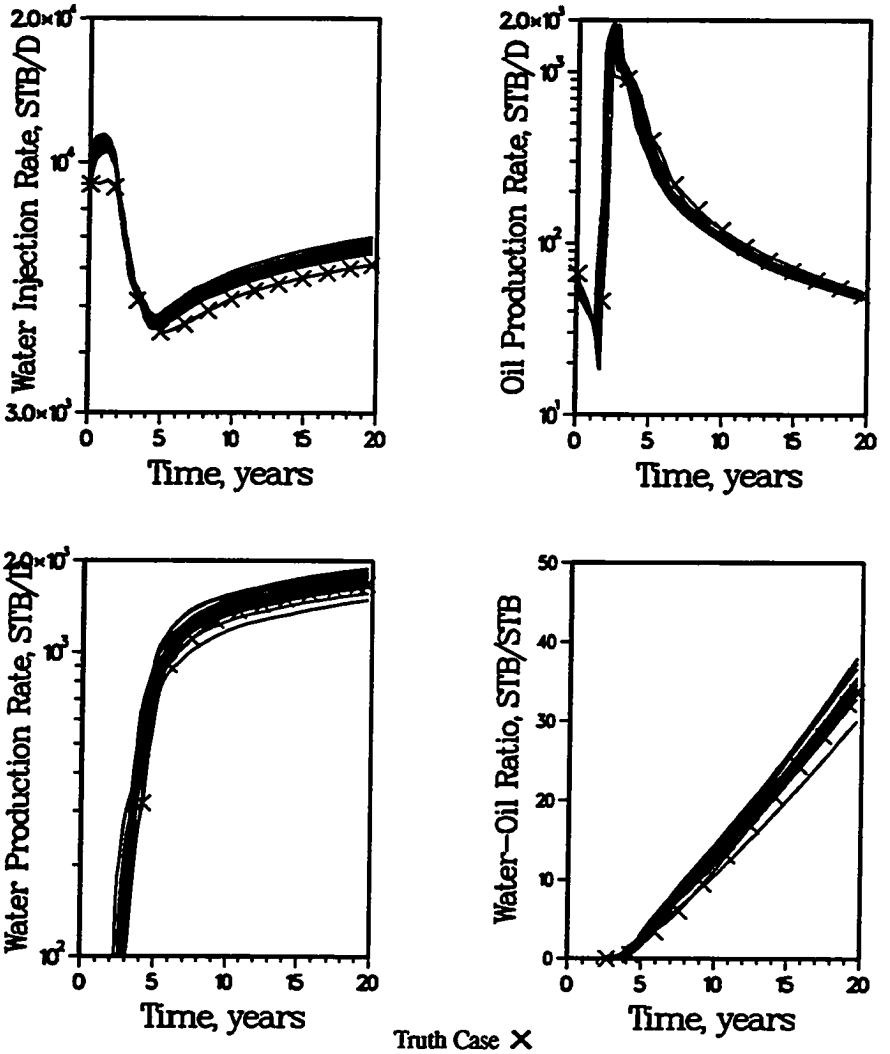

Figure 4.43 - k_{NW}, CV_{k^*} and k_{PAT} indirect performance constraints without variogram constraint case waterflood performance for the inner five-spot pattern wells; extended five-spot pattern study using the more heterogeneous permeability distribution

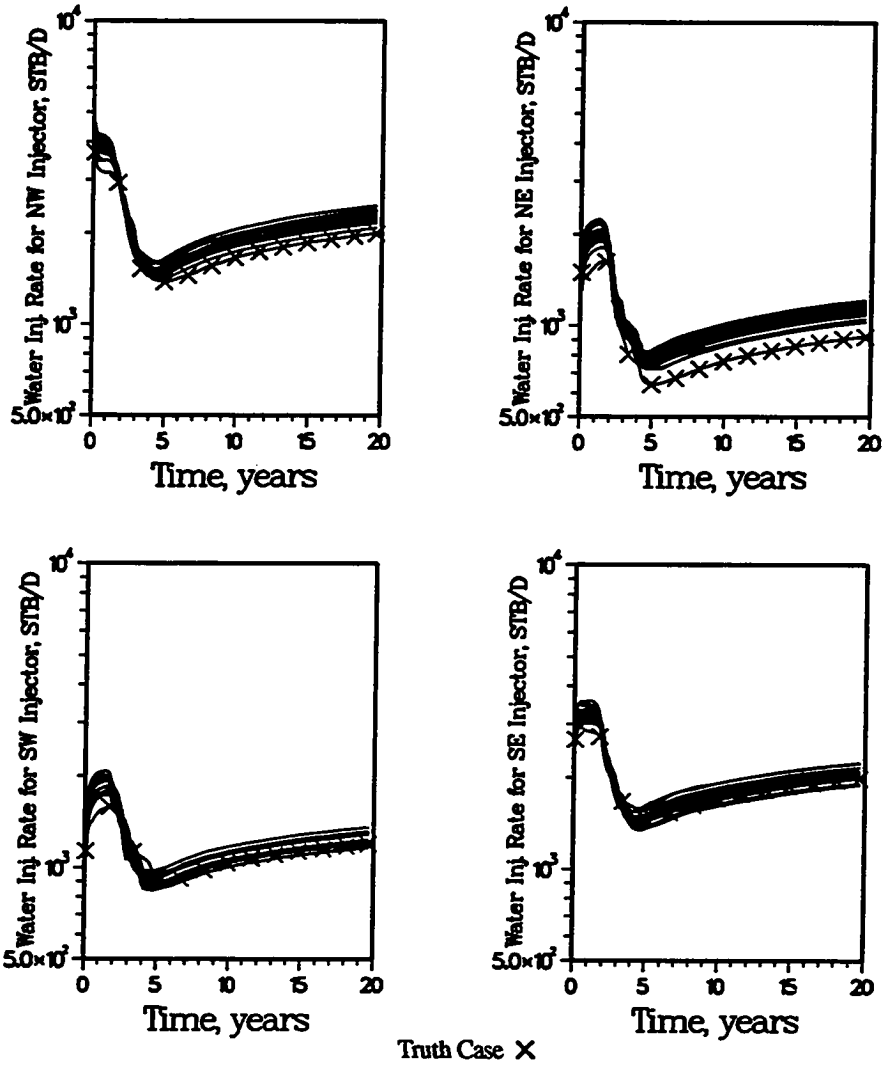

Figure 4.44 - k_{NW}, CV_{k^*} and k_{PAT} indirection performance constraints without variogram constraint case waterflood performance for the inner five-spot pattern injection wells; extended five-spot pattern study using the more heterogeneous permeability distribution

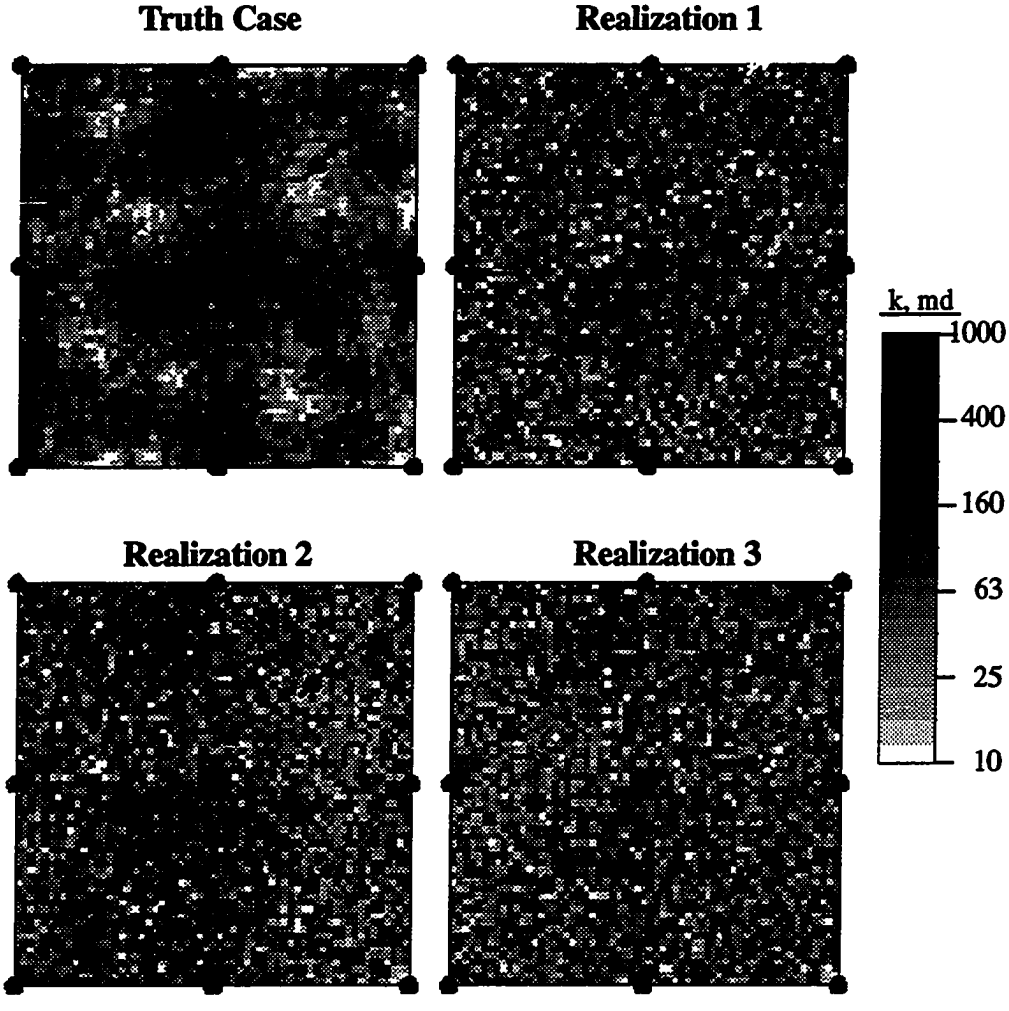

Figure 4.45 - Comparison of extended five-spot pattern truth case permeability field to three permeability fields generated using indirect performance constraints k_{NW}, CV_{k^*} and k_{PAT} but not including variogram constraint

obvious in each of the three realizations. In fact, the realizations appear almost to be completely random in nature. It is very surprising that these permeability fields are characterized by essentially the same waterflood performance as the truth case. The lack of similarities between the truth case and the 20 permeability realizations is further demonstrated when comparing the respective probability of exceedance maps (Figure 4.46). This synthetic case study is a good example of the problem of non-uniqueness encountered in history matching simulation studies. An unlimited number of permeability fields, similar to the three included in Figure 4.45, can be generated having the same waterflood performance as the truth case but possessing extremely different spatial properties.

An important point to make is that these results all assume there aren't any changes in the operating conditions. If the above approach (i.e., no variogram constraint) was used to obtain a reservoir description via history matching waterflood performance, the success of the study would be totally dictated by the objectives. For example, if the study was being performed just to predict future waterflood rates and recoveries under existing operating conditions, it appears that the above approach should give realistic results. However, if the above approach was being used to develop a reservoir description for determining the optimum recovery scheme for future operations, the resulting conclusions could be misleading.

Oil saturation maps were generated to further compare the fluid flow performance of the truth case and the permeability fields derived without the variogram constraint. The maps depicted in Figures 4.47 and 4.48 correspond to the Truth Case and Realization 2 results (see Figure 4.45 for permeability fields), respectively, at four flow simulation times. Although differences do exist between the two cases, they do not appear to be extremely significant. Subsequent flow simulation of other operating schemes (infill drilling, tertiary recovery) would have to be investigated to determine the significance of these differences. Other scenarios can be envisioned which may result in more diverse

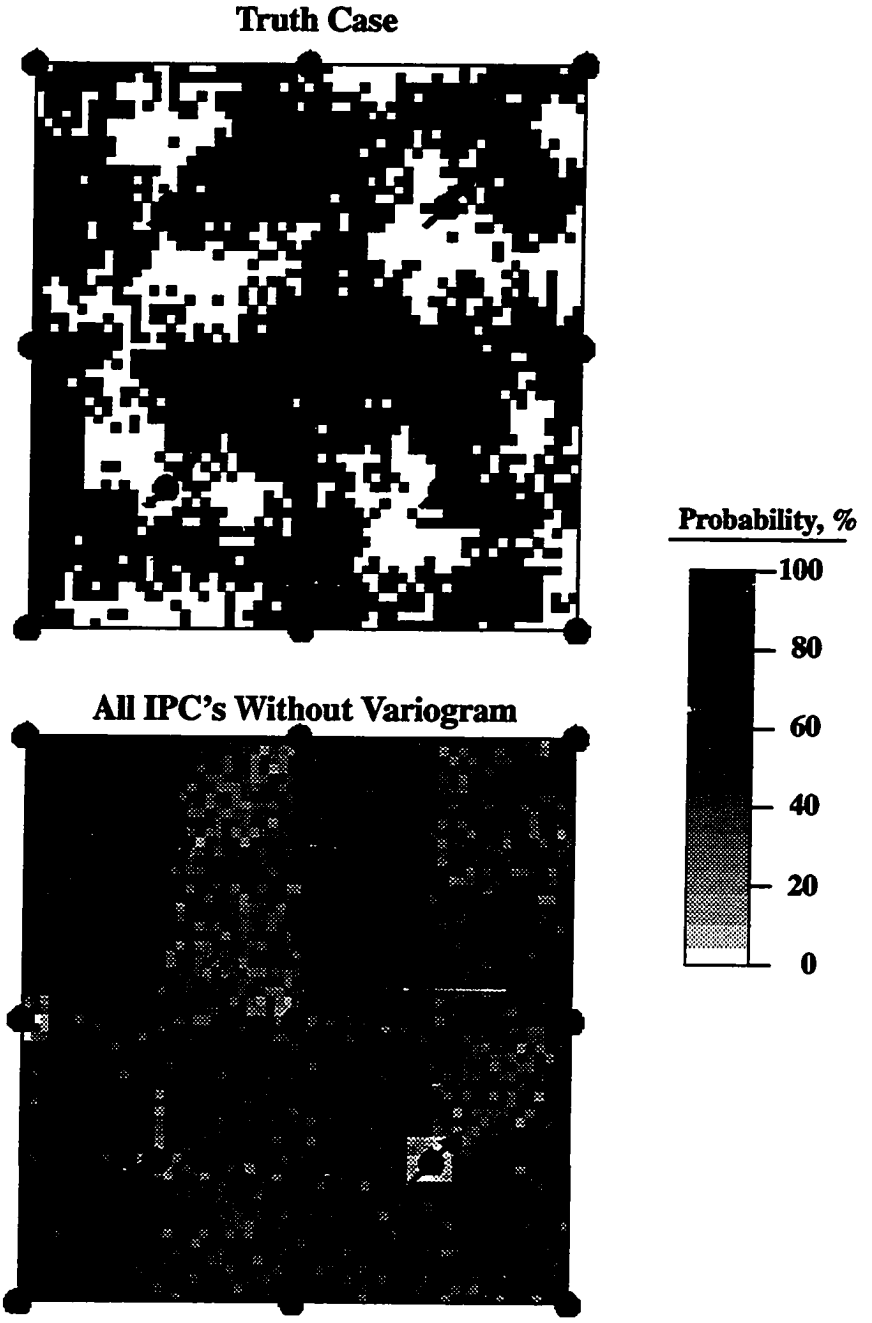

Figure 4.46 - Comparison of extended five-spot pattern probability of exceedance maps at the 30th permeability percentile cutoff for the truth case and k_{NW}, CV_{k^*} and k_{PAT} indirect performance constraints without variogram constraint case

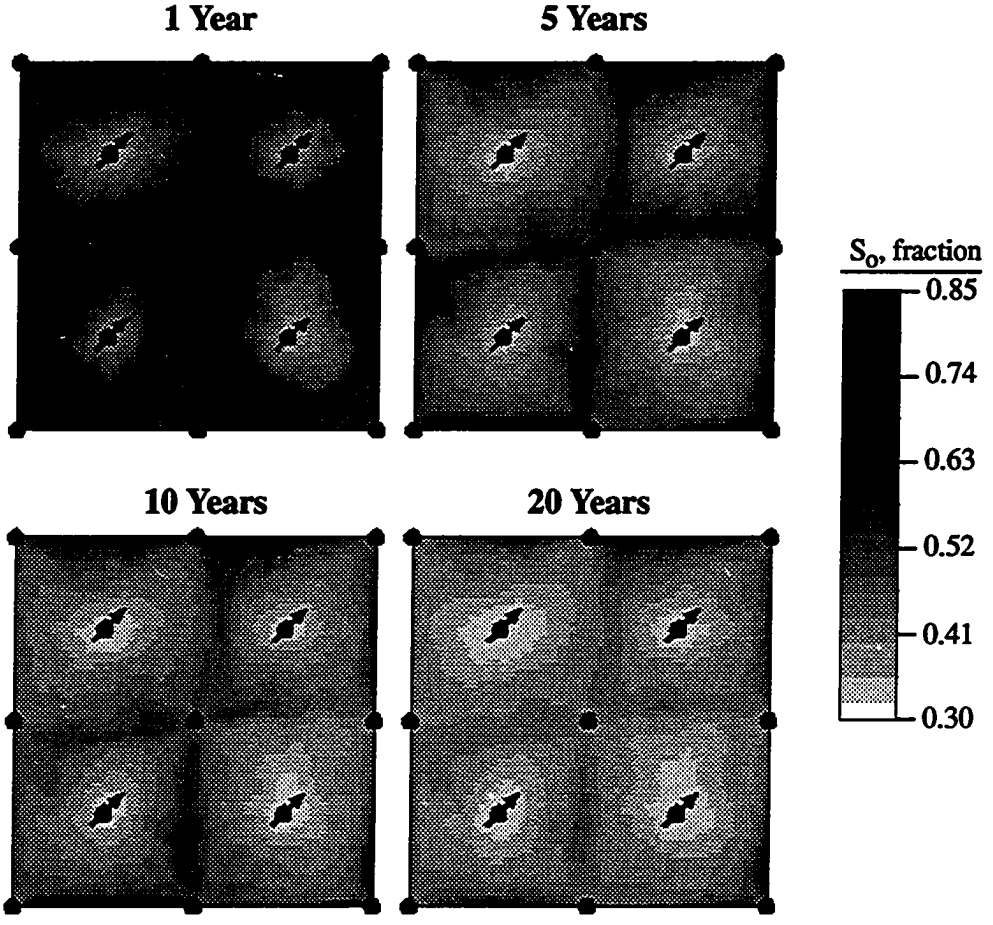

Figure 4.47 - Oil saturation maps for extended five-spot pattern truth case after waterflooding for 1, 5, 10 and 20 years

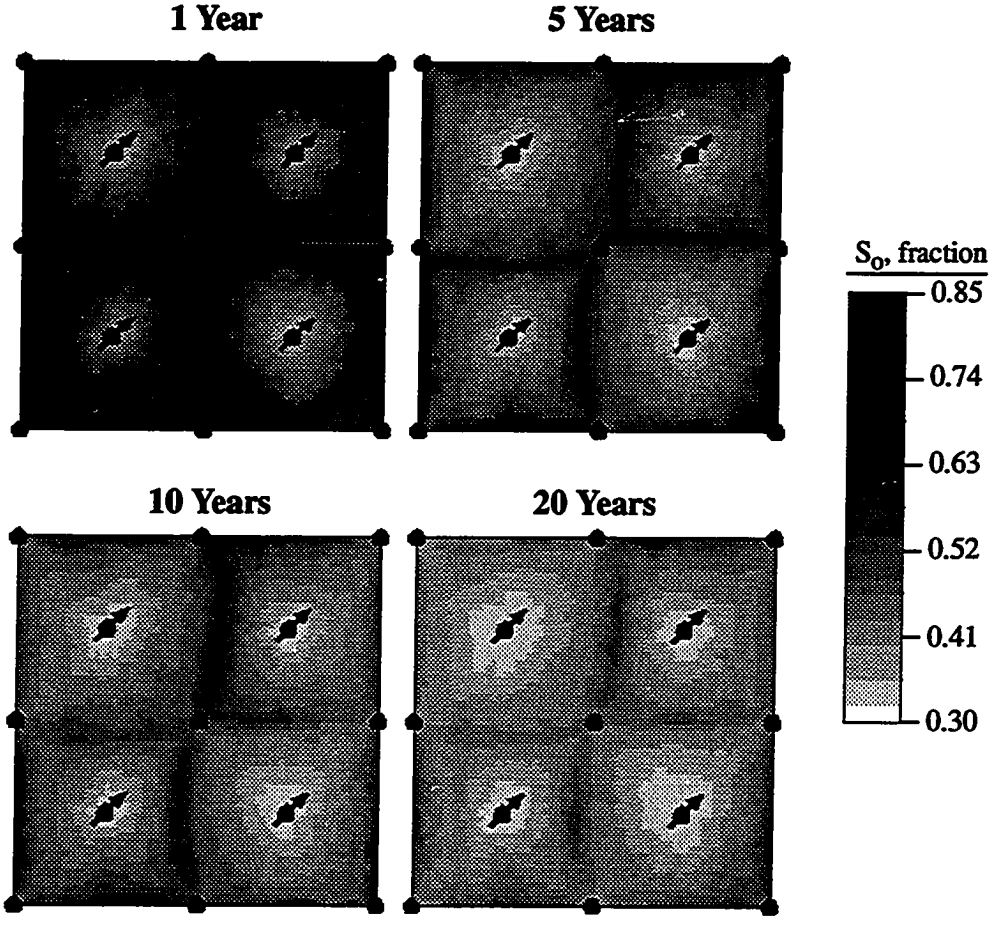

Figure 4.48 - Oil saturation maps for extended five-spot pattern Realization 2 (see Figure 4.45 for permeability field) after waterflooding for 1, 5, 10 and 20 years

results, such as the inclusion of extremely low permeabilities (i.e., unfloodable grid blocks) and modeling of regions encompassing much more than 13 wells. Neglecting the permeability variogram constraint creates permeability fields in which low and high permeability grid blocks are intermixed. This would probably result in optimistic recoveries for reservoirs characterized by large areal regions of low permeability.

This particular synthetic waterflood case study emphasizes the value of geological information when characterizing a reservoir. Geological information, as represented by the variogram, is essential if the objective is to obtain a realistic spatial description of reservoir properties. This sort of information cannot be extracted from production data alone.

Summary of Results

Waterflood performance was shown to be more sensitive to reservoir heterogeneities than primary recovery. The reservoir characteristic identified as having the biggest impact on waterflood recovery efficiency was reservoir connectivity. Two reservoir connectivity parameters were defined, p_{tH} and CV_{k*}. The latter connectivity parameter was found to give better results when used as a conditional simulation constraint. The parameter CV_{k*} was determined to correlate strongly with water breakthrough time and cumulative water-oil ratio.

One-quarter five-spot pattern flow simulations were used to show that so-called "equally probable" realizations of permeability generated using conventional conditional simulation constraints were found to result in widely varying simulated well performance. When the CV_{k*} constraint was combined with conventional constraints and a near well effective permeability constraint (referred to as "indirect performance constraints"), the resulting permeability realizations exhibited very similar simulated waterflood performance. Probability of exceedance maps were used to determine the effectiveness of conventional and indirect performance constraints in reducing the uncer-

tainty in spatial distributions of reservoir permeability. The indirect performance constraints were shown to significantly reduce the uncertainty in identifying high and low permeability regions.

Full five-spot pattern flow simulations of heterogeneous permeability fields appeared to be anomalously affected by the orthogonal no-flow boundaries imposed by the numerical model. It was concluded that the edge grid block permeabilities overly influenced simulated waterflood performance.

Extended five-spot pattern simulations were performed to evaluate the effectiveness of the indirect performance constraints given the interaction of multiple injector/producer pairs. It was discovered that an additional indirect performance constraint, k_{PAT}, may be required for multiple injector/producer systems. This parameter becomes important when the average permeability for neighboring injector/producer areas of influence varies significantly. Permeability realizations generated using conventional constraints were found not to provide any assistance in identifying low and high permeability regions. Inclusion of the indirect performance constraints greatly reduced the uncertainty in spatial properties. An interesting discovery was that permeability fields could be generated having very similar waterflood performance by using the indirect performance constraints without including the variogram constraint. However, the resulting permeability realizations were nearly spatially random and poorly reproduced the desired spatial distribution of high and low permeabilities. It was concluded that spatial correlation structures cannot be inferred from production data; such information must be obtained from geological inferences.

CHAPTER V

TWO-DIMENSIONAL FULL-FIELD STUDY

Introduction

Previous chapters investigated the impact porosity or permeability heterogeneities have on primary and/or secondary performance. Only one petrophysical parameter was varied at a time; all others were assumed to be constant. Simulations were performed for limited areal coverage. Thus, only local spatial heterogeneities were considered. The impact of global trends superimposed on local variations were not addressed. The work included in this chapter has been performed to investigate these additional complications.

After summarizing the procedure used to generate the two-dimensional (2D) full-field truth case, its exhaustive reservoir properties will be described. Univariate and spatial statistical properties of the exhaustive data set will be compared with well values to identify important differences which directly impact conditional simulation results. Truth case field and well performance are then compared to results obtained using varying degrees of available well performance data, most notably primary performance constraints versus primary and secondary performance constraints. Such a comparison illustrates the relative importance of the various constraints. This is important information considering certain performance constraints are obtainable only during specific phases of a well's life and are known with different degrees of certainty.

Procedure

The 2D full-field reservoir description was generated by combining properties from Flow Units 3, 4 and 5 of the 3D Truth Case described in Chapter II. Recall that these

three flow units represent the main sand body and thus dominate the reservoir performance for the 3D Truth Case. The spatial distribution of sand thickness was obtained by summing the thicknesses of Flow Units 3, 4 and 5. Porosity values were obtained using thickness-weighted arithmetic averages from these same three flow units. Permeabilities were determined using a permeability-porosity correlation. Exhaustive reservoir properties were not defined on the fine-scale, but using flow simulation grid block dimensions of 220 ft by 220 ft. The total number of conditional simulation and flow simulation grid blocks were 3888 (108 by 36) for the 4.5 mile by 1.5 mile system. Conditional simulations were performed using large grid blocks to make the study more manageable considering the large number of realizations and flow simulations generated. It is not believed that this "compromise" invalidated the results of the full-field study.

The study assumed conditioning data included well grid block porosities and sand thicknesses. Variograms for these two variables were estimated from the well data. It was also assumed that the grid block scale permeability-porosity correlation was known. The spatial distribution of sand thickness was obtained using the well data derived variogram and kriging. Unlike the spatial distributions of permeability and porosity, kriged sand thickness results were assumed to adequately represent the actual reservoir, i.e., the sensitivity of reservoir performance on alternative sand thickness realizations was not investigated. Either well block porosities or permeabilities could be specified as conditioning data since a unique correlation between the two parameters was assumed. Swapping of paired values during the simulated annealing process required updating each objective function component because of the interdependency of porosity and permeability. The simulated annealing algorithm used for the full-field study is illustrated in Figure 5.1. Additional information regarding the conditional simulation program developed for performing this case study is included in Appendix B.

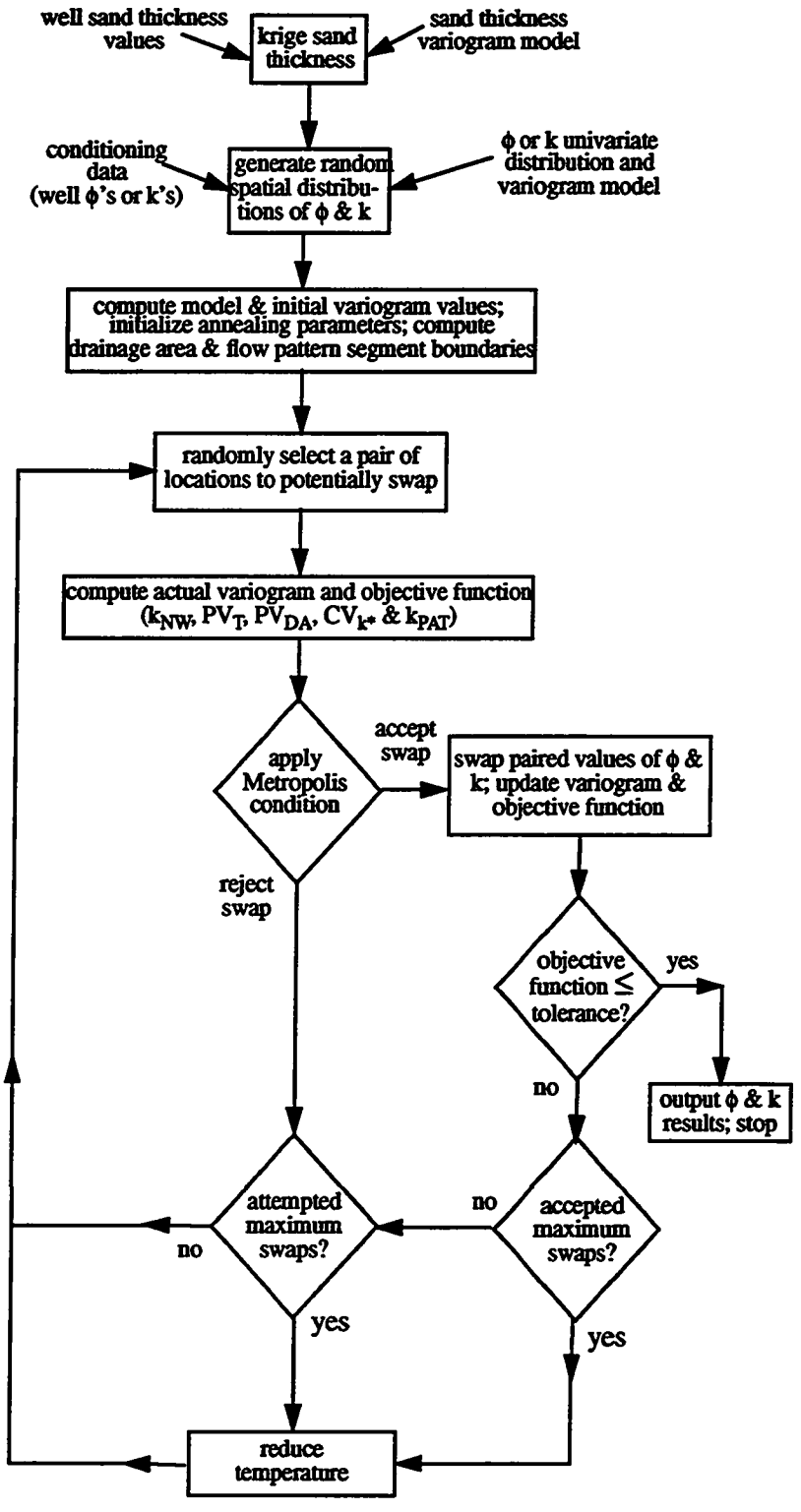

Figure 5.1 - Flow diagram of simulated annealing algorithm for the full-field study

Exhaustive Reservoir Properties

Univariate and Bivariate Distributions

A histogram of pay thickness for the 2D full-field truth case is shown in Figure 5.2. Grid block thicknesses range from 14 to 72 ft with the mean thickness equaling 36.4 ft. Thickness values are essentially normally distributed having a standard deviation of 10.4 ft. Half of the thickness values fall between 29 and 44 ft. Grid block porosities range from 0.12 to 0.28 (Figure 5.3). Porosities are also normally distributed having a mean of 0.204 and a standard deviation of 0.027. The porosity interval 0.185 to 0.224 includes the middle 50 percent of the overall range. The linear regression coefficients of Flow Unit 3 log(permeability) vs. porosity core data were used to generate permeability values. The permeability histogram derived from the porosity values and the log(permeability) vs. porosity correlation is depicted in Figure 5.4. The log-normally distributed permeabilities range from less than 1 md to more than 300 md. Approximately 75% of the permeability values are 100 md or less.

Spatial Correlations

The experimental variogram for sand thickness of the truth case grid block values is shown in Figure 5.5. Two directional variograms are illustrated--one at N90°E, the major direction, and the other along the minor direction of N0°E. The sand thickness correlation length along the major direction is about 12,000 ft. This is about three times the correlation length of the minor direction. The nugget effect is essentially zero. Directional experimental porosity variograms are contained in Figure 5.6. A correlation length in excess of 12,000 ft exists in the major direction of N90°E. The porosity variogram has an anisotropy ratio of about 5 with the minor direction of N0°E having a correlation length of only 3000 ft. A nugget of about 20 percent exists for the variogram.

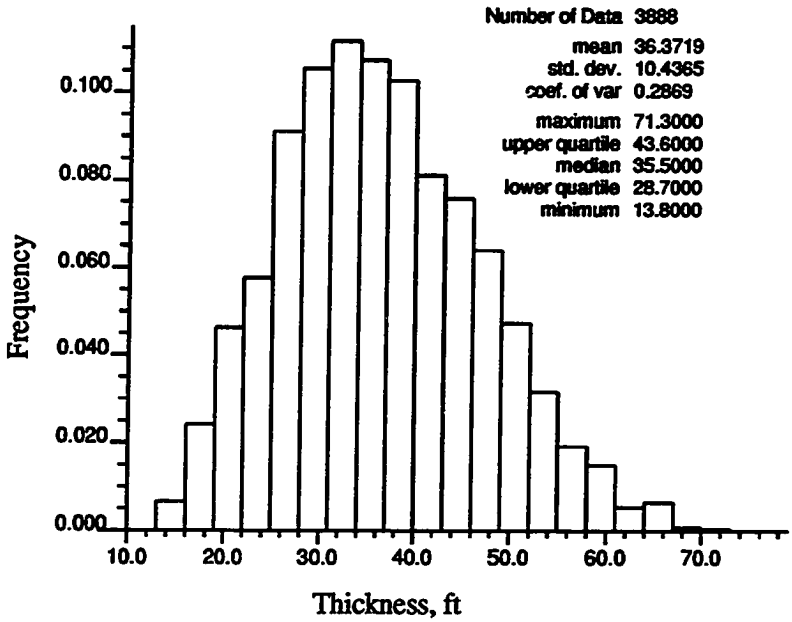

Figure 5.2 - Pay thickness histogram for the full-field truth case

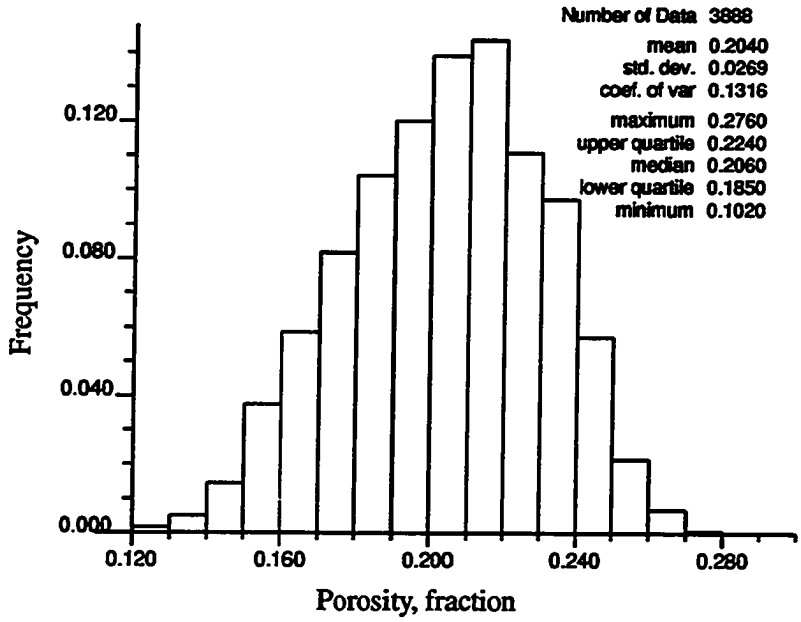

Figure 5.3 - Porosity histogram for the full-field truth case

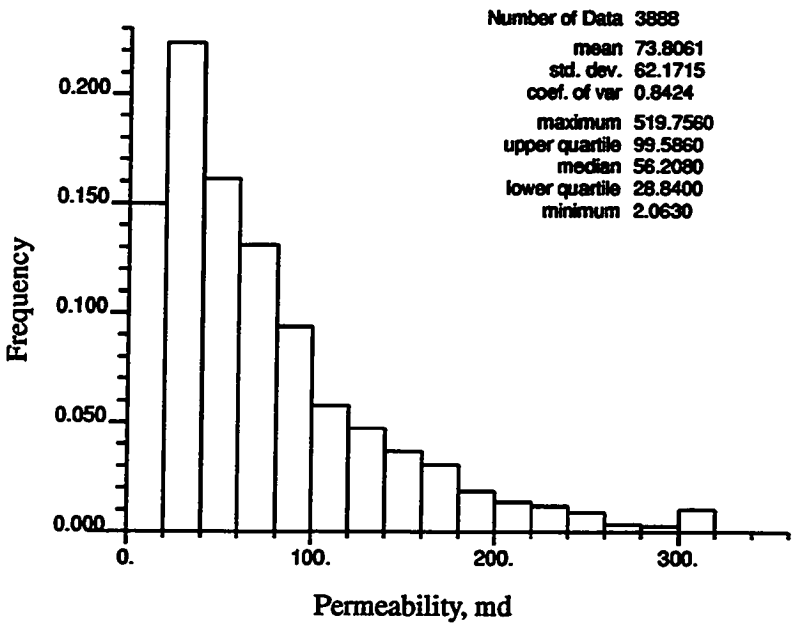

Figure 5.4 - Permeability histogram for the full-field truth case

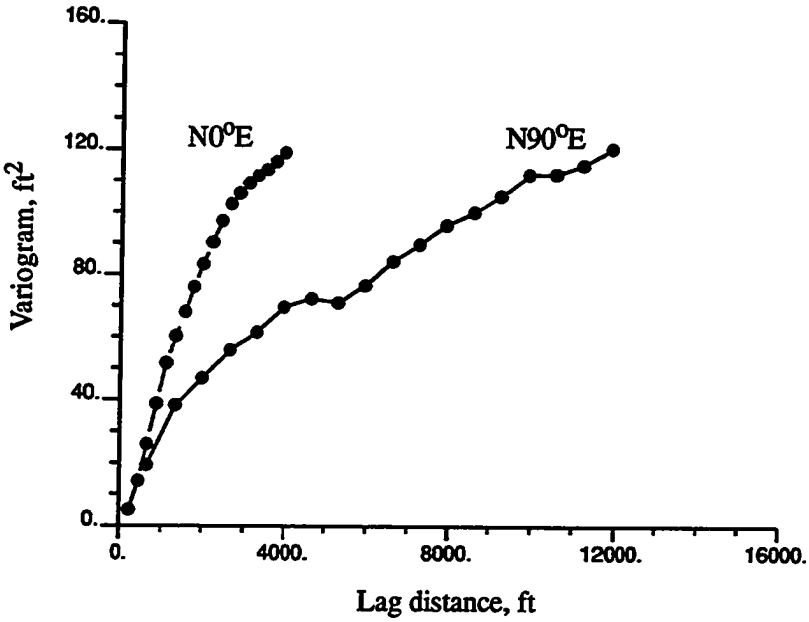

Figure 5.5 - Variogram for sand thickness; full-field truth case

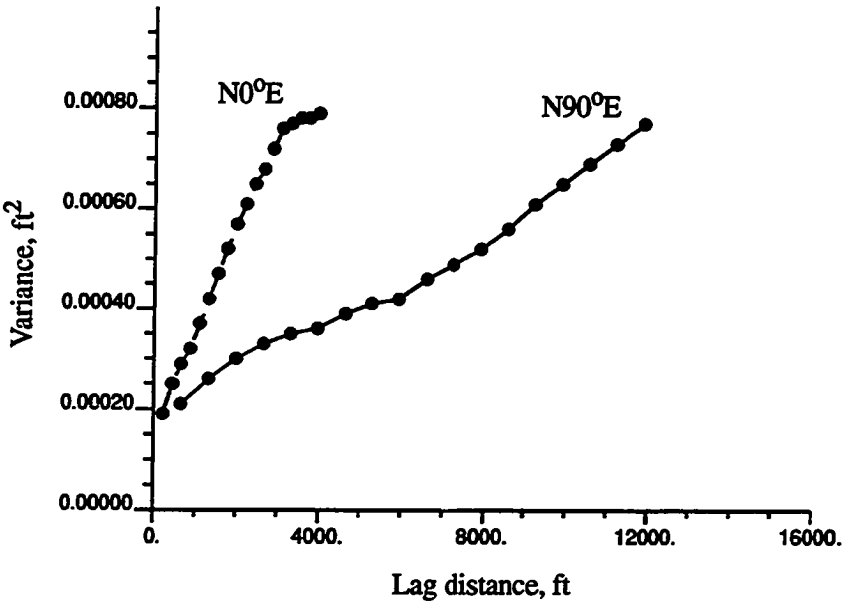

Figure 5.6 -Variogram for porosity; full-field truth case

Spatial Properties

Figure 5.7 contains a map of pay thickness for the full-field truth case. Locations of the 59 wells are also included in the figure. Sand thickness is seen to be greatest in the northwest and thinnest to the southwest and east-central. Although the strong east-west correlation is evident in many areas of the field, some areas (e.g., the southeast region) is more isotropic. The exhaustive porosity field is depicted in Figure 5.8. Note the strong east-west directional trend. The average porosity on the west side is approximately 0.23, decreasing to about 0.17 on the east side. The strong porosity trend branches off to the northeast and southeast near the east end of the field. Since permeabilities are derived directly from porosities, the spatial distribution of permeability is very similar to porosity. The exhaustive permeability field is shown in Figure 5.9. Large regions containing average permeabilities in excess of 200 md exist on the west side of the field. Much of the southwest and northeast contain average permeabilities in the 25 md range.

Well Derived Reservoir Properties

The 2D full-field case study was performed assuming that well block porosity, permeability and sand thickness values are statistically representative of the exhaustive properties. This is typically assumed in geostatistical studies, except for situations requiring declustering--not a complicating factor in this particular study because of the regularly-spaced wells. The porosity and sand thickness variograms used as constraints in the conditional simulations were based on analysis of the well data only. Therefore, many of the discrepancies between the exhaustive data set and the simulated reservoir properties are due to errors introduced by assuming exact statistical representation of the exhaustive properties by the well data, and not the inadequacies of the methodology. However, such an approach was selected because of its realistic nature. The amount of error introduced

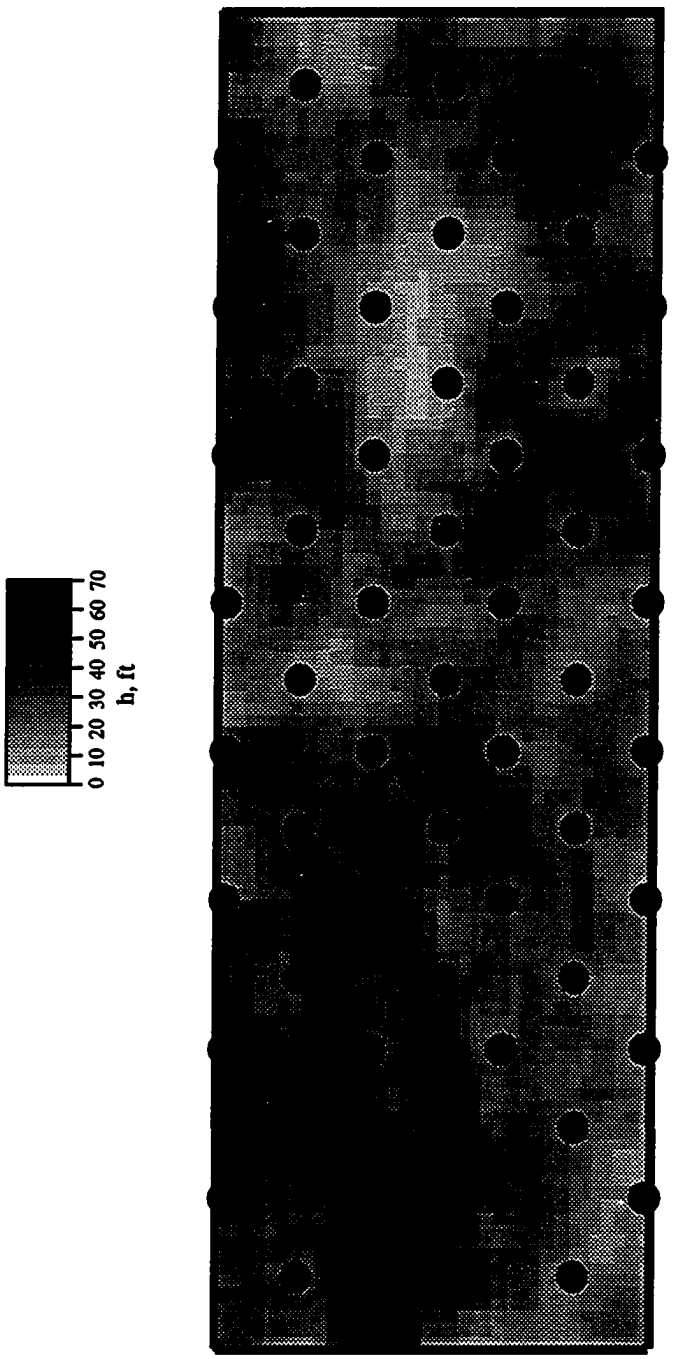

Figure 5.7 - Exhaustive pay thickness map for the full-field truth case

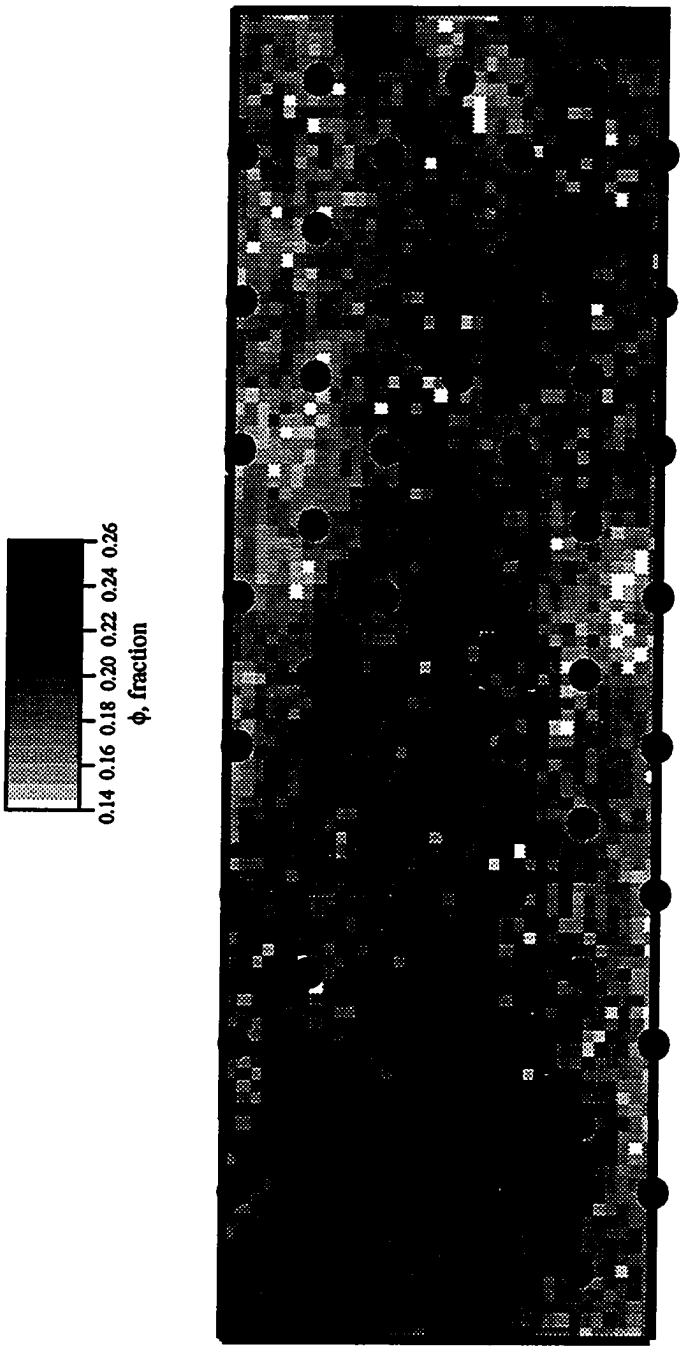

Figure 5.8 - Exhaustive porosity field for the full-field truth case

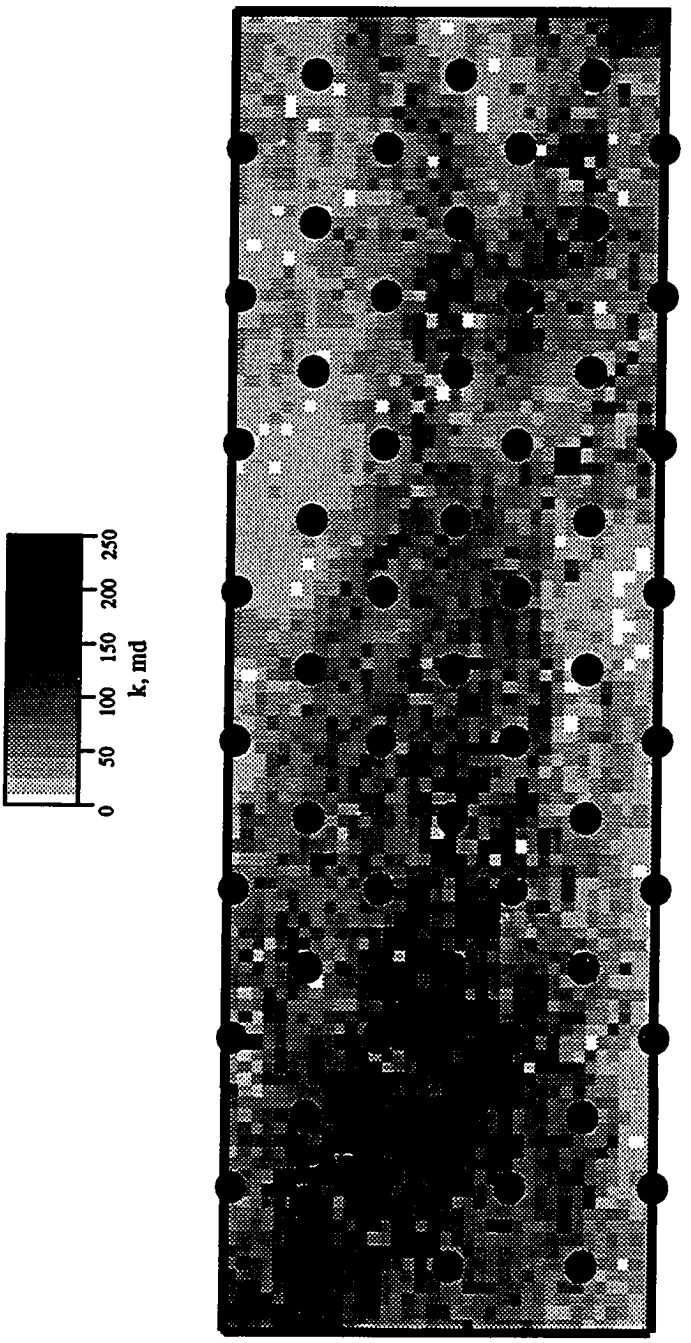

Figure 5.9 - Exhaustive permeability field for the full-field truth case

by assuming statistical representation by the well data can be estimated, or at least appreciated, by comparing field and well statistics. Such a comparison follows.

Univariate and Bivariate Distributions

A histogram of well grid block sand thickness is shown in Figure 5.10. When compared to the exhaustive sand thickness histogram (Figure 5.2), the biggest discrepancy is in the disproportionate fraction of high values in the well data. Whereas only about 7 percent of the exhaustive sand thicknesses exceed 52 ft, this cutoff is exceeded by about 13 percent of the well data. Figure 5.11 is the porosity histogram for the 59 wells. A comparison of Figures 5.3 and 5.11 shows many similarities between the field and well porosity statistics. A close comparison indicates that the exhaustive porosity histogram is slightly positively skewed and the well porosity histogram is slightly negatively skewed. The well block permeability histogram is illustrated in Figure 5.12. Again, many similarities exist between exhaustive and well permeability statistics. As would be expected with such a limited data set, the well block permeabilities do not contain the extreme high and low values existing in the exhaustive data set.

Spatial Correlations

The experimental variogram (inverse covariance form[80]) of well block sand thickness is depicted in Figure 5.13. The correlation length in the major direction of N90°E is 9000 ft, somewhat less than that of the exhaustive data set (Figure 5.5). The minor direction sand thickness variograms of the well and exhaustive data are very similar. Based on the comparison of Figures 5.5 and 5.13, it appears that little error is introduced by assuming the well based porosity variogram is representative of the full-field. The well based porosity inverse covariance for the major and minor directions (N90°E and N0°E, respectively) are shown in Figure 5.14. These variogram functions compare extremely

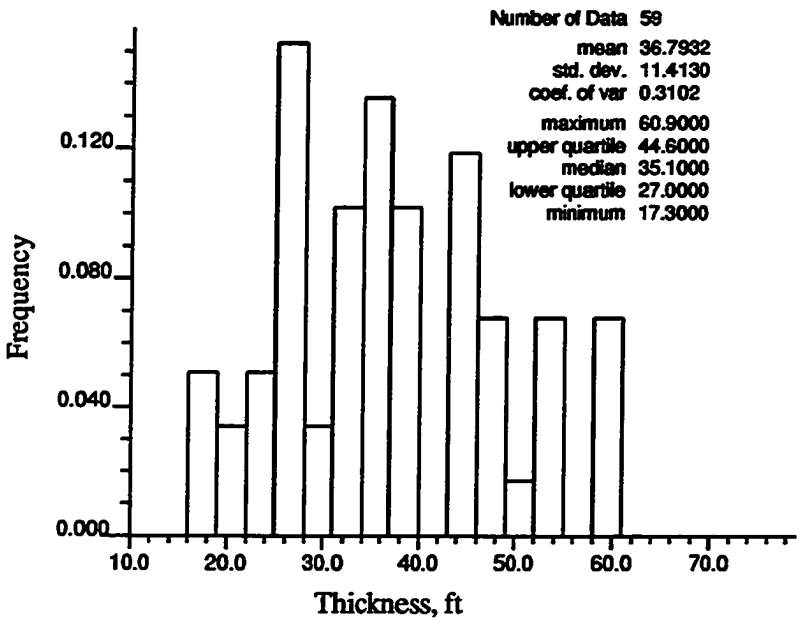

Figure 5.10 - Pay thickness histogram for full-field well data

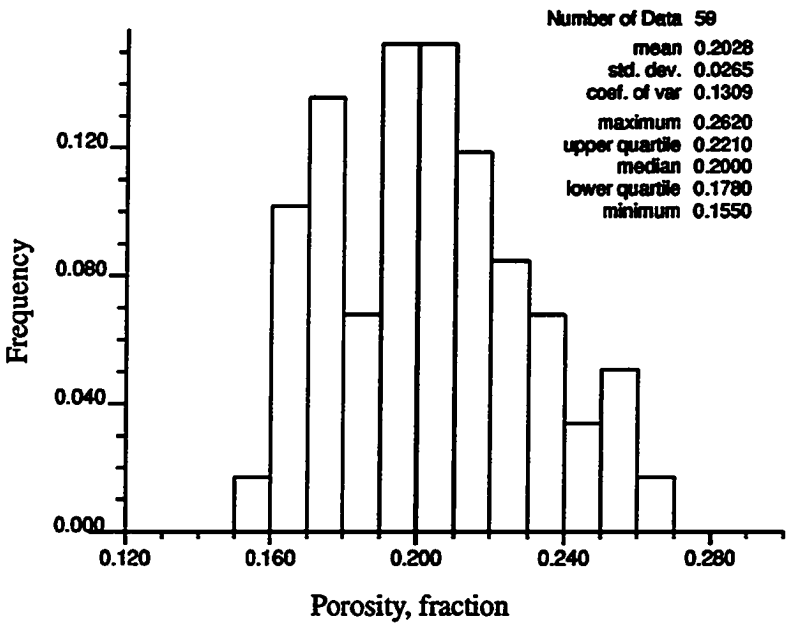

Figure 5.11 - Porosity histogram for full-field well data

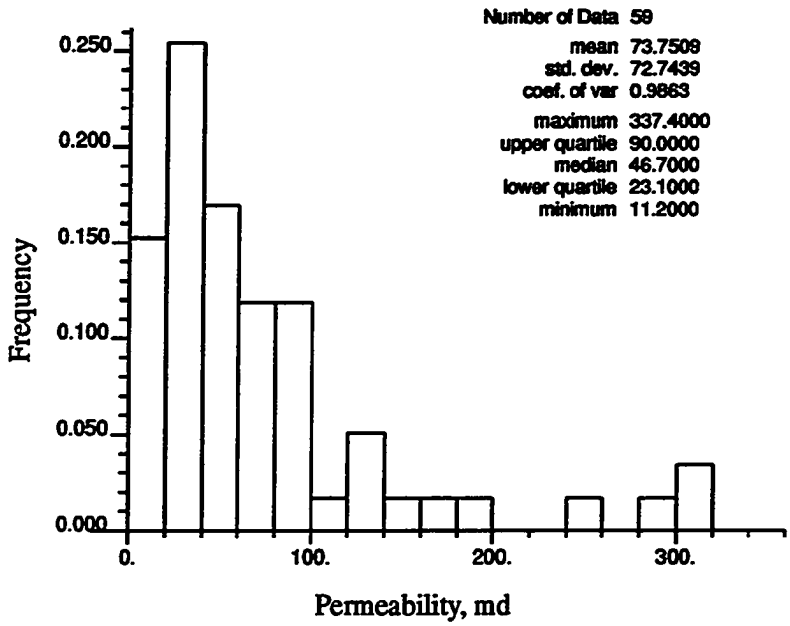

Figure 5.12 - Permeability histogram for full-field well data

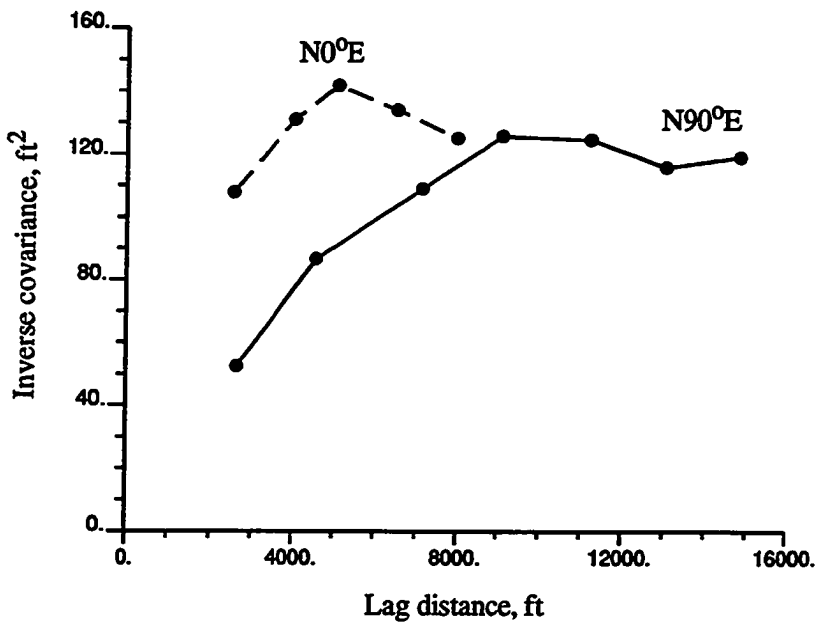

Figure 5.13 - Inverse covariance for sand thickness based on the full-field truth case well data

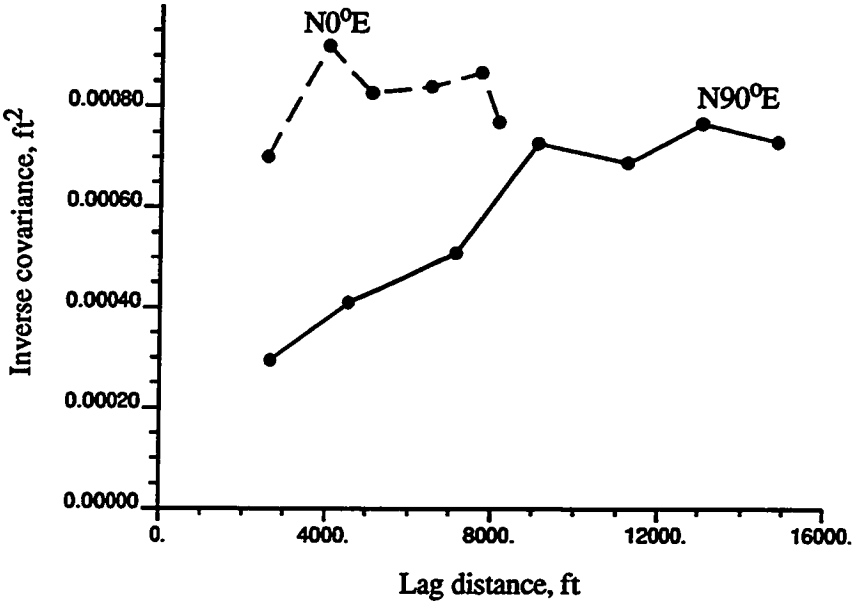

Figure 5.14 - Inverse covariance for porosity based on the full-field truth case well data

well with the exhaustive porosity direction variograms contained in Figure 5.6. Insignificant errors should result in using the porosity variograms of Figure 5.14 to represent the true porosity spatial correlation of the full-field.

Spatial Properties - Kriged Sand Thickness

The sand thickness histogram and variogram derived from the well data were used to krige sand thickness. The resulting sand thickness map is depicted in Figure 5.15. Although many of the local variations exhibited by the exhaustive sand thickness map (Figure 5.7) are not captured by kriging, most of the important sand thickness trends are honored. Once again, sensitivities to reservoir performance due to sand thickness errors were not considered in this study.

Primary Constraints Results

Similar to previously described synthetic case studies, the effectiveness of the performance constraints will be measured by the ability of resulting alternative reservoir descriptions to 1) simulate well performance which is similar to the truth case well performance and 2) have spatial characteristics which are similar to the truth case. In each case, ten alternative reservoir descriptions were generated using the same constraints. Well configurations, well operating conditions, rock properties and fluid properties are the same as previous case studies. Pertinent data are listed in Table 5.1. Flow simulations were performed assuming 10 years of primary production followed by 10 years of waterflooding. A total of 32 producers were converted to injection wells upon initiation of the waterflood, resulting in 27 five-spot patterns. The producer and injection well locations are the same as those used in the 3D Truth Case (see Figures 2.29 and 2.30).

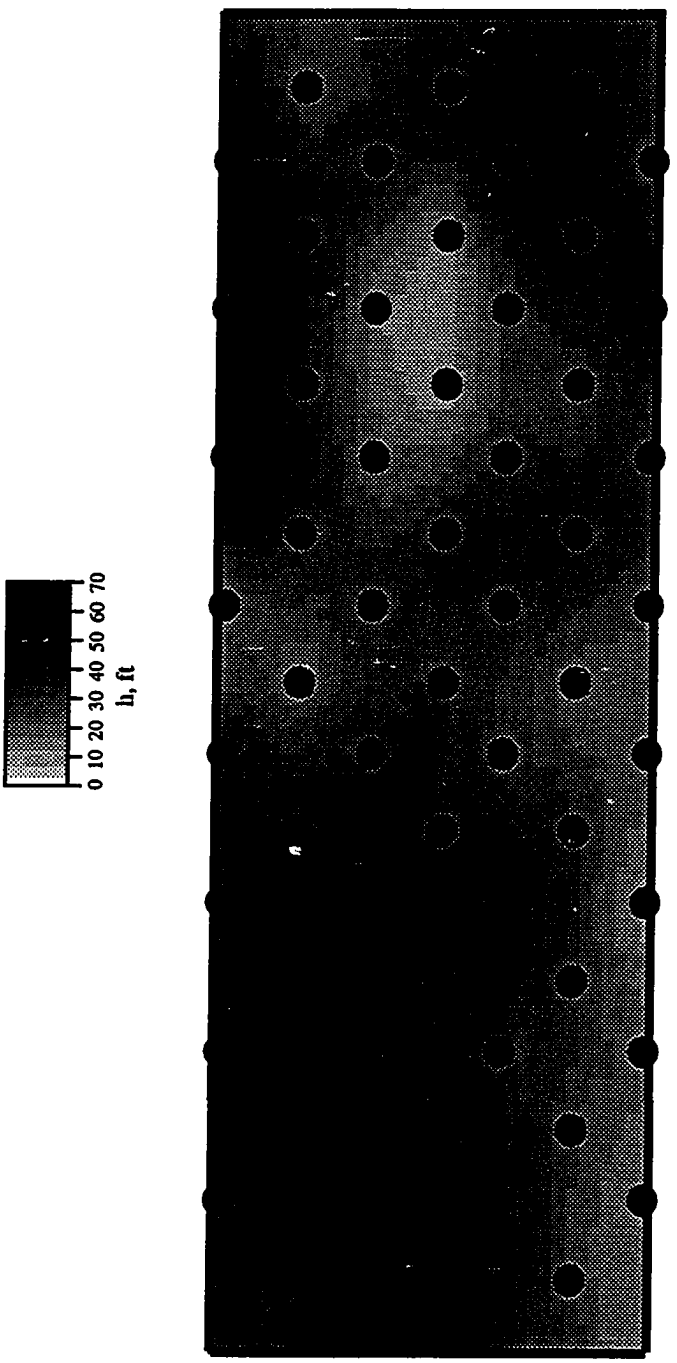

Figure 5.15 - Kriged pay thickness for the full-field truth case

Table 5.1

Pertinent data used in two-dimensional full-field simulations

Type of Simulation	2D Primary & Waterflood
Waterflood pattern type	1:1 five-spot
Well spacing	80 Ac
Waterflood pattern size	160 Ac
Areal grid dimensions	220 ft by 220 ft
Areal grid density	108 by 36
Thickness, porosity & permeability	variable
Number of primary wells	59
No. of waterflood producers/injectors	32/27
Mobility ratio	0.96
Initial/bubble point pressures	1200/1024 psi
Producing/injecting pressures	300/2000 psi

k_{NW} Constraint

Since large grid blocks (220 ft by 220 ft) were used for conditional simulation and well blocks were used as conditioning data, the base case results are equivalent to including a near well effective permeability constraint. A comparison of the exhaustive porosity field to one of the porosity realizations generated using conventional and k_{NW} constraints is displayed in Figure 5.16. Although many of the truth case global trends are captured using the k_{NW} constraint, this one performance constraint is not sufficient to identify local heterogeneities. The corresponding permeability fields are compared in Figure 5.17. Note the large permeability discrepancies in the northwest and northeast corners. These regions have estimated permeabilities which are in error by an order of magnitude or more. Probability of exceedance maps at the 30^{th} porosity percentile for the truth case and the k_{NW} constraints case are compared in Figure 5.18. Consistent with the porosity fields shown in Figure 5.16, only some of the global high and low porosity regions are identified, with inappropriately estimated low probabilities existing throughout the periphery of the field. These results show that the k_{NW} constraint is not sufficient to accurately identify the location of high and low porosity/permeability regions.

The truth case and the 10 reservoir descriptions based on the k_{NW} constraint were flow simulated for comparison. The resulting field performances are illustrated in Figure 5.19. The k_{NW} constraint is seen to do an excellent job in generating reservoir descriptions which behave similar to the truth case in terms of total field primary performance. These results show that it is possible to match historical total field primary performance by honoring near well effective properties, univariate frequency distributions and general spatial variability characteristics. Also included in Figure 5.19 is the waterflood performance for the truth case and the 10 k_{NW} constrained reservoir descriptions. The secondary total field oil rate curves are all fairly similar. The most noticeable discrepancies are the water breakthrough times and secondary water production rates. All

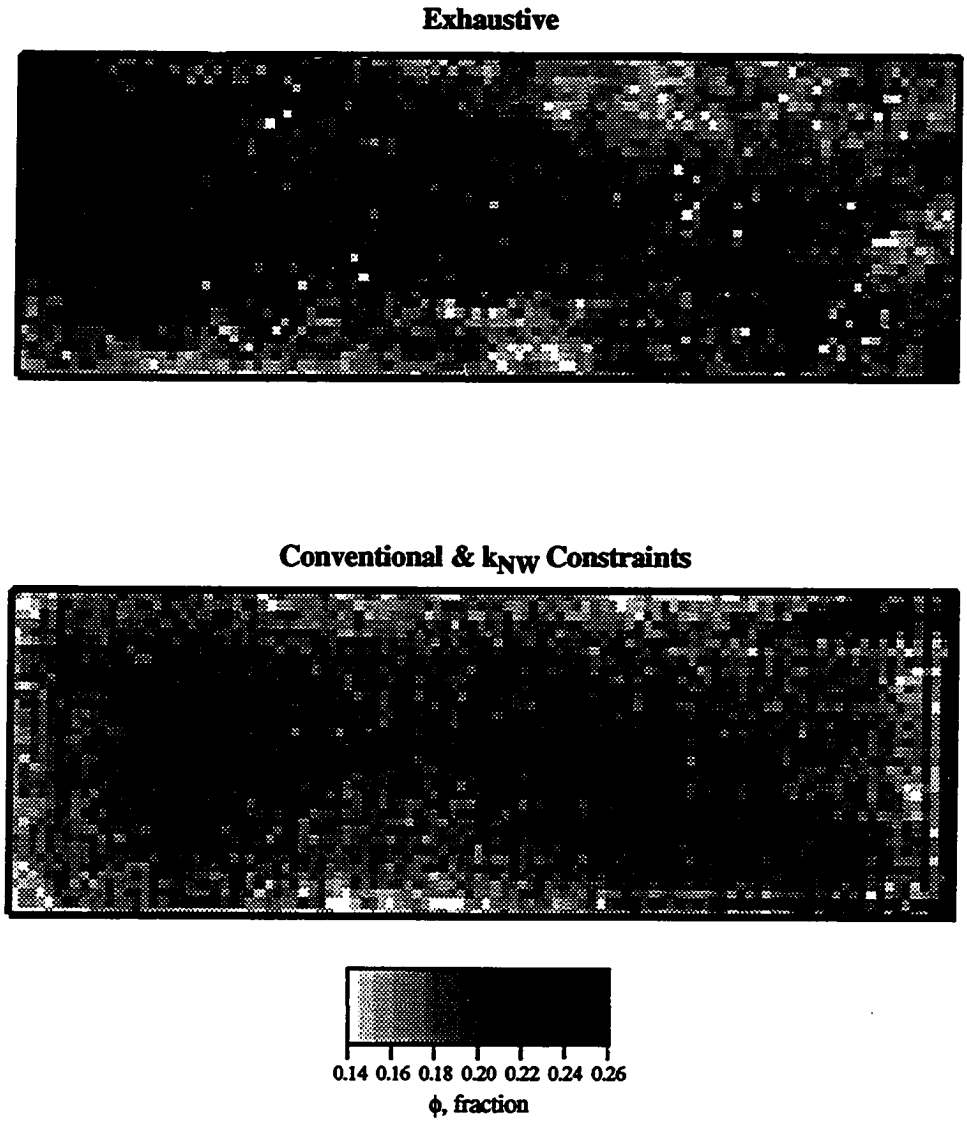

Figure 5.16 - Comparison of full-field exhaustive porosity field to porosity realization obtained using conventional and k_{NW} constraints

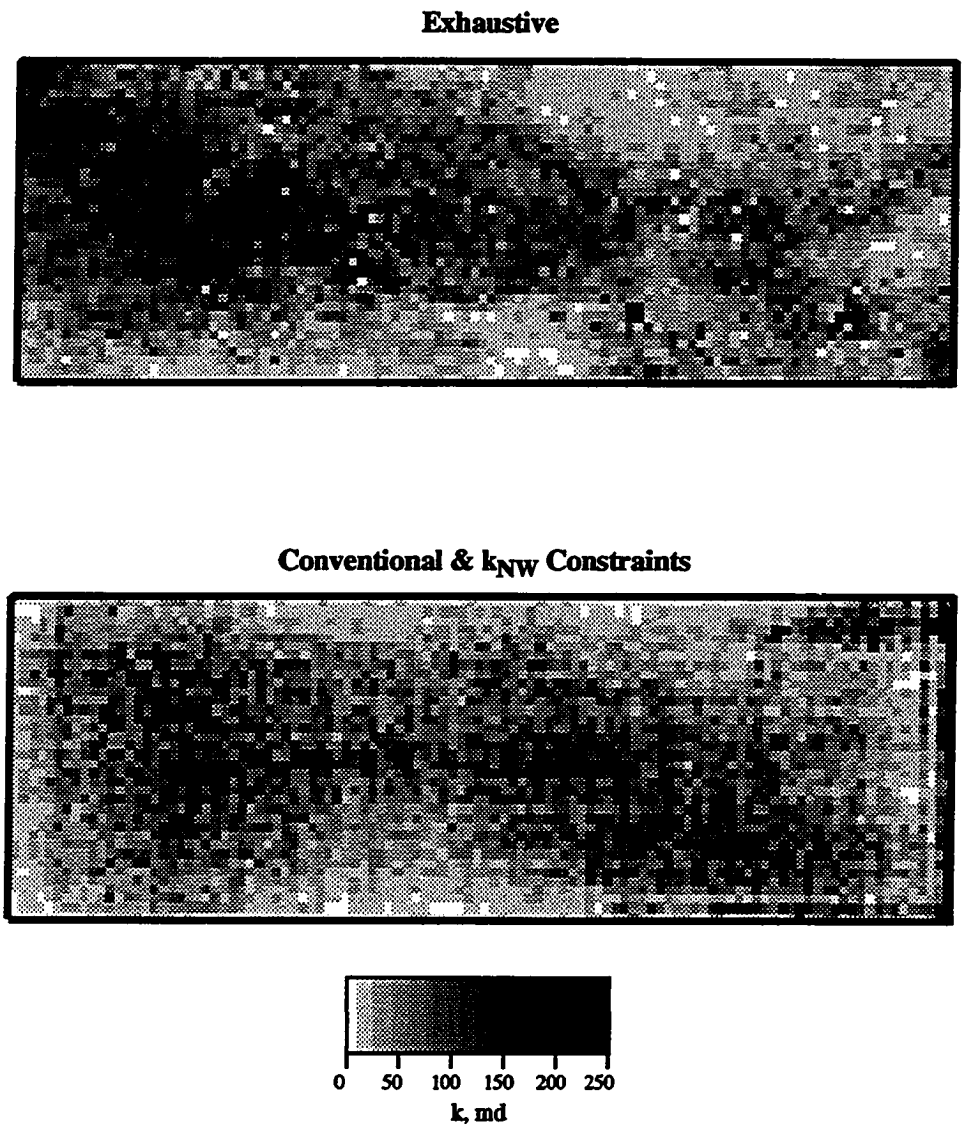

Figure 5.17 - Comparison of full-field exhaustive permeability field to permeability field obtained using conventional and k_{NW} constraints

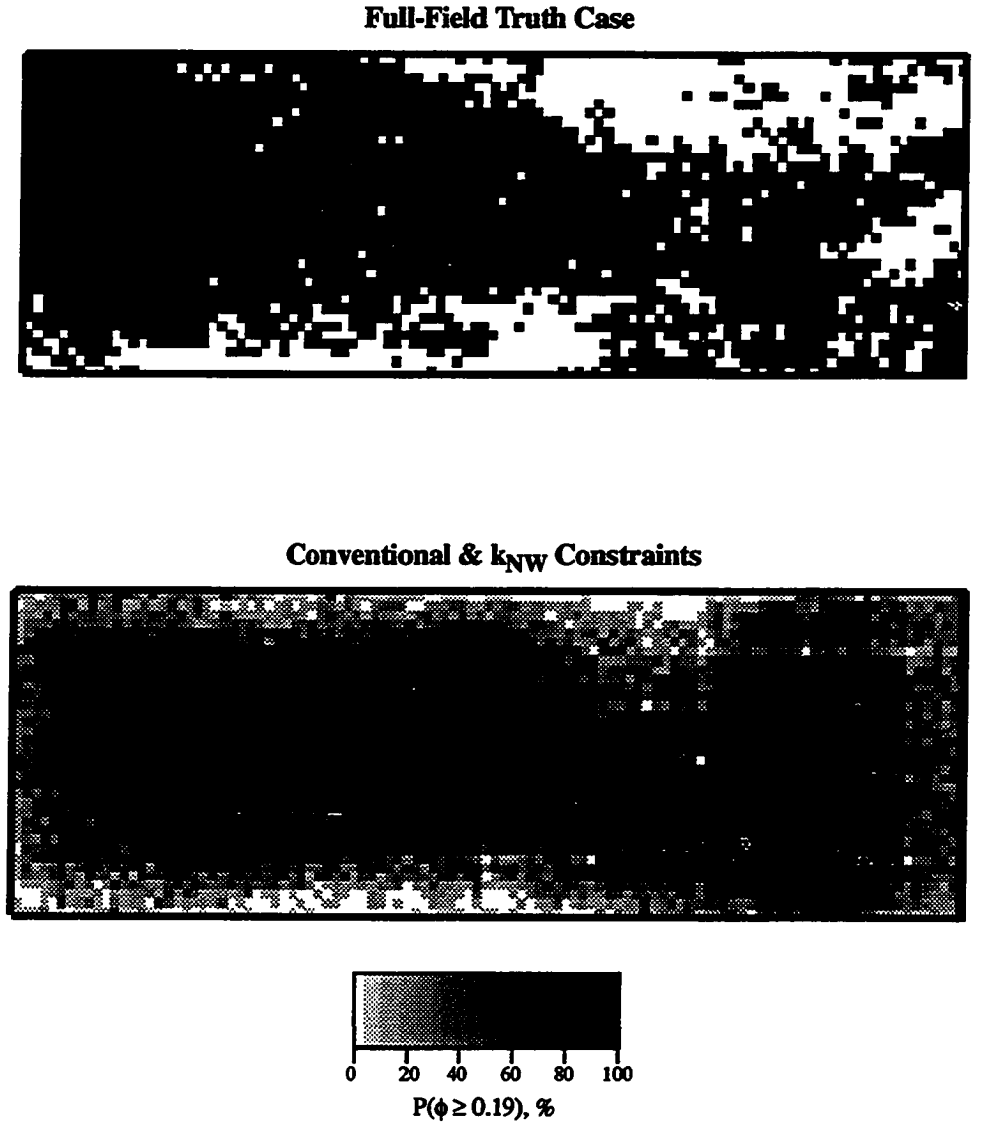

Figure 5.18 - Comparison of porosity probability of exceedance maps at the 30th porosity percentile; full-field truth case vs. results obtained using conventional and k_{NW} constraints

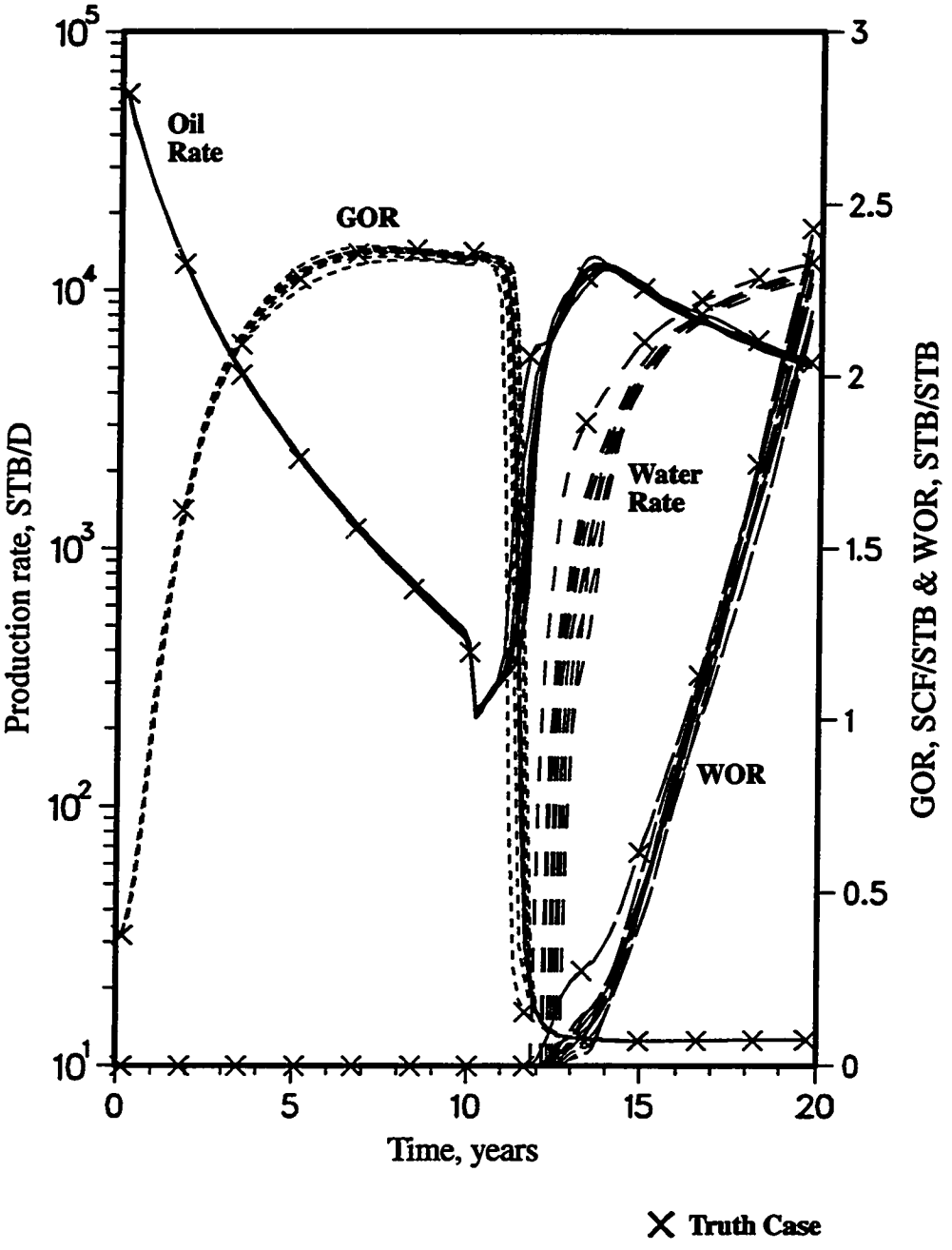

Figure 5.19 - Comparison of full-field truth case performance vs. performance of 10 reservoir descriptions generated using conventional and k_{NW} constraints

of the realizations predict water breakthrough later than the truth case. One realization predicts water breakthrough approximately one year too late. At this time, actual water production had already increased to about 3000 STB/D. As expected, the k_{NW} constraint results in significant improvement in primary performance characteristics but is inadequate as a waterflood constraint.

Matching individual well performance is considerably more important than reproducing total field performance from a reservoir management viewpoint. Being able to make appropriate operational changes on a well-by-well basis is more economically effective than implementing global operational changes. Well performance for 8 producers distributed throughout the field were plotted to evaluate the effectiveness of the various performance constraints. The location of the 8 wells are depicted in Figure 5.20. The corresponding performance plots for the wells are included in Figures 5.21 and 5.22. Primary well performance for all reservoir descriptions compares favorably with the truth case performance. Such is not the case for individual well performances during water injection. Significant variability and truth case discrepancies exist for all of the wells during the 10 years of waterflooding. Note that the realizations can greatly overpredict (Well P50) and underpredict (Well P51) secondary response compared to the truth case performance. These well performance comparisons substantiate the conclusions reached based on comparing the spatial distributions of porosity and permeability, i.e., local reservoir characteristics are not captured using just the k_{NW} constraint.

k_{NW}, PV_T and PV_{DA} Constraints

Near well permeability is frequently the first well performance characteristic that can be estimated from field data (well tests). As more primary production data is collected, pore volume estimates can be made through material balance calculations. Sometimes volumetric calculations can be made from structure and fluid contact contours even

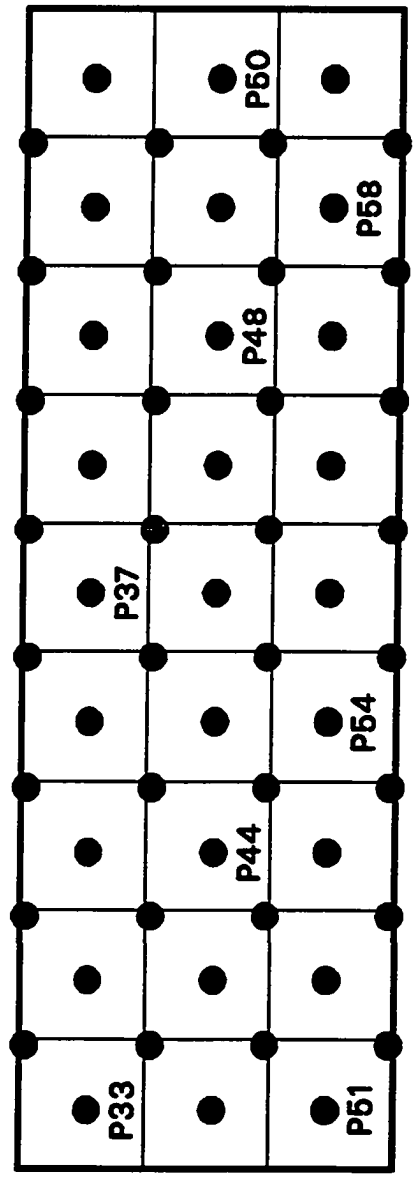

Figure 5.20 - Location of selected full-field producers

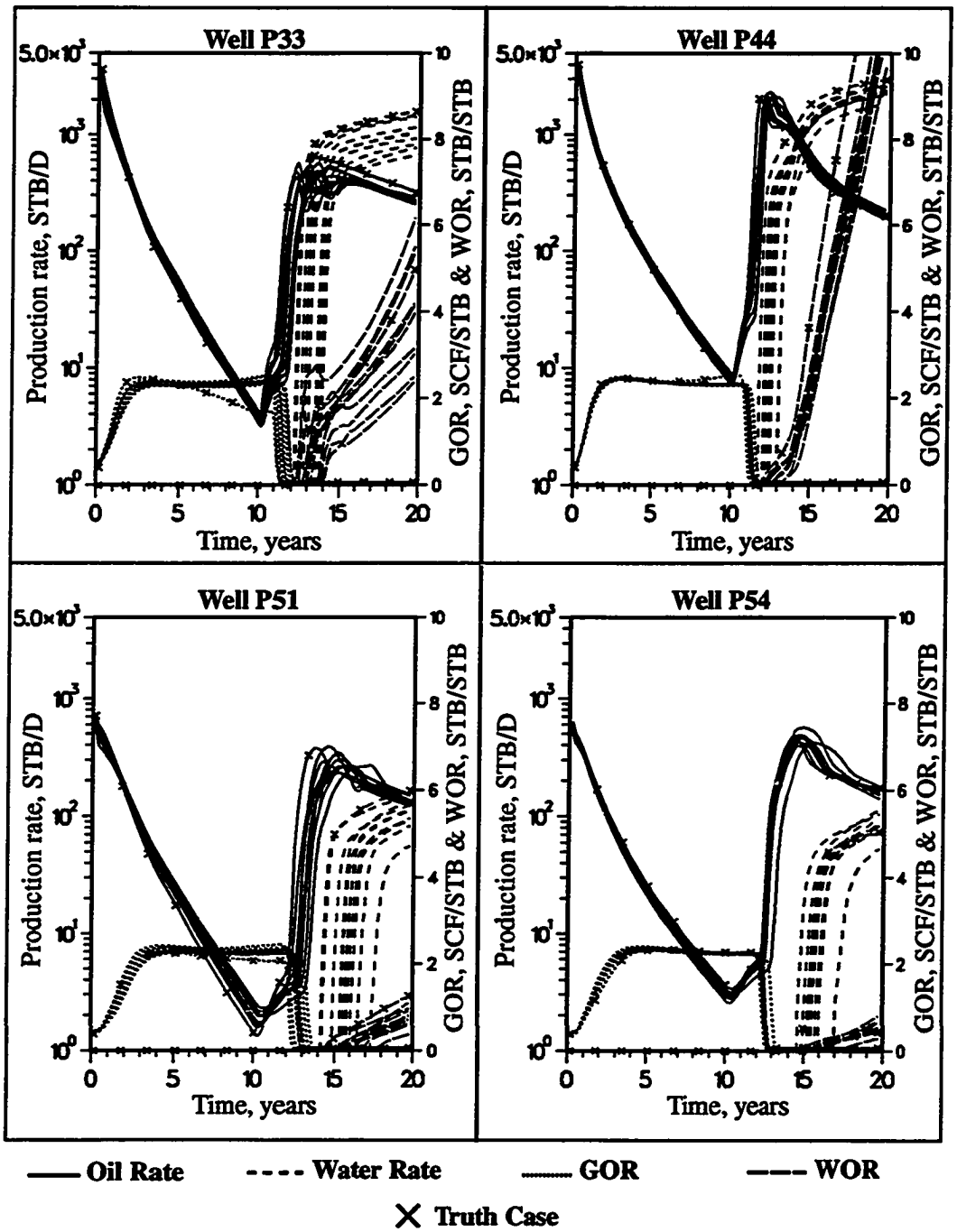

Figure 5.21 - Performance plots for Wells P33, P44, P51 and P54; full-field reservoir descriptions based on conventional and k_{NW} constraints

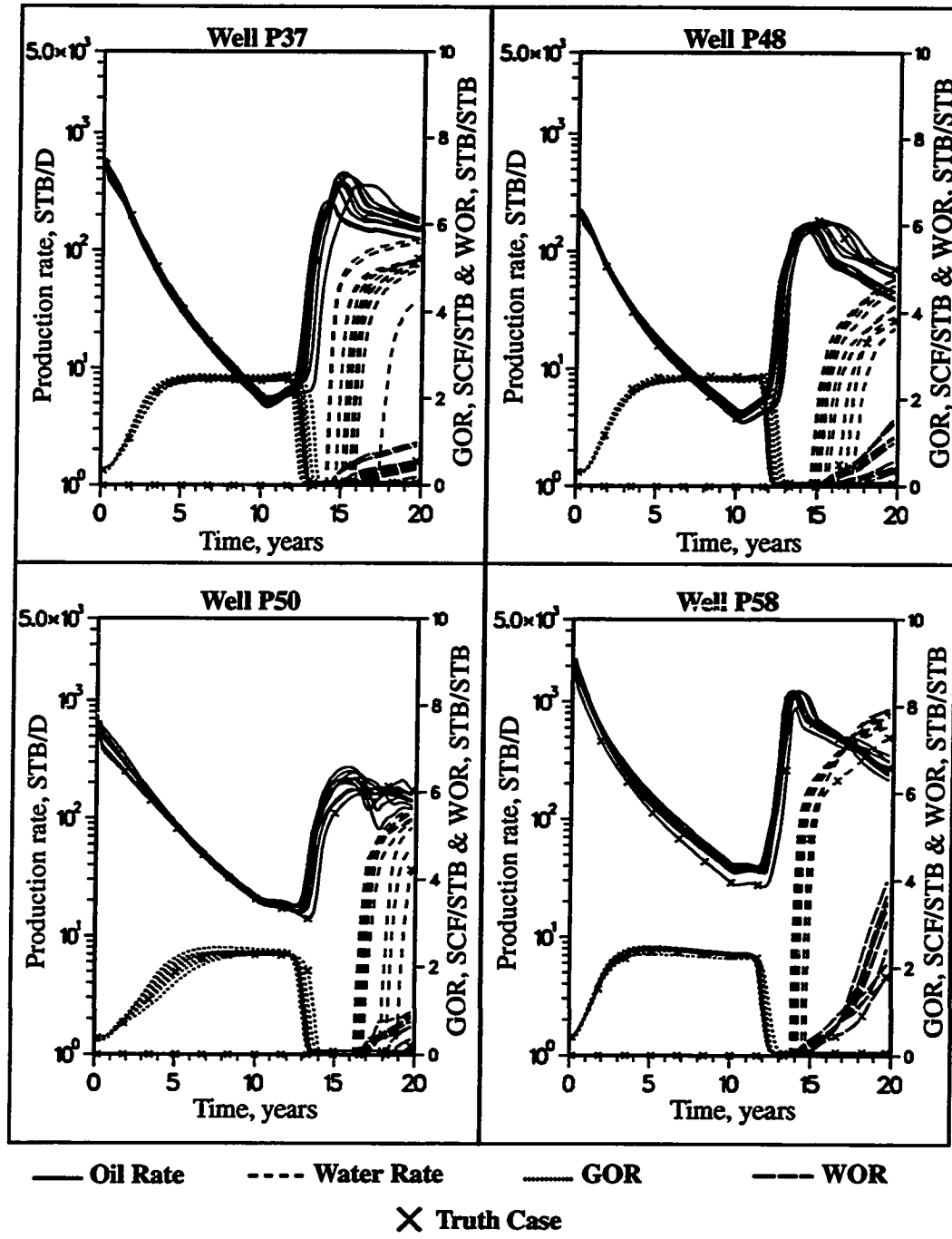

Figure 5.22 - Performance plots for Wells P37, P48, P50 and P58; full-field reservoir descriptions based on conventional and k_{NW} constraints

before any significant production has occurred. With this in mind, additional reservoir descriptions were generated assuming total field pore volume and individual well drainage area pore volume estimates were available as constraints, in addition to conventional and k_{NW} constraints. For simplicity, these constraints will be referred to as primary (production) constraints.

The truth case porosity field is compared to a porosity realization generated using all of the primary constraints in Figure 5.23. This comparison is significantly better than previous results based on the k_{NW} constraint by itself. The global porosity trends are reasonably reproduced. There is still room for improvement in honoring local high and low porosity regions. For completeness, the corresponding permeability images are shown in Figure 5.24. The probability of exceedance maps illustrated in Figure 5.25 indicate that although pore volume constraints improve the ability to predict the locations of high and low porosity (and permeability) regions, many of the local heterogeneity characteristics are not identified.

Full-field performance comparisons are made in Figure 5.26. When compared to Figure 5.19, the most obvious improvement is to more consistently predict water production rates during secondary recovery. For this case study, predicting total field performance during primary and secondary recovery is not a problem when all primary constraints are employed. The performance of the same 8 wells previously illustrated for the k_{NW} constraint results are depicted in Figures 5.27 and 5.28. Consistent with the improvement in the estimation spatial properties, individual well performance results are also better than when just including the k_{NW} constraint. However, significant spread in waterflood performance still exists for several of the wells. Much of the improvement in waterflood performance is due to assuming the direct one-to-one correlation between porosity and permeability; i.e., specifying each well's pore volume also specifies the average permeability of the region drained by the well. This average permeability has some commonality with the effective permeability of nearby injector/producer areas of

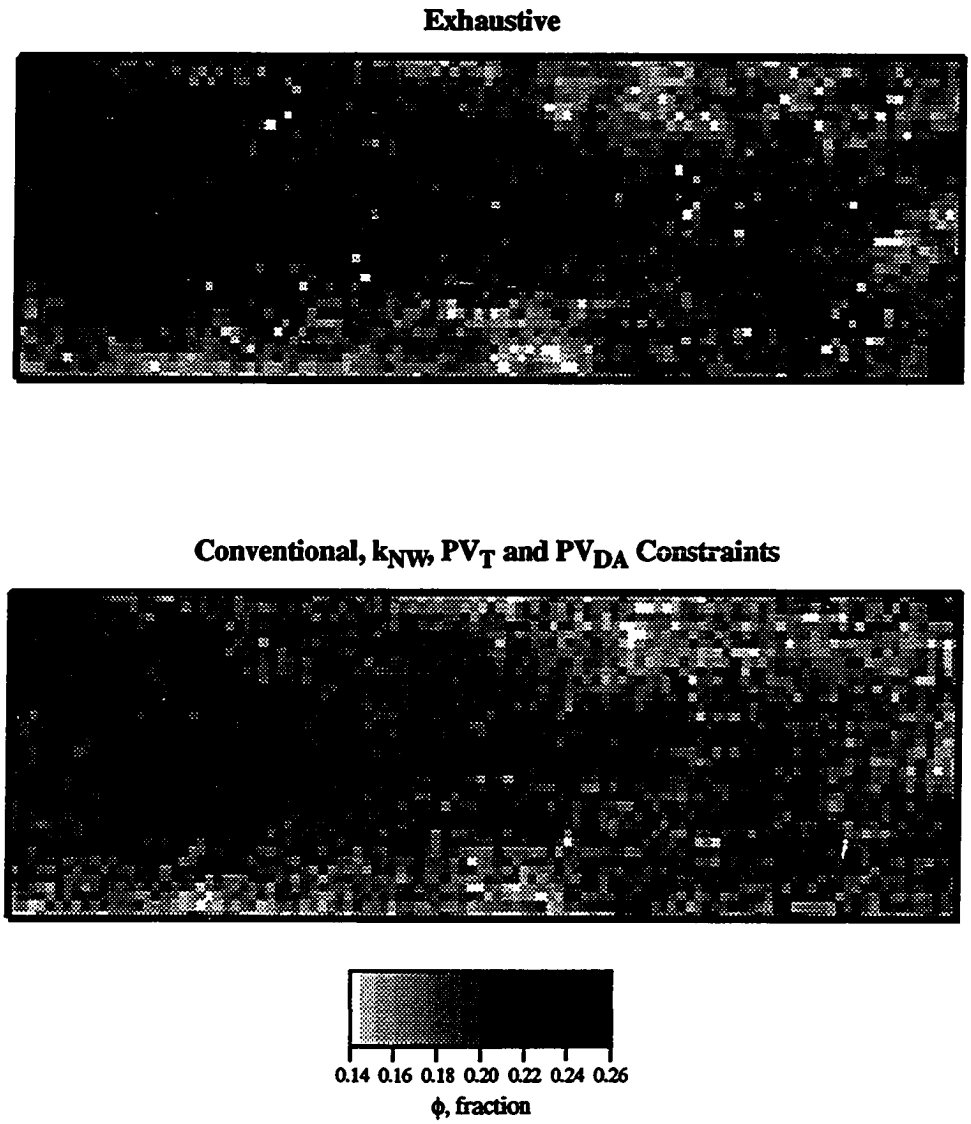

Figure 5.23 - Comparison of full-field exhaustive porosity field to porosity realization obtained using conventional, k_{NW}, PV_T and PV_{DA} constraints

Exhaustive

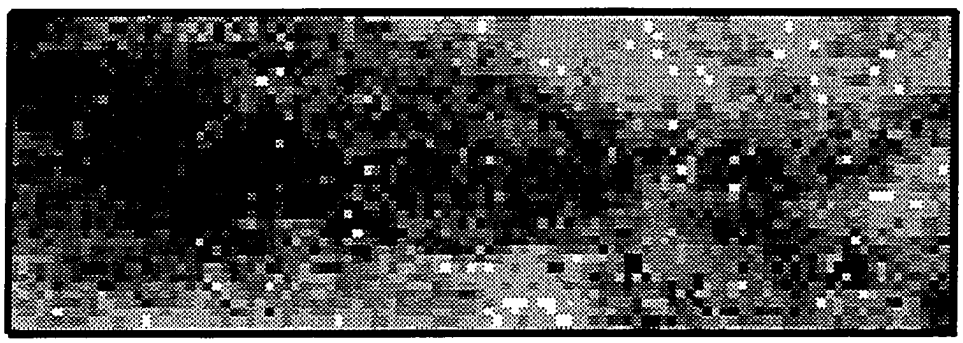

Conventional, k_{NW}, PV_T and PV_{DA} Constraints

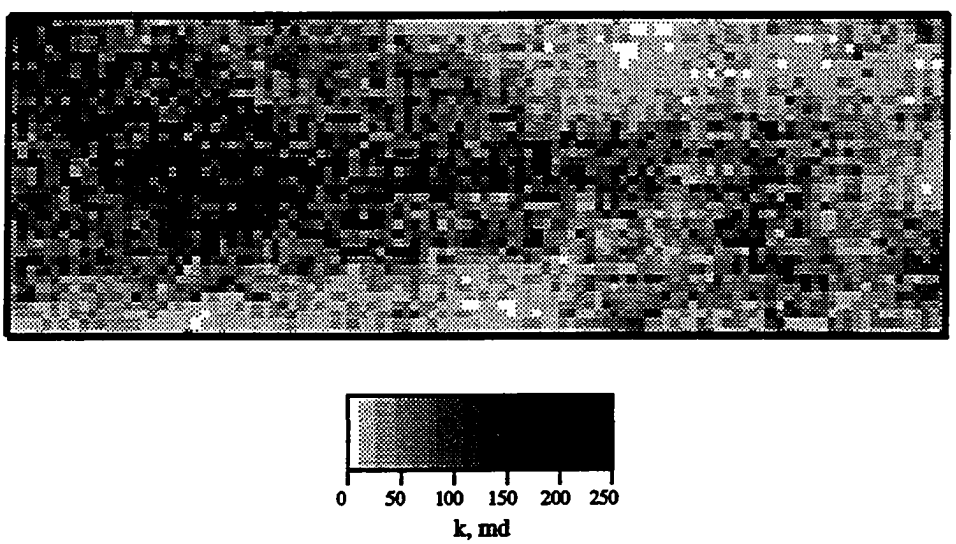

Figure 5.24 - Comparison of full-field exhaustive permeability field to permeability field obtained using conventional, k_{NW}, PV_T and PV_{DA} constraints

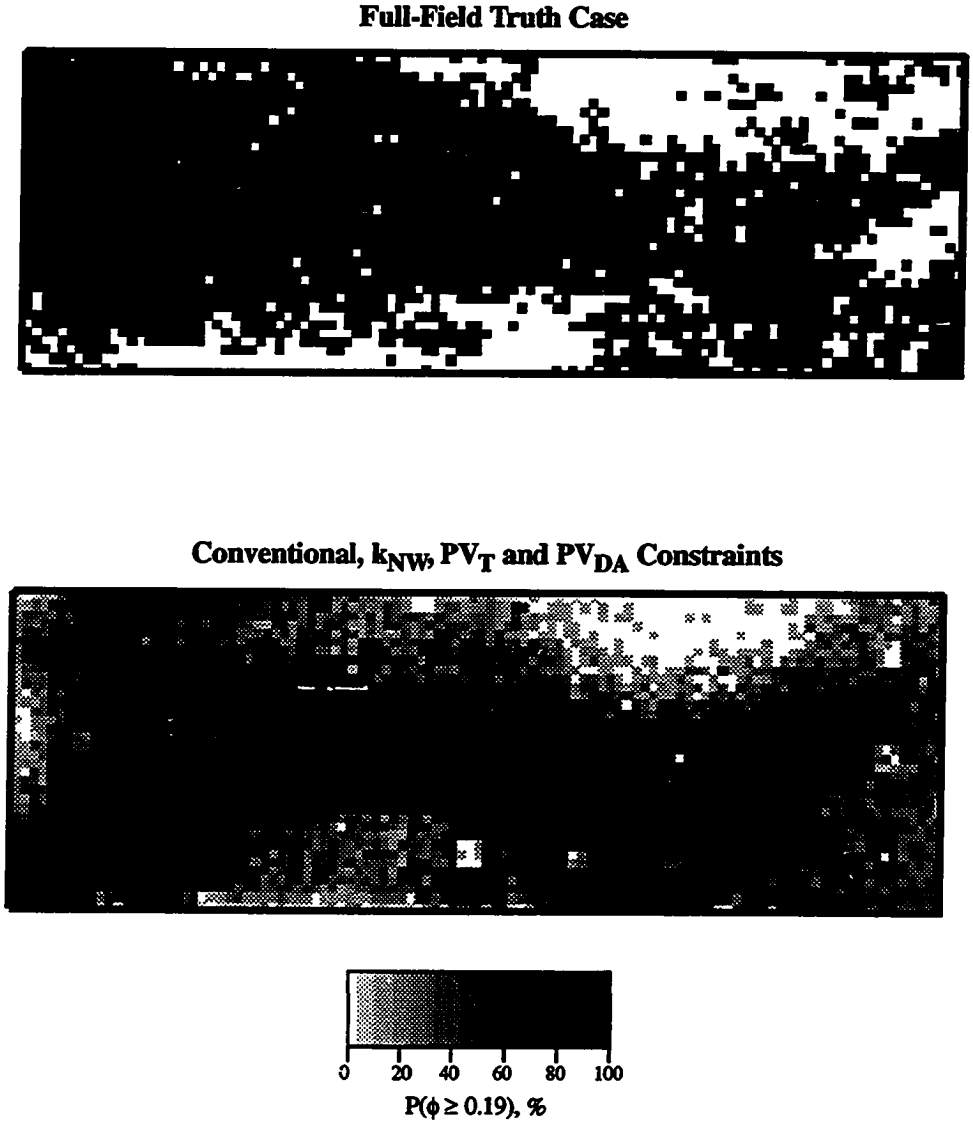

Figure 5.25 - Comparison of porosity probability of exceedance maps at the 30th porosity percentile; full-field truth case vs. results obtained using conventional, k_{NW}, PV_T and PV_{DA} constraints

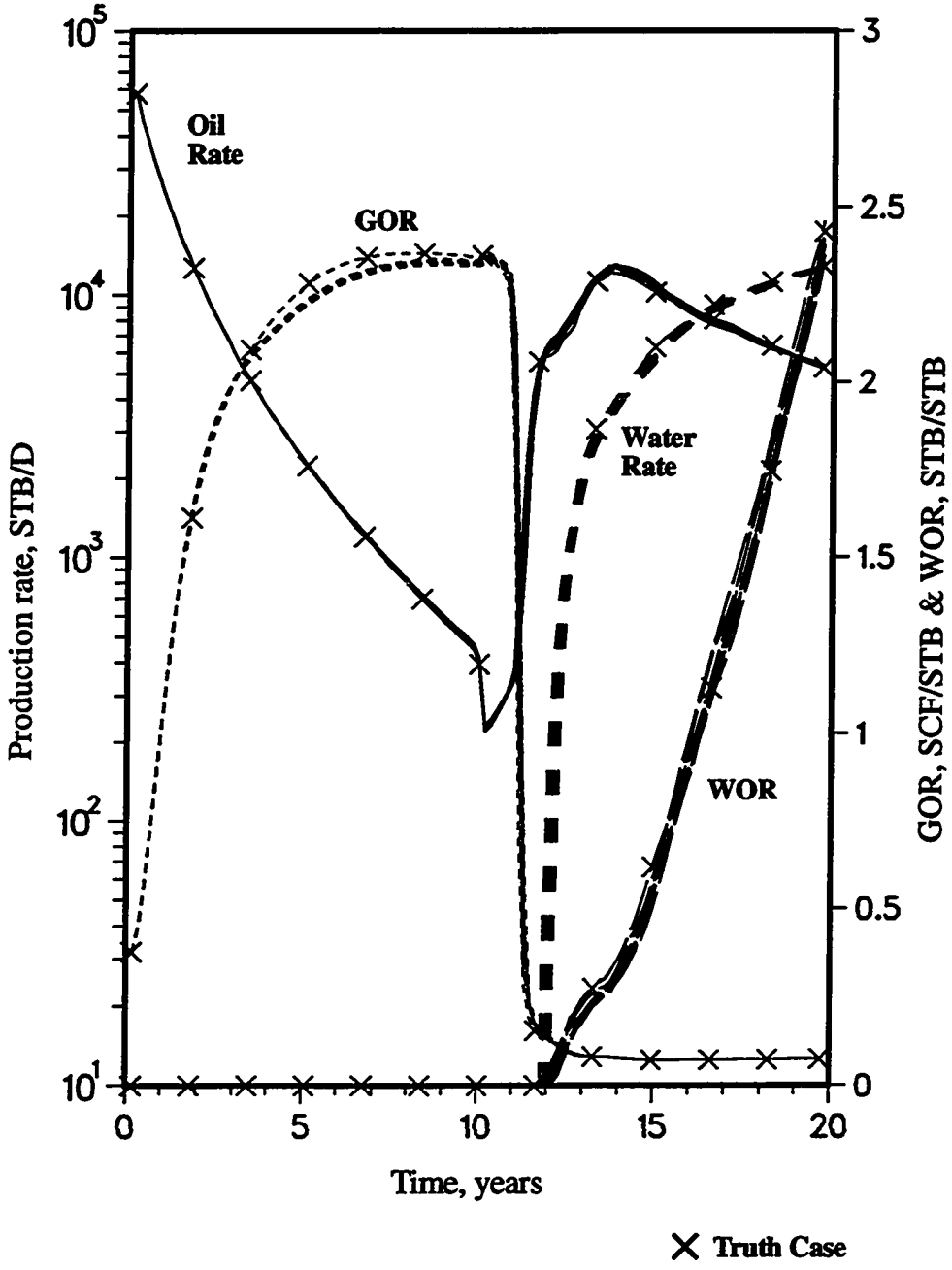

Figure 5.26 - Comparison of full-field truth case performance vs. performance of 10 reservoir descriptions generated using conventional, k_{NW}, PV_T and PV_{DA} constraints

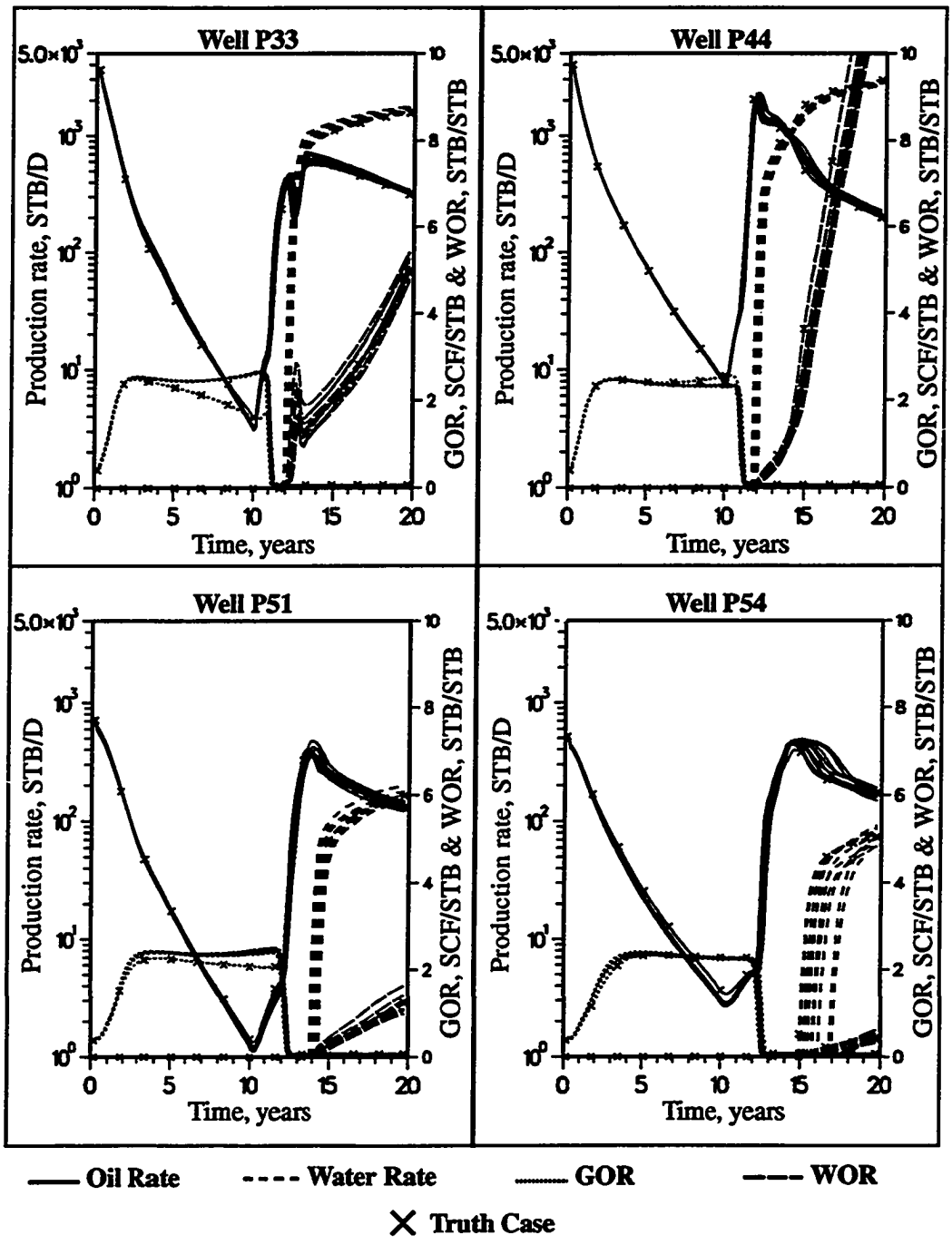

Figure 5.27 - Performance plots for Wells P33, P44, P51 and P54; full-field reservoir descriptions based on conventional, k_{NW}, PV_T and PV_{DA} constraints

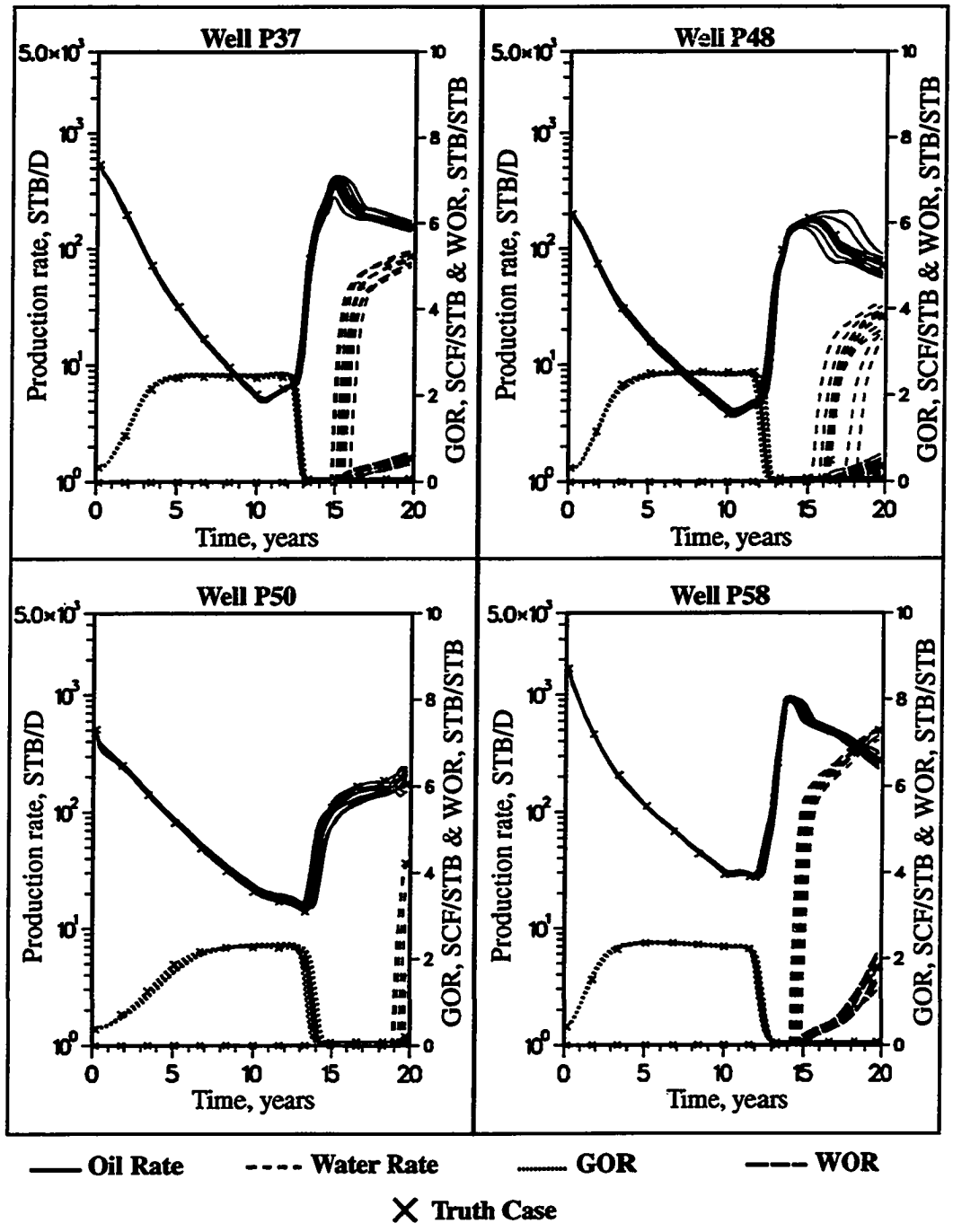

Figure 5.28 - Performance plots for Wells P37, P48, P50 and P58; full-field reservoir descriptions based on conventional, k_{NW}, PV_T and PV_{DA} constraints

influence.

Primary and Secondary Constraints Results

The above results were based on the use of conventional and primary performance constraints only. As expected, the resulting field and well performance behaved very similar to the truth case performance during primary production; however, some discrepancies existed during waterflooding. The following case studies assume sufficient secondary performance data is available to make accurate estimates of the secondary performance constraints CV_{k*} and k_{PAT}. Sensitivities are performed to determine the relative importance of these two parameters for the full-field truth case.

Primary, CV_{k*} and k_{PAT} Constraints

All conventional, primary and secondary performance constraints have been utilized in this particular study. Figure 5.29 contains a comparison of the truth case porosity field and one of the resulting porosity fields. The corresponding permeability fields are shown in Figure 5.30. Both global and local spatial characteristics of the truth case are well reproduced in both figures. It appears that a sufficient number of constraints have been imposed to allow the generation of realistic reservoir descriptions. Additional evidence of the method's effectiveness is shown in Figure 5.31. Here, probability of exceedance maps (30^{th} percentile cutoff of porosity) of the truth case and the realizations generated using all constraints are compared. The location of actual high and low porosity regions are not only accurately identified, but they are identified with high certainty as indicated by the extreme probabilities (i.e., almost 0% or 100%). It should be noted that the simulated annealing objective function contains 327 components for this particular case study: 1 PV_T constraint, 59 PV_{DA} constraints, 59 k_{NW} constraints, 96 CV_{k*} constraints, 96 k_{PAT} constraints and 16 variogram constraints (2 directions, 8 lags each).

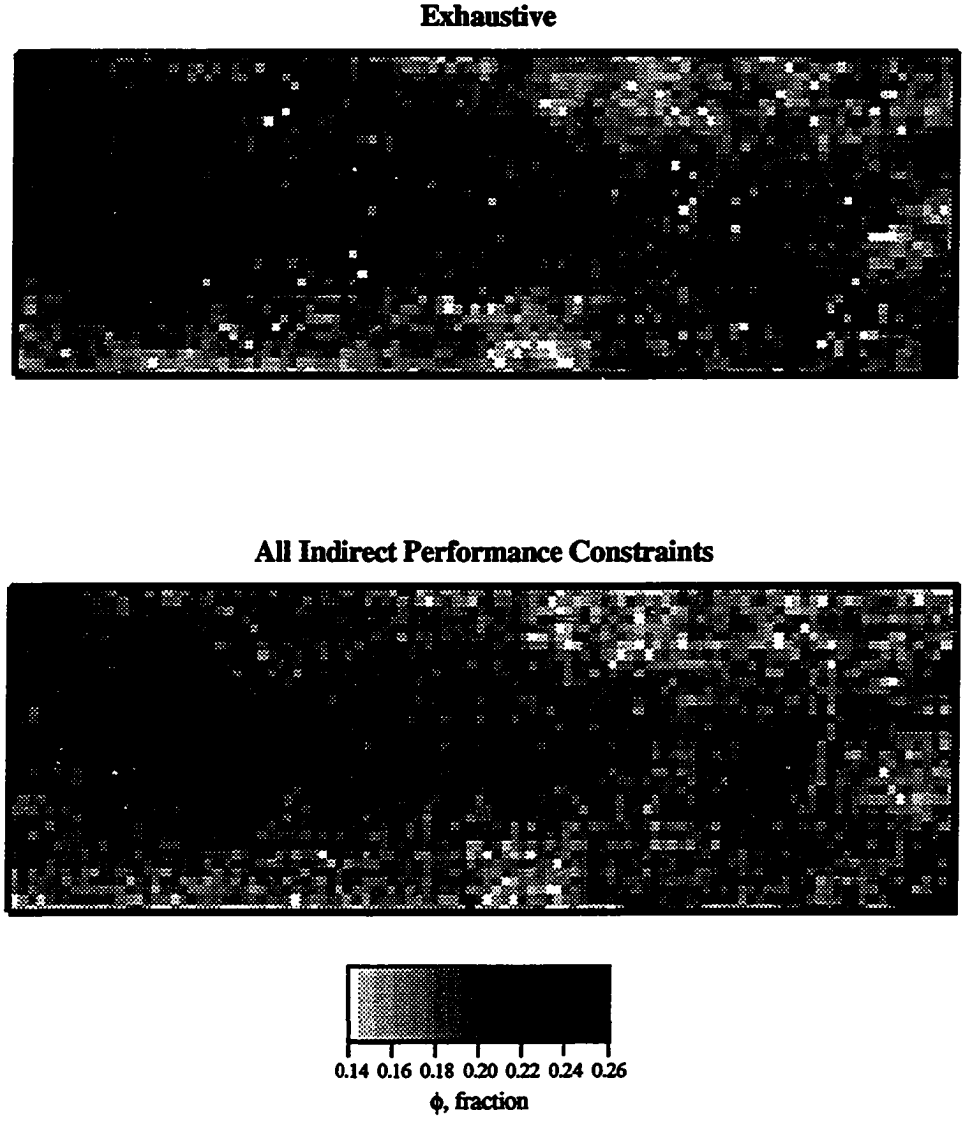

Figure 5.29 - Comparison of full-field exhaustive porosity field to porosity realization obtained using conventional, k_{NW}, PV_T, PV_{DA}, CV_{k^*} and k_{PAT} constraints

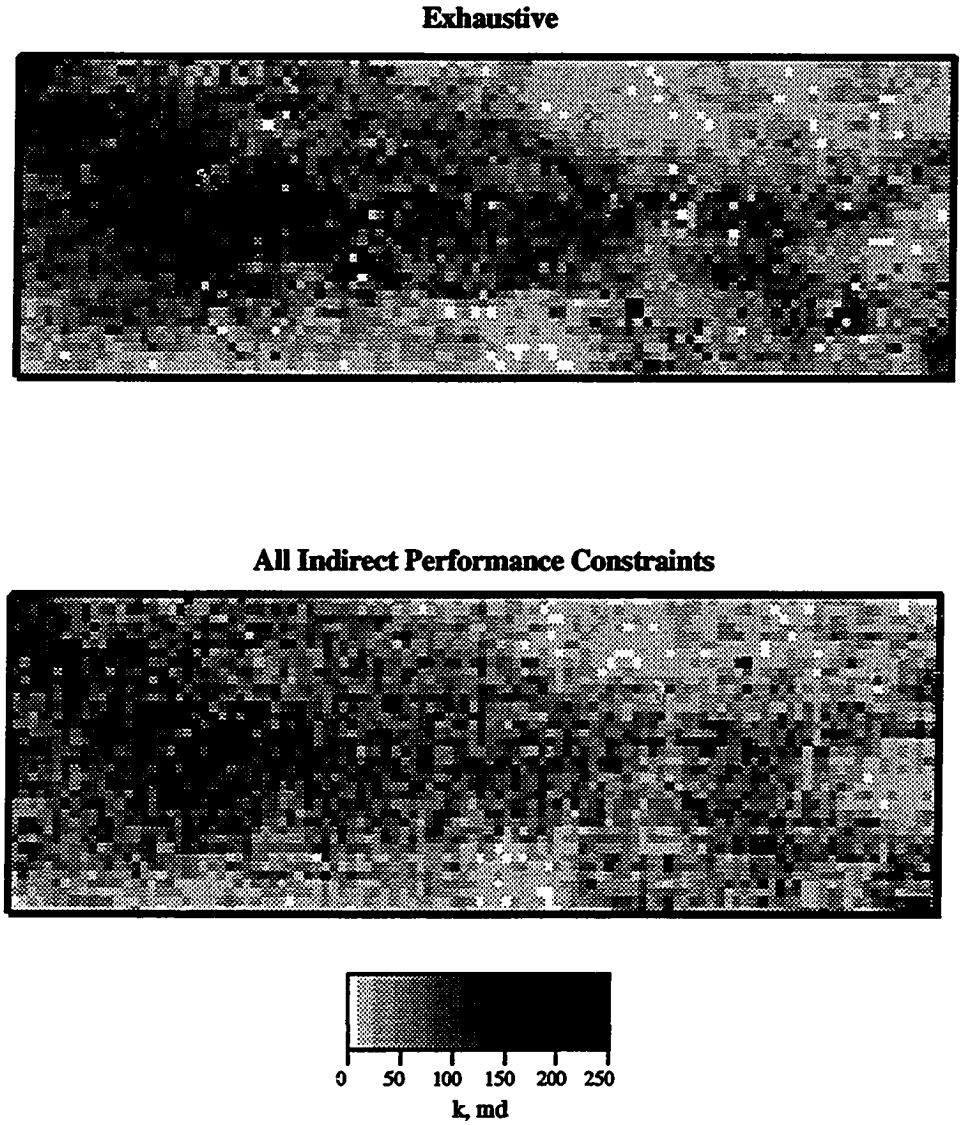

Figure 5.30 - Comparison of full-field exhaustive permeability field to permeability field obtained using conventional, k_{NW}, PV_T, PV_{DA}, CV_{k^*} and k_{PAT} constraints

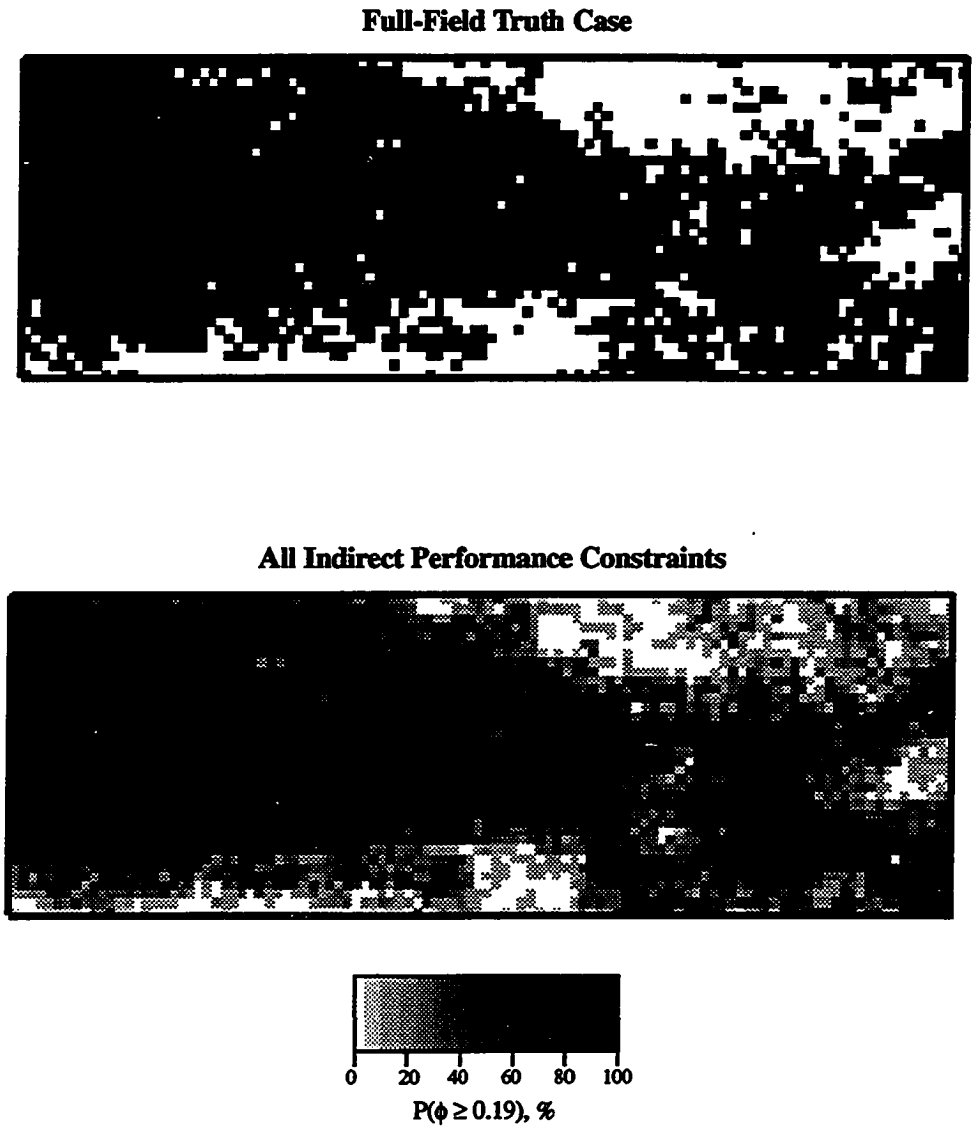

Figure 5.31 - Comparison of porosity probability of exceedance maps at the 30th porosity percentile; full-field truth case vs. results obtained using conventional, k_{NW}, PV_T, PV_{DA}, CV_{k^*} and k_{PAT} constraints

It is highly unlikely that this much information would be available for a real field study; however, these results emphasize the flexibility and robustness of the method.

Total field performance for the 10 alternative reservoir descriptions and the truth case are shown in Figure 5.32. The responses for all cases are nearly indistinguishable. The only inconsistency is in the GOR curve during part of primary production. The reason for this GOR anomaly is unknown. Nearly as impressive is the individual well performances shown in Figures 5.33 and 5.34. The most difficult waterflood parameters to match, water breakthrough time and WOR trend, are well reproduced for each well; extremely well reproduced for some wells. The total field and individual well performance results are consistent with the spatial distribution results, i.e., the primary and secondary performance constraints are sufficient for the purpose of generating reservoir descriptions which are very similar to the actual reservoir description and have very similar well performance.

Primary and k_{PAT} Constraints

This case study was performed using all performance constraints except CV_{k^*}, i.e., indirect performance constraints included k_{NW}, PV_T, PV_{DA} and k_{PAT}. Porosity and permeability field comparisons are shown in Figures 5.35 and 5.36. Probability of exceedance maps at the 30^{th} porosity percentile are illustrated in Figure 5.37. A close comparison of these figures to their counterparts obtained when all constraints were used (Figures 5.29, 5.30 and 5.31) shows there is a slight loss in the capability to reproduce the truth case spatial distributions when CV_{k^*} is not used as a constraint. These deficiencies are in terms of local, not global spatial properties.

Since CV_{k^*} is a waterflood efficiency constraint, the biggest impact on not including it as a constraint should be in the resulting water breakthrough times and WOR's of the total field and individual wells. This is confirmed when comparing total field and

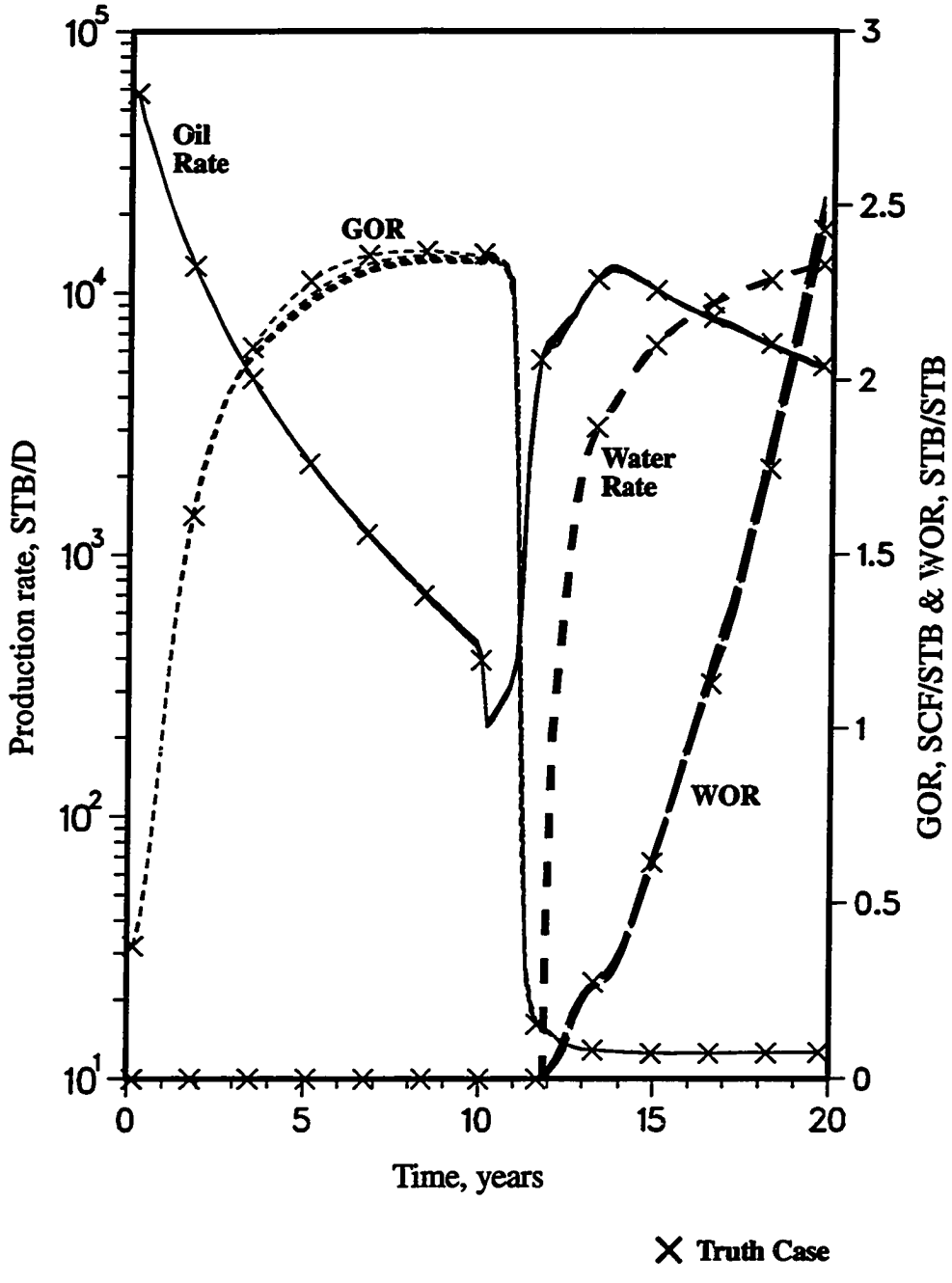

Figure 5.32 - Comparison of full-field truth case performance vs. performance of 10 reservoir descriptions generated using conventional, k_{NW}, PV_T, PV_{DA}, CV_{k^*} and k_{PAT} constraints

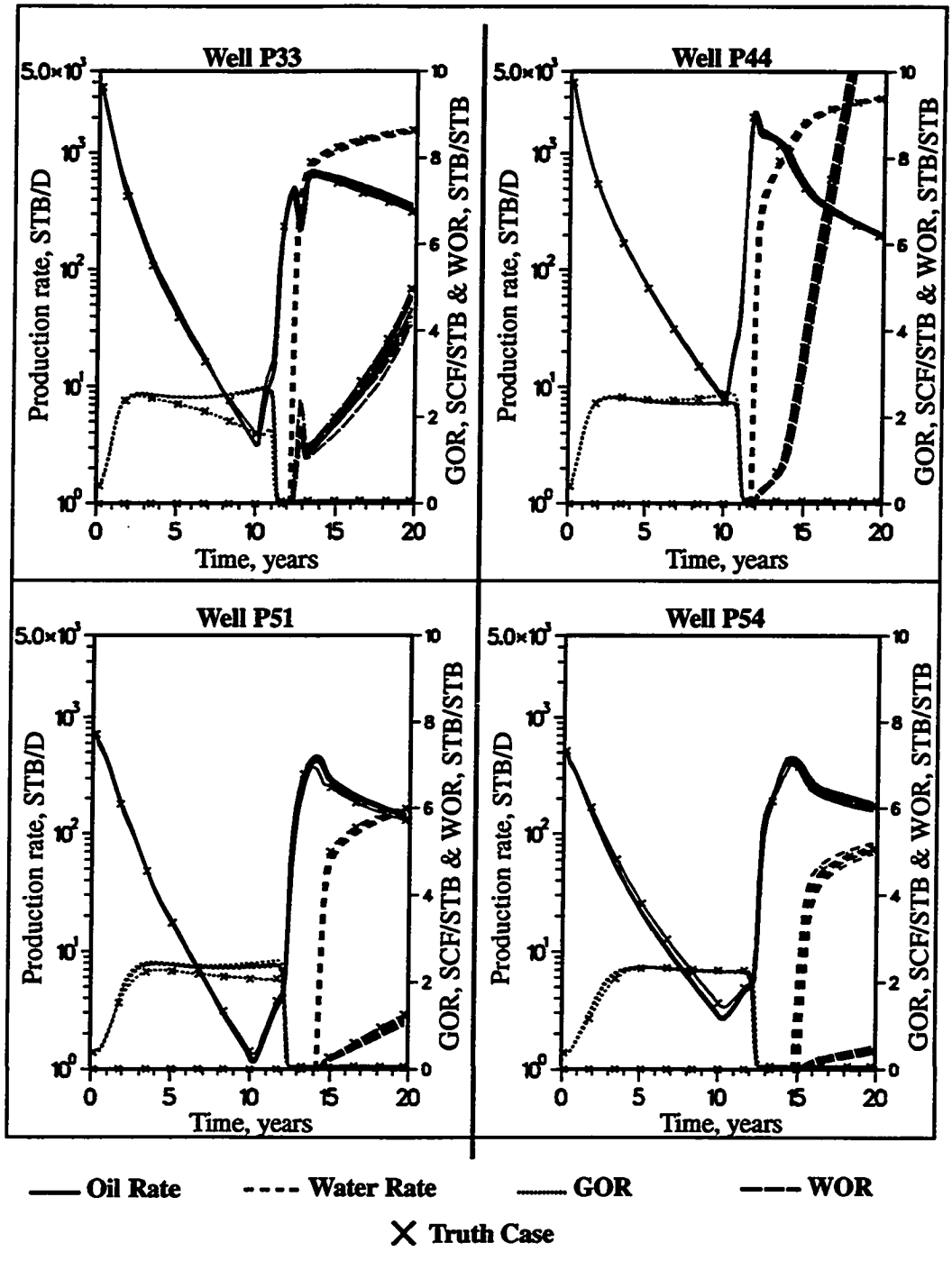

Figure 5.33 - Performance plots for Wells P33, P44, P51 and P54; full-field reservoir descriptions based on conventional, k_{NW}, PV_T, PV_{DA}, CV_{k*} and k_{PAT} constraints

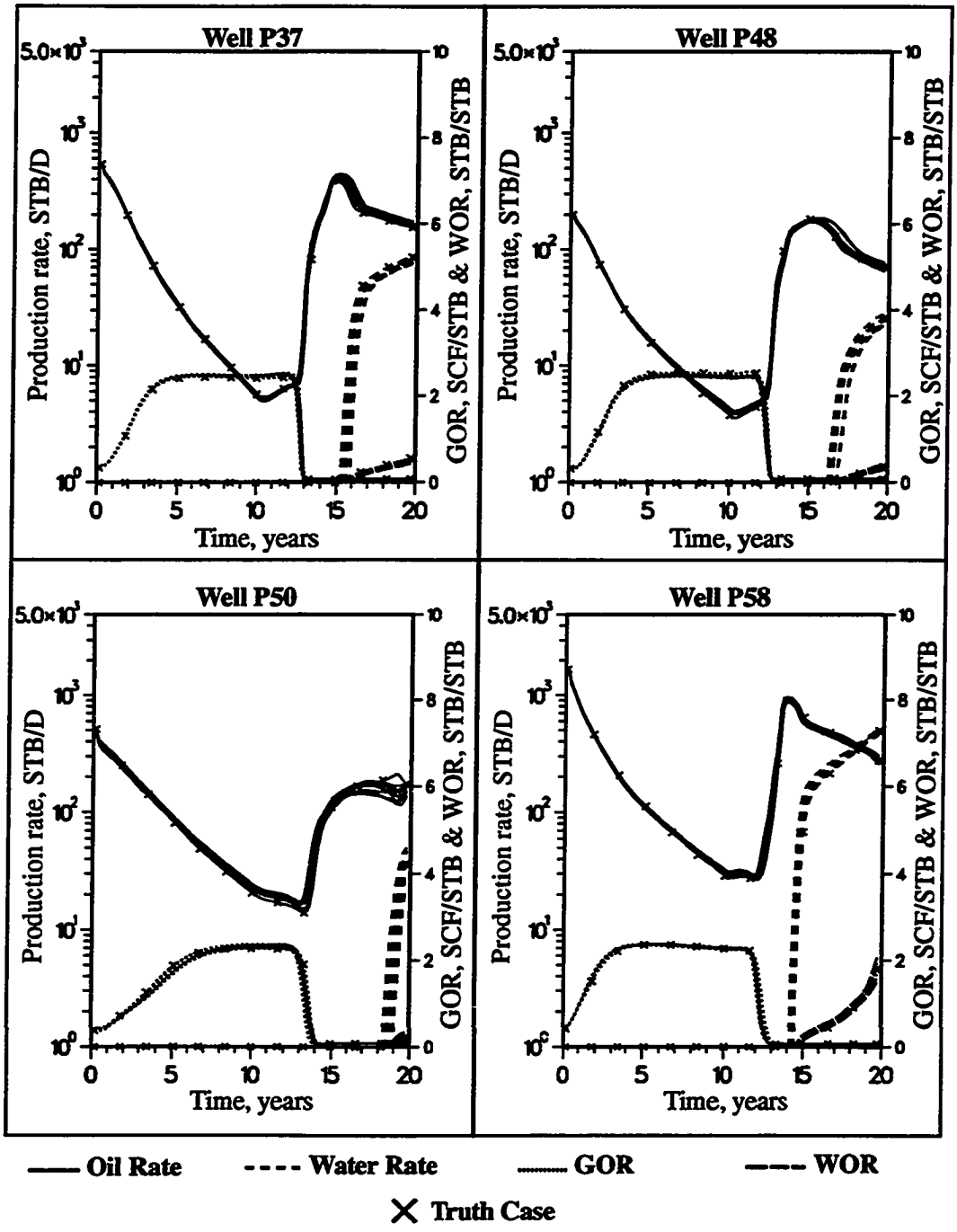

Figure 5.34 - Performance plots for Wells P37, P48, P50 and P58; full-field reservoir descriptions based on conventional, k_{NW}, PV_T, PV_{DA}, CV_{k^*} and k_{PAT} constraints

Exhaustive

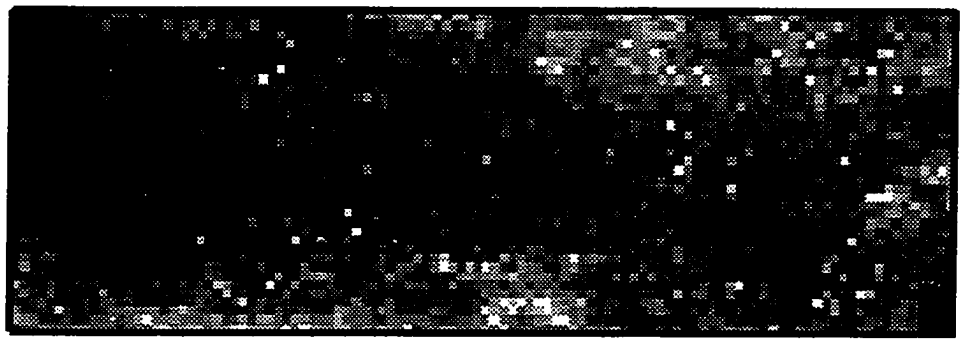

All Indirect Performance Constraints Except CV_{k^*}

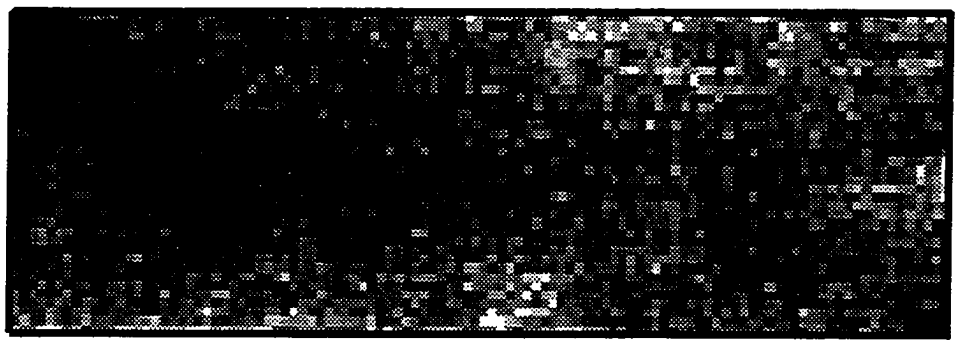

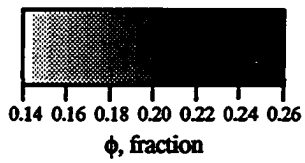

Figure 5.35 - Comparison of full-field exhaustive porosity field to porosity realization obtained using conventional, k_{NW}, PV_T, PV_{DA} and k_{PAT} constraints

Exhaustive

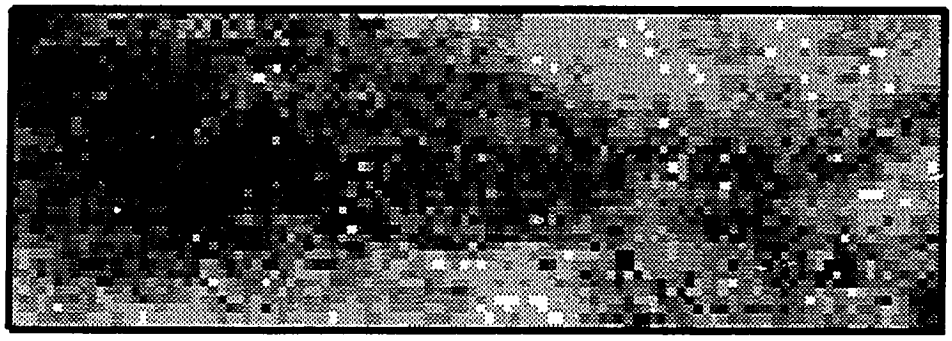

All Indirect Performance Constraints Except CV_{k^*}

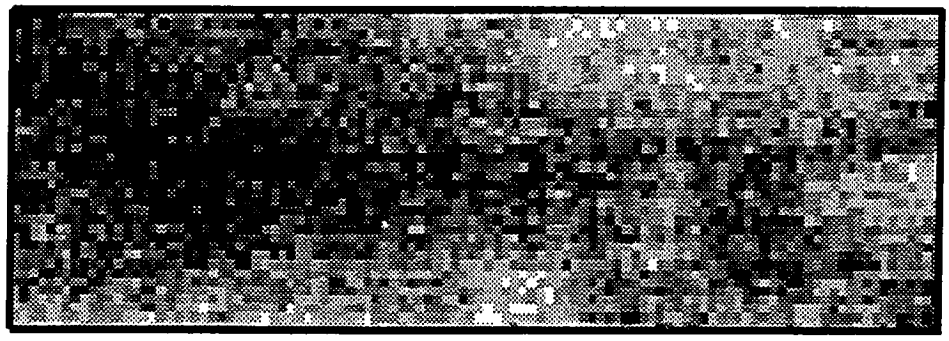

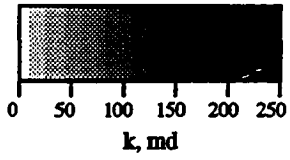

Figure 5.36 - Comparison of full-field exhaustive permeability field to permeability field obtained using conventional, k_{NW}, PV_T, PV_{DA} and k_{PAT} constraints

Full-Field Truth Case

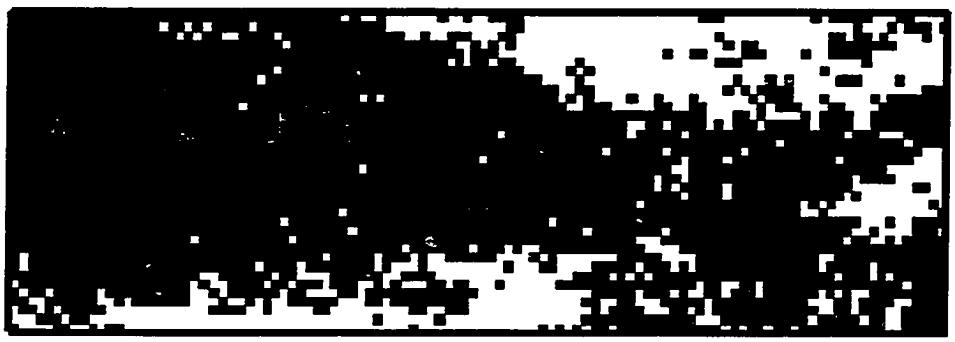

All Indirect Performance Constraints Except CV_{k*}

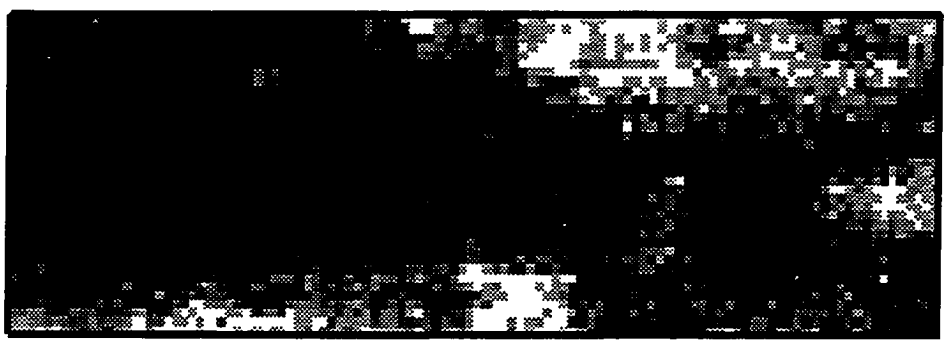

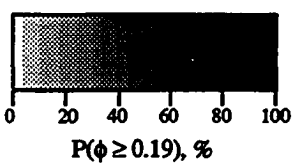

Figure 5.37 - Comparison of porosity probability of exceedance maps at the 30th porosity percentile; full-field truth case vs. results obtained using conventional, k_{NW}, PV_T, PV_{DA} and k_{PAT} constraints

individual well performance plots of the case study (Figures 5.38 - 5.40) to those based on using all performance constraints (Figures 5.32 - 5.34). The truth case waterflood performance is slightly better reproduced when CV_{k^*} is included as a constraint. Based on the results of the previous case studies, it is believed that the importance of CV_{k^*} increases when strong directional permeability trends exist between specific injector/producer pairs.

Primary and CV_{k^*} Constraints

One additional case study was made, this time all primary and secondary constraints were included except k_{PAT}. Comparisons of these results to the truth case results are summarized in Figures 5.41 - 5.46. The spatial distribution maps (Figures 5.41 - 5.43) indicate that ignoring the k_{PAT} constraint has about the same impact as ignoring the CV_{k^*} constraint, i.e., there are a few more local inconsistencies between the truth case spatial distributions and the resulting realizations when compared to the results obtained when all performance constraints are included.

Total field and individual well performance plots are included in Figures 5.44 - 5.46. Although the total field performance for the 10 alternative reservoir descriptions compare as favorably with the truth case as the previous case study (no CV_{k^*} constraint) did, some of the individual well performances do not compare as favorably. These results support the conclusion that the relative importance of the two secondary performance constraints, CV_{k^*} and k_{PAT}, is case dependent. In some cases it is more important to honor the effective permeability level of an injector/producer area of influence than the connectivity between the two wells. In other cases, it is more important to honor the connectivity. This will depend not only on the reservoir properties directly between two wells, but will also be dependent on the properties of adjacent wells since the effect of an injector/producer k_{PAT} value is dependent on offset injector/producer pair k_{PAT} values.

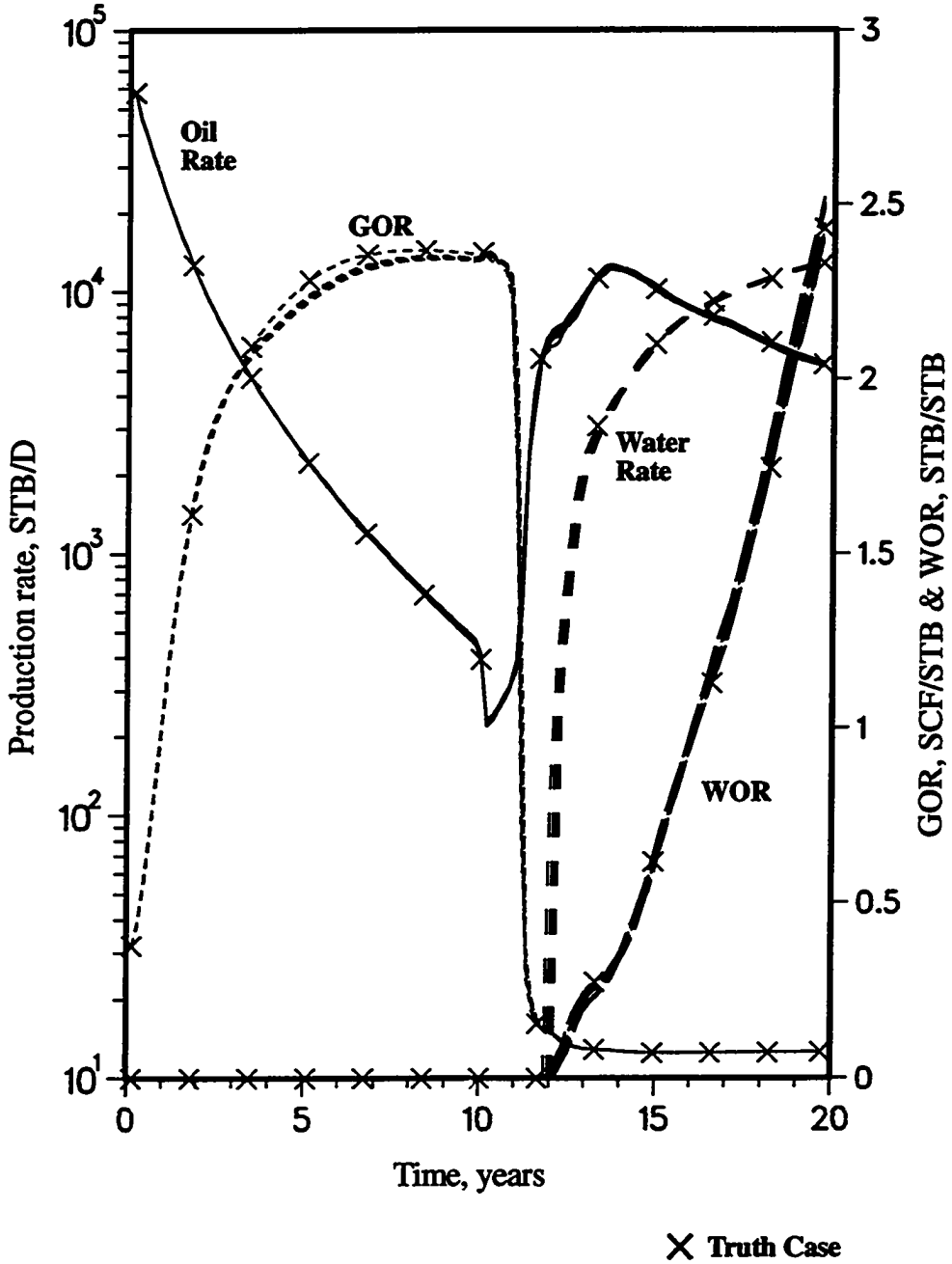

Figure 5.38 - Comparison of full-field truth case performance vs. performance of 10 reservoir descriptions generated using conventional, k_{NW}, PV_T, PV_{DA} and k_{PAT} constraints

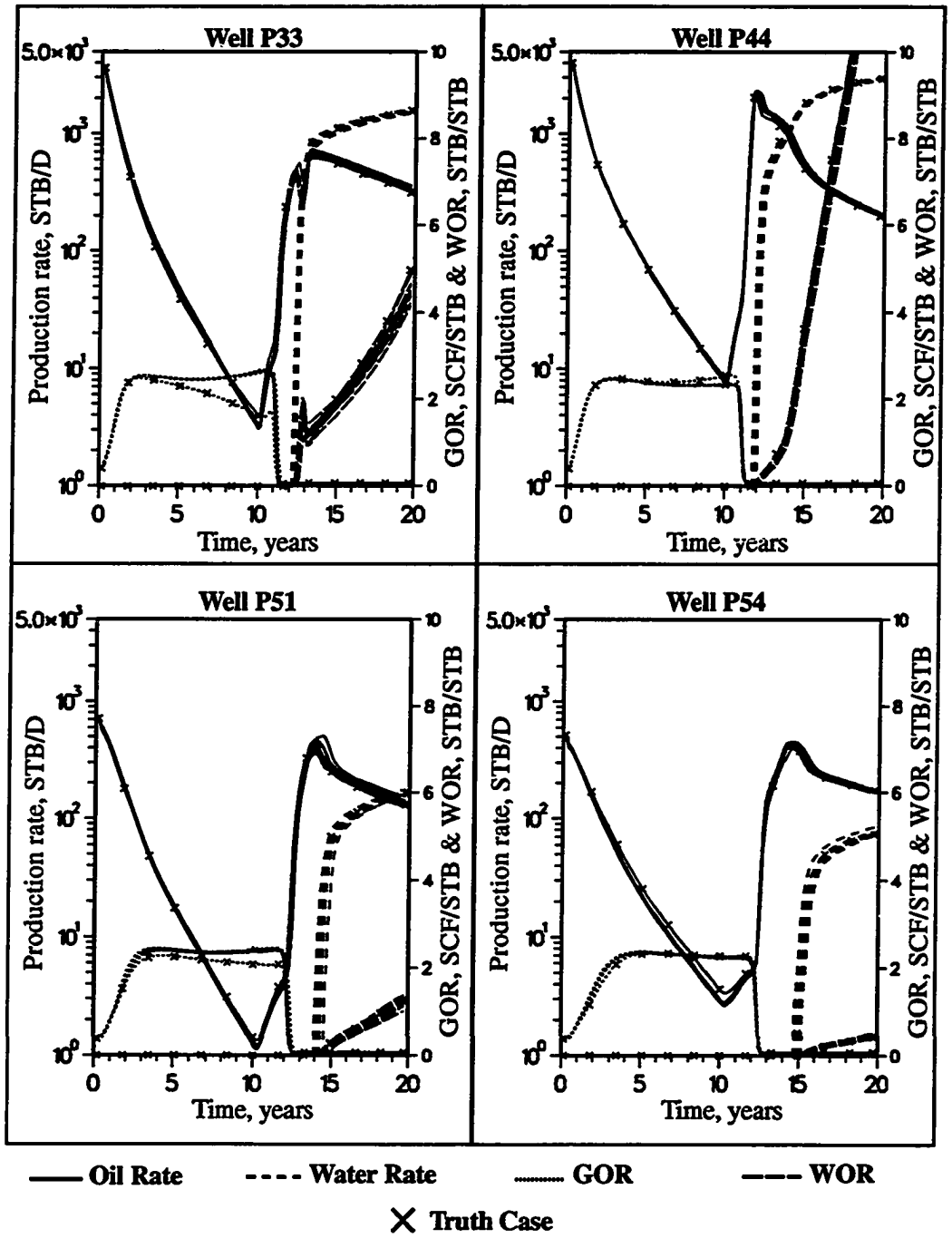

Figure 5.39 - Performance plots for Wells P33, P44, P51 and P54; full-field reservoir descriptions based on conventional, k_{NW}, PV_T, PV_{DA} and k_{PAT} constraints

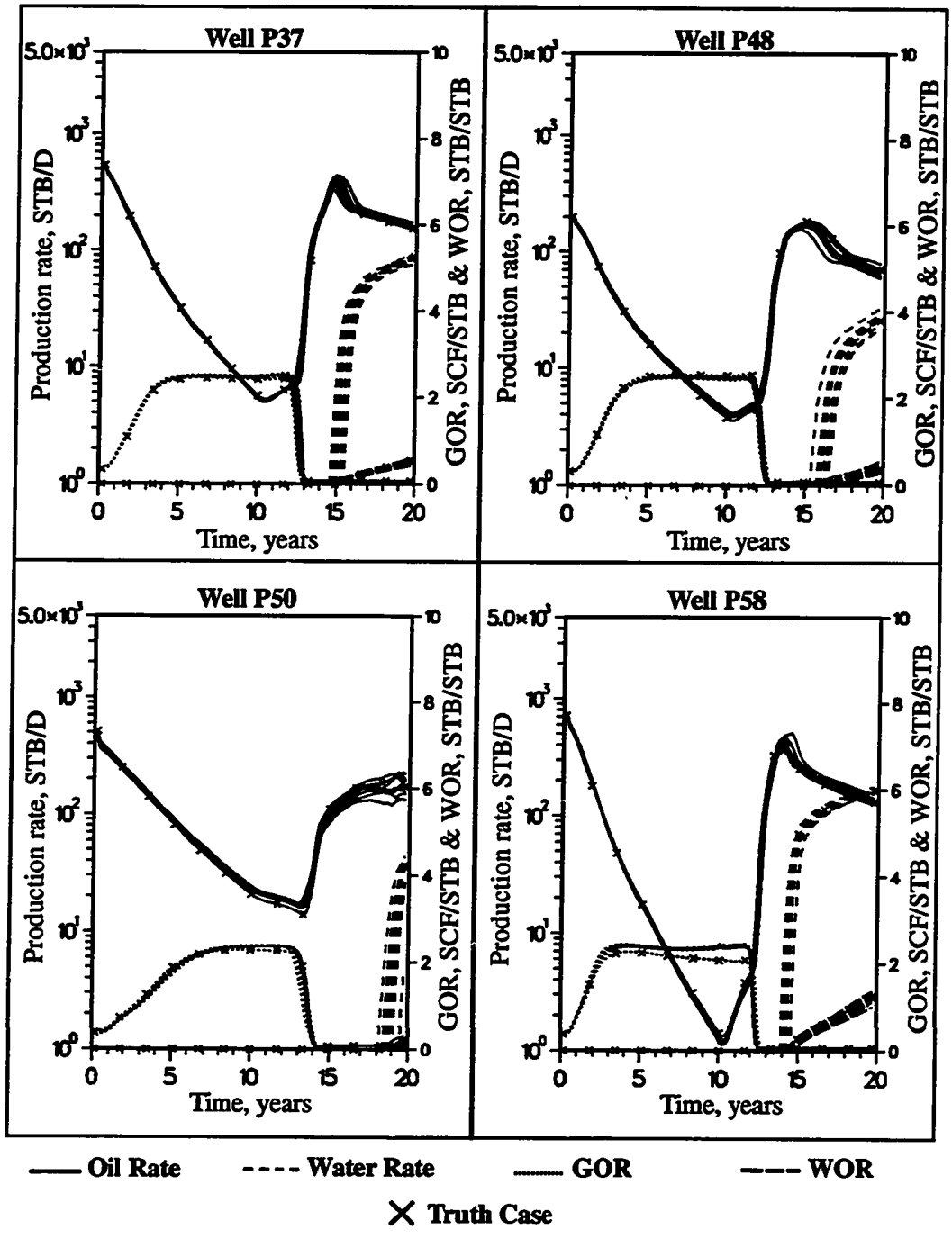

Figure 5.40 - Performance plots for Wells P37, P48, P50 and P58; full-field reservoir descriptions based on conventional, k_{NW}, PV_T, PV_{DA} and k_{PAT} constraints

Exhaustive

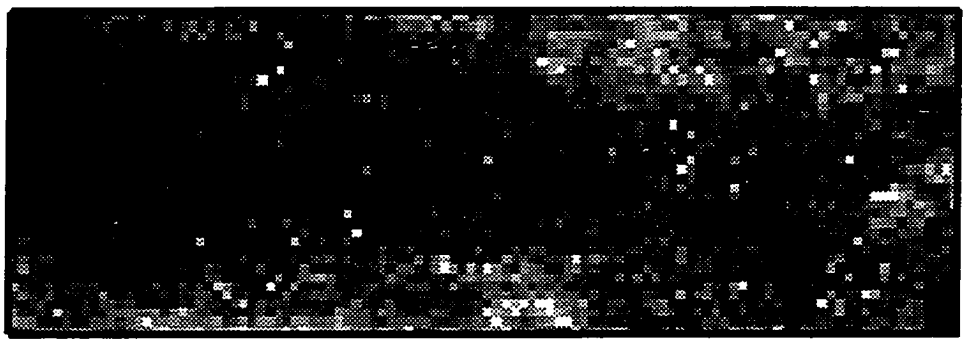

All Indirect Performance Constraints Except k_{PAT}

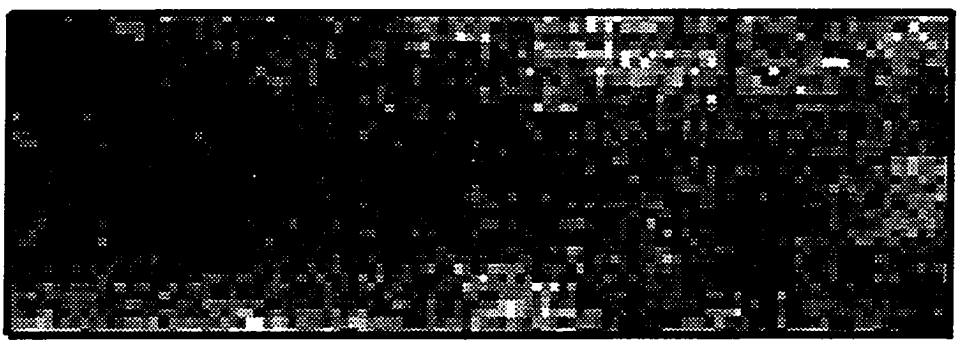

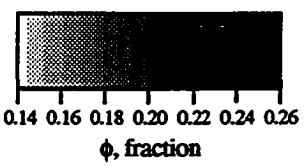

Figure 5.41 - Comparison of full-field exhaustive porosity field to porosity realization obtained using conventional, k_{NW}, PV_T, PV_{DA} and CV_{k^*} constraints

Exhaustive

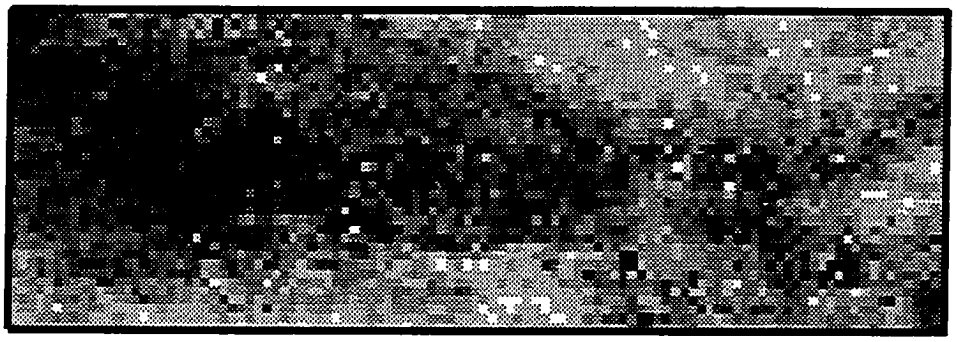

All Indirect Performance Constraints Except k_{PAT}

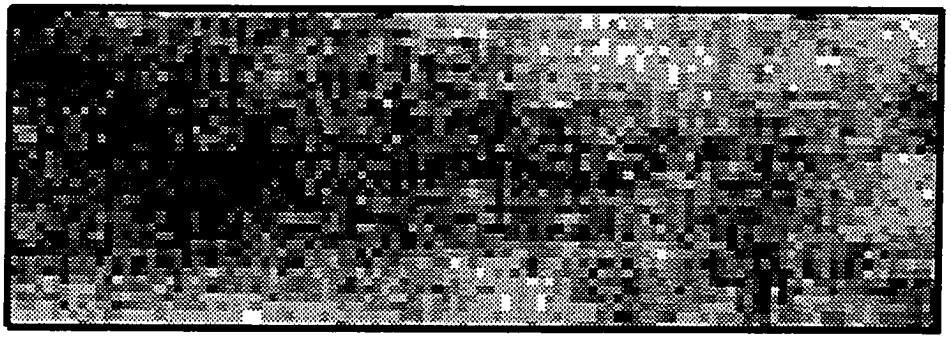

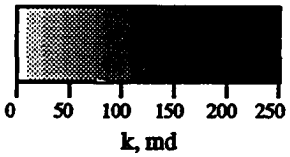

Figure 5.42 - Comparison of full-field exhaustive permeability field to permeability field obtained using conventional, k_{NW}, PV_T, PV_{DA} and CV_{k^*} constraints

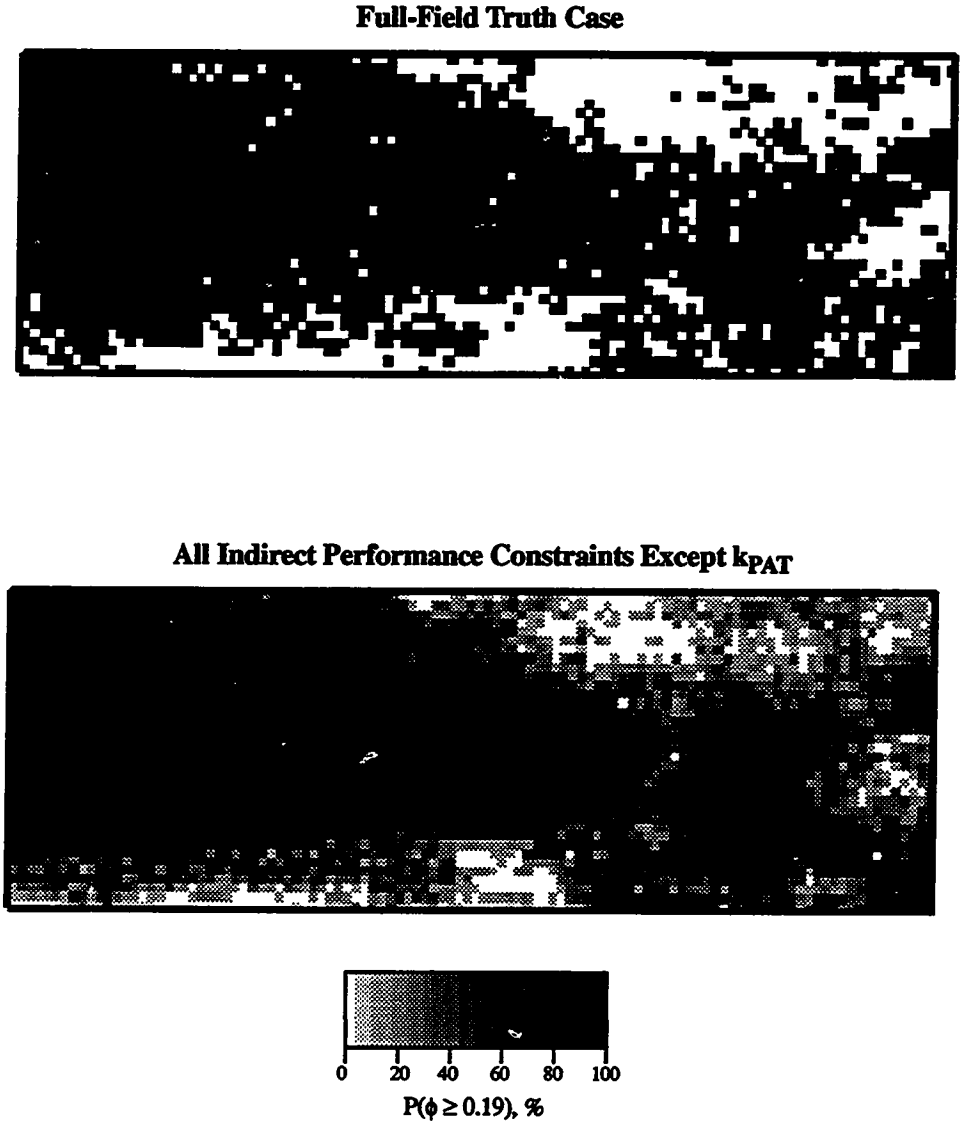

Figure 5.43 - Comparison of porosity probability of exceedance maps at the 30th porosity percentile; full-field truth case vs. results obtained using conventional, k_{NW}, PV_T, PV_{DA} and CV_{k^*} constraints

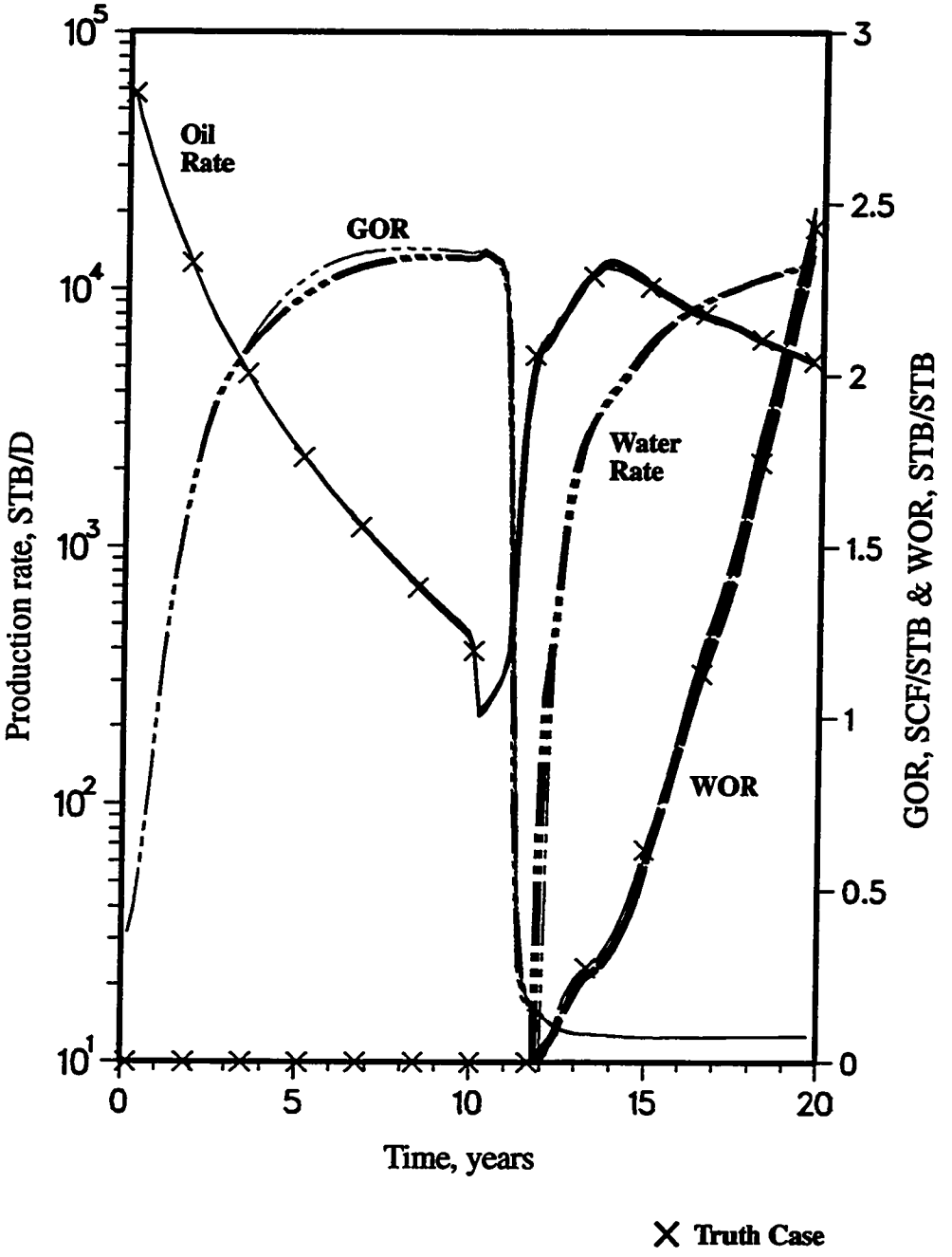

Figure 5.44 - Comparison of full-field truth case performance vs. performance of 10 reservoir descriptions generated using conventional, k_{NW}, PV_T, PV_{DA} and CV_{k^*} constraints

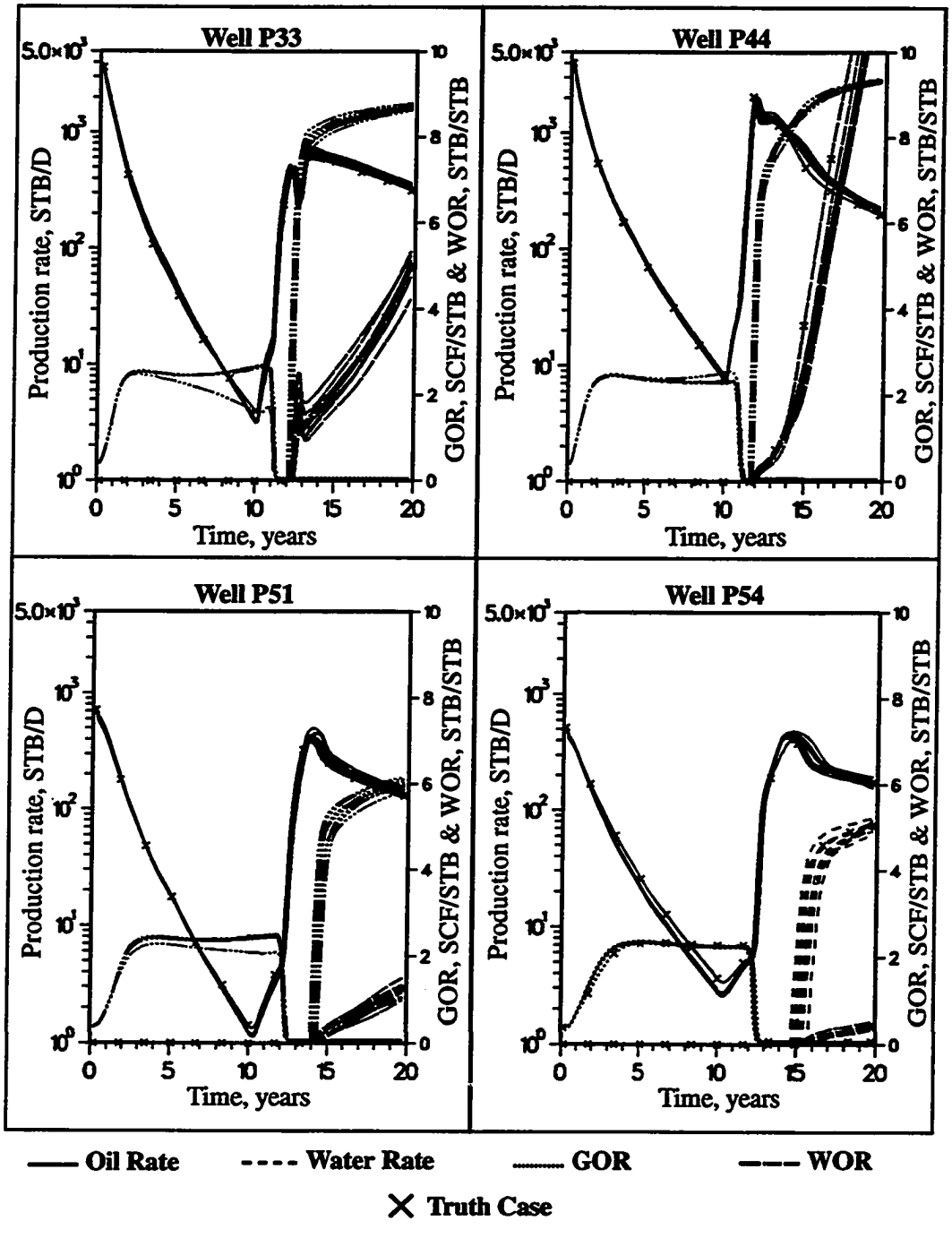

Figure 5.45 - Performance plots for Wells P33, P44, P51 and P54; full-field reservoir descriptions based on conventional, k_{NW}, PV_T, PV_{DA} and CV_{k*} constraints

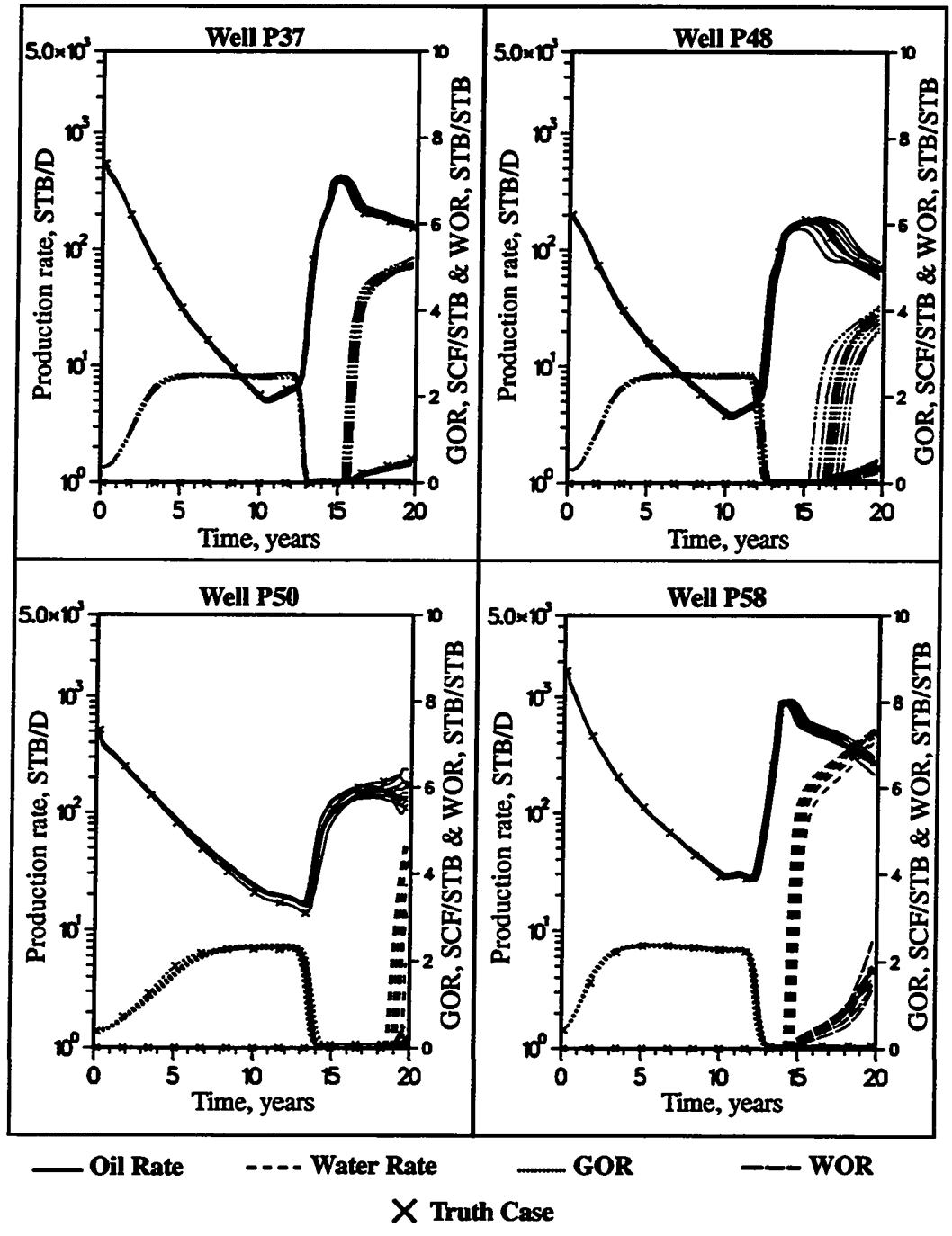

Figure 5.46 - Performance plots for Wells P37, P48, P50 and P58; full-field reservoir descriptions based on conventional, k_{NW}, PV_T, PV_{DA} and CV_{k^*} constraints

Summary of Results

This two-dimensional full-field study used the results from previous chapters to develop and test an integrated conditional simulation approach. Conventional and indirect performance constraints were used to simultaneously generate porosity and permeability fields. Sensitivities were performed to determine the relative contribution of the various indirect performance constraints. The results were evaluated by comparing simulated primary and waterflood performance and spatial distributions of porosity and permeability to the "truth case" results. Probability of exceedance maps were used to quantify the degree of spatial distribution uncertainty.

Well data were found to provide reasonable estimates of the exhaustive univariate statistics and spatial correlation structures of pay thickness, permeability and porosity. The spatial distributions of permeability and porosity and simulated well performance compared extremely well with the truth case when all conventional and indirect performance constraints were applied. Considering the large number of constraints (327 objective function components), this particular evaluation underscores the flexibility and robustness of the developed methodology.

The various combinations of indirect performance constraints investigated were consistent with the order in which the appropriate information would typically become available. The results obtained when just conventional and the near well effective permeability constraint were imposed were sufficient for honoring primary performance but inadequate for reproducing waterflood performance and spatial distributions of porosity and permeability. Total field performance was well reproduced in each case, indicating that it is only necessary to honor global spatial characteristics if the objectives do not include matching individual well performances. The addition of pore volume constraints greatly reduced the spread in individual well waterflood performance and the correctness of the porosity and permeability realizations. It was noted that this improvement was greatly influenced by the assumed one-to-one correlation between porosity and perme-

ability. The relative importance of the two waterflood constraints, CV_{k^*} and k_{PAT}, was found to be case and well dependent. Injector/producer pairs which have unusually high or low reservoir connectivity would require a CV_{k^*} constraint and those pairs which have anomalously high or low k_{PAT} values would require a k_{PAT} constraint. In either case, the inclusion of at least one of the waterflood indirect performance constraints improves results compared to when only primary indirect performance constraints are used.

CHAPTER VI

CONCLUSIONS

Although world-wide reserves are dwindling, substantial quantities of remaining hydrocarbon reserves exist. A better understanding of the internal reservoir architecture is required before these reserves can be extracted economically. This requires the development of better reservoir characterization techniques. The literature search documented in Chapter I indicates that although significant recent improvements have been made in stochastic modeling technology, little has been done to allow integration of performance data when generating alternative reservoir descriptions. The inclusion of performance data is very important because such data represent the proper scale and type of information desired when performing reservoir simulation studies. This dissertation investigated means for integrating performance data into stochastic reservoir descriptions. The intent is to use all available data in developing alternative reservoir descriptions so that the uncertainty in forecasting future rates and reserves can be minimized.

A three-dimensional reservoir description was developed in Chapter II using actual data from the Burbank Field located in Osage County, Oklahoma. Although there was no attempt to reproduce historical well performance, the resulting simulated well performances were similar in variability and magnitude as that of the actual wells. This synthetic reservoir description and resulting simulated primary and waterflood performance can be used to evaluate reservoir description methodologies. It was shown that well data based kriged estimates can be significantly in error when compared to actual properties. Important fluid flow characteristics such as spatial variability and anisotropy are not captured using kriging. Conditional simulation provides the means for generating these spatial characteristics.

A mathematical description of the simulated annealing algorithm was presented in

Chapter III. The potential for using this optimization procedure for integrating many different data types to obtain alternative reservoir descriptions was emphasized. The main purpose of Chapter III was to identify reservoir properties which could be estimated from primary performance data and subsequently be used as conditional simulation constraints. In general, it was found that primary performance is rather insensitive to reservoir heterogeneities (fault/fracture effects were not addressed). It was concluded that near well effective permeability dominates early time primary well performance. This was illustrated by showing the strong correlation between initial producing rates and near well effective permeability. The geometric mean was shown to adequately represent the near well effective permeability. The inclusion of near well effective permeability as an indirect performance constraint within the simulated annealing framework was shown to result in permeability fields which all have similar early time primary performance characteristics. Fortunately, the parameter k_{NW} can be estimated early in the life of a well from well test data.

The impact of porosity heterogeneities on well performance was also investigated in Chapter III. Results indicate that porosity heterogeneity characteristics cannot be estimated from primary well performance. However, it was shown that total field and well drainage area pore volume constraints should be used as conditional simulation constraints. Pore volume estimates are often available by combining available well and primary performance data with volumetric or material balance calculation methods.

The influence of reservoir heterogeneities on waterflood performance was investigated in Chapter IV. Waterflood performance was found to be much more sensitive to reservoir heterogeneities than primary performance. Reservoir connectivity was identified as being one of the most important reservoir properties which could be quantified from waterflood performance. Two reservoir connectivity measures were defined, p_{tH} and CV_{k^*}, and were found to be good indirect performance constraints. One-quarter five-spot pattern case studies indicated that the second reservoir connectivity measure, CV_{k^*},

was the more robust indirect performance constraint. It was shown that so-called "equally probable" realizations of permeability can result in widely varying simulated well performance. These studies also illustrated the importance of including k_{NW} as an indirect performance constraint when generating alternative permeability fields having similar waterflood performance. Based on the strong correlation between CV_{k*} and two important waterflood efficiency measures (water breakthrough time and cumulative water-oil ratio), it was concluded that such correlations could be used to estimate the value of CV_{k*} from historical performance and waterflood simulation sensitivities. Probability of exceedance maps were shown to be useful tools for quantifying uncertainty of spatial reservoir properties and comparing capabilities of conditional simulation techniques. The inclusion of k_{NW} and CV_{k*} as indirect performance constraints was shown to reduce the uncertainty in identifying low and high permeability regions. Such information is important when evaluating potential operating strategies, such as infill drilling.

The application of simulated annealing using indirect performance constraints was also evaluated using full five-spot pattern simulations. This was done to evaluate the impact of multiple injector/producer pairs. It was discovered that the synthetic, orthogonal no-flow boundaries imposed by the numerical model created anomalous waterflood performance characteristics when using heterogeneous spatial distributions of permeability. Edge grid block permeabilities overly influenced the simulated results.

Extended five-spot pattern synthetic case studies showed that the effective permeability between an injector/producer pair, k_{PAT}, can be another important indirect performance constraint. This parameter becomes important if significant variations in k_{PAT} exists amongst offset injector/producer pairs. The relative importance of the indirect waterflood constraints CV_{k*} and k_{PAT} is case dependent, i.e., injector/producer pairs which have strong connectivity characteristics will require the CV_{k*} constraint whereas patterns having large variations in the effective permeability of injector/producer areas of influence will require the k_{PAT} constraint. It was shown that conventional conditional

simulation constraints (well conditioning data, univariate distribution and variogram) do not reduce the uncertainty in identifying low and high permeability regions. However, the inclusion of k_{NW}, k_{PAT} and CV_{k*} as indirect performance constraints within the simulated annealing framework was shown to greatly reduce the uncertainty in the spatial distribution of permeability. Results obtained which did not include the permeability variogram as a constraint illustrated the importance of integrating geological information into the reservoir description. This particular case study emphasized the problem of non-uniqueness associated with reservoir description. It was shown that innumerable permeability realizations could be generated which were nearly random spatial distributions, but exhibited the same simulated waterflood performance as highly correlated permeability distributions. These results demonstrate that the spatial correlation structure cannot be extracted from historical primary and waterflood performances.

Primary and waterflood indirect performance constraints were applied to a two-dimensional full-field case study in Chapter V. This required simultaneously simulating porosity and permeability realizations so that all constraints could be honored. The successful application of all constraints (327 components to the objective function) in generating extremely realistic reservoir descriptions illustrated the flexibility and robustness of the technique. Total field performance and primary well performance were fairly easy to reproduce; only spatial correlation and k_{NW} constraints were required. Discrepancies resulted when actual secondary well performances were compared to simulated well performances. This case study concluded that improvements could be obtained by adding additional indirect performance constraints. As more constraints were added, the ability to reproduce the actual reservoir description and well performances was improved. However, certain wells required only one of the two imposed waterflood constraints (CV_{k*} and k_{PAT}).

In summary, this investigation identified and quantified important primary and waterflood performance constraints. A conditional simulation technique was developed

which incorporated these constraints and conventional constraints. The resulting alternative reservoir descriptions can be considered "equally probable" in that all reservoir and field data are honored. This technique can be used to significantly reduce uncertainty when evaluating alternative operational strategies.

NOMENCLATURE

Symbols

B	= formation volume factor
B_g	= gas formation volume factor
B_o	= oil formation volume factor
B/D	= barrels per day
cdf	= cumulative distribution function
C_H	= fractional area connected of permeabilities exceeding cutoff
C_L	= fractional area connected of permeabilities below cutoff
CV_{k*}	= coefficient of variation for flow pattern segment normalized permeability
E	= expected value
f_T	= annealing temperature multiplicative factor
GOR	= gas-oil ratio
h	= lag interval
h	= formation thickness
k	= permeability
k_e	= effective permeability
$k_{e,a}$	= actual, or experimental effective permeability
$k_{e,new}$	= effective permeability after swap
$k_{e,old}$	= effective permeability prior to swap
$k_{e,t}$	= true, or model effective permeability
k_i	= inner region permeability for composite system
k_i	= permeability at *i*th location prior to swap

$k_{i'}$ = permeability at *i*th location following swap

k_{NW} = effective near well permeability

$k_{NW,a}$ = actual, or experimental effective near well permeability

k_{NWi} = effective near well permeability of injection well

k_{NWp} = effective near well permeability of producer

$k_{NW,t}$ = true, or model effective near well permeability

k_o = outer region permeability for composite system

k_{PAT} = effective permeability of injector/producer area of influence

k^* = flow pattern segment normalized permeability

l = flow pattern segment length

l_D = dimensionless flow pattern segment length

l_o = interwell diagonal length

MMBO = million barrels of oil

N_b = number of grid blocks

N_D = number of variogram directions

N_f = number of functions comprising the objective function

N_L = number of lag intervals

N_S = number of flow pattern segments

$N_{S,a}$ = maximum number of accepted swaps

$N_{S,t}$ = maximum number of tried swaps

O = objective function

O_i = initial objective function

$O_{k_{e,i}}$ = initial objective function of the effective permeability function

$O_{k_{NW,i}}$ = initial objective function of the effective near well permeability function

OOIP = original oil-in-place

O_T = total objective function

p = pressure

p_e = external boundary pressure

p_i = inner region permeability for composite system

p_o = outer region permeability for composite system

p_t = permeability percentile connectivity threshold

p_{tH} = permeability percentile threshold for connectivity of high values

p_{tL} = permeability percentile threshold for connectivity of low values

p_{wf} = flowing wellbore pressure

q_r = bottomhole flowrate

r = radial distance

r_e = external boundary radius

r_i = radius of inner region for composite system

R_s = solution gas-oil ratio

r_w = wellbore radius

S_o = oil saturation

STB/D = stock tank barrels per day

T = annealing temperature

T_s = specified annealing temperature

T_o = initial annealing temperature

V = variable value before swap

V_a = actual, or experimental variable value

V_{new} = updated variable value

V_{old} = previous variable value

v_r = radial velocity

V_t = true, or model variable value

V' = variable value after swap

w_f = weighting factor

WOR = water-oil ratio

w_v = variogram weighting factor

w_{k_e} = effective permeability weighting factor

$\gamma(h)$ = variogram at lag interval h

$\gamma_a(h)$ = actual, or experimental variogram at lag interval h

$\gamma_t(h)$ = true, or model variogram at lag interval h

$\hat{\gamma}(h)$ = variogram estimator at lag interval h

κ = k_I/k_O, ratio of inner region to outer region permeability

λ_D = dimensionless correlation length

μ = mean

μ_{k^*} = flow pattern segment normalized permeability mean

μ = viscosity

μ_g = gas viscosity

μ_o = oil viscosity

ϕ = porosity

σ = standard deviation

σ_{k^*} = flow pattern segment normalized permeability standard deviation

π = pi, 3.1416...

REFERENCES

1. Jacquard, P.: "Improved Oil Recovery in the Global Energy Perspective," paper presented at the 1991 6th European Symposium on Improved Oil Recovery, Stavanger, May 21-23.
2. Chierici, G.L.: "Economically improving oil recovery by advanced reservoir management," Journal of Petroleum Science and Engineering (August 1992) 205-219.
3. Fisher, W.L.: "Texas crude oil--some positive trends," Interstate Oil Compact Commission, 1985 midyear meeting, Austin, TX.
4. Dubrule, O.: "A Review of Stochastic Models for Petroleum Reservoirs," paper presented at the 1988 British Society Reservoir Geologists Meeting on Quantification of Sediment Body Geometries and Their Internal Heterogeneities, London, March 1-2.
5. Haldorsen, H.H., Brand, P.J. and MacDonald, C.J.: "Review of the Stochastic Nature of Reservoirs," *Mathematics in Oil Production*, S. Edwards and P. King (editors), Oxford Science Publications, Clarendon Press, Oxford (1988) 109-209.
6. Haldorsen, H.H. and MacDonald, C.J.: "Stochastic Modeling of Underground Reservoir Facies (SMURF)," paper SPE 16751 presented at the 1987 Annual Technical Conference and Exhibition, Dallas, TX, Sept. 27-30.
7. Haldorsen, H.H. and Damsleth, E.: "Stochastic Modeling," Journal of Petroleum Technology (April 1990) 404-12.

8. Alabert, F.G. and Modct, V.: "Stochastic Models of Reservoir Heterogeneity: Impact on Connectivity and Average Permeabilities," paper SPE 24893 presented at the 1992 SPE Annual Technical Conference and Exhibition, Washington, D.C., Oct. 4-7.

9. Delhomme, A.E.K. and Giannesini, J.F.: "New Reservoir Description Techniques Improve Simulation Results in Hassi-Messaoud Field, Algeria, paper SPE 8435 presented at the 1979 SPE Annual Technical Conference and Exhibition, Las Vegas, NV, Sept. 23-26.

10. Clementsen, V., Hurst, A., Knarud, R. and Omre, H.: "A Computer Program for Evaluation of Fluvial Reservoirs," paper presented at the 1989 Intl. Conference of North Sea Oil and Gas Reservoirs, Trondheim, Norway, June 8-11.

11. Henriquez, A., Tyler, K. and Hurst, A.: "Characterization of Fluvial Sedimentology for Reservoir Simulation Modeling," SPE Formation Evaluation (Sept. 1990) 211-216.

12. Chiles, J.P.: "Fractal and Geostatistical Methods for Modeling of a Fracture Network," Mathematical Geology (1988) vol. 20, 631-654.

13. Journel, A.G. and Huijbregts, C.J.: "*Mining Geostatistics*, Academic Press, New York, NY (1978).

14. Clark, I.: *Practical Geostatistics*, Elsevier Science Publishers, New York, NY (1979).

15. David, M.: *Geostatistical Ore Reserve Estimation*, Elsevier Science Publishers, Amsterdam (1977).

16. Isaaks, E.H. and Srivastava, R.M.: *Applied Geostatistics*, Oxford University Press, New York, NY (1989).

17. Matheron, G.: *The Theory of Regionalized Variables and Its Applications*, Ecole des Mines, Fontainebleau, France (1971).

18. Kirkpatrick, S., Gelatt, C.D., Jr. and Vecchi, M.P.: "Optimization by Simulated Annealing," Science (May 13, 1983) 671-80.

19. Cerny, V.: "Thermodynamical Approach to the Traveling Salesman Problem: An Efficient Simulation Algorithm," Journal of Optimization Theory and Applications (1985) vol. 45, no. 1, 41-51.

20. Metropolis, N., Rosenbluth, A.W., Rosenbluth, M.N., Teller, A.G. and Teller, E.: "Equation of State Calculations by Fast Computing Machines," The Journal of Chemical Physics (June 1953) 1087-92.

21. Geman, S. and Geman, D.: "Stochastic Relaxation, Gibbs Distributions, and the Bayesian Restoration of Images," IEEE Transactions on Pattern Analysis and Machine Intelligence (Nov. 1984) vol. PAMI, no. 6, 721-41.

22. Aarts, E. and Korst, J.: *Simulated Annealing and Boltzmann Machines: A Stochastic Approach to Combinatorial Optimization and Neural Computing*, John Wiley & Sons Ltd., Chichester (1989).

23. Collins, N.E., Eglese, R.W. and Golden, B.L.: "Simulated Annealing - An Annotated Bibliography," *Simulated Annealing (SA) & Optimization: Modern Algorithms with VLSI, Optimal Design, and Missile Defense Applications*, M.E. Johnson (editor), American Sciences Press, New York, NY (1988) 209-307.

24. Farmer, C.L.: "Numerical Rocks, The Mathematical Generation of Reservoir Geology," paper presented at the 1989 Joint IMA/SPE European Conference, Cambridge University, July 25-27.

25. Perez, G.: *"Stochastic Conditional Simulation for Description of Reservoir Properties,"* Ph.D. dissertation, The University of Tulsa, Tulsa, OK (1991).

26. Deutsch, C.V.: *"Annealing Techniques Applied to Reservoir Modeling and the Integration of Geological and Engineering (Well Test) Data,"*, Ph.D. dissertation, Stanford University, Stanford, CA (1992).

27. Ouenes, A.: *"Application of Simulated Annealing to Reservoir Characterization and Petrophysics Inverse Problems,"* Ph.D. dissertation, New Mexico Tech, Socorro, NM (1992).

28. Haldorsen, H.H.: "Simulator Parameter Assignment and the Problem of Scale in Reservoir Engineering," *Reservoir Characterization*, L.W. Lake and H.B. Carroll, Jr. (editors), Academic Press, Inc. (1986) San Diego, CA.

29. Sharma, B., Honarpour, M.M., Szpakiewicz, M.J. and Schatzinger, R.A.: "Critical Heterogeneities in a Barrier Island Deposit and Their Influence on Various Recovery Processes," SPE Formation Evaluation (March 1990) 103-112.

30. Tyler, N. and Finley, R.J.: "Architectural Controls on the Recovery of Hydrocarbons from Sandstone Reservoirs," *The Three-Dimensional Facies Architecture of Terrigenous Clastic Sediments & Its Implications for Hydrocarbon Discovery & Recovery*, A.D. Miall and N. Tyler (editors), Society of Economic Paleontologists and Mineralogists (1991).

31. Hearn, C.L., Ebanks, W.J., Tye, R.S. and Ranganathan, V.: "Geological Factors Affecting Reservoir Performance of the Hartzog Draw Field, Wyoming," Journal of Petroleum Technology (1984) vol. 38, no. 8, 1335-1344.

32. Silseth, J.K., MacDonald, A.C., Alvestad, J., Buller A.T. and Torp, S.B.: "Impact of Flow-Unit Reservoir Description on Simulated Waterflood Performance," SPE Reservoir Engineering (Feb. 1993) 27-33.

33. MacDonald, A.C., Hoye, T.H., Lowry, P., Jacobsen, T., Aasen, J.O. and Grindheim, A.O.: "Stochastic flow unit modelling of a North Sea coastal-deltaic reservoir," First Break (April 1992) vol. 10, no. 4, 124-132.

34. Omre, H., Solna, K., Tjelmeland, H., Claesson, L., and Holter, C.: "Calcite Cementation: Description and Production Consequences," paper SPE 20607 presented at the 1990 Annual Technical Conference and Exhibition, New Orleans, LA, Sept. 23-26.

35. Silva, R.J., Niko, H., van den Bergh, J.N. and Sancevic, Z.A.: "Numerical Modeling of Gas and Water Injection in a Geologically Complex Volative Oil Reservoir in the Lake Maracaibo Area, Venezuela," paper SPE 18322 presented at the 1988 Annual Technical Conference and Exhibition, Houston, TX, Oct. 2-5.

36. Lucia, F.J. and Fogg, G.E.: "Geologic/Stochastic Mapping of Heterogeneity in a Carbonate Reservoir," Journal of Petroleum Technology (Oct. 1990) 1298-1303.

37. Weber, K.J. and van Geuns, L.C.: "Framework for Constructing Clastic Reservoir Simulation Modes," Journal of Petroleum Technology (Oct. 1990) 1248-1297.

38. Weber, K.J.: "How Heterogeneity Affects Oil Recovery," *Reservoir Characterization*, L.W. Lake and H.B. Carroll, Jr. (editors), Academic Press, Inc. (1986) San Diego, CA.

39. Barber, A.H., Jr., George, C.J., Stiles, L.H. and Thompson, B.B.: "Infill Drilling To Increase Reserves--Actual Experience in Nine Fields in Texas, Oklahoma, and Illinois," Journal of Petroleum Technology (Aug. 1983) 9-17.

40. Weber, K.J.: "Influence of Common Sedimentary Structures on Fluid Flow in Reservoir Models," Journal of Petroleum Technology (March 1982) 665-672.

41. Lowry, P. and Raheim, A.: "Characterization of Delta Front Sandstones from a Fluvial-Dominated Delta System," *Reservoir Characterization*, L.W. Lake and H.B. Carroll, Jr. (editors), Academic Press, Inc. (1986) San Diego, CA.

42. Haldorsen, H.H. and Lake, L.W.: "A New Approach to Shale Management in Field-Scale Models," Journal of Petroleum Technology (August 1984) 447-457.

43. Budding, M.C., Paardekam, A.H.M. and van Rossem, S.J.: "3D Connectivity and Architecture in Sandstone Reservoirs," paper SPE 22342 presented at the 1992 International Meeting on Petroleum Engineering, Beijing, China, March 24-27.

44. Handyside, D.D., Karaoguz, O.K., Deskin, R.H. and Mattson, G.A.: "A Practical Application of Stochastic Modeling Techniques for Turbidite Reservoirs," paper SPE 24892 presented at the 1992 SPE Annual Technical Conference and Exhibition, Washington, D.C., Oct. 4-7.

45. Budding, M.C., Eastwood, K.M., Herwweijer, J.C., Livera, S.E., Paardekam, A.H.M. and Regtien, J.M.M.: "Probabilistic Modelling of Discontinuous Reservoirs," paper presented at the 1988 Annual Convention of the Indonesian Petroleum Association, Oct.

46. Bridge, J. and Leeder, M.: "A simulation model of alluvial stratigraphy," Sedimentology (1979) vol. 26, 335-348.

47. Begg, S. and Williams, J.: "Algorithms for Generating and Analysing Sand-Body Distributions," *Reservoir Characterization II*, L.W. Lake, H.B. Carroll, Jr. and T.C. Wesson (editors), Academic Press, Inc. (1991) San Diego, CA.

48. Journel, A. and Alabert, F.: "Focusing on Spatial Connectivity of Extreme-Valued Attributes: Stochastic Indicator Models of Reservoir Heterogeneities," paper SPE 18324 presented at the 1988 Annual Technical Conference and Exhibition, Houston, TX, Oct. 2-5.

49. Srivastava, R.: "An Application of Geostatistical Methods for Risk Analysis in Reservoir Management," paper SPE 20608 presented at the 1990 Annual Technical Conference and Exhibition, New Orleans, LA, Sept. 23-36.

50. Jacquard, P. and Jain, C.: "Permeability Distribution From Field Pressure Data," Society of Petroleum Engineers Journal (Dec. 1965) 281-94.

51. Coats, K.H., Dempsey, J.R. and Henderson, J.H.: "A New Technique for Determining Reservoir Description From Field Performance," Society of Petroleum Engineers Journal (March 1970) 325-37.

52. Chavant, G., Dupuy, M. and Lemonnier, P.: "History-Matching by Use of Optimal Theory," Society of Petroleum Engineers Journal (Feb. 1975) 74-86.

53. Watson, A.T., Seinfeld, J.H., Gavalas, G.R. and Woo, P.T.: "History-Matching in Two-Phase Petroleum Reservoirs," Society of Petroleum Engineers Journal (Dec. 1980) 521-32.

54. Carlson, F.M. and Stein, M.H.: "Automatic Waterflood History Matching Using Dimensionless Performance Curves," paper SPE 24897 presented at the 1992 Annual Technical Conference and Exhibition, Washington, D.C., Oct. 4-7.

55. de Marsily, G., Lavedan, G., Boucher, M. and Fasanino, G.: "Interpretation of Interference Tests in a Well Field Using Geostatistical Techniques to Fit the Permeability Distribution in a Reservoir Model," *Geostatistics for Natural Resources Characterization, Part 2*, G. Verly, et al. (editors), D. Reidel Publishing Company, Dordecht (1987) 831-49.

56. Moffitt, P.D., Zornes, D.R., Moradi-Araghi, A. and McGover, J.M.: "Application of Fresh Water and Brine Polymerflooding in the North Burbank Unit (NBU), Osage County, Oklahoma," paper SPE 20466 presented at the Annual Technical Conference and Exhibition, New Orleans, LA, Sept. 1990.

57. Bass, N.W., Leatherock, C., Dillard, W.R. and Kennedy, L.E.: "Origin and Distribution of Bartlesville and Burbank Shoestring Oil Sands in Parts of Oklahoma and Kansas," Bulletin of American Association of Petroleum Geologists (Jan. 1937) vol. 21, no. 1, 30-66.

58. Trantham, J.C., Threlkeld, C.B. and Patterson, H.L., Jr.: "Reservoir Description for a Surfactant/Polymer Pilot in a Fractured, Oil-Wet Reservoir - North Burbank Unit Tract 97," Journal of Petroleum Technology (Sept. 1980) 1647-56.

59. Trantham, J.C. and Moffitt, P.D.: "North Burbank Unit 1,440-Acre Polymer Flood Project Design," paper SPE/DOE 10717 presented at the 1982 Joint Symposium on Enhanced Oil Recovery, Tulsa, OK, April.

60. Szpakiewicz, M.J., McGee, K. and Sharma, B.: "Geological Problems Related to Characterization of Clastic Reservoir for Enhanced Oil Recovery," paper SPE/DOE 14888 presented at the 1986 Joint Symposium on Enhanced Oil Recovery, Tulsa, OK, April.

61. Jackson, S.R., Tomutsa, L., Szpakiewicz, M., Chang, M.M., Honarpour, M.M. and Schatzinger, R.A.: "Construction of a Reservoir Model by Integrating Geological and Engineering Information - Bell Creek Field, A Barrier/Strandplain Reservoir," *Reservoir Characterization II*, L.W. Lake, H.B. Carroll, Jr. and T.C. Wesson (editors), Academic Press, Inc. (1991) San Diego, CA.

62. Journel, A.: "Non-Parametric Estimation of Spatial Distributions," Mathematical Geology (1983) vol. 15, 445-68.

63. Deutsch, C. and Journel, A.: *GSLIB: Geostatistical Software LIbrary*, Oxford University Press, New York, NY (1992).

64. Gomez-Hernandez, J. and Srivastava, M.R.: "isim3d: A 3-dimensional Multiple Indicator Simulation Program," Computer and Geosciences (1990), vol. 16, no. 4, 396-440.

65. Warren, J.E. and Price, H.S.: "Flow in Heterogeneous Porous Media," Society of Petroleum Engineers Journal (Sept. 1961) 153-69.

66. Young, L.C. and Stephenson, R.E.: "A Generalized Compositional Approach for Reservoir Simulation," Society of Petroleum Engineers Journal (Oct. 1983) 727-42.

67. *SURFER Reference Manual, Version 4*, Golden Software, Inc., Golden, CO (1990).

68. Metropolis, N., Rosenbluth, A.W., Rosenbluth, M.N., Teller, A.G. and Teller, E.: "Equation of State Calculations by Fast Computing Machines," The Journal of Chemical Physics (June 1953) 1087-92.

69. Muskat, M.: *Physical Principles of Oil Production*, McGraw-Hill Book Co., Inc., New York, NY (1949).

70. Desbrarats, A.J.: "Numerical Estimation of Effective Permeability in Sand-Shale Formations," Water Resources Research (Feb. 1987) 273-286.

71. Deutsch. C.V.: "Calculating Effective Absolute Permeability in Sandstone/Shale Sequences," SPE Formation Evaluation (Sept. 1989) 343-48.

72. Dimitrakopoulos, R.: "Geostatistical Modeling of Gridblock Permeabilities for 3D Reservoir Simulators," SPE Reservoir Engineering (Feb. 1993) 13-18.

73. Dagan, G.: "Models of Groundwater Flow in Statistically Homogeneous Porous Formations," Water Resources Research (1979) vol. 15, no. 1, 47-63.

74. Gelhar, L.W. and Axness, C.L.: "Three-Dimensional Stochastic Analysis of Microdispersion in Aquifers," Water Resources Research (Feb. 1983) vol. 19, no. 1, 161-80.

75. King, P.R.: "The Use of Renormalization for Calculating Effective Permeability," Transport in Porous Media (1989) vol. 4, 37-58.

76. Pratts, M.: "The Influence of Oriented Arrays of Thin Impermeable Shale Lenses or of Highly Conductive Natural Fractures on Apparent Permeability Anisotropy," Journal of Petroleum Technology (Oct. 1972) 1219-21.

77. Begg, S.H. and King, P.R.: "Modeling the Effects of Shales on Reservoir Performance: Calculation of Effective Vertical Permeability," paper SPE 13529 presented at the 1985 Symposium on Reservoir Simulation, Dallas, TX, Feb. 10-13.

78. Dykstra, H. and Parsons, R.L.: "The Prediction of Waterflood Performance with Variation in Permeability Profile," Production Monthly (1950) vol. 15, 9-12.

79. Gringarten, A.C.: "Interpretation of Tests in Fissured and Multilayered Reservoir with Double-Porosity Behavior: Theory and Practice," Journal of Petroleum Technology (April 1984) 549-64.

80. Isaaks, E.H. and Srivastava, R.M.: "Spatial Continuity Measures for Probabilistic and Deterministic Geostatistics," Mathematical Geology (1988) vol. 20, no. 4, 313-341.

81. Englund, E. and Sparks, A.: *Geo-EAS 1.2.1 User's Guide, EPA Report #60018-91/009*, EPA-EMSL, Las Vegas, NV (1988).

APPENDIX A

THREE-DIMENSIONAL TRUTH CASE

DATA SET

A description of the 3D Truth Case data set is presented is this appendix. The corresponding data files have been included on a 3-1/2" diskette attached to this dissertation and is in ASCII format. For discussion purposes, the data set contents have been subdivided into three categories: 1) well data, 2) grid block data and 3) flow simulation data.

Well Data

These files are assumed to represent flow unit scale average values at each of the 59 wells. The information is representative of that which would be obtained by well logs and subsequently averaged to obtain single values for each flow unit. Each well data file is listed and described below.

well2d.dat

This file contains the following four columns of two-dimensional well information: 1) well name, 2) x-axis coordinate, 3) y-axis coordinate, 4) top of Burbank Sandstone and 5) gross sand thickness. Five descriptive header lines are provided at the top of the file.

porwxy.dat

Porosity values for each of the 10 flow units at each of the 59 well locations are included in this file. These porosity values represent average values for each of the 10 flow units. In some cases, the flow unit is absent at a particular well location. A -999.0 is used to identify this special situation. The data is provided in columns and in the following order: 1) well name, 2) x-axis coordinate, 3) y-axis coordinate and 4 - 13) Flow Units 1 - 10 flow unit scale porosity values. Five descriptive header lines are included at the top of the file.

thickwxy.dat

This file is similar to the previous file but contains flow unit sand thickness values for each of the 59 wells instead of porosities. Four descriptive header lines are followed by the following columns of data: 1) well name, 2) x-axis coordinate, 3) y-axis coordinate and 4 - 13) Flow Units 1 - 10 sand thickness.

Grid Block Data

This group of data files represents flow simulation grid block scale data. Refer to Chapter II for details regarding the procedure used to generate the grid block scale values from the fine-scale conditional simulation results. The data is dimensioned 108 x 36 x 10. The areal grid blocks have a uniform size of 220 ft x 220 ft. The 10 vertical grid blocks are variable in size, being equal to the flow unit thickness at that particular grid block location.

porgb.dat

This file contains the grid block scale porosity values in Geo-EAS[81] format. Recall that for this format, the data is in one column, with x cycling faster than y cycling faster than z (i.e., the x-direction is incremented first; the z-direction is incremented last).

prmgb.dat

These grid block scale permeability values were derived from flow unit scale log(permeability) vs. porosity correlations and fine-scale porosity values. This data is also in Geo-EAS[81] format.

thkgb.dat

Unlike the grid block scale porosity and permeability values, the flow unit sand thick-

ness values contained in this file were directly obtained using conditional simulation at the grid block scale. These values were assumed to apply also at the fine-scale. Again, the data is in Geo-EAS[81] format.

Flow Simulation Data

The data files contained in this section summarize the information required for making the 3D Truth Case flow simulation. The only additional information needed is the grid block data itemized in the previous section.

misc.dat

This file contains miscellaneous flow simulation information, such as well operating conditions and grid dimensions.

fldprop.dat

A fluid property table is included in this file. Black oil fluid properties are listed as a function of reservoir pressure.

krog.dat

The oil-gas relative permeability table used in the flow simulation is contained in this file.

krow.dat

The oil-water relative permeability table used in the flow simulation is contained in this file.

fieldrat.dat

This file contains the simulated field performance, including total field oil, water and gas production rates and water injection rates. The rates represent monthly averaged values for the 10 years of primary production and 10 years of waterflooding. The data are presented in columnar format.

wellprod.dat

Monthly averaged individual well production rates are documented in this file. Well oil, water and gas production rates for primary and waterflood recovery are included. The data are presented in columnar format.

wellinj.dat

This file contains individual well injection rates on a monthly averaged basis. The data are presented in columnar format.

APPENDIX B

EXAMPLE PARAMETER FILE AND ASSOCIATED VARIABLES

This appendix provides additional information regarding the conditional simulation computer program developed during this study. An example parameter file is presented and associated variables are defined. This information, along with the discussion presented in the text, should be sufficient for those who are interested in pursuing this topic further. The simulated annealing program SASIM (Version 1.2) in the software package GSLIB[56] was used as a starting point for computer code development. The ensuing discussion will be limited to the modifications/additions made to the SASIM data input requirements and program variables.

Figure B-1 contains an example parameter file for the two-dimensional full-field case study presented in Chapter V. For illustrative purposes, only five conditioning wells have been included in the data set. The five wells are PI12, PI13, PI20, PI21 and P46, which represent the central five-spot pattern of the field. Refer to Figure 2.30 for well locations. Reference line numbers have been included in the first column of the parameter file for discussion purposes only and are not a part of the actual parameter file. The reference line numbers are used to identify parameter file lines.

- Output files (reference lines 1 - 3)

  The program generates both porosity and permeability realizations as output. Similar to the variogram output file, an indirect performance constraints file is generated which compares the computed values for the specified constraints based on the initial random spatial distribution to the corresponding values at the end of the conditional simulation.

- Variogram Model (reference lines 4 - 8)

  Two variogram model specification options are included. The first option is the same as that used in SASIM. For this option, analytical variogram models are specified, including spherical, exponential, gaussian and power models. Variogram modeling is usually restricted to the above models because of the positive definiteness restric-

reference line		
	Simulated Annealing With Indirect Performance Constraints (ipc's)	
	**********	
	START OF PARAMETERS:	
	well.dat	conditioning data (if any)
	1 2 3	columns: x, y, porosity
	-1.0E21	minimum value (missing values)
	0	0=non parametric; 1=Gaussian
	por.dstb	non parametric distribution
	1 0	columns: porosity, weight
	1 0.102	lower tail option and parameter
	1 0.276	upper tail option and parameter
1	por.out	output file for porosity simulation
2	perm.out	output file for permeability simulation
	por.var	output file for variogram results
3	example.ipc	output file for ipc's
	1 10000	debug level, reporting interval
	example.dbg	output file for debugging
	1	annealing schedule (0=auto)
	0.04 0.6 200000 200000 2 0.00005	manual schedule: t0, lambda, ka, k, e, Omin
	1	1 or 2 part objective function
	123456	random number seed
	1	number of simulations
	108 110.0 220.0	nx, xmn, xsiz
	36 110.0 220.0	ny, ymn, ysiz
	15000.	radius
4	2 09 1	ndir, nlag, method(0=conventional)
5	2 0	ixl(1), iyl(1)
6	0.000192	gam(1,1)
6	0.000234	gam(1,2)
6	0.000258	gam(1,3)
6	0.000290	gam(1,4)
6	0.000311	gam(1,5)
6	0.000329	gam(1,6)
6	0.000347	gam(1,7)
6	0.000355	gam(1,8)
6	0.000372	gam(1,9)
7	0 2	ixl(2), iyl(2)
8	0.000250	gam(2,1)
8	0.000323	gam(2,2)
8	0.000417	gam(2,3)
8	0.000519	gam(2,4)
8	0.000613	gam(2,5)
8	0.000717	gam(2,6)

Figure B-1 - Example parameter file

reference line		
8	0.000782	gam(2,7)
8	0.000789	gam(2,8)
8	0.000660	gam(2,9)
9	thick.out	thickness input file
10	1	column for thickness
11	1 2.54E+08	iflgpv, pvmdl
12	1 -1.093 13.8	ikval(0=k, 1=log(k)), akphi(int), bkphi(slope)
13	5	no. of wells
14	48 24 1 1	iwell, jwell, iflgkw, iflgpd (PI12)
15	1.912 47 49 23 25	kwmdl, ikwfs, ikwls, jkwfs, jkwls (PI12)
16	2.49E+6 42 54 18 30	pdmdl, ipdfs, ipdls, jpdfs, jpdls (PI12)
14	60 24 1 1	iwell, jwell, iflgkw, iflgpd (PI13)
15	1.757 59 61 23 25	kwmdl, ikwfs, ikwls, jkwfs, jkwls (PI13)
16	2.40E+6 54 66 18 30	pdmdl, ipdfs, ipdls, jpdfs, jpdls (PI13)
14	48 13 1 1	iwell, jwell, iflgkw, iflgpd (PI20)
15	1.811 47 49 12 14	kwmdl, ikwfs, ikwls, jkwfs, jkwls (PI20)
16	2.44E+6 42 54 7 19	pdmdl, ipdfs, ipdls, jpdfs, jpdls (PI20)
14	60 13 1 1	iwell, jwell, iflgkw, iflgpd (PI21)
15	1.937 59 61 12 14	kwmdl, ikwfs, ikwls, jkwfs, jkwls (PI21)
16	2.50E+6 54 66 7 19	pdmdl, ipdfs, ipdls, jpdfs, jpdls (PI21)
14	54 18 1 1	iwell, jwell, iflgkw, iflgpd (P46)
15	2.026 53 55 17 19	kwmdl, ikwfs, ikwls, jkwfs, jkwls (P46)
16	2.51E+6 48 60 12 24	pdmdl, ipdfs, ipdls, jpdfs, jpdls (P46)
17	4	no. of inj/prod pairs
18	05 01 1 1	idprd, idinj, iflgkp, iflgcv
19	1.9523 48 5 18 24	kpmdl, ikpfs, ikpls, jkpfs, jkpls
20	0.204	cvkmdl
18	05 02 1 1	idprd, idinj, iflgkp, iflgcv
19	1.8292 54 60 18 24	kpmdl, ikpfs, ikpls, jkpfs, jkpls
20	0.1772	cvkmdl
18	05 03 1 1	idprd, idinj, iflgkp, iflgcv
19	1.9335 48 54 13 18	kpmdl, ikpfs, ikpls, jkpfs, jkpls
20	0.2418	cvkmdl
18	05 04 1 1	idprd, idinj, iflgkp, iflgcv
19	1.9601 54 60 13 18	kpmdl, ikpfs, ikpls, jkpfs, jkpls
20	0.2798	cvkmdl
21	0.20 0.25 0.10 0.15 0.15 0.15	frcvar, frcnw, frcda, frcpat, frccvk, frcpv

Figure B-1 - Example parameter file (continued)

tion required when solving the kriging equations for kriging-based conditional simulation algorithms.[16] However, simulated annealing does not have any such restrictions. The actual variogram values at various lags and directions can be specified. This eliminates the need to model the variograms. However, caution must be used to assure that the experimental variogram values make "geologic sense." The specification of experimental variogram values represents the second variogram model option. In Figure B-1, experimental variogram values for nine equally-spaced lag intervals are specified along the major and minor axes directions.

- Total system constraints (reference lines 9 - 10)

  The method assumes that the spatial distribution of sand thickness is known. Consistent with other SASIM input data files, the sand thickness file is assumed to be in a data format similar to what is required for the software package Geo-EAS.[81] The user must specify which column of the data file represents the thickness variable. Total system pore volume is also specified. This can be input in ft^3 or bbls. It is assumed that porosity and log(permeability) and linearly correlated. Hence, the intercept and slope of the linear relationship are required input. An option is included to allow either permeability or log(permeability) values to be specified for permeability-based constraints.

- Primary indirect performance constraints (reference numbers 13 - 16)

  The indirect performance constraints which influence primary performance are specified on reference lines 13 - 16. The number of wells are specified on reference line 13. Reference lines 14 - 16 are repeated for each well. The (i,j) location of the well, an on/off k_{NW} flag and an on/off PV_{DA} flag are included on reference line 14. The on/off flags remove the restriction specifying all indirect performance constraints for a particular well. For example, an estimate of the near well effective permeability may be available for a well but not enough well data may have been collected to estimate the

drainage area pore volume. Reference line 15 is used to specify k_{NW} and the corresponding area (lower left and upper right (i,j) points defining the rectangle). Similarly, the well drainage area pore volume and the corresponding (i,j) limits (assuming a diamond-shaped geometry) are input on reference line 16.

- Waterflood indirect performance constraints (reference lines 17 - 20)

  The next section of the parameter file specifies the waterflood indirect performance constraints. The number of injector/producer pairs is listed on reference line 17. Information regarding each injector/producer pair is included on reference lines 18 - 20. The identification number of both the producer and injector and on/off flags for k_{PAT} and CV_{k*} are specified on reference line 18. The identification numbers refer to the sequential order by which the wells were first identified on reference line 14. The on/off flags are used to specify whether or not the particular constraint is to be imposed or not. Reference line 19 is used to specify the permeability (or log(permeability) value representing k_{PAT} and the (i,j) points defining the respective rectangular area. The value of CV_{k*} is indicated on reference line 20.

- Relative contribution (reference line 21)

  The last entry, reference line 21, represents the weighting factors applied to each of the six constraints: variogram, k_{NW}, PV_{DA}, k_{PAT}, CV_{k*} and PV_T. The relative weights should reflect the degree of confidence which exists in each constraint. Refer to Eq. 3.22 and the related discussion for more information on how the weighting functions were mathematically implemented.